AEOLIAN PROCESSES ON MARS: ATMOSPHERIC MODELING AND GIS ANALYSIS

Thesis by

Lori K Fenton

In Partial Fulfillment of the Requirements for the

Degree of

Doctor of Philosophy

CALIFORNIA INSTITUTE OF TECHNOLOGY

Pasadena, California

2003

(Defended February 3, 2003)

"…Combining this evidence with that we already possess of the presence of water in its liquid, vaporous, and solid states, upon the surface, and with the certainty that the red tint of parts of the planet is due to a real ruddiness of substance (corresponding to the tint of certain soils upon our own earth), we cannot but recognise the extreme probability that in all essential habitudes the planet Mars resembles our own earth."

— Richard A. Proctor, *The Orbs Around Us,* 1872.

"But it does not seem too much to hope that some day (haply not so far distant) that the lesson taught us by Professor Smyth's Teneriffe experiment will be appreciated as it deserves. Then a telescope surpassing in power any yet constructed shall be placed where alone the power of such an instrument can be efficiently exerted – where Newton long since told men that such an instrument should be placed – far above the denser atmospheric strata whose disturbances never cease, and are magnified and aggravated by every increase of telescopic power. When this is done, we may look in Mars for that which has long been sought for fruitlessly upon the lunar surface – the signs of life, of change, of progress, of decay."

— Richard A. Proctor, *Essays on Astronomy,* 1872

ACKNOWLEDGMENTS

The list of people who are responsible for getting me to this point is incredibly long. I will undoubtedly leave out people who deserve recognition simply because their contributions have slipped my mind, and I hope that my forgetfulness is not mistaken for a lack of gratefulness. The first people to thank are my parents, who always encouraged my independence and persistence. Without my mother's creative thought and my father's fascination with science, I doubt I would be here today.

I have had numerous mentors since I was an undergraduate. My advisor Arden Albee has always forced me to consider all sides of a problem, even when I'm convinced I've already solved it. I don't think we would have had as much fun if we weren't both such stubborn people. Mark Richardson has provided nonstop support and enthusiasm since he arrived at Caltech, and he has been very generous with providing and arranging for computer time for model runs. I was fortunate enough to acquire an advisor at the USGS in Flagstaff, AZ: Wes Ward gave me the resources to begin my GIS analysis and took some time out of his busy schedule for field trips and many rather invaluable conversations. Bruce Murray took me on when I first came to Caltech, introducing me to the world of Martian image analysis. My undergraduate advisors also deserve recognition: John Pearl at GSFC who started me on the path of Mars science with his patient explanations and wry humor, and Shymala Dason who guided me into the practicalities of the working world.

A number of students (and former students) have given me support or help over the years here. Sometimes it's advice or a listening ear, and sometimes it's data or a routine vital to my research. A short and by no means complete list consists of Shane Byrne, Ben Lane, Dave Camp, James Dennedy-Frank, Josh Bandfield (of

ASU), Anthony Toigo, Sarah Stewart-Mukhopadhyay, Antonin Bouchez, Margaret Belska, Zane Crawford, Michelle Koutnik, Anton Ivanov, Ashwin Vasavada, Adam Showman, Emily Brodsky, and Dave Kass. JPL'ers and other researchers who have provided support include Ken Herkenhoff and Tom Farr. Technical support in the form of debugging programs, providing nifty routines, or making computers, models, and equipment function properly is vital to any research program, and these people are greatly appreciated for their last-minute miracles as well as their conversation. Most notably this list includes Shawn Ewald, Trent Hare (of the USGS), JoAnne Gibson, Mike Black and recently, Ian McEwan. Susan Leising in the GPS library has magically produced articles and books for me that I was sure were impossible to find. Not to be forgotten, the office administrators who make the world go around (they make it look so easy): Irma Black, Leticia Calderon, Nora Oshima, and Kay Campbell in the Planetary Science office, and Carolyn Porter, Donna Sackett, and Marcia Hudson in the GPS office. A special note goes to Terri Gennaro who taught me 4x4 driving and has always been there to share a laugh or a story.

Friends from outside Planetary Science and the division have given me a measure of sanity and balance that is necessary to survival. Those closest to me have been Gilead Wurman, Chad Parker, and Aaron Eichelberger, and without their support and encouragement I would feel much older than I do. I give a special thanks to Loretta Hidalgo for introducing me to the world of Landmark Education. I also thank the Caltech Ballroom Dance Club, the old milonga group (especially Fabrizio Pinto and Taffy Beauvais), and the LARPers (especially Jordan Lees and Nick Burden). Without these people my life would have been much less interesting.

ABSTRACT

Wind is currently the dominant geological agent acting on the surface of Mars. A study of Martian aeolian activity leads to an understanding of the forces that have sculpted the planet's face over the past billion years or more and to the potential discovery of climate shifts recorded in surface wind features that reflect ancient wind patterns. This work takes advantage of newly available tools and data to reconstruct the sedimentary history reflected in aeolian features on Mars. The thesis is divided into two main projects. In the first section, a widely accepted hypothesis, that oscillations in Martian orbital parameters influence atmospheric circulation patterns, is challenged. A Mars global circulation model is run at different obliquity, eccentricity, and perihelion states and the predicted surface wind orientations are correlated with observed aeolian features on the Martian surface. The model indicates that orbital parameters have little effect on wind patterns, suggesting that aeolian features not aligned with the current wind regime must have formed under atmospheric conditions unrelated to orbital parameters. In the second project, new spacecraft data and a mesoscale model are used to determine the sedimentary history of Proctor Crater, a 150 km diameter crater in the southern highlands of Mars. Using high-resolution imagery, topography, composition, and thermal information, a GIS was constructed to study the aeolian history of the crater, which was found to have a complex interaction of deposition and erosion. Surficial features include 450 m of sediments filling the crater basin, small bright bedforms, dust devil tracks, and a dark dunefield consisting of coarse, basaltic sand and containing slipfaces indicative of a multidirectional, convergent wind regime. All wind features, both ancient and contemporary, are coaligned, indicating that formative wind directions have changed little since the first aeolian features formed in this area. Mesoscale model runs over Proctor Crater indicate that two dune slipfaces are created by winter afternoon geostrophic westerlies and summer evening katabatic easterlies, and that dust devil tracks are created by summer noontime rotational westerlies. Using all available tools, this thesis begins the work of understanding how aeolian processes have influenced the Martian surface.

TABLE OF CONTENTS

LIST OF ILLUSTRATIONS AND/OR TABLES

Number *Page*

NOMENCLATURE

GCM – General Circulation Model

GFDL – Geophysical Fluid Dynamics Laboratory

GIS – Geographical Information System

L_s – Solar Longitude of Mars' orbit around the sun, a measure of season (0° – 360°, where 0° = northern spring equinox/southern fall equinox, 90° = northern summer solstice/southern winter solstice, 180° = northern fall equinox/southern spring equinox, and 270° = northern winter solstice/southern summer solstice)

MGS – Mars Global Surveyor

MM5 – Mesoscale Model 5

MOC – Mars Orbiter Camera

MOLA – Mars Orbiter Laser Altimeter

MPF – Mars Pathfinder

TES – Thermal Emission Spectrometer

VL 2 – Viking Lander 2

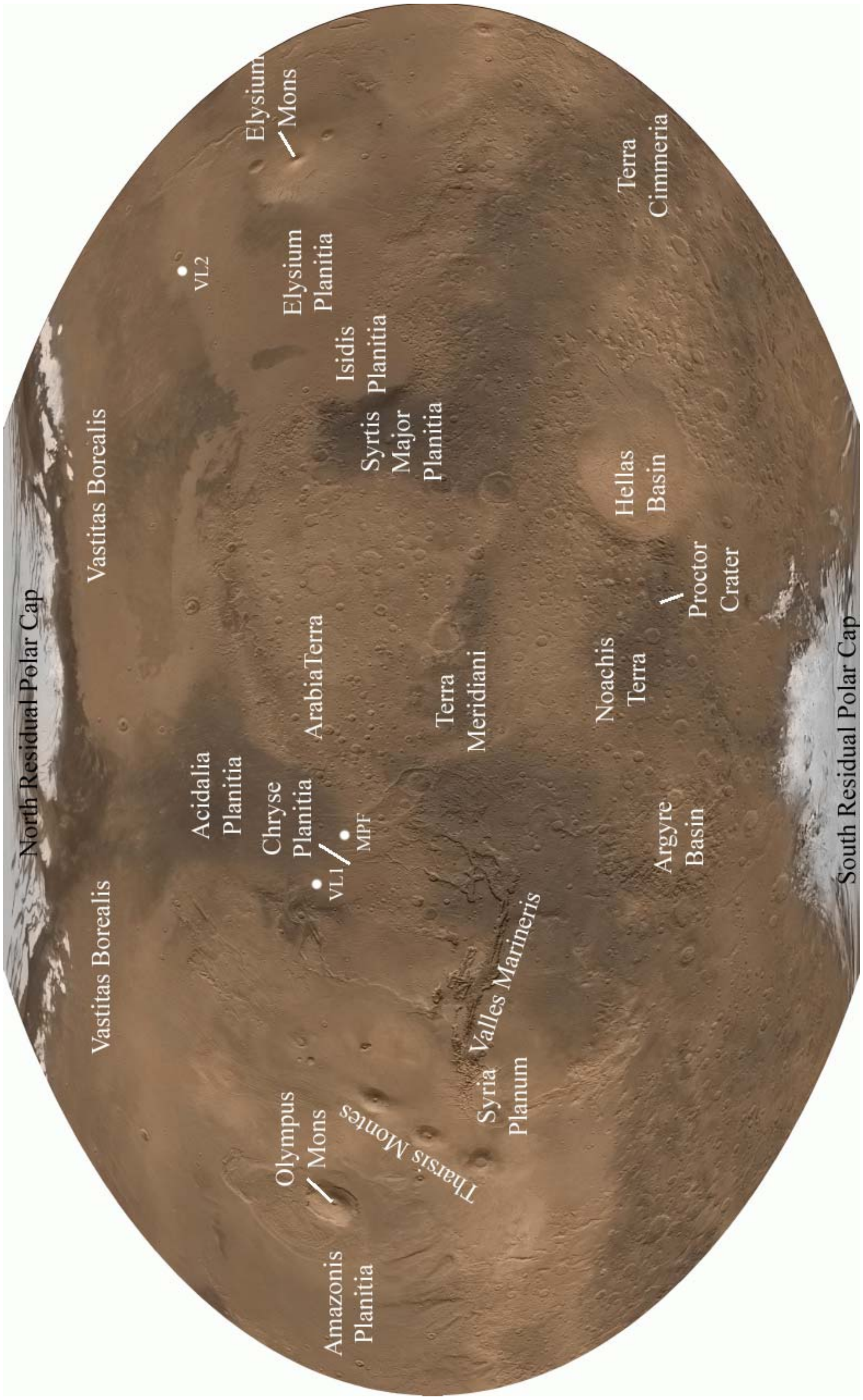
North Residual Polar Cap
Vastitas Borealis
Vastitas Borealis
Amazonis Planitia
Olympus Mons
Tharsis Montes
Syria Planum
Valles Marineris
VL1
Chryse Planitia
MPF
Acidalia Planitia
ArabiaTerra
Terra Meridiani
Noachis Terra
Argyre Basin
Proctor Crater
Hellas Basin
Syrtis Major Planitia
Isidis Planitia
Elysium Planitia
VL2
Elysium Mons
Terra Cimmeria
South Residual Polar Cap

Chapter 1

INTRODUCTION AND OVERVIEW

Wind is currently the dominant geological agent acting on the surface of Mars. The general lack of contemporary aqueous, volcanic, and tectonic features suggests that aeolian (*i.e.,* wind) processes have prevailed on the Martian surface for a geologically significant period of time. Thus a study of aeolian activity leads to a better understanding of the forces that have sculpted the face of Mars over the past billion years or more. Furthermore, such a study has the potential for the discovery of climate shifts recorded in aeolian features that reflect ancient wind patterns. The instruments on the Mars Global Surveyor (MGS) spacecraft have provided data on the Martian surface with unprecedented detail, revealing wind-related features such as tracks eroded by dust devils as they travel downwind, small bright bedforms indicative of persistent strong winds, and sand dunes where previous spacecraft imagery indicated only dark "splotches." MGS images have also shown layered sediments with complex stratigraphic relationships, indicative of several episodes of successive erosion, deposition, and inactivity, all of which may well have been produced by aeolian activity [*e.g., Malin and Edgett,* 2000a]. In addition, mesoscale models of the Martian atmosphere with horizontal resolutions down to tens of meters are now available and can be used to study small-scale interactions between the surface and atmosphere. Given the acquisition of new data and the advent of these new tools, there has been no better time to investigate Mars' ubiquitous aeolian features to develop an understanding of how and when they formed, and how they are influenced by and subsequently reflect changes in climate.

I chose this work for its obvious potential implications on recent climate change on Mars, as well as for the excitement of studying a currently active process on a body that has so often been termed "dead." There are a number of advantages in taking on such a thesis topic at this time. One such benefit is that with the new high-resolution spacecraft data and mesoscale models, the study of Mars has shifted from an astronomical to a geological perspective. That is, in the past, typical studies encompassed a large part or all of the Martian surface, with conclusions indicating regional or global trends in cratering, dust mantling, ice cover, and the like. The new data and models allow for detailed studies of small areas which produce an understanding of local histories and conditions. These small-scale studies must ultimately be tied in with the regional and global-scale studies, but they add a refinement and precision that the larger-scale studies cannot provide. Both scales of studies are necessary for a complete understanding of the Martian history, and for the first time both types of study are possible.

Another advantage may be gained from using the new data and models. The availability of high-resolution imagery, topography, thermal, and compositional data as well as high spatial- and temporal-resolution atmospheric model output may be used in concert, each data set adding its own unique "piece of the puzzle" to the geological and climatic interpretation. The careful combination of geologic data with atmospheric data is particularly important for aeolian studies because they depend on one another. In the past, most work utilized only atmospheric or geological data to study aeolian features on Mars, occasionally leading to errors such as mislabeling aeolian features (which then propagates through the scientific community) or inaccurate estimation of sand and dust transport parameters. However, such interdisciplinary research on aeolian processes from both a geological and an atmospheric perspective is necessary for understanding how the surface and atmosphere interact with one another. It is vital from a geological perspective in that it is the only way to thoroughly study the most active surface process on Mars today, and it is vital from an atmospheric perspective in that surface features provide the only "ground truth" for verification of modeled wind circulation patterns and stresses. For the first time, data and models are available to allow such investigations to proceed, and this thesis work takes full advantage of this technique.

This thesis consists of three chapters, each of which discusses a self-contained research project. The thesis topic was chosen after an extensive research of existing literature on terrestrial and Martian aeolian geomorphology and sedimentology, as well as remote sensing techniques. Originally I had begun work on a sand transport model, which used modeled wind stresses and velocities to determine where the global sand sinks and sources are currently located, but too little is known about the distribution of mobile sand and surface roughness on the Martian surface, and so I decided that it was unlikely that the transport model would produce realistic results. The completed work and motivation for each chapter is described briefly below. Chapter 2 was supported in part by a PG&G grant (NRA 98–OSS–03); Chapter 2 was supported in part and Chapter 3 was supported in full by an MDAP grant (NRA 00–OSS–01 MDAP).

Chapter 2. The obliquity, orbital eccentricity, and argument of perihelion of Mars oscillate significantly over long time periods, with unknown consequences on the planet's climate. Some surface features, such as dunes and bright streaks, match well with the currently predicted wind patterns, and other types of aeolian features, such as yardangs, dark streaks, and ventifacts, do not. As a result, it has long been hypothesized that the astronomical variations change wind circulation patterns, and thus creating aeolian features that do not match present-day wind patterns. To test this hypothesis, my coauthor and I ran the GFDL Mars general circulation model (GCM) at different obliquity, eccentricity, and argument of perihelion states. Using a higher time resolution than has been applied before, we established that dark streaks are contemporary features produced by a wind that in previous studies had been washed out due to poor time resolution. More importantly, we also showed that orbital parameters have little effect on wind circulation patterns, concluding that the aeolian features that do not align with current winds must have been produced under very different conditions unrelated to varying orbital parameters.

Chapter 3. Before the Mars Global Surveyor mission, Martian sand dunes were considered mysterious features. They were known to exist in a sand sea ringing the north polar cap, and as small accumulations in the floors of several craters in the southern highlands. It was not known whether or not they were active. Furthermore, only dunes with a morphology indicative of unidirectional winds appeared to be present in abundance, and it was not clear why this would be the case when on the Earth dunes indicating bimodal and multimodal wind regimes also occur. The introduction of MGS data changed this view drastically, showing that these dark dunes are much more prevalent than previously thought, and that much smaller bright bedforms are visible in high-resolution images where before such features were only hinted at. Noting both a lack of a detailed study of aeolian features in any particular region of Mars, as well as the abundance of new data, I decided to conduct such a study. I built a geographical information system (GIS) for Proctor Crater, a 150 km diameter crater in the southern highlands containing a large dark dunefield. Proctor Crater was the first place where dunes were discovered on Mars during the Mariner 9 mission in 1971–72, and as such it has become the type location for studies on dune morphology, thermal inertia, and composition. Using GIS analysis, I found that the sedimentary history of Proctor Crater has involved a complex interaction of deposition and erosion, much of which is likely to be aeolian in origin. The crater has accumulated as much as 450 m of sediments, the top layer of which now comprises the present-day crater floor. Small bright bedforms, dust devil tracks, and sand drifts abound, indicating that aeolian processes dominate as expected. Close inspection of dunes indicates that the dunefield is located in a multidirectional wind regime, consisting of reversing transverse and star dunes, contrary to what was expected in pre-MGS days. The dark dunes are composed of coarse, basaltic sand that is probably volcaniclastic in origin, and which was blown into the crater from the southwest (locating the provenance of the sand requires a broader regional study). The dunes are undoubtedly active, but because they are located in a convergent wind regime they have little (if any) net transport (thus the lack of dune movement does not necessarily indicate that they are inactive). All observed aeolian features, from the potentially ancient bright duneforms, to the nearly erased remnant of a sand transport pathway into the crater, to the long-lived dunes themselves, and to the annually created and erased dust devil tracks, indicate an unchanging wind pattern, consistent with the model predictions from Chapter 2. A detailed study such as this greatly changes the way dunes and other aeolian features on Mars are regarded, answering many of the old pre-MGS questions but creating new ones as more and more is discovered. Further inquiries of this sort will continue to answer these questions and create a general understanding of how aeolian processes influence the Martian surface.

Chapter 4. The newly developed mesoscale atmospheric models are necessary, although largely unexplored, tools for investigating interactions between the surface and atmosphere. In the past, GCM's predicted only large-scale winds with horizontal scales on the order of hundreds of kilometers. They could not predict small-scale flow dictated by local topography, and often were run with too large a timestep to predict shifts in daily winds (as shown in Chapter 2). Thus the newly developed mesoscale atmospheric models are necessary, although still largely unexplored, tools for investigating interactions between the surface and atmosphere. My coauthors and I applied the Mars Mesoscale Model 5 (MM5) to the atmosphere over Proctor Crater, the same area studied in Chapter 3. In some sense the model output may be regarded as yet another data set to be included in the GIS described in Chapter 3. A Martian atmospheric model has never before been run in conjunction with a thorough geological study of a particular area. In addition, a Martian atmospheric model has never been applied with the intent of understanding the morphology of a dunefield and other nearby aeolian features. The MM5 predicted two of the three observed dune slipface orientations as well as the winds that produce dust devil tracks in the summer. The wind producing the more prevalent of the dune slipfaces (the primary winds) was the strongest of the year, blowing in the fall and winter during the early afternoon as geostrophic-enhanced westerly winds. The wind producing the least prevalent of dune slipfaces (the tertiary winds) blows in the spring and summer evening as easterly katabatic flows down the rim of Proctor Crater, influencing only the eastern portion of the dunefield. Winds producing the remaining dune slipfaces are not predicted by the model, and it may be that these winds are produced by rare storms that the model does not capture. Wind stresses are still not high enough to predict sand saltation, and the reason for this is due to a low model resolution, even though this study used a higher spatial resolution than has been applied in the past. Although there are issues with the model output, the MM5 does a superb job of explaining the forces driving dune morphology and other nearby aeolian features.

The chapters are similar in their approach and their research goals. Each chapter describes research that changes what is known about aeolian processes on Mars by varying different parameters and using higher resolution data and models than before. Chapter 2 challenges an old hypothesis that astronomical oscillations are responsible for ancient wind circulation patterns by running a GCM under those conditions and comparing the results to observed surface features. Chapter 3 uses new high-resolution imagery, topography, thermal, and compositional data to perform the first detailed and comprehensive study of the aeolian history of a region. Finally, Chapter 4 applies a mesoscale model to the study area of Chapter 3 to explain the regional wind patterns behind the observed aeolian features, supporting the aeolian history described in Chapter 3. This thesis takes the first steps towards applying modern methods and viewpoints to the study of Martian surface processes.

Chapter 2

MARTIAN SURFACE WINDS: INSENSITIVITY TO ORBITAL CHANGES AND IMPLICATIONS FOR AEOLIAN PROCESSES

Lori K. Fenton and Mark I. Richardson

Division of Geological and Planetary Sciences, California Institute of Technology, Pasadena, California

Abstract. Aeolian features observed on the surface of Mars provide insight into current, and potentially past, surface wind systems. In some cases the features are clearly transient and related to the lifting and settling of atmospheric dust. Other features, like dunefields, yardangs, and ventifacts, are more persistent and likely require significant time to form. In this study we analyze the observed directions of selected aeolian features with the aid of the Geophysical Fluid Dynamics Laboratory Mars general circulation model (GCM). Initially, we examine bright and dark streaks which have been observed to form in association with global dust storms. The ability to match these features with Mars GCM wind directions provides an important validation of the model. More important, we are able to define best fit seasons and local times for both types of features which provide the basis for extension and modification of the *Veverka et al.* [1981] model of bright and dark dust streak formation. In addition these best fit times correspond well with the dark streak "wind storm" model of *Magalhães and Young* [1995]. The primary focus of this paper is to provide constraints on the range of mechanisms proposed to explain inconsistencies between current wind direction patterns and long-term wind indicators (for example, the misalignment of rock tail and ventifact orientations at the Mars Pathfinder landing site). Specifically, we assess

whether changes in planetary obliquity, precession, or global dust opacity could significantly alter patterns of surface wind directions. In all cases we find the seasonal and annual average wind direction patterns to be highly invariable. While changes in the dust loading (hence the partitioning of solar absorption between the surface and atmosphere) and in the surface latitude of maximum solstitial insolation cause the vigor of the large-scale circulation to increase (especially the Hadley cell), the spatial patterns of the surface wind orientations remain essentially unchanged. In the case of perihelion during northern summer (opposite of the current perihelion position), the northern summer Hadley cell remains weaker than the southern summer cell despite the strengthened heating in the northern hemisphere. Taken together, these results cast significant doubt on orbital explanations for surface wind changes. It is thus suggested that significant changes in topography (*e.g.,* Tharsis uplift, true polar wander) or climate (*e.g.,* the existence of a significantly thicker atmosphere or an ocean at some point in the past) are more likely explanations for long-term wind indicators such as the ventifact orientations at the Mars Pathfinder landing site.

1. Introduction

Wind is currently the dominant geological agent acting on Mars. This is evidenced by images of the Martian surface which show ubiquitous aeolian landforms [*e.g., Greeley et al.,* 1992]. These landforms include sand dunes, wind streaks, yardangs, deflation pits, which have been observed in images returned by Mars Global Surveyor and the Viking Orbiters [*Ward et al.,* 1985], and ventifacts, which have been observed by the Viking and Mars Pathfinder landers [*Greeley et al.,* 1999]. The ongoing activity of aeolian processes is evidenced by the observation of dust suspended in the atmosphere, variations over time in the shapes and locations of albedo features on the surface, and temporal variations in the occurrence of wind streaks.

A large body of work on Martian aeolian features has accumulated since the Mariner 9 mission in 1970-1971. Examination of both lander and orbiter images has revealed a number of aeolian landforms on the basis of their strong similarity to known, wind-formed features on the Earth, the best-studied of which are the following:

1. Yardangs are large, free-standing, streamlined blocks that are observed to form in terrestrial deserts. In a number of locations on the Martian surface, cut and streamlined blocks exist which are nearly identical to aerial images of terrestrial yardangs, suggesting a very similar origin [*Ward,* 1979].

2. Close-up examination of rocks at the Viking and Mars Pathfinder landing sites has revealed aligned pits, grooves, flutes, and rills [*Bridges et al.,* 1999]. Similar preferential alignment of such features on terrestrial desert rocks is ascribed to the action of persistent wind as an erosive agent. These rocks have thus been interpreted as ventifacts.

3. Sand dunes provide very direct evidence for aeolian activity which not only generates sand-sized particles through erosion but subsequently transports and sculpts the sand deposits into dunes and dunefields. Because of their crispness, lack of superimposed features, and evidence for slipface avalanching [*Edgett and Malin,* 2000], some dunes are thought to be recently or currently active. In contrast to terrestrial dunes, almost all Martian dunes at large scales are transverse, indicating formation by predominantly unidirectional winds, based on terrestrial experience.

4. Windblown streaks of material are observed on a variety of scales across the Martian surface. These streaks are analogous to tails of material observed to form in the lee of topographic features in windy, desert locations on the Earth [*e.g., Edgett and Malin,* 2000]. A number of different bright and dark streaks occur in

spacecraft images of Mars, and it is believed that some streaks are composed of dust and some of sand. Further, in some cases, streaks may represent regions of material depletion and in others they may represent regions of accumulation.

With the potential exception of wind streaks, all four types of features require a significant time to form. For example, on Earth, ventifacts form in tens of years to thousands of years [*Sharp,* 1964, 1980] (*i.e.,* orders of magnitude less than the periods of orbital oscillations). If, in addition, these features exhibit distinct directionality, it is likely that the dominant, persistent wind direction at the time of formation is recorded by the features. Martian aeolian landforms do, in fact, provide strong evidence for unidirectionality of the dominant winds. The nearly exclusive transverse nature of large Martian dunes provides evidence for unidirectionality of winds in the recent past (*i.e.,* that portion of geological time over which sand deposit morphologies have been determined). Additional evidence for near unidirectionality comes from the preferential orientation of ventifact pits and sand streaks at various scales. Some care must be taken in interpreting the aeolian bedform record. Streamline directionality in yardangs may be structurally controlled by the rock out of which they are carved, and the directionality of small dunes in channels and craters will be created by winds strongly controlled by the local topography [*Ward,* 1979; *Greeley et al.,* 1993]. However, the fact that aeolian bedforms may provide a record of wind directionality provides one very important motivation for studying these features.

The nature and significance of the aeolian bedform record of wind directionality provide the primary subject matter for this paper. This wind record is important because of the degree to which surface winds are coupled to the processes driving atmospheric circulation and climate. Thus the record provides a unique constraint on models of the climate. However, this relationship is reciprocal, as models of the climate and circulation can then be used to interpret the bedforms. The problem is relieved of circularity by the multiplicity of distinct aeolian features. Examination of this range of features has already generated some apparent contradictions and puzzles. At the Mars Pathfinder landing site, sand tails and small duneforms were found to align well with the strongest wind directions predicted by the NASA Ames general circulation model (GCM) [*Greeley et al.,* 1999]. However, at the same site, grooves and flutes in ventifacts were found to be oriented roughly orthogonal to the prevailing winds. This disagreement has been interpreted as demonstrating that the ventifacts were cut when the circulation was significantly different [*Bridges et al.,* 1999]. Another example is provided by the observed formation of bright and dark wind streaks during and after the second great dust storm of 1977. Wind streaks form in association with crater rims and other topographic features and likely represent material deposition or erosion due to airflow modification by topography. Within a belt near 30° S, both bright and dark streaks were observed to form, but with rather different directionalities, even when originating from the same topographic feature [*Veverka et al.,* 1981].

Analytic models of the surface winds generated by tropical Hadley cell circulations have been used to demonstrate, in a longitudinally averaged sense, that observed bright streaks are consistent with expected, current wind patterns [Magalhães, 1987]. This work has been expanded to consider the effects of longitudinal variations due to topography by *Greeley et al.* [1993] using a Mars GCM in which diurnally averaged winds corresponded well with bright streaks and some dune directions, but not dark streaks or yardangs. Further application of the GCM to dune forms supports the idea of strongly unidirectional Martian winds [*Lee and Thomas,* 1995]. These results suggest that bright streaks and dunes provide a representative record of current winds, while yardangs, dark streaks, and ventifacts do not. There must be two distinct reasons for the nonagreement of dark erosional streaks with diurnal-average modeled current winds and the disagreement between yardangs and ventifacts with these same modeled winds. This distinction is necessitated by the nature of the features. Yardangs and ventifacts are features which require significant time to form either by the deflative action of the wind or by the abrasive action of saltating sand. Thus this disparity in alignment between yardangs and ventifacts with current winds has led to the proposal that the observed yardangs and ventifacts are no longer being formed and hence record ancient wind regimes. The question then arises of what could cause significant variations in the global wind regime. Do these indicators record winds generated at times when the orbital eccentricity and planetary tilt were very different, or are they related to a thicker, early atmosphere or variations in topography? Unfortunately, there are no yardangs near the Pathfinder landing site that could provide a comparison between the winds that formed them. Dark streaks are entirely different. They are observed to form over timescales of days by orbiter imaging and under distinct meteorological conditions. Specifically, they are observed to form in the late stages of dust storm decay [*Veverka et al.,* 1981]. Thus dark streaks do not require persistent winds over extended periods and, further, occur when the surface dust distribution has been perturbed by settling of dust from a global dust storm. Despite the good observational record of dark streaks, the mechanism of their origin remains uncertain, and their directions remain unexplained.

In this paper we employ the Mars GCM developed at the Geophysical Fluid Dynamics Laboratory (GFDL) as a tool with which to examine the various aeolian bedforms on Mars. Specifically, we address two questions. First, we ask how well wind direction predictions generated by the Mars GCM can explain both the bright and dark wind streaks. Since it is certain that these features are contemporary, failure to agree with these features casts significant doubt on the ability of such models to tell us anything about ancient wind regimes. Having established that the wind streak directions can be fully explained with the Mars

GCM (and providing strong evidence for a nighttime lee wave/windstorm mechanism for their formation, as argued by *Magalhães and Young* [1995]), we move on to examine the variation of surface wind directional regimes as the planetary orbital and spin properties change (precession of the equinoxes and cycles of obliquity vary on timescales of 10^4-10^5 years [*Ward,* 1992]). These numerical experiments are designed to ask how well such changes can explain the occurrence of aeolian bedform directions, as represented by ventifacts and yardangs, which do not agree well with dunes or Mars GCM predictions. Put simply, we examine the hypothesis that ventifacts and yardangs record wind direction patterns associated with secular orbital variations.

In most of the cases that we discuss, the surface winds have been diurnally averaged and then averaged over a season or longer. It is reasonable to question how accurately such winds could predict the orientation of long-standing aeolian features. For example, it is possible that dunes in a sand sea could shift orientation during a short-lived local dust storm that becomes washed out in the seasonally averaged winds, thus leading to dune orientations that do not coincide with average wind directions. However, we regard this situation as unlikely. It has long been known that the vast majority of the large Martian dunes as seen in the Viking Orbiter and Mariner 9 images are transverse in form [*Breed et al.,* 1979], indicating that the winds strong enough to initiate saltation and form dunes are almost without exception unidirectional [*Wasson and Hyde,* 1983]. This is supported by the GCM calculations of wind modality made by *Lee and Thomas* [1995]. In addition, both ventifacts and yardangs require strong, unidirectionally consistent winds to form. Thus averaged winds are likely to reflect the winds that form these long-standing persistent features.

We begin in the next section by describing the GFDL Mars GCM, which provides the numerical model used in analyzing the aeolian bedform data. In

Section 3 we briefly describe the global surface wind patterns resulting from the Mars GCM when it has been tuned to provide the best simulation of a non-dust storm Martian year. Section 4 provides a discussion of how surface winds vary if the dust optical depth is increased from this control value, as happens during dust storms. These descriptions are provided for comparison with later simulations in which orbital parameters are varied and allow some sense of the (small) error in surface wind directions associated with not knowing how dust opacity will vary with changes in orbital forcing. In Section 5 we test the ability of the GFDL Mars GCM to explain the observed contemporary streak data. Correlation of model predictions with observations is undertaken as a function of season and local time for a simulation which produces a good match to surface pressure and air temperature observations of the second great dust storm of 1977. The GCM explains the streak data well, and on the basis of this analysis we propose a model for the formation of bright and dark streaks which builds on, but significantly modifies, the model of *Veverka et al.* [1981] and in its explanation of dark streaks is very closely aligned with that of *Magalhães and Young* [1995]. Having tested the Mars GCM against current data, we proceed to use the model as a guide as to whether orbital variations might explain noncontemporary wind indicators. Equally well, the question could be restated as asking how strict a constraint on the age of dunes and well-aligned features is provided by the fact that they correspond well with current wind directions. In Section 6, we investigate the impact of obliquity changes alone. In Section 7, we vary both obliquity and phasing of the equinoxes. These simulations demonstrate a remarkable persistence of the primary surface wind direction patterns, which are dominated in the tropics on an annual-average basis by the southern summer Hadley flow. We take the particular example of the Mars Pathfinder landing site (Section 8) and show that for no combination of obliquity or precession considered can the ventifact directions be explained.

We conclude that nonaligned features are unlikely to be explained by secular orbital changes and hence are unlikely to be explained by circulations occurring during the recent periods of Martian geological history in which the topography, climate, geologic activity, and polar orientation have remained consistent with current conditions. This conclusion also suggests that the alignment of dunes and other features with contemporary winds does not necessarily imply that those features themselves are contemporary

2. Model Description

In this paper we use the Mars general circulation model (GCM) developed at the Geophysical Fluid Dynamics Laboratory (GFDL). The Mars GCM is based on the GFDL Skyhi terrestrial model, with the physical parameterizations modified to reflect Martian conditions. Versions of the model are described by *Wilson and Hamilton* [1996], *Wilson* [1997], *Richardson* [1999], and *Wilson and Richardson* [2000]. Briefly, the model includes a CO_2 cycle resulting in time-varying seasonal ice caps and global average surface pressure, atmospheric radiative heating due to CO_2 and dust in the visible and infrared, specified injection and global transport of dust, a water cycle involving atmospheric vapor and ice transport, and condensation/sublimation of surface water ice.

As used in this study, the model has been modified in one important sense. The prescription of solar insolation, which results from an orbital calculation, has been generalized to allow for arbitrary selection of planetary eccentricity, obliquity, and timing of perihelion passage. Thus issues of climatic response to changes in planetary orbit and spin orientation can now be addressed with the GFDL Mars GCM. We use this capability in Sections 6 and 7 to examine variations in surface wind patterns applicable to the recent past (last few million years).

In all simulations the surface maps have been smoothed to the model resolution of 5º of latitude by 6º of longitude (discretization in the vertical uses mixed sigma-P coordinates, with 20 levels between the surface and roughly 85 km [see *Wilson and Hamilton,* 1996]). The lowest model level is roughly 200 m above the surface. The surface boundary conditions for the simulations described in this paper are defined by Mars Orbiter Laser Altimeter (MOLA) topography [*Smith et al.,* 1999], Viking Infrared Thermal Mapper (IRTM) albedo [*Pleskot and Miner,* 1981], and thermal inertia [*Palluconi and Kieffer,* 1981], all of which have been smoothed to the 5º x 6º grid of the model. The latter two have been modified following *Haberle and Jakosky* [1991] assuming a dust opacity of 0.3. The boundary layer is described with two schemes. To represent the surface layer, a Monin-Obukov drag formulation is used, where the drag coefficients depend on the Richardson number, the lowest-layer thickness, and the surface roughness. Above the surface layer a Richardson-number-dependent vertical diffusion scheme is used to mix heat, momentum, and tracers [see *Wilson and Hamilton,* 1996, and references therein]. In previous simulations with the GFDL Mars GCM, a surface roughness of 16.8 cm has been used, which is likely too high. To test the importance of this parameter, we have undertaken duplicate simulations with 1 cm surface roughness for a few of the simulations to be discussed within this paper. While the surface wind speeds (and consequent stresses) could differ by as much as many tens of percent, the simulated surface wind directions were affected very little. The 16.8 cm and 1 cm roughness length simulations possessed global wind field directions that correlated to better than 0.97. The simulated wind direction patterns are far less sensitive to surface roughness variations than to the other parameters varied in this study. Given that it is wind direction that we concentrate on in this paper, we consider surface roughness errors to be unimportant.

In addition to orbital parameters, the dust amount is varied as part of the study reported here. The dust amounts at each location are converted into equivalent opacities which are used as input to the radiative heating calculations. The dust amount is not prescribed in the GFDL Mars GCM but evolves under the influence of model winds and mixing. Only the rate of dust injection into the lowest model level from the surface is prescribed. In most of the calculations described here, the injection is constant with longitude and local time but decreases sinusoidally from the equator to both poles. The rate of dust injection at the surface is tuned to produce an annual cycle of opacity that results in a good fit to observed, midlevel air temperatures. For a given injection rate the model will not continue to accumulate dust, but rather, a seasonally varying cycle of dust develops which is repeatable from model year to model year. The constant, single-valued dust injection rate works therefore as a control on the "dustiness" of the mean model climate. In some simulations this global dust injection is augmented by stronger, localized sources which aim to represent lifting associated with dust storms. Again, the injection rate is not determined *a priori* but is gauged from its impact on air temperatures and on the strength of the thermal tides [see *Wilson and Hamilton,* 1996].

3. Present-Day Winds as Predicted by the GCM

We begin by describing the current seasonal average surface wind patterns. A more detailed description of surface winds generated in a GCM is given by *Joshi et al.* [1997]. Figure 2.1 shows plots of global winds averaged over each season. The seasonal average winds are nearly identical to wind maps produced for periods of < 10 days centered on the respective equinoxes and solstices, so few if any extreme winds have been obliterated by this seasonal averaging. The seasonal surface winds from this simulation are shown as a control for model experiments

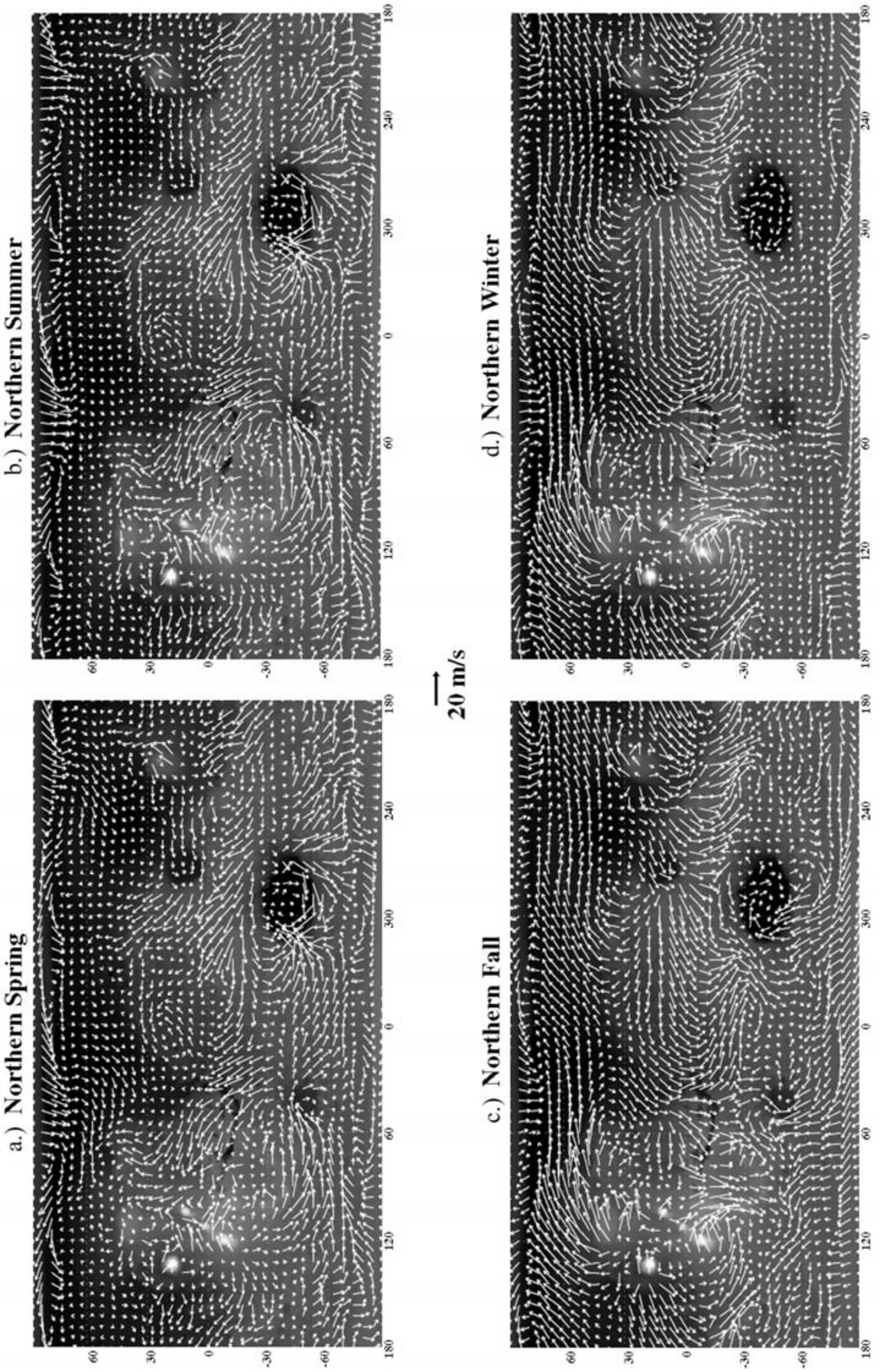
a.) Northern Spring

b.) Northern Summer

c.) Northern Fall

d.) Northern Winter

Fig. 2.1. Present-day seasonal average surface winds superimposed on a grayscale MOLA topographic map. Wind velocity is represented by vector length.

to be described in later sections in which the dust opacity and orbital parameters are varied.

The primary influences on daily averaged global surface winds can be grouped (somewhat arbitrarily) into four main factors: Hadley circulation, planetary rotation, topographic obstruction, and thermal contrast. Because of Fourier filtering performed by the GCM, the calculated winds poleward of 75º N and 75º S are not reliable and thus are not described in this work. Daily averaged winds in the tropics are dominated by the Hadley circulation. Flow at surface levels proceeds from the downwelling branch in the winter hemisphere toward the upwelling branch in the summer hemisphere (the Hadley return flow). Rotation modifies this flow such that a given parcel of air crosses the equator well to the west of its upwelling and downwelling longitude. All else being equal, this large-scale circulation would result in a longitudinally uniform belt of parabolically shaped winds. However, peak daytime heating of the air in the summer hemisphere is far from zonally uniform. Nonuniformity results from variations in topography as well as albedo and thermal inertia. Consequently, upwelling is not longitudinally uniform, resulting in the concentration of surface winds into distinct currents [*Greeley et al.,* 1993]. In turn, these currents can be modified where significant topography occurs west of a strong upwelling region. As it is easier for air to flow around rather than over an obstacle, topography can redirect and concentrate surface currents. Such concentrations have been identified as Western Boundary Currents and simulated by *Joshi et al.* [1995].

Away from the tropics the large-scale circulation is primarily determined by thermal contrasts and planetary rotation, with secondary modification by topography. In the winter hemisphere at the midlatitudes, pressure gradients associated with the temperature contrast between the cold polar air mass and the warmer extratropical air mass result in geostrophic westerly winds. In the summer hemisphere, much weaker and sometimes reversed temperature contrasts result in exceptionally light winds that can trend easterly.

In the northern spring (L_s = 0º - 90º) a number of these processes are evident (Figure 2.1a). Equatorial easterlies are strong in Elysium Planitia and Lunae Planum. The southern midlatitude westerlies appear only west of Hellas and Argyre Planitiae, and in both cases they may be enhanced by the drop in elevation to the east. A Hadley return flow is evident in the southeasterly winds north of Hellas, in Syrtis Major, across the dichotomy from Terra Cimmeria to Elysium Planitia, and across Valles Marineris. Midlatitude easterly and northeasterly winds are present at 60º N in Vastitas Borealis. Topography strongly affects the spring winds in Figure 2.1a in a number of ways. Flow is diverted around topographic lows such as Hellas and Argyre and highs such as Syria Planum. High surface stresses are associated with strong drainage flows near Olympus Mons and Elysium Mons. Winds in Elysium and Chryse Planitiae formed by the Hadley return flow cross the dichotomy boundary and form Western Boundary Currents as they hug the west side of the Planitia basins. Averaged summer surface winds (L_s = 90º - 180º) are similar to the spring winds with the exception that the northern midlatitude easterly winds have subsided (Figure 2.1b).

Surface winds from northern fall, or southern spring (L_s =180º - 270º), are shown in Figure 2.1c. There is a drastic shift in wind direction as the Hadley cell reverses in direction, causing the Hadley return flow to run from north to south. South of the dichotomy boundary the winds speed up in an upwelling zone at 30º S. The upwelling winds are northwesterly, with the westerly component caused by Coriolis deflection. There is some evidence of flow from the seasonal south polar cap in the northern fall at 60º S. There are many wind vectors pointing off-pole south of 60º S. There is a slight easterly tendency to these outflow winds which is associated with Coriolis deflection. In the zone between 40º N and 70º N there is a strong temperature-driven (geostrophic) westerly wind. Near Tharsis the topography deflects the flow northward. The increased wind velocity north of Tharsis is a reflection of the need to conserve mass when the flow becomes constrained (*i.e.,* the Bernoulli effect).

During northern winter, or southern summer, the surface winds are very similar to northern fall winds. The only difference is that at high southern latitudes the winds are almost nonexistent (Figure 2.1d). The loss of the seasonal CO_2 ice cap removes the northward outflow responsible for the off-cap easterly winds observed during northern fall.

4. Effects of Dust Loading on Surface Winds

4.1. Global Winds

Suspended dust affects atmospheric heating more strongly than any other time-varying component of the Martian atmosphere. During a dust storm, elevated dust heats the atmosphere at high altitudes while shading and cooling the near-surface atmosphere. Because of the increased heating during large dust storms, the dust amplifies both the diurnal tide and Hadley circulation [*Zurek et al.,* 1992; *Haberle et al.,* 1982; *Wilson,* 1997]. Although this change in heating is known to affect high-altitude winds, the global-scale effects of a dust storm on surface wind velocities and specifically orientations have not been well studied.

We simulated two dust storms in the model by prescribing a pulse in dust injection that decayed with an e-folding timescale of 7 sols (Martian days). The dust injection rate was defined to be four times stronger in the band from 40° S to 60° S than in the region from 40° S to 40° N. The lower, nominal injection rate (*i.e.,* that which results in observed air temperatures) was used elsewhere. The injection pulse was prescribed to begin at $L_s = 251°$. In the milder case the zonal-average optical depths during the storm peak at roughly 1.6, with general global values near 0.8. The larger zonal storm has a peak optical depth of 5, with general global values of 1.5 (see Figure 2.2b).

Figure 2.2 shows three cases of surface winds averaged over $L_s = 251° - 291°$. The maps show results for the case without a dust storm (Figure 2.2a, also described in the previous section, here called the control), with the moderate dust storm (Figure 2.2c, $\tau < 1.6$), and with the more severe dust storm (Figure 2.2e, $\tau < 5.0$). The wind maps show that while there can be significant changes in wind speeds (and hence stresses), there is very little change in global surface wind directions as the dust amount increases (Figures 2.2d and 2.2f). This lack of change in wind direction is emphasized by calculation of correlation coefficients between the wind directions in the control simulation and each of the dust storm cases. Between the control and the smaller storm, global surface wind directions are correlated with a coefficient of 0.72; between the control and the larger storm the coefficient is 0.81. As dust optical depth increases, surface winds can decrease in speed as well as increase, depending on location. In general surface winds increase in strength within the Hadley cell region by < 3 m/s (representing changes of about 10% or so) between our non-dust storm and largest dust storm cases. One notable exception to this is the Hadley upwelling belt, where surface winds can increase by over 10 m/s (100% and greater). This increase represents less of an expansion of the surface expression of the Hadley cell than it does an increase in the latitudinal extent of the region wherein air is strongly drawn into the upwelling branch of the Hadley cell (*i.e.,* it represents intensification rather than expansion). There is, however, a slight poleward growth by a few degrees in the cell that can be seen in Figure 2.2f. There is little obvious evidence for poleward expansion of the downwelling branch of the Hadley cell. Small changes in wind can be seen in the northern tropics, but there is no consistent

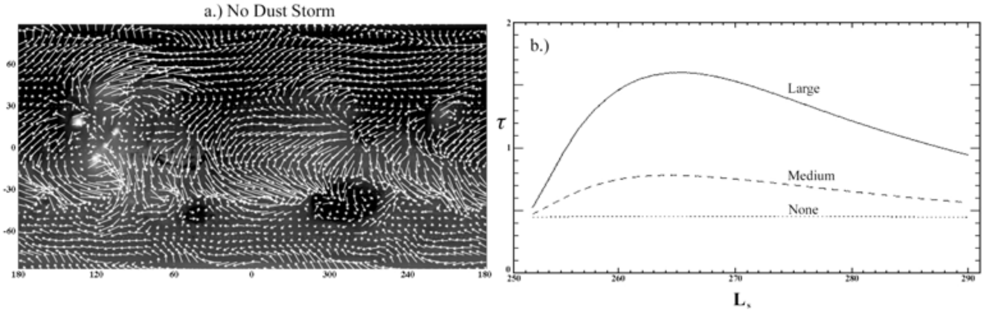
a.) No Dust Storm

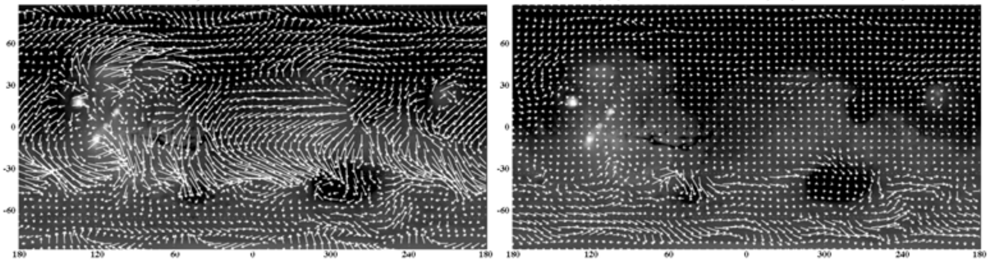
c.) Medium Dust Storm

d.) (Medium Dust Storm) - (No Dust Storm)

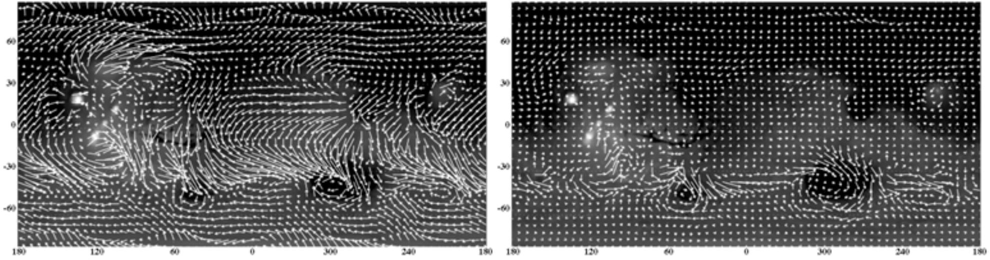

e.) Large Dust Storm

f.) (Large Dust Storm) - (No Dust Storm)

Fig. 2.2 a.) Global surface winds averaged from L_s = 251° to L_s = 291° in a year with no dust storm. b.) Average global dust optical depth as a function of time for the three storm cases shown in this figure. c.) Global surface winds over the same time period in a year with moderate dust lifting between 20° and 40° S (maximum dust opacity ~1.6). d.) Changes in wind strength and direction of the moderate storm case relative to the non-dusty case. e.) Global surface winds over the same time period in a year with strong dust lifting between 20° and 40° S (maximum dust opacity ~5). f.) Changes in wind strength and direction of the strong storm case relative to the non-dusty case.

pattern to the change that would suggest significant poleward expansion, unlike the case in the southern hemisphere (but see Section 4.2 describing the Viking Lander 2 site). The change in stress pattern closely resembles that of wind velocities, where on a zonal average basis the percentage changes in wind speed and stress are nearly identical. In short, while there is significant evidence for wind speed and hence wind stress increases with opacity, especially within the Hadley upwelling region and by factors of 2 or more, the wind directions change very little and the Hadley cell expansion at surface level is extremely limited, in stark contrast to its extravagant expansion at upper levels [*Wilson,* 1997].

4.2 At the Viking Lander 2 Site

The Viking Lander 2 (VL2) pressure and wind data from the period of the second global dust storm of 1977 have long been taken as strong evidence for a significant poleward expansion of the Hadley cell at the surface level. The measured wind data (see Figures 2.3a and 2.3b) clearly show a transition from a light, prestorm westerly flow ($U > 0$, $V \sim 0$), characteristic of the midlatitudes, to a stronger northeasterly flow ($U < 0$, $V < 0$), characteristic of the "trade winds" or the return flow of the Hadley cell, during the peak of the storm. These data have been considered as strong evidence for the entrainment of the VL2 site within the Hadley cell domain, and the fact that the VL2 site is at 48° N suggests that a zonally uniform Hadley cell would need to expand many (probably tens of) degrees to accomplish this [*Haberle et al.,* 1982]. This seems to strongly contradict the results described in Section 4.1.

To test the validity of Mars GCM-predicted surface winds and their change with varied forcing, we have used output from a Mars GCM simulation of the 1977b dust storm in which the dust injection has been tuned to match surface pressure and global air temperature observations. This simulation is more fully described and compared with surface wind streak observations in Section 5. We have used daily averaged winds from the model for the nearest GCM grid point to location of the VL2 site (47.5° N, 228° W versus the actual landing location of 47.97° N, 225.74° W). These winds are shown in Figures 2.3a and 2.3b and demonstrate that the model does a very good job in capturing both the nature of the wind

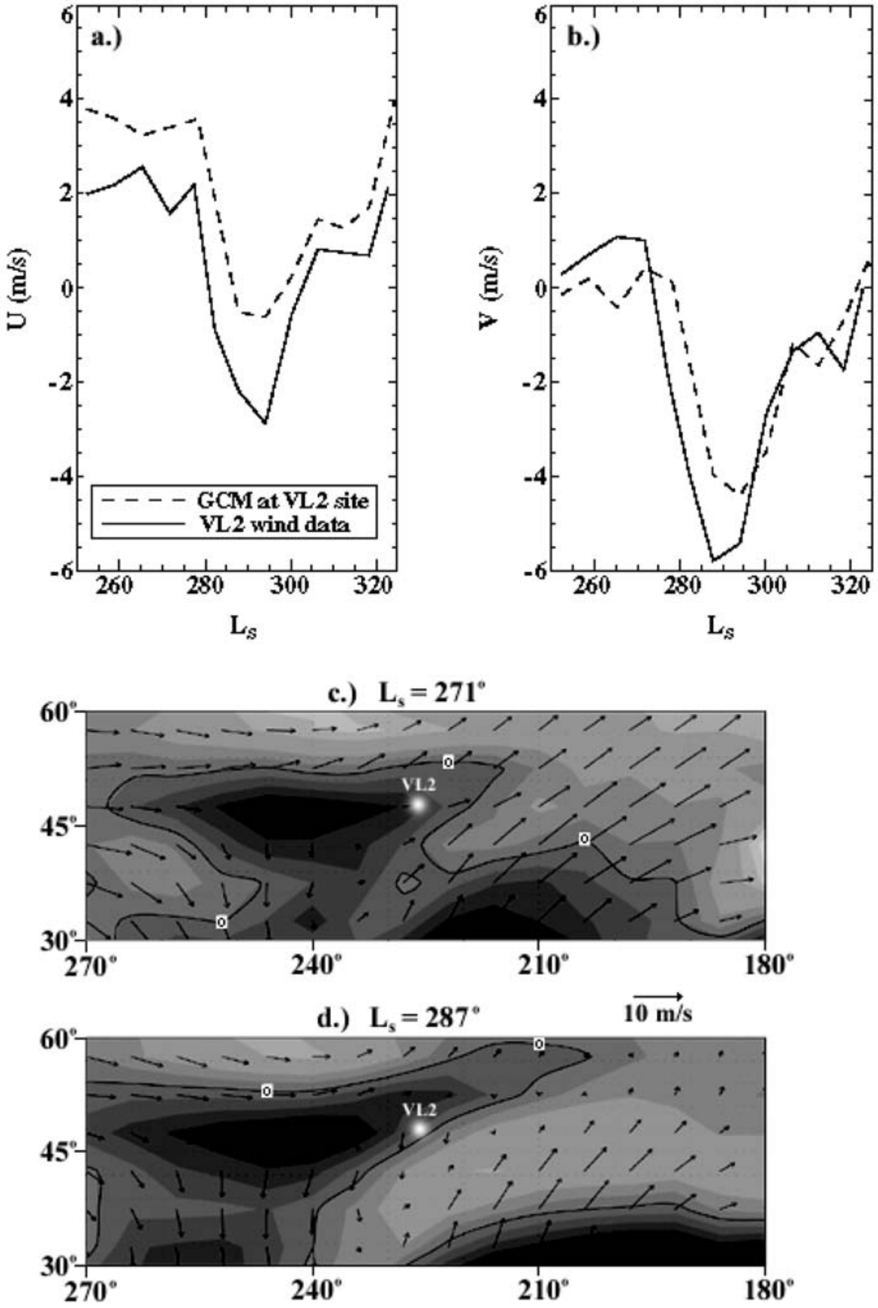

Fig. 2.3. A comparison of a.) zonal (westerly) and b.) meridional (southerly) winds measured by Viking Lander 2 and predicted by the general circulation model (GCM) over the lander site. Wind speed, direction, and divergence are shown c.) before the 1977b dust storm at $L_s = 271°$ and d.) during the dust storm at $L_s = 287°$. Convergence (upwelling) is shown as light shades; divergence (downwelling) is shown as darker shades. The line labeled 0 delineates the change from convergence to divergence.

shift and the magnitude of the winds. It is important to note that this simulation was not specially tuned to match the surface winds at the Viking Lander sites, that it is the same simulation used in matching the wind streak data, and that the wind patterns produced by this tuned simulation correlate strongly with those produced by the simpler simulations discussed in Section 4.1. In short, the "expansion" of the Hadley cell as evidenced by the VL2 is somehow completely consistent with the nearly negligible change in global surface wind patterns predicted by the Mars GCM.

The apparent contradiction between the GCM results and the VL2 observations results from the oversimplified reasoning in the introduction to this section: it is well known that the "Hadley cell" is not zonally uniform. As discussed in Section 3 and by *Joshi et al.* [1995], the cell is more likely composed of zonally concentrated currents, which in turn are strongly modified by topography. Examination of the global wind fields just before and just after the start of the model 1977b storm (Figures 2.3c and 2.3d) does suggest a very slight expansion of the Hadley cell, manifested as an increase in northerly winds in some locations, decreases in southerly winds in others, and some wind vector rotation. However, at most latitudes and longitudes in the northern descent belt (roughly 25° N to 55° N), winds do not rotate to northeasterly, as they do at VL2, and are only slightly deflected in most cases. Exceptions occur over the northwestern portions of Arabia Terra and near Phlegran Montes, where winds do become more consistent with entrainment in an expanded Hadley cell. One still has to be careful, as it is easy to find examples, such as over southern Acidalia, in which winds rotate away from the "trade wind" northeasterly to "extratropical" southwesterly with the onset of the storm and presumed expansion of the cell. Winds at the VL2 site can be thought of in two related ways. First, the circulation in the vicinity of the VL2 site (the Isidis - Utopia Planitia region) can be described using a stationary (high-pressure and hence anticyclonic) eddy model. During the dust storm this circulation becomes elongated, and the northeasterly component of the circuit becomes extended and "reaches" up along the northwest edge of Elysium Mons and the northeast trending Phlegran Montes. This northeasterly extension sweeps through a very small (few degrees) region which encompasses the VL2 landing site. The existence of this stationary cyclonic system is directly related to the Hadley flow as the high-pressure results from a descending plume (part of the Hadley downwelling). As the storm begins, this downwelling increases and expands, spreading the downwelling plume into the area around the VL2 site (*i.e.,* Figures 2.3c and 2.3d show divergent, or downwelling, winds as darker shades near the VL2 site). In this plume, winds begin as westerlies before the global dust storm begins (L_s = 271°, Figure 2.3c) and rotate to the northerlies expected for Hadley return flow during the dust storm (L_s = 287°, Figure 2.3d). East of this downwelling plume is an arc of upwelling and thus convergence (*i.e.*, light shaded region in Figures 2.3c and 2.3d) where winds do not rotate in accordance with the classical Hadley return flow. Thus, a short distance away from the VL2 site, circulation is not dominated by the expected Hadley downwelling plume. Examination of Figures 2.3c and 2.3d, in fact, shows that the very "clean" signal of the Hadley cell expansion seen by VL2 during the storm appears to be something of a fluke. In addition to the longitudinal variation, there is also a latitudinal change in Hadley downwelling strength. For example, the clear signs of Hadley expression measured by VL2 at a latitude of 48° N imply that the classical downwelling should intensify to the south. Inspection of Figures 2.3c and 2.3d shows that the most strongly divergent, downwelling winds (*i.e.,* darker shades) are located west of the VL2 landing site and that there is no southward intensification of this divergence. In short, while some modification of surface winds occurs and the Hadley cell does expand, the expansion is very much weaker and more complex than suggested by simple (axisymmetric) interpretation of the VL2 data. Aside from suggesting that the Mars GCM does a very good job in matching surface winds for a variety of dust-forcing conditions, these results point to obvious dangers in relying on very small numbers of surface probes to determine global circulation patterns.

5. Formation of Wind Streaks

Several types of wind streaks have been documented and studied using Viking and Mariner 9 images [*Arvidson,* 1974; *Thomas et al.,* 1981, 1984; *Veverka et al.,* 1981]. The most widespread and prevalent are bright streaks (see Fig. 2.4a), thought to be dust deposited in the lee of craters and other obstacles (called type I(b) by *Thomas et al.* [1981]). *Greeley et al.* [1993] and *Magalhães* [1987] showed that these bright streaks correlate well with the strong surface winds predicted during northern fall and winter.

A less populated set of streaks is the dark erosional streaks, called I(d) by *Thomas et al.* [1981]. These dark erosional streaks are to be distinguished from dark depositional streaks that are associated with sediment deposits, called type II, which are not discussed in this work. The dark erosional streaks are thought to be formed when turbulent flow behind obstacles activates sand saltation, which in turn kicks dust into suspension. These streaks (shown in Fig. 2.4b) are concentrated in a band at 30º S and point in almost the opposite direction as the bright streaks. Surprisingly, many craters in this region have both bright and dark streaks emanating from them, implying that the processes that produce bright and dark features overlap spatially [*e.g.,* see *Fenton and Richardson,* 2001a, Figure 1]. *Thomas and Veverka* [1979] determined that dark erosional streaks form while major seasonal dust storms subside and subsequently remain fairly stable until the onset of the next seasonal storm. However, GCM-produced diurnally averaged surface winds during the northern fall and winter do not reproduce the easterly winds that must form these dark streaks [*Greeley et al.,* 1993]. How two sets of surface streaks with differing orientations and albedos could form during the

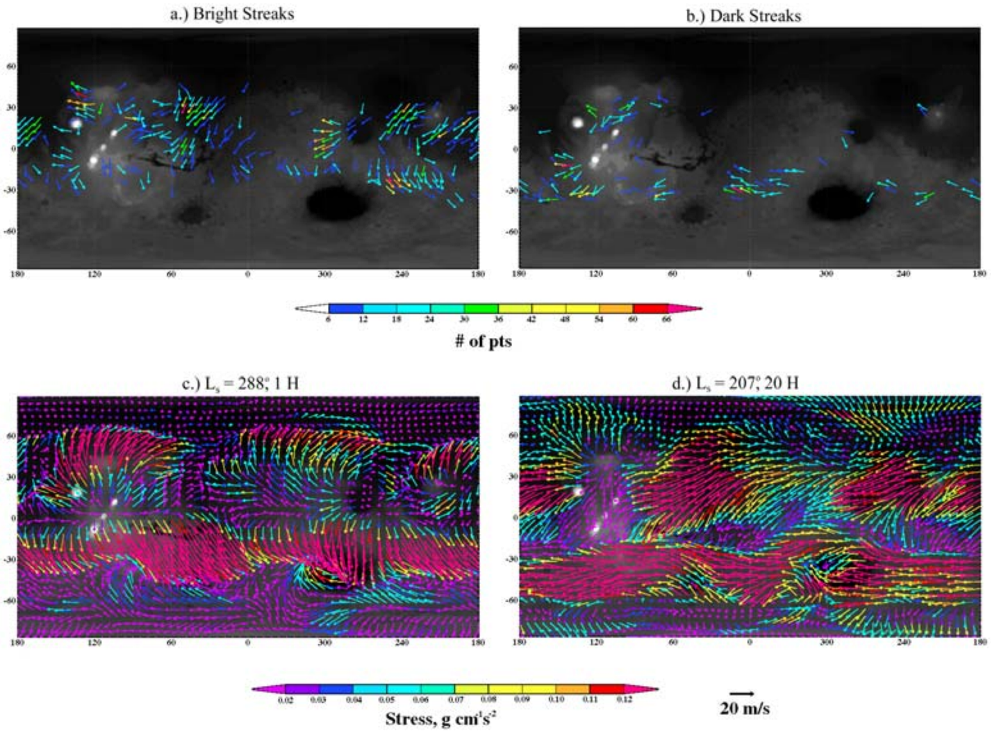

Fig. 2.4. a.) Bright depositional streaks and b.) dark erosional streaks binned to the 5° by 6° resolution of the GCM (courtesy of P. Thomas). c.) GCM surface winds that correlate best with bright streaks between 20° S and 40° S, shown at L_s = 288° and the same time of day, 1 H, at all longitudes. d.) GCM surface winds that correlate best with dark streaks between 20° S and 40° S, shown at L_s = 207° and the same time of day, 20 H, at all longitudes.

same season, and in some cases in the same location, has remained a mystery.

Although *Greeley et al.* [1993] showed that a Mars GCM can match bright steak orientations to a moderate degree of accuracy (with a maximum global correlation coefficient of ~0.5), the predicted surface winds used in this study were averaged over a full diurnal cycle. However, dust travels in suspension, and so the differential ability of dust to settle through a turbulent, daytime boundary layer versus a stagnant, nighttime boundary layer may provide some diurnal bias [*Veverka et al.,* 1981]. Thus bright depositional streaks may form at a specific time of day when winds allow dust to settle out of the atmosphere, and dark erosional

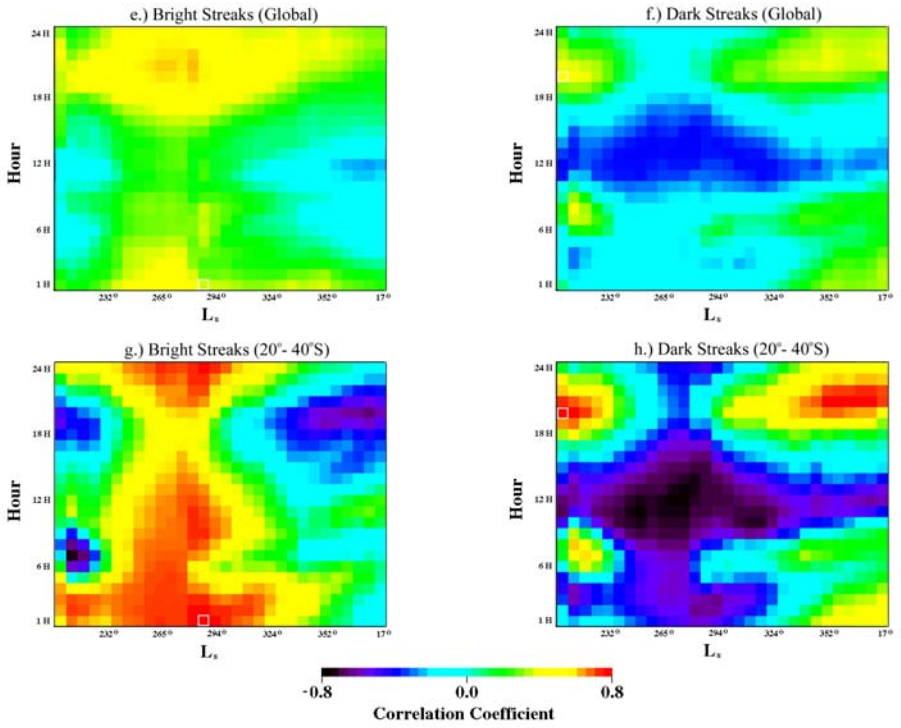
e.) Bright Streaks (Global)

f.) Dark Streaks (Global)

g.) Bright Streaks (20°- 40°S)

h.) Dark Streaks (20°- 40°S)

Fig. 2.4 (cont.) e.) Correlation of bright streaks with global GCM surface winds and f.) correlation of dark streaks with global GCM surface winds as a function of L_s and time of day. g.) Correlation of bright streaks with surface winds between 20º S and 40º S. h.) Correlation of dark streaks with surface winds between 20º S and 40º S. The location of the map in Fig. 2.4c is outlined in the plots of Figs. 2.4e and 2.4g, and the location of the map in Fig. 2.4d is outlined in the plots of Figs. 2.4f and 2.4h.

streaks may form at a specific time of day when winds are strong enough to cause saltation to kick up dust into suspension. Because of their transient nature, wind streaks are likely affected by wind variation such that even diurnally averaged winds cannot describe them, whereas other more persistent aeolian features (such as yardangs and sand seas) can be described by seasonally or annually averaged winds.

To examine whether bright and dark streaks could both be accommodated by winds predicted with the GFDL Mars GCM, we examined model surface winds as a function of both local time and season. In order to produce the best possible match, we examined output from a simulation in which the dust injection rate had been tuned to provide a good fit to the 1977a and 1977b global dust storms. The quality of the fit was checked by comparison with Viking Orbiter air temperature and Viking Lander surface pressure measurements [*Wilson and Richardson,* 1999]. Figs. 2.4c and 2.4d show GCM output surface winds at 1 H, L_s = 288° and at 20 H, L_s = 207°, respectively. The winds in Fig. 2.4c resemble the pattern of bright streaks, and the winds in Fig. 2.4d resemble the pattern of dark streaks. Fig. 2.4e and 2.4f show correlation coefficients of the fit between model winds and observed streak orientations for each hour of the day and for 30 L_s periods ranging from L_s = 207° to L_s = 17°. Global winds correlate well with bright streaks at all times of day during solstice at the peak of the dust storm (Fig. 2.4e), with a maximum correlation coefficient of 0.64. For dark streaks, good fits were found only in the evening before and after the dust storm (before and after the solstice) (Fig. 2.4f), with a maximum value of 0.43.

Although these fit values are reasonable, they still suggest significant error in fitting the full, global streak orientations. However, two things are to be noted: the bright steaks are "fit," on a global scale, almost equally well at all local times and visual comparison of the dark streak data (Fig. 2.4b) with the 20 H, L_s = 207° GCM output (Fig. 2.4d) suggests that almost all the global error is being introduced by the dark streaks located on or around the Tharsis Plateau. The relatively high correlation of the GCM with the bright streaks at all local times around solstice is interesting, implying that wind directions are consistent at all hours of the day in this seasonal window. While not shown owing to limitations of space, comparison of the bright streak data from different regions with the hourly GCM output suggests that the dominant, bright streak-forming winds occur at different times in different locations. This can be demonstrated by considering only the region between 20° S and 40° S (Fig. 2.4g). Here the maximum correlation coefficient of the fit is 0.8. The global insensitivity of the

GCM wind streak fit to local time provides a useful explanation for the relatively good fit of diurnally averaged GCM surface winds to bright streaks found by *Greeley et al.* [1993]. In fact, upon inspection of the GCM output, we found that bright streaks seem to be located in areas where winds rotate the least during the global dust storm (80º or less). Locations with the more typical 360º daily wind rotation do not contain these streaks, probably because any accumulation of bright dust in the lee of these features is immediately destroyed as winds shift direction.

The very definite preference of dark streaks for nighttime winds provides an equally good explanation for the *Greeley et al.* [1993] failure to fit the dark streaks, in that these winds are "washed out" in diurnal averaging. However, the global dark streak fit found in this study is less than spectacular. To demonstrate the impact of the modeled winds in and around Tharsis, we again consider only data and output from 20º S to 40º S (Fig. 2.4h). This results in a maximum fit coefficient (for the same time of day as Fig. 2.4f) of 0.78. In this case we believe that the model is not adequately resolving the details of the near-surface circulation in the topographically complex Tharsis region.

Figures 2.4c and 2.4d show that in many locations, surface wind directions rotate significantly between 20 H and 1 H. In the southern tropical belt the winds can shift by up to 180º in direction. These large-scale, diurnal changes in the winds are a component of the global tides. The tides result from the movement of the region of peak solar heating in longitude as the planet rotates. At a crude level this sets up a low-pressure system that lags the longitude of peak heating, with a compensating high-pressure system on the opposite side of the planet. The tidal flow response to this pressure gradient is a global nighttime-to-daytime flow, which creates easterlies in the 20º S to 40º S belt after midnight and westerlies during the afternoon.

We have mentioned that the dark streaks and the bright streaks are best fit with the GCM winds at different times during the southern summer season. The best fits to the dark streaks occur before L_s = 225° and after L_s = 325°, while the bright streaks are best fit between L_s = 250° and L_s = 300°. A central question when pondering the mechanisms by which wind streaks form is whether the dominant factor determining the change in large-scale circulation patterns is seasonal (the bright streak best fits are at solstice, while the dark streak fits stradle solstice) or due to the global dust storm which began at L_s = 270° (the bright streaks are best fit during the storm, while the dark streaks are best fit before and after). The fact that the bright streaks are well fit for some significant time before the dust storm was initiated in the model suggests that seasonal factors are more important. To test this, we reproduced the correlation calculations undertaken for the "dust storm" simulation with the uniform dust injection "control" simulation (without a global dust storm) described in Section 3. This produced coefficient fit matrices very similar to those shown in Figs. 2.4e and 2.4f. The shift in winds is then primarily a seasonal effect, as would be expected from Section 4.1, in which the general insensitivity of global wind patterns to dust loading was demonstrated.

The only previous published attempt to explain the occurrence of bright and dark streaks in similar locations was put forward by *Veverka et al.* [1981]. They argued that bright streaks would form at times of high static stability, relatively low wind speed, and high dust opacity. The high dust opacity provides a dust source, while the wind and stability provide conditions conducive to the development of flow blocking (development of stagnant air) in the lee of craters and other obstacles. For dark streaks they argue that high winds and low static stability produce the turbulence necessary to erode dust in the lee of obstacles. In this case the wind possesses enough momentum to flow over the obstacles, as opposed to the previous case, where wind is forced to flow around obstacles. On the basis of these arguments they predicted that bright streaks would form during dust storms when the atmosphere is most subadiabatic and that dark streaks would form after the end of the global dust storm during the afternoon when surface heating would produce the most turbulence.

Our results suggest that two factors are important in determining whether air flows over or around obstacles: wind speed and atmospheric instability. A stable atmosphere grows warmer with height ($dT/dz > 0$), and an unstable atmosphere grows cooler with height ($dT/dz < 0$); an isothermal atmosphere defines the boundary between these states ($dT/dz = 0$). The combination of wind velocity and atmospheric stability creates four possible conditions (see Figure 2.5): (1) In a thermally unstable atmosphere, low winds flowing over an obstacle produce a convergent plume (upward flow), and never reach the opposite side. (2) Higher winds in an unstable atmosphere would be able to climb over an obstacle, creating a lee wave that would not strongly affect the surface flow. (3) In a thermally stable atmosphere, low winds diverge around obstacles, leaving a quiet zone in the wake, possibly allowing for deposition behind the obstacle. (4) Higher winds in a stable atmosphere can climb over obstacles but immediately flow back down the lee side, possibly leading to erosion in the wake.

Bright streaks appear to be formed under condition 3 during large dust storms, when winds are low and the atmosphere is stable but near isothermal, leading to a shadow zone in which dust may quietly fall out. Although strong winds also occur during dust storms, the more isothermal nature of the atmosphere may cause weak lee waves to form (in between conditions 2 and 4), thus keeping the deposits from being eroded. This is consistent with the theory of *Veverka et al.* [1981].

Dark streaks are likely caused by condition 4 during the evening hours as large

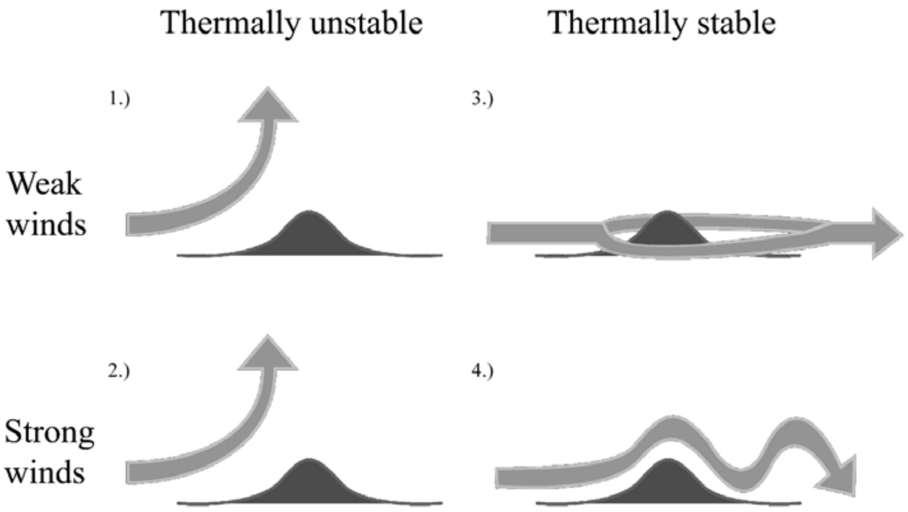

Fig. 2.5. The four possible situations produced by horizontal flow over an obstacle.

dust storms disperse. The strongest winds of the day do occur during the evening at this time of year, and in addition, the increasingly clear atmosphere is very stable at night.

One has to be careful in considering the effect of turbulence on "near-surface" winds. The lowest level of the GCM is at roughly 200 m. For the very lowest layers, within a few to a few tens of meters of the surface, which are permanently within the boundary layer, winds will in fact peak during the day when turbulence mixes momentum from higher levels downward. In terms of interactions with topography on vertical scales of hundreds of meters, the winds at somewhat higher levels are more significant. Here the atmosphere is within the boundary layer during the day, and hence is slowed by momentum loss to the surface, and in the "free atmosphere" at night when winds can become much stronger, decoupled from the surface. It also means that winds deflected by the obstacles are less likely to generate a lee flow but rather a convergent plume (upward flow). Higher static stability promotes the development of lee flows provided that the wind is sufficiently strong to surmount the obstacle. The strongest winds (at roughly 200 m) develop during the night, when stability is high, suggesting that maximum erosion occurs as a result of lee-wave development and turbulent modification of that lee flow through interaction with the surface. Our finding of good correlations at night and inference of a lee-wave mechanism strongly support the mechanism proposed by *Magalhães and Young* [1995]. Thus, in contrast to the *Veverka et al.* [1981] dark streak model, we support the *Magalhães and Young* [1995] model in which strong wind flow in a stable, nighttime atmosphere results in the development of downslope wind storms as the flow becomes supercritical [see also *Holton,* 1992]. The wind storms produce strong acceleration of winds in the downslope and lee of obstacles that can generate saltation and dust clearing from the surface.

In conclusion, we find that in most cases, winds will neither concentrate nor erode dust deposits and that streaks form under two end-member conditions. Bright streaks require high stability, low winds, and ample atmospheric dust; dark streaks require high stability and high winds (that are further accelerated in the lee of obstacles) and likely require easily erodible surface materials.

6. Effects of Obliquity Extrema on Surface Winds

Large variations in planetary obliquity will result in significant modification of surface and atmospheric heating patterns. Thus it has been suggested that obliquity and other orbital variations may result in very different surface wind patterns that can explain the fact that such features as ventifacts and yardangs do not align with current surface winds [*Bridges et al.,* 1999; *Greeley et al.,* 2000]. In order to investigate how wind patterns vary, we ran the GCM over a Martian year for obliquities of 15° and 35°, which provide bounds for the majority of the past 10 Myr [*Ward,* 1992]. For these simulations the argument of perihelion has been set to $L_s = 251°$, which is within a few tenths of a degree of the present argument of perihelion. The resulting seasonal winds show the shifting dominance of midlatitude westerlies versus Hadley circulation.

At high obliquity the difference in heating between hemispheres is at a maximum, feeding the global Hadley cell. Figures 2.6a and 2.6b show the northern spring and fall seasonal average surface winds at an obliquity of 35°. In the northern spring the northward Hadley return flow is stronger in Arabia Patera, Amazonis Planitia, and Valles Marineris. In the northern fall the northern midlatitude westerlies have decreased in strength, but the upwelling zone of the Hadley cell at 30° S has intensified. These changes reflect an intensification of the Hadley cell circulation without significant poleward expansion of its surface expression. The correlation coefficient for northern spring between surface winds at high and current obliquity is 0.62; for northern fall the value is 0.78. This high correlation for northern fall is similar to what was found in Section 4.1, in which dust loading was varied. The lower correlation for northern spring suggests more significant variation in wind direction during that season. However, an important point is that the northern spring winds are significantly weaker than those in northern fall. This is a point which is returned to and expanded upon in Section 8.

Figures 2.6e and 2.6f show the northern spring and fall seasonal average surface winds at an obliquity of 15°. The current obliquity seasonal winds are shown in Figures 2.6c and 2.6d for reference. As obliquity is decreased, the northern fall Hadley cell winds decrease markedly in strength, and the northern midlatitude westerlies intensify. However, the basic pattern of surface winds remains nearly constant. The correlation coefficient value between low and current obliquity for northern fall is 0.90. In the northern spring the return Hadley flow has all but disappeared in Elysium and Amazonis Planitia, and it is greatly weakened over Valles Marineris. Here the correlation coefficient between low and current obliquity is 0.82. As the obliquity decreases from 35° to 15°, winds in Chryse

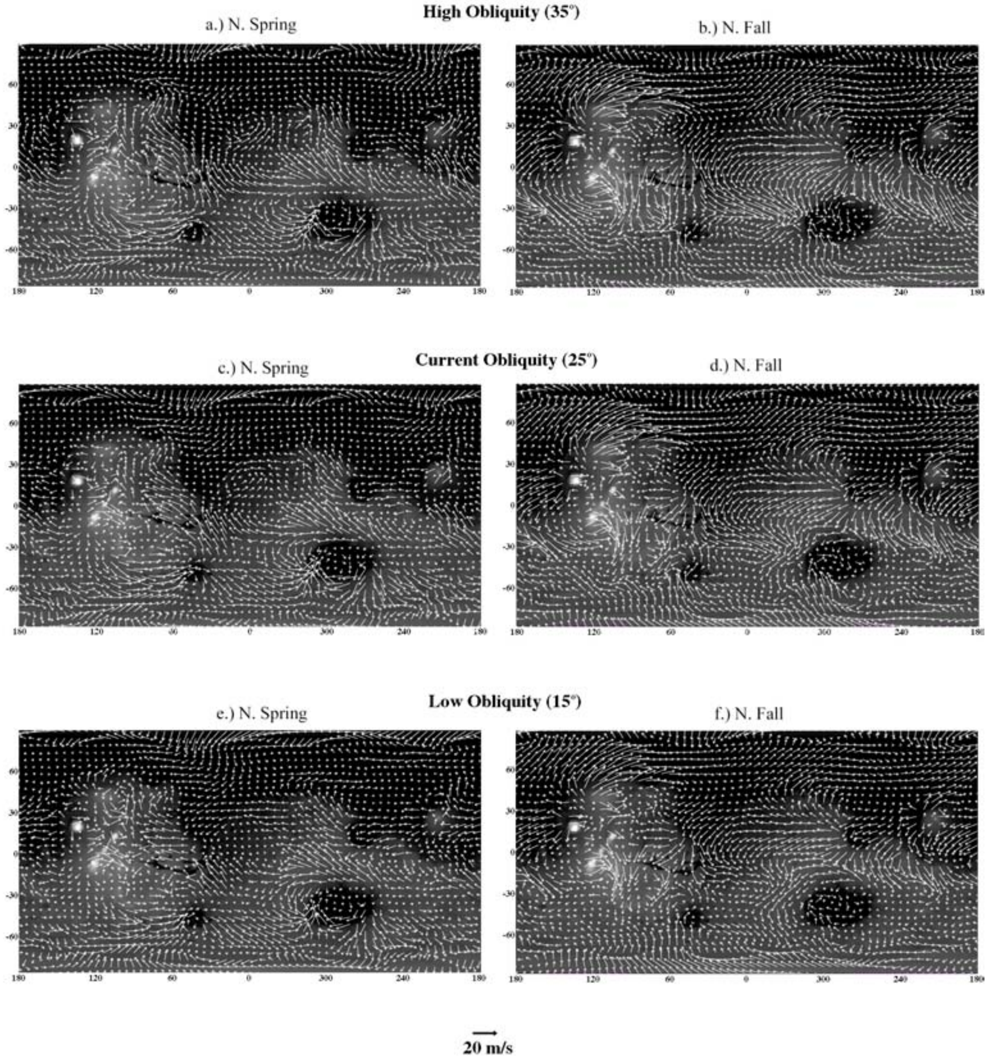

Fig. 2.6. Global surface winds at high obliquity (35°) averaged over a.) northern spring and b.) northern fall. Global surface winds at the current obliquity (25°) averaged over c.) northern spring and d.) northern fall. Global surface winds at low obliquity (15°) averaged over e.) northern spring and f.) northern fall.

Planitia, and at the Pathfinder landing site, rotate from a weak westerly flow to a stronger northeasterly flow. To the east of Chryse the winds become predominantly easterly. These changes may reflect the influence of northern Arabia Terra where it slopes toward the dichotomy boundary. Alternatively, these easterly and northeasterly winds may indicate that as obliquity decreases no single Hadley cell becomes dominant during northern spring and summer.

The primary effect of changing obliquity is to vary the relative influence of the Hadley cell. This influence is expressed more as an increase in surface wind speeds, for increasing obliquity, than in a poleward expansion of the trade wind zone (Hadley cell return flow). In a few localities near the equator the surface winds may be more easterly at low obliquity and more northerly or southerly at high obliquity, but these cases are fairly rare. The generally high correlation coefficients found for all seasons and obliquities suggest that while obliquity impacts wind speeds, it does not significantly affect wind orientations.

7. Obliquity Extrema At Opposite Perihelion Passage

Another astronomical variation that has the potential to affect surface winds is the argument of perihelion. In the current epoch, Mars reaches perihelion near the northern winter solstice at $L_s = 251^\circ$. Thus the southern hemisphere's summer is short and intense, providing a strong driving force for the Hadley circulation. It would be reasonable to suspect that if perihelion passage were moved out of phase by 180°, then the northern spring and summer Hadley cell might be stronger than that of southern spring and summer. However, there is a strong zonal-average topographic gradient from the north to south pole, and it is possible that this influences the relative intensities of the Hadley cell in northern and southern summer.

In order to test the impact of precession we performed simulations for the same obliquities as used in Section 6 but with the perihelion passage occurring at $L_s = 70^\circ$ (just before northern summer solstice). The annual average global surface wind maps for each obliquity extrema and each perihelion state are shown in Figure 2.7. We concentrate on annual average maps to determine the relative importance of the northern versus southern summer large-scale circulations. In Sections 4 and 6 we showed that for a given season wind patterns change very little, and this also holds true when the argument of perihelion is changed (not shown). Here we show only annually averaged wind patterns because any change in the relative strength of the northern summer circulation relative to the southern summer circulation would most easily be recognized as a change in the annual average wind directions.

Figure 2.7 shows the annual average wind patterns for extrema of obliquity and at both precessional states. These wind patterns exhibit the best correlation between any simulations presented in this paper. The coefficient of correlation between wind directions in the simulations with passage of perihelion at 250º and 70º at high obliquity is 0.89; at low obliquity it is 0.92. For comparison, the fits between high and low obliquity at the two perihelion states are roughly 0.76 in both cases. Clearly, perihelion passage timing has little if any effect on surface wind direction. For completeness, we also examined cases in which the eccentricity was set to 0.0, finding very similar results. As changing the argument of perihelion should, if anything, make northern summer circulation stronger than that of the south, the only remaining explanation for this seasonal asymmetry in circulation strength is the zonal-average elevation change. This implies that the hemispheric asymmetry in topography is the dominant factor in determining asymmetry in large-scale circulation.

8. Winds at the Pathfinder Landing Site

The surface wind patterns modeled by a GCM can be compared to known winds in a specific location as a form of "ground truth." This provides both a test of the sensitivity of the GCM and some insight into when observed small-scale aeolian features may have been formed. The abundance of aeolian features at the Mars

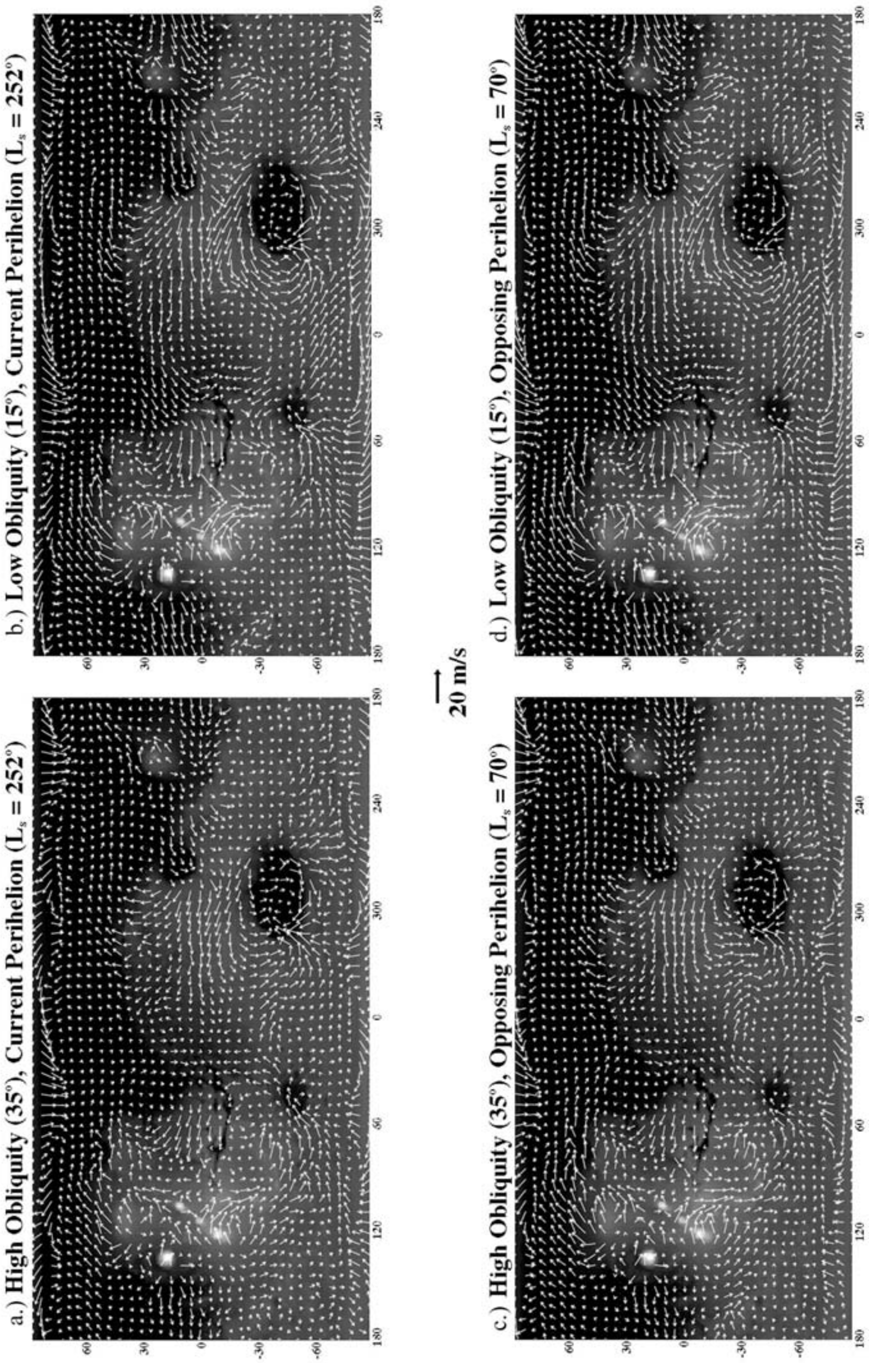

a.) High Obliquity (35°), Current Perihelion (L_s = 252°)

b.) Low Obliquity (15°), Current Perihelion (L_s = 252°)

c.) High Obliquity (35°), Opposing Perihelion (L_s = 70°)

d.) Low Obliquity (15°), Opposing Perihelion (L_s = 70°)

Fig. 2.7. Global annual surface winds at a.) high obliquity (35º) at the current perihelion passage (L_s = 251º), b.) low obliquity (15º) at the current perihelion passage (L_s = 251º), c.) high obliquity (35º) at the opposing perihelion passage (L_s = 70º), and d.) low obliquity (15º) at the opposing perihelion passage (L_s = 70º).

Pathfinder landing site makes this location ideal for comparison with modeled winds. In addition, the availability of meteorological data for a limited portion of the year collected by the lander allows a thorough comparison of GCM predictions with directly observed winds. For the late northern summer period observed, the GCM does a very good job of simulating the diurnal cycle of wind directions (*e.g., Toigo and Richardson* [2001]). Examining the aeolian features at the landing site, *Greeley et al.* [2000] found that most of the features, such as rock wind tails, small barchanoid duneforms, wind streaks, and bright ridges seen in Viking images are aligned with the northeast winds predicted by a GCM during northern winter. Our results support this argument (see Figs. 2.8c and 2.8d). In addition, *Greeley et al.* [2000] observed that other aeolian features did not align well with any predicted surface wind pattern. These features include the ventifacts studied by *Bridges et al.* [1999] and the degraded rims of nearby craters. The ventifacts and eroded crater rims correspond to winds from either the ESE or WNW, with a slight preference for the ESE.

Figure 2.8 shows seasonally averaged surface winds for the current climate and for each combination of low and high obliquity with current passage of perihelion (L_s = 251°) and the opposing passage of perihelion (L_s = 70°). Regardless of orbital state, the strongest surface winds always come from the northeast, and they always occur in the northern fall and winter. Wind orientations vary tremendously during the northern spring and summer (hence the relatively low, 0.62, global correlation coefficients found for current and high obliquity found in Section 6), but their velocities never exceed those of fall and winter surface winds. In particular, no ESE or WNW winds are predicted. It is possible that ESE or WNW winds occur during the northern spring or summer during an intermediate stage of orbital states. However, such spring or summer winds are not likely to be strong enough to produce ventifacts or erode crater rims, and in any case these results show that any such spring or summer winds will be weaker than the

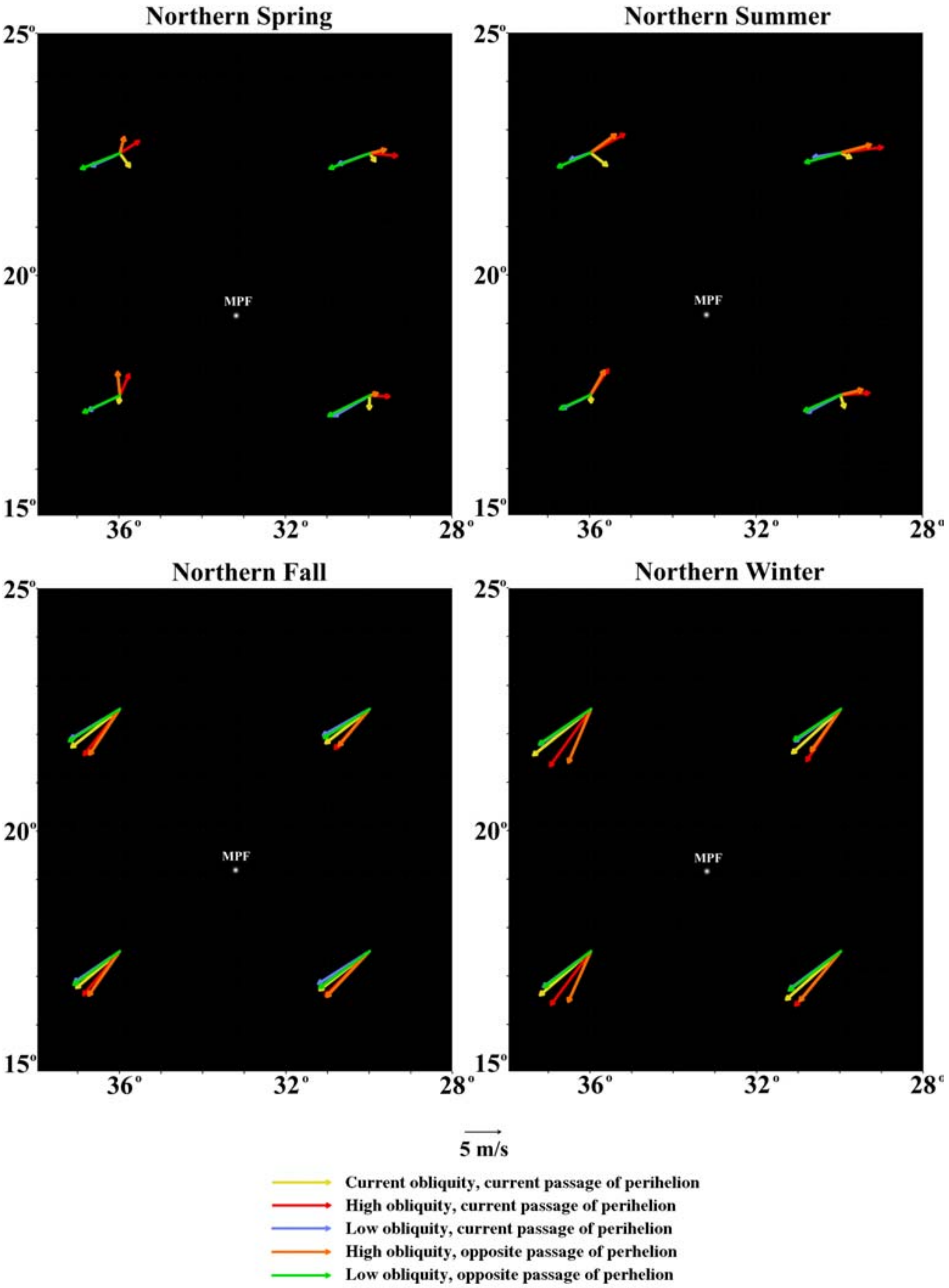

Fig. 2.8. Winds at the Mars Pathfinder landing site for differing obliquity and perihelion states. Note how the strongest surface winds always come from the northeast in the northern fall and winter regardless of astronomical oscillations.

corresponding northeasterly fall and winter winds.

We conclude that orbital variations alone do not affect surface wind orientations enough to account for the observed features at the Mars Pathfinder landing site. It is possible that climatic shifts unrelated to Mars' orbital state are responsible for forming the ventifacts and degraded crater rims. It is also possible that topographical changes, such as late Tharsis uplift, could significantly modify local surface winds to produce these ESE or WNW winds. Regardless of the mechanism that changed them, the winds that formed ventifacts and eroded crater rims are of sufficient age that they cannot be produced in models without significant modification of boundary conditions or climatic state.

9. Conclusion

In this work we have addressed a number of broad topics regarding changes in surface wind patterns. Here we summarize each in turn and discuss their implications.

Wind streaks are by far the youngest of the wind features observed from orbit. Because they can be so transient, it is logical to study surface wind patterns over a short period of time, within both the season and the time of day in which they form. Thus we have determined that the bright depositional streaks can form at any time of day at southern summer solstice, when the atmosphere is stable as a result of heating of atmospheric dust and when the winds are low. In this case, obstacles such as craters block flow, creating a “dead zone” in their lee in which dust may settle. Bright streaks in the zone between 20º S and 40º S follow the northwesterly winds of the Hadley cell, which is greatly intensified by the global dust storms and the diurnal tide. Dark streaks form in the early evening hours before and after southern summer solstice, when the atmosphere is stable (because the Sun has set) and when the winds are strong. In this case the winds are strong enough to climb over obstacles, rebounding down on the far side, creating a wave of turbulence. These conditions favor the development of downslope "wind storms" [*e.g., Holton,* 1992], as discussed by *Magalhães and Young* [1995], likely providing the wind acceleration necessary to remove dust. Dark streaks in the 20º S - 40º S zone are created by easterly winds associated with the diurnal tide that dominate the zone at night, when the Hadley cell upwelling is at its weakest. This explanation of the origin of both bright and dark streaks requires that the light material deposited in bright streaks and eroded from dark streaks is dust rather than sand, which is at variance with the interpretation of sandy bright streaks by *Edgett and Malin* [2000].

Importantly, the bright and dark streaks provide a record of surface wind directions which are not significantly modified by a global dust storm itself. The presence of a dust storm only provides the material with which to record these wind directions; it does not by itself influence the large-scale circulation pattern. In this sense we predict that dust storms significantly earlier in the dust storm season that produce streaks will result in streak orientations rather different than those produced by the 1977b storm.

We studied how changes in dust loading, obliquity, passage of perihelion, and eccentricity affect surface wind patterns. Our results are greatly strengthened by testing the changes in wind orientation at the Viking Lander 2 site. The Mars GCM-predicted winds agree well with the lander observations in both strength and direction and indicate a wind reversal with the onset of the 1977b dust storm. The change in wind direction has long been thought to be an indication of significant northward expansion of the Hadley cell, induced by the global dust storm [*e.g., Haberle et al.,* 1982]. However, the model suggests that a "clean" signature of expansion is exhibited in very few locations, of which one is the Viking Lander 2 site. In most other locations the direction changes are greatly subdued, nonexistent, or even reversed with respect to what one would expect for Hadley cell expansion. These spatial variations in wind behavior are a consequence of the fact that the downwelling branch of the Hadley cell takes the form of individual currents rather than a continuous and longitudinally uniform belt and the fact that longitudinal circulation patterns exist which respond modestly to variations in forcing which can locally mask, mimic, or intensify changes in the meridional overturning cell. In fact, despite the transition from "midlatitude" westerlies to "tropical" northeasterlies at the onset of the storm, the modeled Hadley cell at the surface expanded very little. This nonrepresentativeness of VL2 wind observations points to obvious dangers in relying on very small numbers of surface probes to determine global circulation patterns.

In general, surface wind directions remain constant when orbital parameters and dust loading are varied. The few places where winds change are constrained to the upwelling zones of the Hadley cell. In the northern hemisphere summer the Hadley return flow is weak, even when the argument of perihelion is shifted so that perihelion occurs at the northern summer solstice. Thus, under certain conditions the northern summer Hadley return flow may strengthen, showing little sign of change, or weaken, allowing other relatively stronger processes to dominate over the wind pattern. An example of this occurs at the Pathfinder landing site, in which northern spring and summer winds shift direction with change in obliquity and perihelion passage, most likely as a result of Hadley return flow being replaced with equatorial easterlies as the Hadley cell weakens. In the southern hemisphere summer the Hadley return flow is present and dominant no matter how the orbital parameters and dust loading are varied. The edges of the upwelling belt do shrink or expand slightly, which could affect long-term wind markers at the edge of the zone. The strength of the southern hemisphere relative to the northern hemisphere upwelling Hadley cell indicates that the parameters we varied are not responsible for this asymmetry. We conclude that the elevation difference between the northern and southern hemisphere causes either enough of a heating differential at midlevels (in analogy to models of terrestrial monsoons [*e.g., Molnar and Emanuel,* 1999]) or a sufficiently strong slope-wind bias to keep the southern hemisphere Hadley cell dominant, regardless of the orbital state.

We examined the Pathfinder landing site in detail to better understand the disparity between wind-tail and ventifact orientations. During the northern fall and winter, no matter what the orbital state, the surface winds are strong and northeasterly, aligning well with the rock wind-tails and crater streaks in the region. During northern spring and summer the winds vary, but they are always weaker than the fall and winter winds. We conclude that the ventifacts, which were formed by ESE or WNW winds, cannot have been produced by any potential spring and summer winds in which the orbital states combine to produce this wind orientation. This seems logical because ventifacts require strong, sustained winds to form, and spring and summer winds tend to be weak and easily variable with orbital states. Because orbital states alone do not account for the ventifact orientations, some other factor, such as a climate variation independent of orbital conditions or a change in topography, must have caused the winds that produced the ventifacts. As pointed out by *Bridges et al.* [1999], the ventifacts may have been carved shortly after the outflow channel formed, when a fresh supply of abrading particles would have been recently deposited and available. It is possible that during such a period the climate would have changed drastically enough to create the winds that eroded the ventifacts.

The most direct conclusion drawn from this work is that global surface wind directions are little affected by orbital parameter or dust-loading variations within ranges that appear applicable to the recent geological past (last few million years, at least). It is important to note that wind speeds are affected by changes in these parameters. A major implication of this finding is that the observed alignment of dunes or other aeolian features with contemporary global wind fields does not necessarily imply that the dunes are contemporary or currently active. The fact that wind speeds can vary significantly with orbital parameters further suggests that the intensity of aeolian activity may be a strong function of orbital parameters (primarily obliquity). For example, if the threshold for significant aeolian activity lies above that provided by currently active wind systems, it is possible that dunes and other aeolian features may only be sporadically active during specific phases of the orbital parameter cycles (such as at the highest of obliquities).

The global surface wind results presented in this paper apply to scales comparable to those of the Mars GCM model from which they arise. This scale is roughly 5° (or 300 km); hence they are directly applicable only to large features such as dune fields, large wind streaks, and extensive yardang complexes. Our ability to apply model results to the Mars Pathfinder landing site largely reflects our good fortune that average surface winds at this site are not strongly modified by local (tens to hundreds of kilometers) topography (*i.e.,* they are well modeled by the Mars GCM) and that we have both contemporary and noncontemporary features to study. As more images become available from the Mars Global Surveyor, it is becoming increasingly apparent that dunes and other aeolian features exist in profusion at almost all locations. In many cases these features show complex and sometimes apparently contradictory orientations. In order to understand the relationship between winds and the orientation and nature of these features, mapping and analysis with the aid of subglobal (meso)scale models [*e.g., Toigo and Richardson,* 2000] will become necessary.

10. Acknowledgments

We wish to thank R. John Wilson and Arden Albee for useful discussions and support throughout this project. Ashwin Vasavada provided a useful review of an early draft. One of us (M.I.R.) also wishes to thank Ashwin Vasavada for providing the initial spark of enthusiasm for studies of aeolian processes and this project in particular. This paper benefited greatly from insightful and very thorough reviews by Bob Haberle and an anonymous reviewer. This research was supported in part by NSF cooperative agreement ACI-9619020 through computing resources provided by the National Partnership for Advanced Computational Infrastructure at the San Diego Supercomputer Center.

Chapter 3

AEOLIAN PROCESSES IN PROCTOR CRATER ON MARS: 1. SEDIMENTARY HISTORY AS ANALYZED FROM MULTIPLE DATA SETS

Lori K. Fenton

Division of Geological and Planetary Sciences, California Institute of Technology, Pasadena, California

A. Wesley Ward

Astrogeology Team, United States Geological Survey, Flagstaff, Arizona

Joshua L. Bandfield

Department of Geology, Arizona State University, Tempe, Arizona

Abstract. The sedimentary history of Proctor Crater is described especially with regards to aeolian processes. Proctor Crater is a 150 km diameter crater in Noachis Terra, within the southern highlands of Mars. The analysis leading to the sedimentary history incorporates several data sets including imagery, elevation, composition, and thermal inertia, mostly from the Mars Global Surveyor mission. The resulting stratigraphy reveals that the sedimentary history of Proctor Crater has involved a complex interaction of accumulating and eroding sedimentation. Aeolian features spanning much of the history of the crater interior dominate its surface, including large erosional pits, stratified beds of aeolian sediment, sand dunes, erosional and depositional streaks, dust devil tracks, and small bright bedforms that are probably granule ripples. Long ago, up to 450 m of layered sediment filled the crater basin, now exposed in eroded pits on the crater floor. These sediments are probably part of an ancient global deposit of aeolian volcaniclastic material. Since then an enormous quantity of this material has been

eroded from the top layers of the strata, perhaps as much as 50 m. Small bright duneforms lie stratigraphically beneath the large dark dunefield. Relative to the large dark dunes, the bright bedforms are immobile, although in places their orientations are clearly influenced by the presence of the larger dunes. Their abundance in the crater and their lack of compositional and thermal distinctiveness relative to the crater floor suggests that these features were produced locally from the eroding basin fill. Dust devil tracks form during the spring and summer, following a west-southwesterly wind. Early in the spring the dust devils are largely restricted to dark patches of sand because they absorb more heat than the surrounding terrain. As the summer approaches, dust devil tracks become more plentiful and spread to the rest of the crater floor, indicating that the entire region acquires an annual deposit of dust that is revealed by seasonal dust devils. The dark dunes contain few dust devil tracks, suggesting that accumulated dust is swept away directly by saltation, rather than by the passage of dust devils. Spectral deconvolution indicates that the dark dunes are composed almost entirely of basalt. The average thermal inertia calculated from TES bolometric temperatures is 277 ± 17 J m^{-2} $s^{-0.5}$ K^{-1}, leading to an effective grain size of 740 ± 170 μm, which is consistent with coarse sand and within the range expected for Martian sand. The coarse basaltic sand that composes the large dunefield originated from outside the crater, saltating in from the southwest. The provenance of this sand is undetermined, but it entered the region in a single event and accumulated in many of the craters of Noachis Terra. Most of the transport pathway that delivered this sand to the dunefield has since been eroded away or buried. The sand was transported to the right-center of the crater floor, where beneath the present-day dunes a 50 m high mound of sand has accumulated. Dune slipfaces indicate a wind regime consisting of three opposing winds, of which the dominant still blows from the west-southwest, the same wind that originally transported dark sand into the crater. Some of these wind directions are correlated with the orientations of dust devil tracks and bright bedforms. The combination of a tall mound of sand and three opposing winds is consistent with a convergent wind regime, which produces the large reversing transverse and star dunes that dominate the dunefield. The dark dunes have both active slipfaces and seemingly inactive slipfaces, suggesting that the dunes vary spatially in their relative activity. Nevertheless, the aeolian activity that has dominated the history of Proctor Crater still continues today.

1. Introduction

Mars has long been known as a place dominated by aeolian processes [*e.g., de Vaucouleurs*, 1954]. Evidence for the action of wind on the surface ranges from the local-scale features discovered at each lander site to the planet-encircling dust storms that occasionally inundate the entire globe. Therefore the study of material transport and landscape evolution on Mars is not complete until aeolian processes are fully understood. Of the many different types of aeolian features, dunes are unique in that their morphology provides information on the complexity of the wind regime in which they reside and the direction of net transport of a specific range of particle sizes. Thus the study of Martian sand dunes can broaden the understanding of the near-surface wind circulation patterns and the erosion, deposition, and transport of sand on the surface. In addition, knowledge of the terrain in the vicinity of a dunefield is necessary to understand how dunes relate and react to their environment. This work incorporates a number of data sets from the Mars Global Surveyor mission to produce a stratigraphic record of the dunes and underlying terrain in Proctor Crater, one of several craters in Noachis Terra containing a large dark dunefield.

The first dunes identified on Mars were found in Mariner 9 images of Proctor Crater [*McCauley et al.,* 1972; *Sagan et al.,* 1972]. Further work following this discovery quickly established the important role of aeolian processes in the modification of the Martian surface [*Smith,* 1972; *Cutts and Smith*, 1973; *Arvidson,* 1974]. Since then, the dunefields of Noachis Terra (formerly known as the Hellespontus dunefields), and especially the dunes of Proctor Crater, have become the type location for the study of dark dunes on Mars. *McCauley et al.* [1972] and *Cutts and Smith* [1973] took a close look at the Proctor dunes, noting the NNW-striking ridges with a spacing of 1–2 km in the center of the dunefield. *Cutts and Smith* [1973] concluded that the dunes are located in an area where the effective sand-saltating winds are balanced, with possible dominant winds from the southwest. *Breed* [1977] compared the spacing and widths of the Proctor dunes to terrestrial crescentic dunes, finding that the Martian dunes are dimensionally similar to dunes in several terrestrial dunefields. *Thomas* [1984] found that the color variations of Proctor Crater dunes, streaks, and plains are similar to but simpler than crater splotches with associated streaks in other areas on Mars. *Lancaster and Greeley* [1987] took a close look at the Noachis Terra dunefields and discovered pyramid-shaped dunes and multiple slipfaces, indicative of dunes produced by a multidirectional wind regime. However, since their discovery, the dunes of Proctor Crater have generally been classified as large transverse and barchan dunes.

Thermal studies have also focused on the Noachian dunefields [*Christensen,* 1983; *Edgett and Christensen,* 1991; *Edgett and Christensen,* 1994; *Herkenhoff and Vasavada*, 1999]. Because dunefields consist of a large quantity of well-sorted unconsolidated particulate material, thermal inertia measurements over such areas provide an ideal condition in which to calculate effective mean grain sizes. Furthermore, such a well-constrained situation is useful for calibrating new thermal inertia techniques. The dunes of Proctor Crater have been targeted several times, producing a thermal inertia consistent with sand.

In this work, the classification of dune morphology follows the terms defined by *Breed and Grow* [1979]. Crescentic or barchan dunes are crescent-shaped features created by unidirectional winds, with the "horns" of the dune pointing downwind. Transverse dunes, like barchan dunes, form slipfaces that are orthogonal to the dominant sand-transporting winds, but occur where more sand is available, and may be considered coalesced barchans [*Wasson and Hyde,* 1983]. Linear or longitudinal dunes are elongate features with slipfaces on either side of the peak, generally indicative of bi-directional winds, and they are aligned generally parallel to the direction of the resultant wind. Star dunes are large piles of sand that accumulate in a multidirectional wind regime (*i.e.,* where winds converge), often displaying overlapping slipfaces that create a star-like shape in plan view. Reversing transverse dunes occur where seasonally shifting winds oriented close to 180° apart change the slipface direction from one side of the dune to the other, so that the dunes appear as transverse dunes at any given time but may seasonally switch slipface directions. More detailed descriptions and examples are discussed in *Breed and Grow* [1979].

The provenance of dune sand in the Noachis area of Mars is largely unresolved. *Christensen* [1983] proposed that the intracrater dunefields on Mars were formed by entrapment of dark material in the topographic lows of craters. *Breed et al.* [1979] explored the reasons why crescentic dunes appear to be so much more abundant than linear dunes on Mars. They considered that linear (longitudinal) dunes represent areas of active sand transport, whereas crescentic dunes represent areas of low or no current sand transport. They concluded that most crescentic dunes, like the ones in Proctor Crater, represent the final accumulation site of sand, and that any linear dunes that might have transported large quantities of sand have since been eroded away. They also propose that many Martian dunes are similar to terrestrial dunes located in closed basins, and that they may have taken millions of years or more to accumulate, like their terrestrial counterparts. While also considering the sand sources discussed above, *Thomas* [1984] suggests that intracrater dunes may have been formed from the aeolian reworking of eroded crater floor deposits, evidenced by the many large pits visible in craters with dunes and the lack of obvious transport pathways outside the craters. Earlier, *Thomas* [1982] proposed that the intracrater dune sand may have been supplied from eroding layered deposits near the south pole. Clearly a more detailed study of sand deposits is necessary to determine the origin of the intracrater dune materials.

This work is the first of two papers describing aeolian processes in Proctor Crater. The second paper (hereafter called Paper 2) discusses the results of mesoscale atmospheric modeling of the winds over the Proctor Crater dunes and relates dune morphology to regional winds and transport systems. In this work, a graphical information system (GIS) is built and used to correlate aeolian features with data products from the Viking Orbiters and Mars Global Surveyor. The GIS incorporates images, albedo, thermal inertia, composition, elevation, and (discussed in Paper 2) wind orientation and stress to provide a tool that aids in understanding how aeolian processes affect the surface of Mars. In Section 2, the method and materials used in building the GIS are described. In Section 3 Proctor Crater is described both from a regional standpoint and at a detailed view to provide a context for the dunefield. The dark dunefield is illustrated in Section 4, with an emphasis on morphology. The composition of the dunes and crater floor are covered in Section 5. Section 6 describes the thermal inertia of the region, including the identification of a trend across the dunes. Finally, in Section 7, a stratigraphic history of the crater interior is proposed, based on the analysis done with the GIS.

2. Method

A number of data sets were incorporated into a Geographic Information System (GIS) in order to study Proctor Crater. A GIS is a thematic mapping system that allows data to be displayed graphically while being stored as a spreadsheet or a database. This is a tremendously powerful tool that can be applied to conduct studies of an area using spatial data. The main advantage of a GIS is that it involves spatial coregistration of any number of data sets, each of which can be displayed separately or in conjunction with other data sets. For example, images of varying resolutions, digital elevation models (DEM's), and any spatial data points can all be combined into a single database and displayed in whole or in part over one another. This allows for identification of spatial and temporal variations, correlations of many different parameters, and statistical calculations of and between different data sets. All of these measurements can in turn be displayed as an overlay on top of any other coregistered data set (*i.e.,* surface slopes steeper than a certain value plotted over a base image). In addition, feature orientations, lengths, areas, and volumes can be measured and plotted over any previously coregistered data set. A GIS is an accumulation of all available data into one database that then allows for further numerical investigation.

The software used was ArcView GIS Version 3.1, created by ESRI (Environmental Systems Research Institute), to build a GIS of Proctor Crater. Our base map is a 250 m/pix MOC WA (Mars Orbiter Camera Wide Angle) image mosaic that has been processed, corrected for gain and radiometric variations, and mapped into a sinusoidal projection using Integrated Software for Imagers and Spectrometers (ISIS) developed by the U. S. Geological Survey. We added in a digital elevation model (DEM) that we constructed from MOLA (Mars Orbiter Laser Altimeter) elevation points at a horizontal resolution of 400 m/pix using Generic Mapping Tools (GMT) software. Inaccuracies in camera pointing information led to spatial offsets in the positioning information of the WA mosaic, and so we used the MOLA DEM as a reference to adjust the position of the WA mosaic in the GIS by hand. All available MOC NA (Mars Orbiter Camera Narrow Angle) images were processed and projected to match the WA mosaic using ISIS software, and each image was added to the Proctor Crater GIS as a separate layer (theme) and at full resolution. Similar camera pointing errors led to hand positioning of each NA image on the WA mosaic. On top of these images we plotted a number of data sets derived from TES (Thermal Emission Spectrometer). These include bolometric thermal inertia [*Mellon et al.,* 2000], compositional endmember concentrations [*Bandfield et al.,* 2000], daytime and nighttime bolometric temperatures, and bolometric albedo. Also included were all available Viking Orbiter images of Proctor Crater, although the resolution of these proved to be no better than the MOC WA images.

Once the data were assimilated into the GIS, a number of parameters were mapped or measured using data from the Aerobraking through Mapping mission phases. Data from the Extended mission phase have since been added to the GIS and have been inspected for consistency with the previous measurements. Among the features mapped over each NA image in Proctor Crater are dune slipface brinks and orientations, dust devil tracks and orientations, bright duneform location and orientation, boulder density, small craters, and the locations of NA images. This additional information allows for a new assessment of dune morphology, sediment volume, and wind regime using all available information. The results of each of these measurements are described below. It should be noted that this discussion contains a set of conclusions drawn by the author based on the analysis of this GIS. However, this work has greatly benefited by the involvement of several researchers to properly describe and utilize the various data sets listed above.

3. Study Area

3.1 Large-scale Overview

3.1.1 Regional Context. Proctor Crater (see Fig. 3.1a) is one of several large impact basins in Noachis Terra, located in the ancient cratered terrain of the southern highlands of Mars. Located at 47º S, 30º E (330º W), it is one of many craters west of Hellas Planitia (see inset) that contains a prominent, dark dunefield. *Peterson* [1977] mapped the crater floor and the surrounding plains as "plains material," interpreting this unit as unconsolidated sediment deposits that in some areas may be underlain by flood lavas. Proctor Crater itself is roughly 150 km across, and the dark dunefield within extends to ~65 km from southwest to northeast and ~35 km from southeast to northwest. The seasonal polar cap reaches northward beyond Proctor crater, covering the entire crater floor and walls with CO_2 frost during the winter. Proctor Crater is well within the limit of the seasonal frost, which extends to 40º S [*James et al.,* 1992].

3.1.2 Prominent Features. Figure 3.1b shows a digital elevation map (DEM) of the crater, combined with a shaded relief map, at a resolution of 400 m/pix. The DEM was constructed from individual MOLA elevations using the Generic Mapping Tools (GMT). Several features that are barely visible in the MOC Wide Angle mosaic are emphasized in the shaded relief map, which been stretched nonlinearly in color to emphasize relief within Proctor Crater (note color bar in Fig. 3.1b). The crater floor is a fairly flat expanse, smooth at the 400 m resolution of the DEM. It is punctuated by two pits, the larger of which is located on the western side of the crater interior, covers one tenth of the crater floor, and is up to a kilometer deep. The interior of the large pit, here called the "western pit," is rugged and contains several large craters. The smaller pit, called the "central pit," is located in the northern central region of the crater floor, has a much smoother floor, and is roughly 100 m deep. Several 10–20 km diameter craters in the

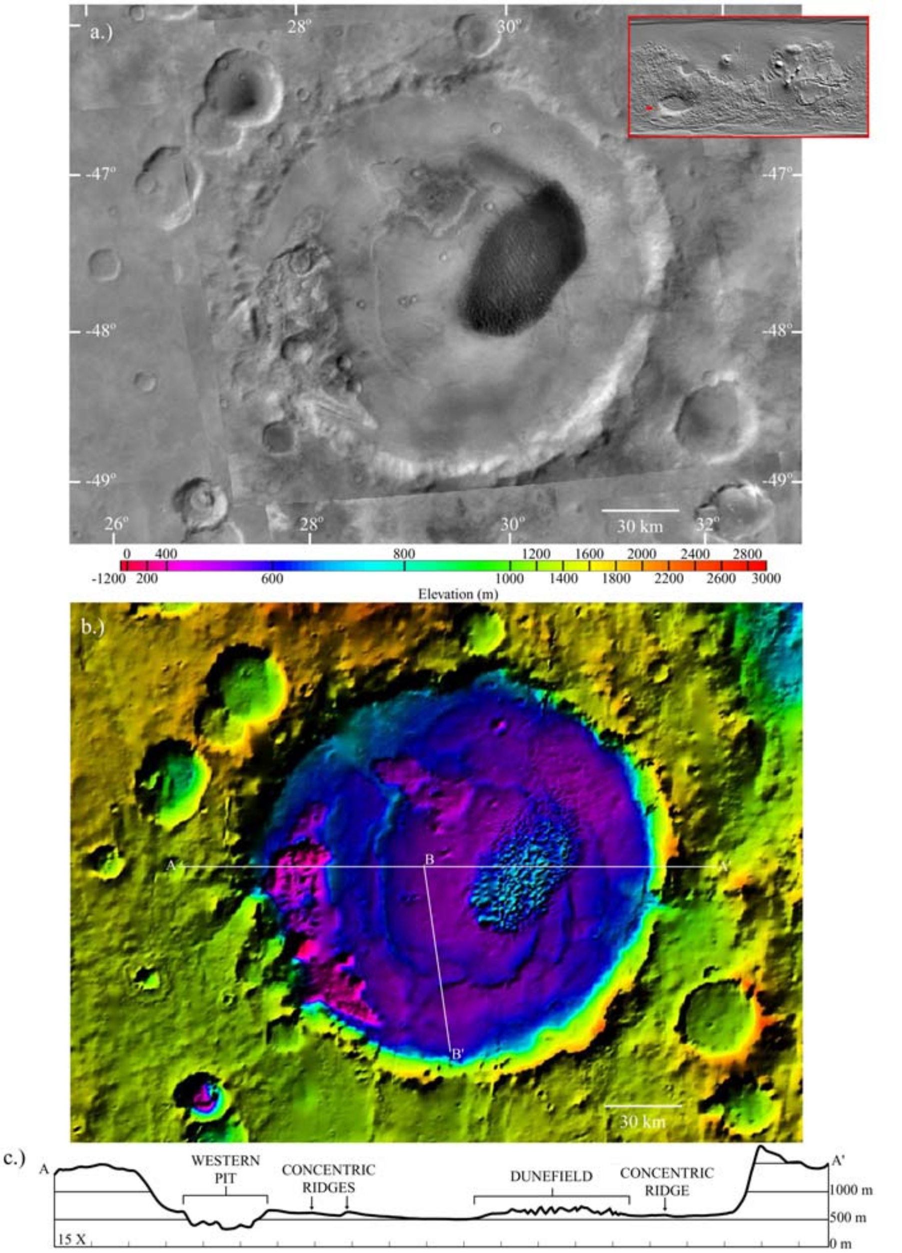

Fig. 3.1. a.) MOC Wide Angle mosaic of the study area, Proctor Crater, at a resolution of 250 m/pix. Proctor Crater is located at 47º S, 30º E (330º W), and it is approximately 150 km across. The small red-bordered inset is a global shaded relief map from MOLA with the study area highlighted in red. b.) MOLA DEM of Proctor Crater at a resolution of 400 m/pix. The elevation scale is stretched nonlinearly to emphasize topography on the relatively flat crater floor (see color bar). Profiles AA' and BB' are shown in Fig. 3.1c and 3.2, respectively c.) Profile AA' across Proctor Crater, with a vertical exaggeration of 15 x. Note that in this and all subsequent images, north is always oriented up.

western pit suggest that the process that eroded the pit may have been triggered by impacts that disrupted the surface, perhaps fracturing and weakening nearby terrain, leaving it susceptible to erosion. However, such craters are not present in the central pit, suggesting that such disruptions are not necessary to initiate pit formation. Figure 3.1b also shows the large dunefield rising above the flat surface as a series of ridges unresolved at the scale of the DEM. There is also a set of ~50 m high ridges ringing the center of the crater at roughly half its diameter (shown in dark violet in Fig. 3.1b, at ~600 m), called the "concentric ridges." *Malin and Edgett* [2001] identify part of a concentric ridge in Proctor Crater (see their Fig. 57), confirming that it is more than just a dust devil track. These ridges are visible as dark rings in MOC Wide Angle images in Fig. 3.1a. Possible origins of these concentric ridges are discussed below.

Figure 3.1c shows a profile crossing the crater, the location of which marked on the map as A–A' in Figure 3.1b. The western pit is a large, rough negative feature that cuts sharply into the crater floor materials. The dunefield appears as a poorly resolved accumulation of material superimposed on the crater floor. Also visible are the concentric ridges, which appear as subtle positive features that are steeper on the slopes facing the crater walls. The remainder of the crater floor is a smooth, fairly featureless plain at the resolution of the DEM.

3.1.3 Basin Fill. It is possible to use crater depth versus diameter measurements to estimate the amount of basin fill within Proctor Crater. Statistics based on MOLA DEM's by *Garvin et al.* [2000] have provided a depth vs. diameter relationship for pristine craters of various sizes. For a crater with a diameter (*D*) larger than 100 km, the original depth (*d*) is estimated at

$$d = 1.27D^{0.12} \tag{1}$$

Thus the estimated unmodified depth of Proctor Crater is 2.31 km. The highest remaining elevation of its now largely degraded rim is 2360 m, placing the original crater floor at a lower limit of 50 m. The current crater floor elevation is roughly 500 m, implying that at most a net value of 450 m of material has accumulated in Proctor Crater since its formation. As discussed below, MOC Narrow Angle images show strata exposed in the walls of the western and central pits, suggesting that this basin fill is part of the same sedimentary units described by *Malin and Edgett* [2000a].

3.1.4 Concentric Ridges. The concentric ridges are a rather enigmatic feature in the floor of Proctor Crater. Such rings in a filled basin are unusual, and thus their origin must be considered carefully. Three possible origins for these structures are considered: that they are eroded outcrops of resistant layers, that they are remnant tops of Proctor Crater's peak ring, and that they are wrinkle ridges that formed after the crater accumulated its sediments.

Malin and Edgett [2000a] found that sedimentary layers interior to a crater tend to conform to the shape of the crater wall. If the sediments filling Proctor Crater accumulated over the entire crater floor at once (*i.e.,* regional versus local deposition) then the strata will be bowl-shaped, like that of a tectonically deformed basin, following the contours of the original crater floor. Any relatively resistant layers will form a ring concentric to the crater's center upon erosion, similar to the ridges on the floor of Proctor Crater. In addition, the presence of steeper slopes facing towards the crater walls (see Fig. 3.1c) is consistent with upturned and exposed layers. Such strata should be traceable around the entire crater floor if not otherwise buried. If this interpretation is correct, then at least 50 m of material, the height of the ridges, has been eroded from the original surface of the crater sediments. The only process operating on Mars that could strip this amount of material without leaving behind telltale erosional markers is aeolian deflation. If this hypothesis is correct, then these resistant strata indicate that a tremendous amount of material has been removed from Proctor Crater by wind action alone. Such a volume of material is nearly five times that of the dark dunefield, which is discussed below in Section 4.3.

The second interpretation requires the assumption that the ridges are part of the original structure of the crater that has been buried by sedimentation and perhaps subsequently exhumed. Peak ring craters are complex craters with diameters between approximately 50 and 300 km [*Pike and Spudis,* 1987]. These craters are large enough to have peak rings rather than just central peaks; hence, they are called peak ring craters whereas the craters with single central peaks are called central peak craters. According to *Wood and Head* [1976], peak ring diameters on Mars are half that of the crater diameter. The average diameter of the concentric ridges on the floor of Proctor Crater is ~80 km, which is roughly half the diameter of the crater (150 km), which is the correct dimension for a peak ring.

As of yet, there are no statistics from MOLA topography on the heights of peak rings [*Garvin et al.* 2000; 2002]. According to *Hale and Grieve* [1982], the heights of lunar central peaks (h_{cp}) follow a predictable trend related to the crater diameter (D) for craters less than 51–80 km wide. At larger crater diameters, the central peak heights asymptotically tail off to a height of 2–3 km until the crater diameter at which peak ring craters begin to form. They report that Schrödinger Crater, with a diameter of ~300 km, has a peak ring with a height of 2–3 km, which appears to follow the roll-off in height reached on the curve by central peaks. As shown by *Pike and Spudis* [1987], the difference between crater dimensions and critical diameter values between the Moon and Mars is quite significant, and thus a direct comparison cannot be made. It is not known at what diameter such a roll-off in central peak heights might occur for Martian craters, or even if it occurs at all. However, assuming that peak ring heights follow the same trend as central peak heights, and using the trend calculated by *Garvin et al.* [2002] for central peak heights of Martian craters,

$$h_{\mathrm{cp}} = 0.04D^{0.51}, \tag{2}$$

where h_{cp} is the central peak height and D is the crater diameter, the first-order estimate of Proctor Crater's peak ring height is 520 m. If the concentric ridges stand ~50 m above the ~450 m of sediments on the Proctor Crater floor, then the resulting total height of 500 m is close to that calculated using Equation 2. Thus crater statistics so far cannot rule out that the concentric ridges are eroded remnants of former peak rings, now embayed by hundreds of meters of sediments.

The third proposed origin of the concentric ridges, that they are wrinkle ridges, is perhaps the most unusual of the three. Wrinkle ridges are long, linear or arcuate features of positive relief, often associated with an elevation offset from one side to the other, and most commonly thought to be formed by tectonic compression [*e.g., Plescia and Golombek,* 1986; *Watters,* 1988; *Golombek et al.,* 1991]. On Mars, wrinkle ridges form in a wide variety of geologic terrains, and appear to be located and oriented largely by large impact basins such as Chryse [*Chicarro et al.,* 1985]. The rings in the floor of Proctor Crater superficially resemble wrinkle ridges in areas, particularly in the southwestern quarter (see Fig. 3.1a). Recent analysis of MOLA topography of wrinkle ridge systems in various regions of Mars show a series of successive offsets, indicating deep tectonic faults, possibly reaching through the planet's crust [*Golombek et al.,* 2001]. Circular features interpreted as wrinkle ridges have been identified in a few places, and they have been proposed to be formed by buckling of emplaced material above the rims of buried craters [*Sharpton and Head,* 1988]. In Noachis Terra, *Mangold et al.* [1998] found curved ridges within craters that are part of larger wrinkle ridges that extend far beyond the crater rim. They argue that deep faults cannot create such arcuate features that are clearly influenced by the structure of the craters they are within, but that instead these ridges must be produced by thrust faults on shallow décollement surfaces. Wrinkle ridges appearing within basin fill, following the shape of a crater rim, and unconnected to outside tectonic features, such as shown by the concentric ridges of Proctor Crater, are not likely to be produced by a deep tectonic thrust. Therefore if the concentric ridges are in fact a wrinkle ridge system, they must be produced by compression at shallow depths as proposed by *Mangold et al.* [1998]. Compression in Proctor Crater could have been produced by subsidence of the basin fill, perhaps by a regional removal of ground water or by cooling of ponded lava. It may be that the weight of 450 m of accumulated sediments alone could have produced a gradual settling of material, perhaps by compaction of the aeolian basin fill. Such subsidence would necessarily have been spatially uniform to produce a thrust fault consistently concentric to the crater walls.

Figure 3.2 shows a MOLA traverse from one of the Narrow Angle images that passes across two concentric ridges (marked as B–B' in Figure 3.1b). Wrinkle ridges tend to show one or more of the following morphological features: a broad rise that extends for several kilometers and peaks at the ridge, a superposed hill that is a few kilometers long and upon which the ridge is situated, and crenulated peaks showing the well-known "wrinkles" of the ridges. Although there is no obvious broad rise present in Fig. 3.2, the two peaks of the ridges are situated on what appears morphologically similar to a superposed hill, following the examples from *Golombek et al.* [1991]. There is no measurable offset, and although offsets are typical of wrinkle ridges, the lack of one here does not preclude this feature from being a wrinkle ridge. The width of the "superposed hill" is 28 km, and if the two peaks are considered two separate wrinkle ridges, then one may consider that the width of the "superposed hill" for each ridge is 14 km. The total relief is

75 m in the case of the inner (northern) ridge and 100 m in the case of the outer (southern) ridge. Given these dimensions, these features do not fit well into the statistical relationships for Martian wrinkle ridges found by *Golombek et al.* [1991], although this relationship is based on measurements of wrinkle ridges in Lunae Planum. The dimensions of the wrinkle ridges of Lunae Planum, which are among those considered by *Golombek et al.* [2001] to be evidence for tectonic faulting that penetrates the Martian crust, may not be representative of all Martian wrinkle ridges, particularly those produced by faulting along shallow décollement surfaces. Based on morphology alone, it is difficult to conclude confidently that these features are indeed wrinkle ridges.

Given the highly eroded state of the concentric ridges, it is difficult to decide on which of these three hypotheses is most likely. It is possible that they are created

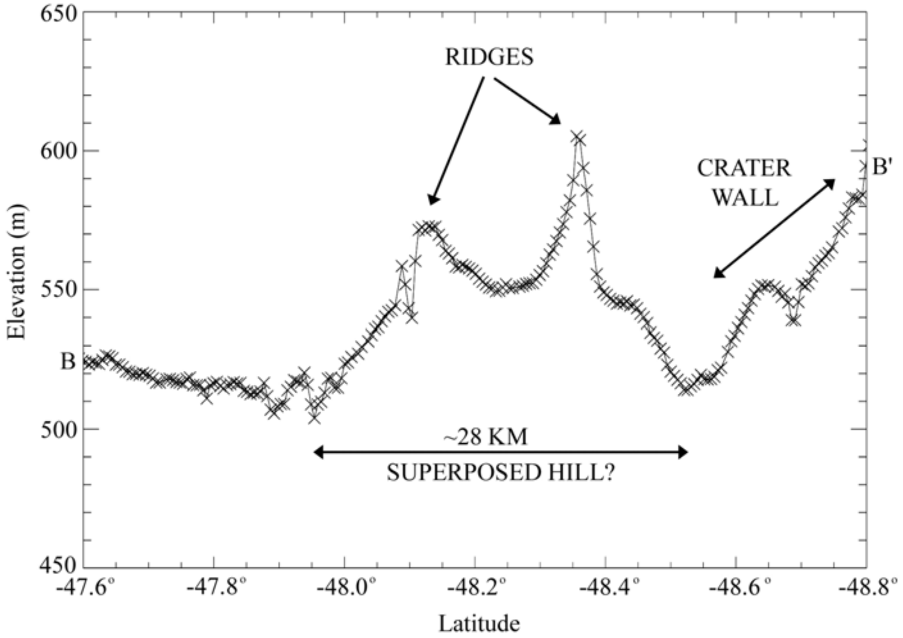

Figure 3.2. Profile BB' (shown in Fig. 3.1b on the MOLA DEM) across two concentric ridges.

by a combination of the above processes. For example, if they are wrinkle ridges, then they may have formed over buried peak rings, in the same way that wrinkle ridge systems have formed over buried crater rims in other areas on Mars. Unless a new development in one of these areas of study precludes one or more of these hypotheses, more information is required to determine what process produced the concentric ridges.

3.2 Overview at MOC Narrow Angle Resolution

High-resolution MOC NA images provide unprecedented detail of the Martian surface that is often surprising when compared with the lower resolution view. *Malin and Edgett* [2001] found that surfaces on Mars appearing to be rugged at hectometer scales typical of Viking, Mariner 9, and MOC WA, are generally smooth at MOC NA resolutions. They show that the converse is true as well. Thus, a full description of Proctor Crater must include both the high- and low-resolution views. Here, some examples of the various types of terrain on the Proctor Crater floor are shown to emphasize the diversity of surface features in the study area. Further sections in this work discuss many of these features in more detail.

Figure 3.3 shows several high-resolution views of the floor of Proctor Crater. Many characteristics of the surface become evident at this scale. Much of the floor is strewn with boulders ranging in size up to 20 m and down to the limit of resolution at 5 m (Fig. 3.3a, b). In Figure 3.3a, the larger boulders have shadows visible at the MOC NA resolution, indicating that they are blocky, positive features on the landscape. Figure 3.3a also shows drifts of dark sand (see arrows) that partially bury some of the boulders, indicating that the boulders are older than the sand drifts, and that the boulders are taller than the sand drifts are deep. There is little evidence for extensive fluvial or glacial activity in the crater, and the Proctor Crater walls are generally too far from most of the crater floor to have

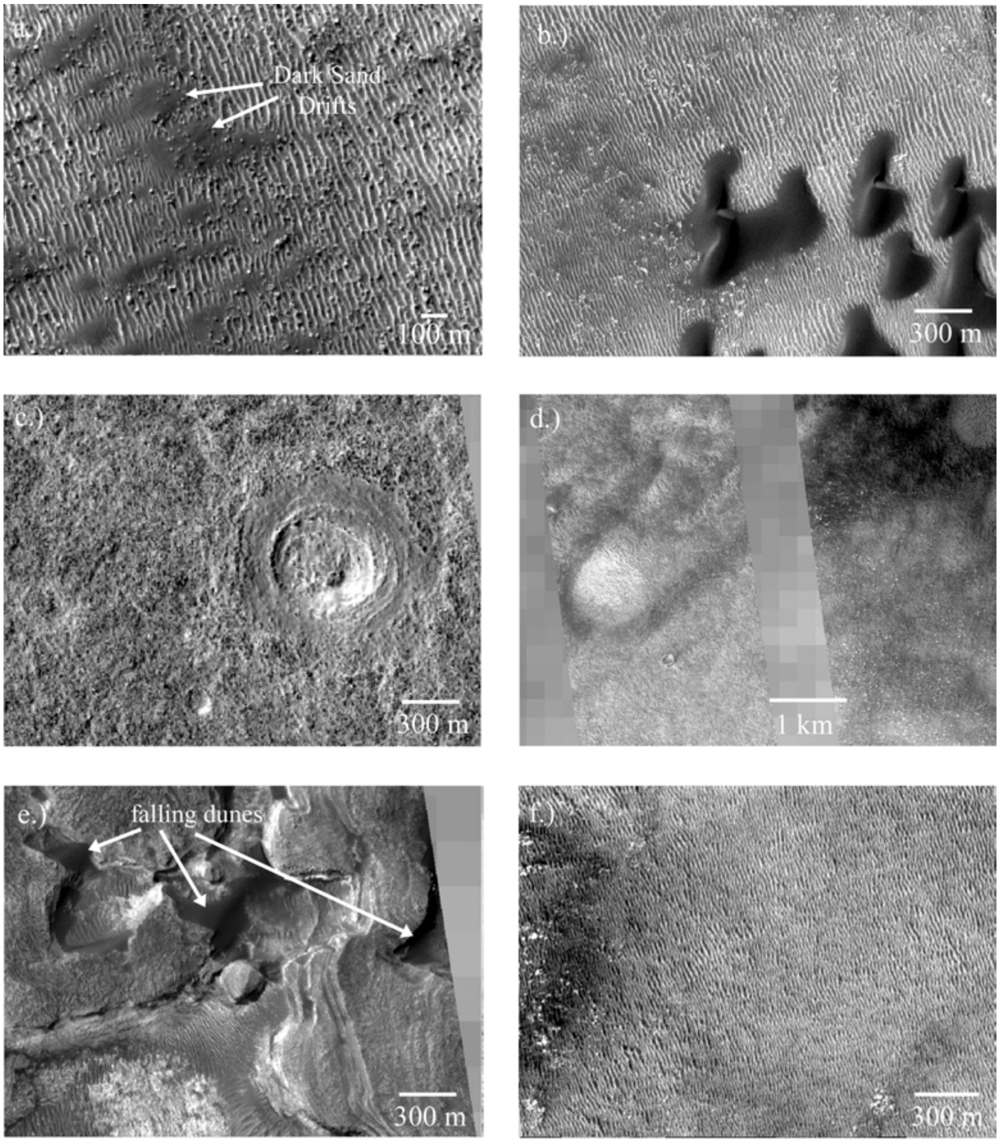

Fig. 3.3. Examples of MOC Narrow Angle images on the Proctor Crater floor. a.) Boulders and sand drifts (MOC NA M2301221), b.) boulders, dark barchans and bright duneforms (MOC NA M0303088), c.) degraded craters on the Proctor Crater floor (MOC NA M0201510), d.) dark erosional wind streaks (MOC NA M0201510, M0306827), e.) strata of basin fill and dark falling dunes in the western pit (MOC NA M0300338), f.) uniform coverage of bright duneforms (MOC NA M0306827).

produced these boulders from mass wasting. Thus, these boulders were most likely emplaced by impact events on the Proctor Crater floor. Boulders produced

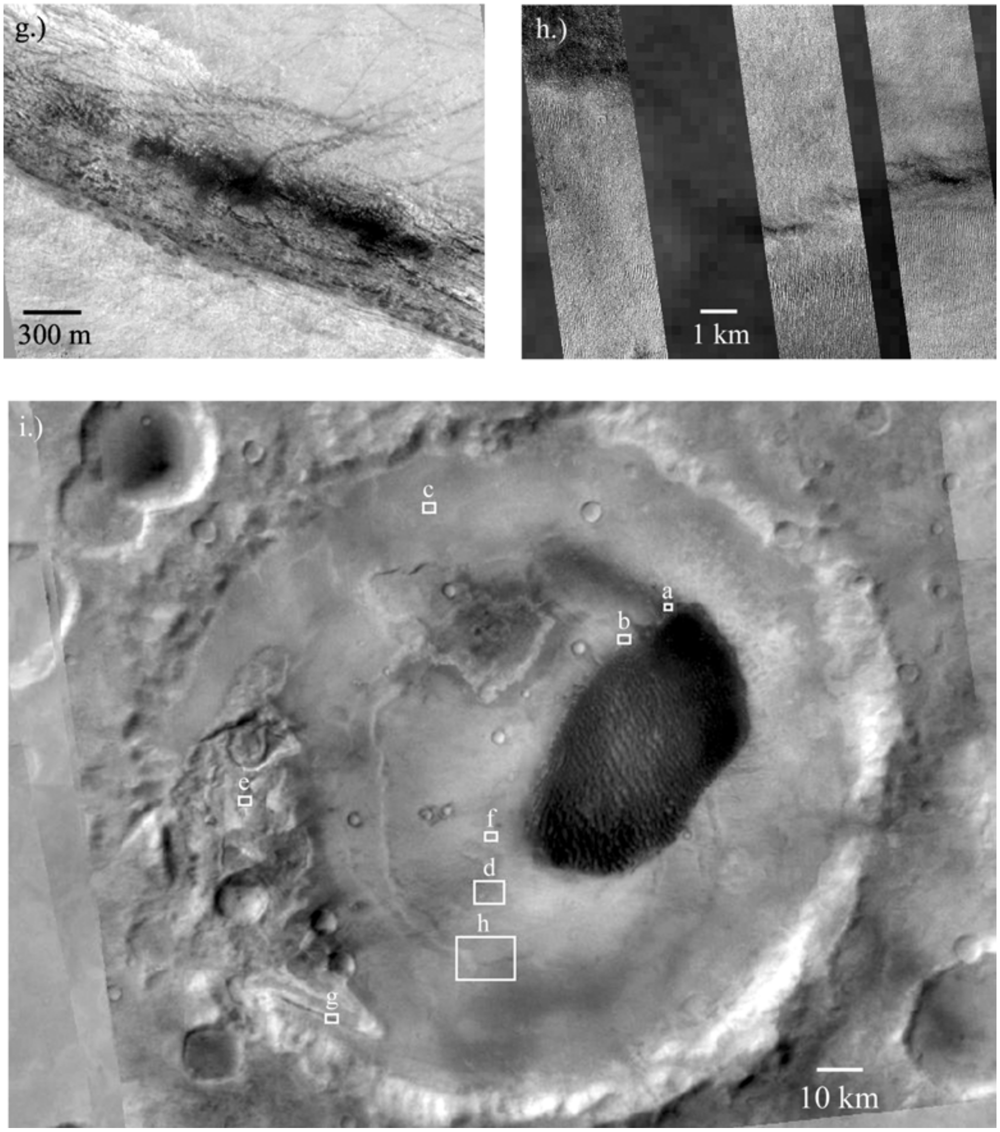

Fig. 3.3. (cont.) g.) dark sand trapped against a northeast-facing hill slope, spawning dust devils as revealed by dark tracks (MOC NA M1103806), h.) mosaic of three MOC Narrow Angle frames over part of a concentric ridge (MOC NA M0201510, M0301614, M0306827), i.) and Wide Angle context for frames a through h.

by crater formation indicate that the surface is consolidated enough to produce coherent blocks that do not shatter or crumble upon landing. *Malin and Edgett* [2000a] state that crater ejecta blankets extend out to one crater radius, far less than what is necessary to explain the ubiquitous boulder fields on the crater floor given the paucity of small craters present both on the floor of and outside the crater. Thus these boulders could not all have come from outside Proctor Crater. Their high abundance on the floor of Proctor Crater must indicate some process by which boulders accumulate relative to other features, and is considered below with regards to the numerous eroded craters on the crater floor. Close views of the dark dunes at the perimeter of the dunefield reveal slipfaces and stoss slopes typical of barchans (Fig. 3.3b). The presence of barchans at the edge of the dunefield indicates that the dunes, when last moved, were left in a state of disequilibrium with their environment. This could mean that the dunefield has yet to reach its final resting location. A more likely conclusion is that the dunefield is mostly in a state of equilibrium, and that these barchans at the edges of the dunefield reflect small variations in relative wind strengths over the course of several centuries or perhaps millennia. Such barchans are typical of dunefield perimeters on Earth, and they tend to be more mobile than the larger interior dunes because they contain less material. Thus they reflect more recent winds.

Beneath the barchans in Fig. 3.3b are smaller, brighter aeolian features, here referred to as “bright duneforms” or “bright bedforms.” These smaller bedforms have been identified in many different terrains on Mars [*Malin and Edgett*, 2001], and in addition they are widespread across the floor of Proctor Crater. Where they coexist with large dark dunes, they consistently lie stratigraphically beneath the larger dunes [*Malin and Edgett*, 2001]. The small bedforms have an appearance more consistent with ripples than with dunes, leading to the proposal that they are large granule ripples [*Zimbleman and Wilson,* 2002]. The superposition relationship and the difference in distribution across the crater floor indicates that the bright duneform and dark dune materials are different populations of aeolian material, and that they were clearly laid down at different times.

There are many small craters in varied states of erosion on the floor of Proctor Crater (Fig. 3.3c). It is tempting to conclude that the subdued appearance of these craters is caused by burial alone, but the ubiquitous boulder fields on the crater floor suggest the situation is more complex. Dust or sand mantles that bury craters should also bury boulders unless there is a constant supply of boulders. The lack of fresh craters indicates that the supply rate of boulders is very low. Thus, the crater floor has undergone extensive erosion and perhaps minor mantling, leaving behind boulders as finer material is blown away, and leading to the highly degraded state of craters observed today. Only deflation by the wind is capable of removing so much material so uniformly across the flat crater floor. Except for the accumulated dunes and bright duneforms, the Proctor Crater floor is currently a landscape dominated by aeolian erosion.

Figure 3.3d shows an area to the southwest of the main dark dunefield, showing dark wind streaks draped downwind of a small crater and a larger relatively bright topographic low that may be a highly degraded crater. Dark streaks such as these may be caused by either the deposition of dark material, such as the dark sand that comprises the dunefield, or by the preferential erosion of relatively bright material, such as the bright duneforms. The streaks are aligned with southwest winds, much like the dark dunes, indicating that the streaks must be aeolian in origin [*Cutts and Smith,* 1973]. The small bright bedforms in this area are oriented roughly transverse to this wind. A greater concentration of boulders within the dark streaks relative to the immediate vicinity is consistent with preferential erosion, and so we consider the dark streaks in this area to be caused by erosional stripping of a relatively bright material over a darker, bouldered surface, as opposed to deposition of dark sand.

A close view of the large western pit (Fig. 3.3e) shows that the crater floor is composed of layered material that appears to be the same sedimentary strata described by *Malin and Edgett* [2000a]. Some surfaces appear rough and may be exhumed volcanic flows, although any source of lava from within Proctor Crater has since been buried by successive infill of sediments. The layers exposed in the pit may comprise all or part of the ~450 m of crater fill. To first order the strata appear to be horizontal beds, indicating that little deformation or faulting has taken place. In the pits the basin fill material has undergone erosion, very likely by wind action, to expose these strata. This erosion occurred after a period of cratering on the surface of the layered unit, but prior to the passage of dark sand through the area. Superimposed on the erosional surface are small ripple-like bedforms and larger accumulations of dark sand. The dark sand is mostly piled against cliffs facing north and east, although some sand stretches across the valleys to reach the opposing wall. These bedforms are "falling dunes," or sand trapped in the lee of topographic highs by prevailing winds from the southwest. Studies of climbing dunes, falling dunes, sand sheets, and dunefields in the terrestrial deserts such as the Mojave of North America [*Zimbleman et al.,* 1995] and the Sahara [*Wilson*, 1971; *Mainguet and Cossus,* 1980] has led to an understanding of sand transport pathways from the original sand source to the final sand sink. For the first time, satellite imagery of Mars is of high enough resolution to allow a similarly detailed pursuit on another planet. These images show that many areas in the large western pit of Proctor Crater have dark falling dunes, indicating that the sand in the large dark dunefield in the center of the crater has traveled from at least as far away as the western pit, and probably from beyond, as the westernmost edges of the western pit also have accumulations of dark sand. The eastern edge of the western pit is not steep enough to inhibit sand from moving up onto the central crater floor.

Small bright bedforms cover much of the crater floor, in addition to lying stratigraphically beneath the large dark dunefield (see Figs. 3.3a, 3.3b, 3.3f, and 3.3h). In several areas they dominate the landscape, obscuring underlying features. In other areas they appear somewhat eroded. In a few areas they are not apparent at all, and it is unclear whether they have completely eroded away or if they never formed in the first place. Figure 3.3f shows one area where the crater floor is uniformly covered by bright duneforms. In this location, these features have a wavelength of ~20 m, and their pattern is broken only by the occasional large boulder. The nearly ubiquitous distribution of bright duneforms across the crater floor with no obvious transport pathways (*i.e.,* no climbing or falling dunes) suggests that these features were probably formed from local materials, such as eroding basin sediments. Bright duneforms and their origin are discussed in detail in Section 3.4.

Dust devil tracks are common features on the floor of Proctor Crater in spring and summer images (see Fig. 3.3g). These tracks are of the typical sort described by *Malin and Edgett* [2001]. They are always dark, most likely indicating the removal of bright dust from a relatively darker substrate. The tracks cross over almost all terrains including the dunefield, and they are commonly ten to fifty meters in width. These are the "long dark filaments" first described by *Cutts and Smith* [1973], although they did not attribute them to dust devils. *Grant and Schultz* [1987] mapped these features in a portion of the Proctor Crater floor in both Mariner 9 and Viking images, noting that they appear in midsummer and disappear in the fall, and that from one year to another their positions change. These tracks almost certainly provide information on the orientations of winds of moderate strength. Weaker winds would not have the strength to move dust devils downwind [*Metzger*, 1999], and very strong winds remove kinetic energy from the boundary layer, preventing dust devils from forming. Dust devils are discussed in detail in the next section (Section 3.3).

In addition to dust devil tracks, Figure 3.3g shows another example of layered material exposures at the southern end of the western pit. In this image the lower left corner is high ground. The layers are visible in a steep wall that crosses the frame from the upper left to the lower right. The upper right corner is low ground, and largely covered in bright dust that has been removed in places by dust devils. The dark splotches on the hillside are interpreted as accumulations of dark sand that has been transported into the region from the southwest (lower left), much like the falling dunes of Figure 3.3e. Some of the dust devil tracks appear to originate in the dark sand, and then to move downwind to the ENE. The surface heating over dark sand will be greater than that over bright dust, and so it is probably easier for dust devils to form over dark sandy surfaces than elsewhere. Further discussions below of dust devils in the vicinity of the dark dunefield support this conclusion. The dust devil tracks also appear darker over the low ground than the high ground, suggesting that more dark sand may be piled up in the bottom of the western pit than is visible in the images, because these deposits are obscured by the accumulation of bright dust.

Figure 3.3h is a mosaic of MOC Wide Angle and Narrow Angle images that shows a close view of one of the concentric ridges that rings the crater floor. Little of the original structure is obvious at this scale. Small bright duneforms are ubiquitous in this image, although they become larger and sharper immediately south of the concentric ridge. To the north of the ridge, dark patches indicate small accumulations of dark material [*Malin and Edgett,* 2001], probably the same dark sand that comprises the dark dunefield and the falling dunes in the western pit. Both the bright duneforms and the dark sand deposits postdate the emplacement of the ridge; however, the different areas and modes of deposition reflect different conditions under which these features formed. The single deposit of dark sand, trapped downwind of the ridge, suggests that this is a remnant of material that previously swept through the region, originating elsewhere. However the commonness of the bright duneforms indicates that the materials forming these features has not moved on downwind, and in fact they may have formed in place.

Examination of small-scale features at the resolution of MOC Narrow Angle images reveals a great deal regarding the nature of the Martian surface. The floor of Proctor Crater has undergone extensive modification by the wind. There are indications of accumulation of sediments from beyond the crater rim as well as the reworking of material composing the strata of the basin fill. Aeolian features range from the vast western pit, probably formed by wind deflation, to the tenuous and temporary dust devil tracks that lightly scour the surface. The sedimentary history of the Proctor Crater floor is clearly a rich and complex chronology of aeolian deposition and erosion.

3.3 Temporal Features

3.3.1. Dust Devil Tracks. Of the twenty-six MOC NA images taken of Proctor Crater before the end of the mapping mission, nine contain features that we interpret as dust devil tracks. Like the features described by *Malin and Edgett* [2001], these tracks are long and thin, up to at least a few kilometers long and ten to fifty meters wide. *Grant and Schultz* [1987] mapped a number of similar features on the floor of Proctor Crater, attributing them to "tornado-like tracks." Dust devils are local vortices produced in unstable atmospheric conditions. The Martian surface, which warms up significantly more than the overlying atmosphere, is an ideal place for the forming of dust devils, particularly during the summer when surface heating is at its peak.

All the dust devil tracks in Proctor Crater are dark features, indicating that the dust devils removed a relatively bright material from the surface as they passed by. The tracks cross dark sand, bright duneforms, and seemingly bare surfaces. Although there are tracks on dark sand sheets at the edge of the dunefield, most dark dunes are free of these features, even in images where the tracks are dense just off the edge of the dunefield. This suggests that if dust devils do pass over dark dunes, there is little bright dust present on the surface of the sand to be removed by a passing dust devil. With two exceptions (described below), the tracks are found in images ranging in season from $L_s = 223–354°$, or from mid spring through late summer. This is the same time of year that they were observed by *Grant and Schultz* [1987] in Mariner 9 and Viking Orbiter images. Seasonal CO_2 frost begins to appear partway through autumn, and remains on shady slopes until late winter. Thus, dust devils appear to form and create erosive tracks during the warmest time of year when surface heating is at a maximum and frost is absent.

Malin and Edgett [2001] describe one feature on the Proctor Crater floor that has the appearance of a dust devil track from a Viking frame, but in a MOC Narrow Angle image is revealed to be the same feature that has been termed a concentric ridge in this work (see Section 3.1). However, part of this feature (marked by arrows in Fig. 57 of *Malin and Edgett* [2001]) is not visible in all MOC Wide Angle images of Proctor Crater (*e.g.,* Fig. 3.1a). The eastern half of the feature is in fact the ridge described by *Malin and Edgett* [2001] and above in Section 3.1. But this ridge, as shown by the MOLA DEM in Fig. 3.1b, does not continue westward like the feature shown by *Malin and Edgett* [2001], but instead curves northward, concentric to the crater rim. Therefore the western half of the feature is probably a dust devil track of the type described by *Grant and Schultz* [1987]. Indeed, it is aligned with most of the other tracks observed both in this work (described below) and by *Grant and Schultz* [1987]. The fact that the western half of the feature is not visible in all MOC Wide Angle images simply reflects the transience of dust devil tracks. This partial misinterpretation is a demonstration of the need for a more complete spatial coverage of high-resolution images as well as careful consideration of all information available.

To determine the daytime wind regime during the summer, the orientations of the most prominent dust devil tracks were measured using an application in Arcview. Fig. 3.4 shows a rose diagram (*i.e.,* a histogram on a polar plot) of the mean orientation of 196 measured dust devil tracks. Because determining the upwind versus downwind direction is impossible from observing most dust devil tracks, all directions shown have been restricted to 0º to 180º. Tracks oriented at 0º or 180º are oriented north-south, and tracks measured at 90º are oriented east-west. One modal direction is evident in Fig. 3.4, with a spread from 60º – 100º, or

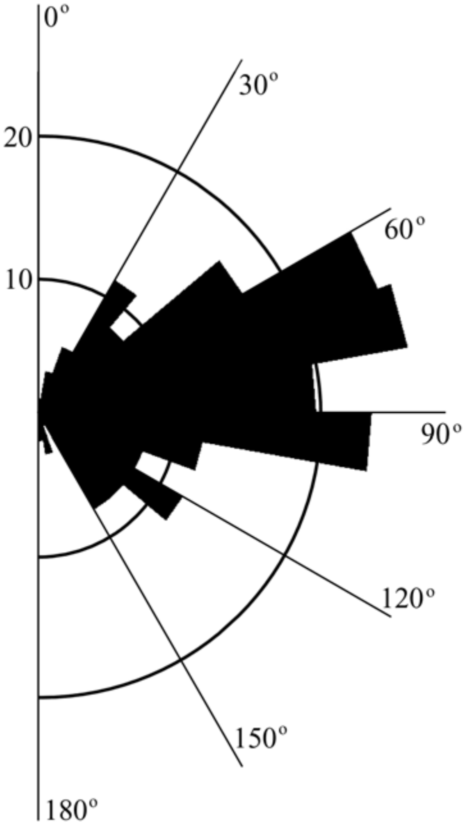

Figure 3.4. Rose diagram of dust devil track orientations. Orientations of 0º or 180º indicate a north-south alignment while an orientation of 90º indicates an east-west alignment. Because of an upwind versus downwind measurement ambiguity, all orientations are restricted to an orientation of 0º–180º. Note the two concentrations of orientations at 60–80º and 90–100º.

generally ENE–WSW. This is the same main orientation of dust devil tracks mapped by *Grant and Schultz* [1987] in both Mariner 9 and Viking Orbiter images. Because of the dust devil tracks appearing to initiate on the sand patch shown in Fig. 3.3g, these dust devil tracks are considered to be formed by winds from the WSW. This direction corresponds to the dune orientations observed by *Cutts and Smith* [1973], as well as those measured in this work, as discussed below in Section 4.2.

The orientation measurements of dunes and dust devil tracks have several implications. The persistence of dust devil track orientations from one mission to another indicates that daytime summer winds are very consistent in direction. Because the dunes in Proctor Crater are so large, they have a much longer memory, and thus reflect the prevailing winds over at least several decades, and possibly over the last million years. The correspondence of dust devil tracks to dune slipface directions indicates that these wind directions have been very typical of this area in the summer for quite a while. Furthermore, dunes require winds above the saltation threshold to shape them, but dust devils may move under lighter winds (*Metzger* [1999] estimates that ~5 m/s winds will move dust devils), and so this alignment indicates that both strong and moderate winds blow in this direction. The correlation of these wind features to modeled surface winds is the topic of Paper 2, although the current wind regime of the crater floor as shown by aeolian features is summarized in this work.

Figure 3.5 shows several examples of dust devil tracks in Proctor Crater. Figure 3.5a shows the locations of each example. Figure 3.5b shows several dust devil tracks that are quite apparent when crossing over a featureless surface, but appear only faintly over a nearby outcrop. The outcrop is likely composed of bedrock of relatively high albedo, covered by little to no dark sand that could be revealed by a passing dust devil. On the other hand, the surrounding terrain is a

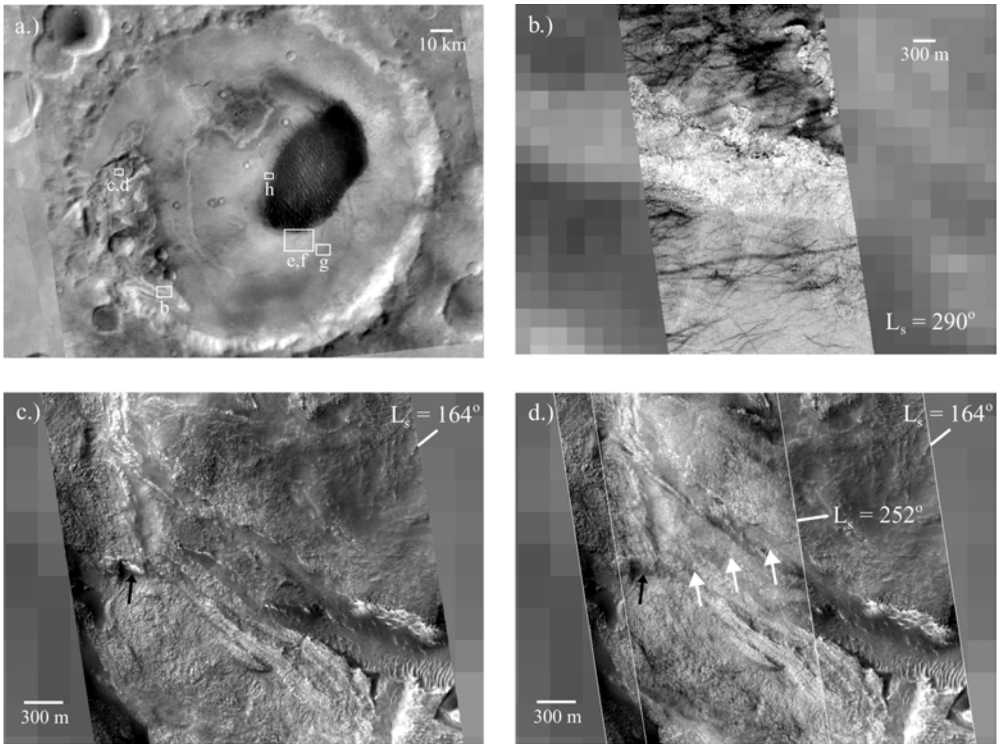

Figure 3.5 Dust devil tracks on the Proctor Crater floor. a.) Context for frames b through h. b.) Tracks crossing featureless plain but not across a bright outcrop (MOC NA M1103806). c.) and d.) are overlapping images in the late winter and late spring, demonstrating the appearance of a dust devil track (MOC NA M0300338, M0906250).

relatively flat area that is likely covered in dark sand overlain by a thin bright layer of dust. Thus the two surfaces produce very different dust devil tracks. If dust devils continue to erode the overlying layer of bright dust on the flatter surface, then it is likely that the albedo and thermal emission spectra will vary accordingly with season.

There are two examples of MOC NA frames that overlap, allowing for a study of dust devil development through the spring and summer. Figures 3.5c and 3.5d show an example from inside the western pit. In Figure 3.5c, an image from late winter, there are no signs of dust devil tracks. In Figure 3.5d, there is one faint

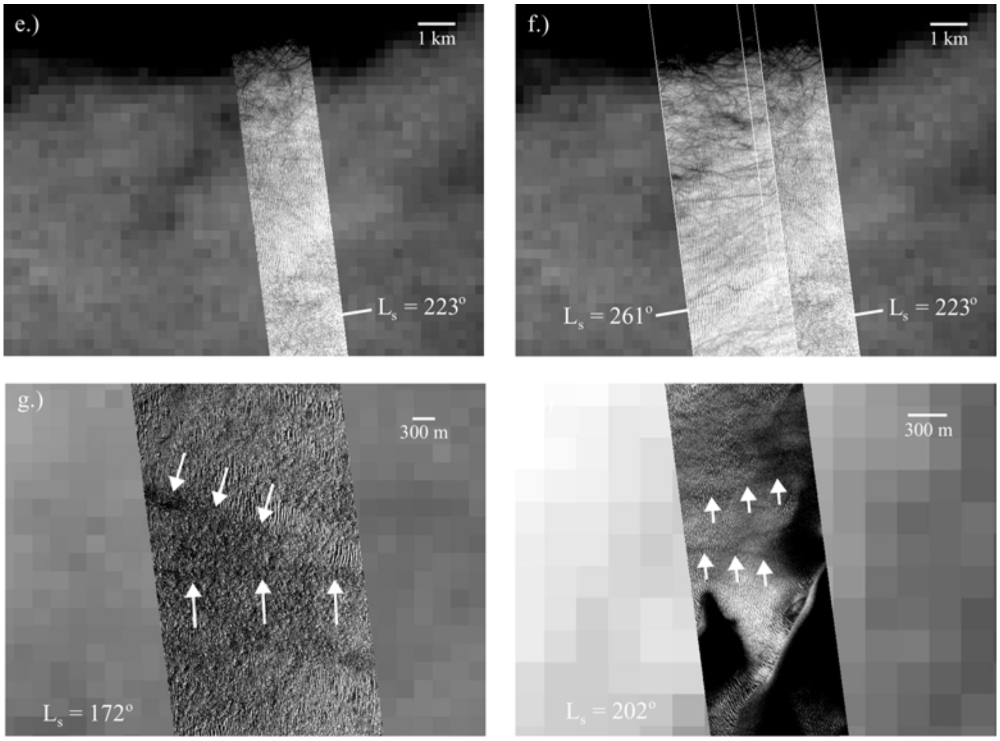

Fig. 3.5 (cont.) e.) and f.) are overlapping images from the late spring showing a growing number of dust devil tracks (MOC NA M0802629, M1001334). g.) (MOC NA M0303087) and h.) (MOC NA M0701445) are images showing potential dust devil tracks in the winter time, although the faintness of the tracks (images have been greatly stretched) may indicate that these tracks are remnant features from the previous summer season.

track marked by white arrows. It is oriented ENE–WSW, consistent with the modal peak in Fig. 3.4. The black arrow shows a patch of CO_2 ice on a shady slope that has disappeared by late spring, when the second frame was taken.

The second set of overlapping images is shown in Figs. 3.5e and 3.5f, which are located just south of the edge of the dark dunefield. In late spring, in Fig. 3.5e, the dust devil tracks are not very abundant and seem to be concentrated near the edge of the dunefield. Dust devils that form early in the season are probably more common on the dark dunes than on the rest of the crater floor because the low albedo of the dune sand should increase surface heating and encourage dust devil formation. Later in the summer, in Fig. 3.5f, dust devils are much more common. Most of the tracks in the overlapping portion of the springtime image are still present in the summertime image, indicating that they are not often erased by strong summer winds. This suggests that, if winds are occasionally strong enough to saltate sand, there is no loose sand readily available that might kick up dust into suspension. The average orientation of dust devil tracks does not appear to change from one frame to the next, indicating no net seasonal shift in wind direction.

There are two examples of dust devil tracks from earlier in the season, shown in Figs. 3.5g and 3.5h (white arrows). In each case the image contrast was stretched a great deal to show these features. Both sets of tracks are oriented with the two dust devil winds. Because of the time of year at which these images were taken and the faintness of the features, we interpret these tracks as old features from the previous summer. They were likely covered by frost over the winter, and have been recently exposed. It may be that in early spring there has not yet been enough dust fallout to obscure them completely, and that a process such as this occurs more commonly throughout spring as the dust loading in the atmosphere steadily increases.

There is only one summertime image on the crater floor that does not contain any dust devil tracks. This is in the same area north and east of the dunefield in which the small bright duneforms appear rounded and eroded (see Fig. 3.3g). If this is a place of constant wind erosion, then there may be no thin layer of settled dust to be lifted by a passing dust devil. Either this is a place where dust is prohibited from settling, perhaps from strong winds, or it is quickly remobilized with a mechanism other than dust devils, such as saltation in local sand sheets. Another explanation may be that there is dust on the surface here, but that there is little contrast between it and the underlying surface. However, thermal inertia calculations, discussed below in Section 6.4, are high enough that there can be very little dust on the surface in this area, supporting the proposal that this area does not accumulate fines. Not surprisingly, the effectiveness of wind action appears to vary spatially across the crater floor.

Dust devil tracks are useful probes of the Martian surface underlying the annual dust fallout. Dark tracks reveal the presence of relatively brighter dust, wind directions at noon during the summer, winds as a function of time throughout the summer as the number of tracks builds up, and surfaces containing darker materials underlying the dust. Only a few outcrops and an area northeast of the dark dunes do not have a darker surface underlying the dust deposits. The orientations of the tracks indicate that local winds in Proctor Crater have remained consistent for many years. Their fresh appearance every summer indicates that dust fallout annually obscures most of the tracks. Further studies of these tracks throughout the summer season can lead to estimates of dust accumulation rates and changes in apparent thermal and compositional properties of the underlying surface.

3.3.2 Frost Features. *Malin and Edgett* [2000b] studied the frosting and defrosting of dunes at both poles. They found that the dunes are generally the first features to develop frosted surfaces during autumn, and they are the last features to lose frost in the spring. They suggest that Martian dunes may trap volatiles, much as *Sharp* [1966] found that the Kelso Dunes of the Mojave Desert trap water. In addition, *Malin and Edgett* [2000b] found that defrosting tends to begin with small dark spots commonly located at the dune margins, which enlarge slowly and coalesce until the entire dune surface is defrosted. They proposed that dark sand beneath thin bright frost accumulations warms more quickly than in other areas, causing the frost to sublimate in patches. Little is known about the relationship between frost and dune sand on Mars, but the MOC Narrow Angle images indicate that the interactions are complex and certainly worth further study.

Although Proctor Crater is located in the midlatitudes (47° S), rather than near the poles, the region is covered in seasonal CO_2 frost each winter. Thus the numerous images of the dunefield provide an opportunity to compare how these dunes frost and defrost relative to the polar dunes. Frost cover begins in mid northern fall, at approximately $L_s = 50°$, and remains in patches on the dunes until late winter at approximately $L_s = 165°$. Because Proctor Crater is located in the midlatitudes, the seasonal frost cover does not last as long as it does closer to the poles. Image coverage during the southern fall is too sparse to determine if the dunes acquire frost before the remainder of the Proctor Crater floor does, as is expected. However, poleward-facing slopes on the dunes are certainly the last surfaces to defrost in late winter, consistent with the observations of *Malin and Edgett* [2000b].

Figures 3.6a and 3.6b show overlapping images during the late winter from two consecutive years. Each image shows partially defrosted dunes within the Proctor Crater dunefield with dark spots similar to those found by *Malin and Edgett* [2000b]. Interpreting images with partial frost cover can be tricky, because features can appear bright from either frost albedo or incident sunlight. Determining whether an area is inherently bright or only apparently so from shading differences requires experience with viewing several MOC images, preferably over different seasons and under different lighting conditions. Figure 3.6c shows an interpretation of the features shown in Figure 3.6b, built from such a knowledge base. Dune crestlines refer to linear peaks of dunes. Slipfaces generally begin from these crestlines, but not all slopes that reach to the crest are necessarily slipfaces. Bright duneforms are located in the interdune flats and thus represent low-lying areas. Slope or slipface adjustments, as defined here,

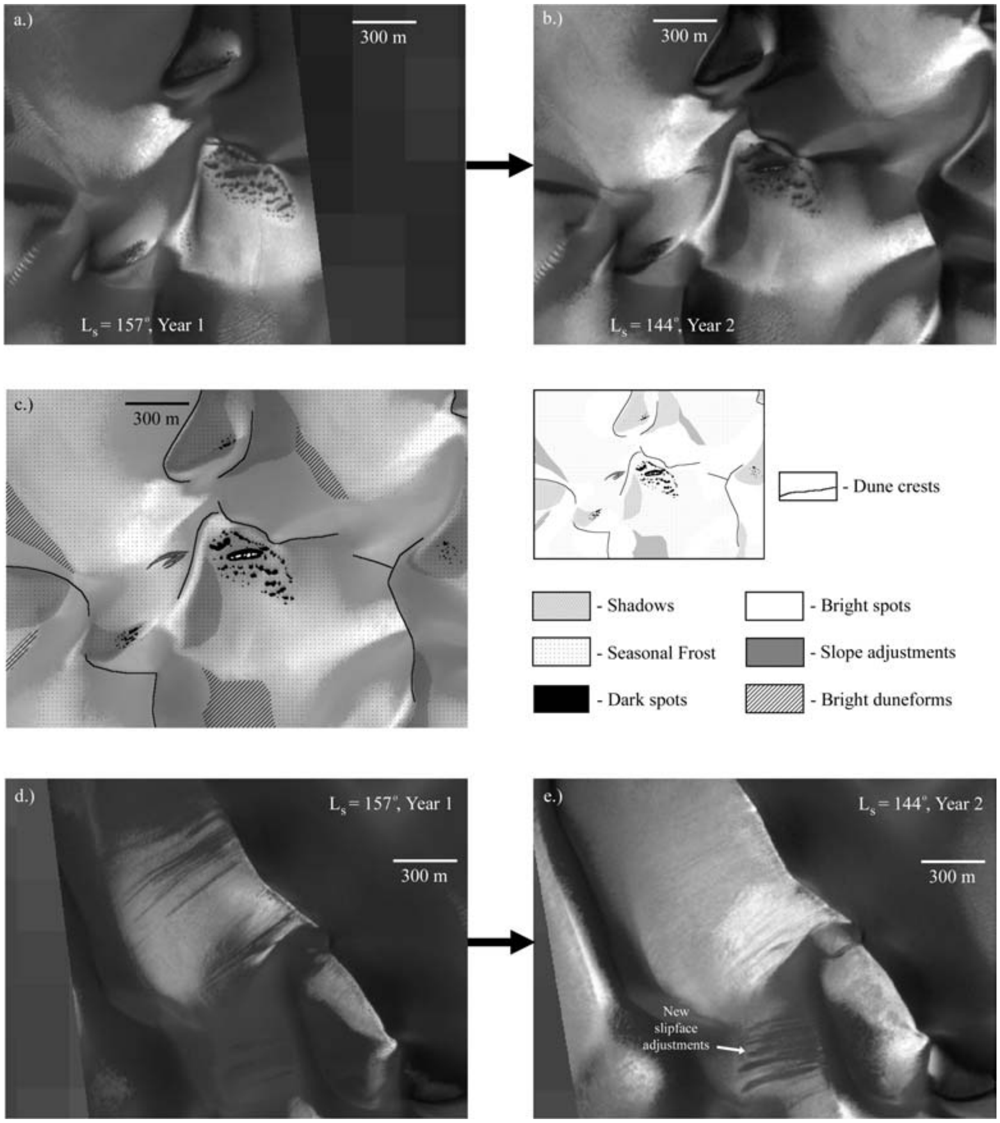

Fig. 3.6. Frost in the dark dunefield. Frames a.) and b.) show the same area nearly one Martian year apart. Defrosting spots occur in the same locations, suggesting that they are produced by some underlying persistent aspect of the dunes (MOC NA M0202711, E0301039). c.) A diagram of the features in b.). Images d.) and e.) show the same region nearly one year apart, with new slipface adjustments formed within the year (MOC NA M0202711, E0301039). Frames f.) , g.) and h.) form a sequence of images over the same area of the dunefield, each showing slope adjustments that persist for at least a year. f.) Late winter image of Year 1, where such adjustments appear to be superimposed on seasonal frost, giving the impression that they are fresh features (MOC NA M0202711).

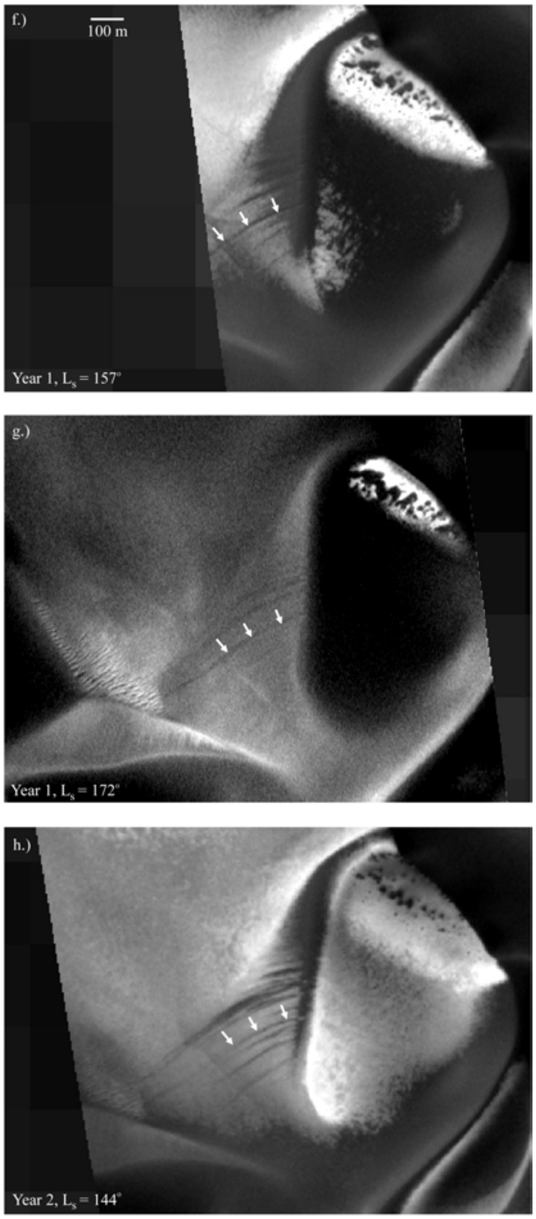

Fig. 3.6. (cont.) Frames f.), g.) and h.) form a sequence of images over the same area of the dunefield, each showing slope adjustments that persist for at least a year. f.) Late winter image of Year 1, where such adjustments appear to be superimposed on seasonal frost, giving the impression that they are fresh features (MOC NA M0202711). g.) Shortly after the frost has disappeared from the slope, the same adjustment scars are still visible (MOC NA M0303088). h.) Nearly a year after the first frame, when the frost has reformed, the slope adjustment scars are still visible, giving the impression that they are recent movements over the seasonal frost. Rather, they must be somewhat older features that inhibit frost formation or allow frost to sublimate more easily (MOC NA E0301039).

are avalanches of sand that has been oversteepened by the wind at the brink of a dune. Such slope adjustments are generally oriented downhill and are good indicators of the local gradient. The patchy seasonal frost is located as drifts in low-lying areas, and on the southern and western sides of dunes. Shadows are located southeast of dune crests, created by a low winter afternoon sun to the northwest.

Like the polar dunes, the Proctor Crater dunes develop dark spots as they defrost. A new development of these features reported here is that they persist in location from year to year. The repetitiveness of dark spot locations indicates that their position is dependent on some relatively stable aspect of the dune surface. Unlike the dark spots on polar dunes, the dark spots on the Proctor Crater dunes are concentrated on steep slopes, rather than along the dune margins. In addition, these features rarely appear on hills facing any direction but towards the pole. The largest spots in Figs. 3.6a–3.6c contain bright cores, which have not been observed in polar dunes. The cores are brighter than frost on the surrounding slope, indicating that this material is not simply a remnant frost patch from the previous uniform cover. *Bridges et al.* [2001] found that dark spots located in small gullies on Mars, similar to the spots on the dunes, are aligned with the local dip and channel trend (*i.e.,* downhill along the channel). In contrast, the spots in the Proctor Crater dunes appear to be aligned either along the strike of the south-facing dune slope or parallel to the crest.

It is possible that the spots are associated with granule ripples that can form on dune slopes. However, in areas where there is summertime coverage of slopes that form dark spots while defrosting, there is no evidence for any features on the smooth dune slopes. Furthermore, there is no physical reason why granule ripples would preferentially form on pole-facing slopes, as the dark spots do. Another idea is that the dark spots are small avalanches over the seasonal frost cover, although no known mechanism causes slope adjustments to form in the same locations in the middle of dune slopes year after year. Finally, it may be that the dark spots are concentrated along interfaces between exposed dune strata. Such strata on terrestrial dunes accumulate water. A similar process could occur on Mars with either H_2O or CO_2 ice, thus keeping the contacts between sand strata cooler than the dark dune sand itself. This could easily cause reprecipitation of sublimating frost, creating the bright cores of the dark spots, much like the mechanism proposed by *Malin and Edgett* [2000b] to explain bright frost halos around dark sublimation spots. Additionally, wind could blow frost from elsewhere into small cracks that are exposed by defrosting, such as the process described for polar "spiders" by *Piqueux et al.* [2002], although summertime images of dunes slopes show a surface devoid of any roughness that could trap windblown ice grains.

Because of the yearly persistence and the lack of associated topographic features, the most likely explanation for these aligned dark spots is preferential sublimation along exposed dune strata. However, it is not clear what process would cause a higher sublimation rate along dune strata, particularly if these strata tend to accumulate seasonal ice. The melting of snow lenses trapped in terrestrial dunes is known to cause unusual surface features, such as small sinkholes and tensional cracks [*Koster and Dijkmans,* 1988]. However, features created by the sublimation of trapped CO_2 frost may be very different from those created by the melting of H_2O snow lenses.

Since these spots mostly form on the shaded slopes and manage to persist much longer into the season than on other slopes, the frost may have enough time to undergo sintering caused by compaction and grain growth in a process modeled by *Eluszkiewicz* [1993]. Thus, preferential sublimation may occur from differential ice grain growth, in which transparent areas absorb more heat from insolation and sublimate faster than opaque areas. This process may in turn be influenced by ice trapped in underlying exposed dune strata. For example, the weight of frost overlying an exposed icy layer between dune strata may compact some of the upper icy layer enough that it sinters into larger grains, which become more transparent to sunlight as they grow. As the frost slowly thins from sublimation, this relatively transparent layer becomes more and more exposed to daily heating until enough heat is collected to begin localized sublimation. There is no reported terrestrial analog for this process, or for defrosting spots on sandy surfaces such as these. This process is similar to that suggested by *Malin and Edgett* [2000b] and *Bridges et al.* [2001] to explain dark sublimation spots. In the case of the Proctor Crater dunes, sintering in the upper layer of ice trapped between dune strata explains the alignment of dark spots along the slope of the dune. The presence of ice lenses may also explain the bright cores, since the remaining ice between dune strata may be cold enough to cause reprecipitation of locally sublimating frost, once the initial wave of defrosting has occurred and swept outward from the center of the spots.

Edgett and Malin [2000] show slipface adjustments in Proctor Crater dunes and propose that they are fresh movements over seasonal frost. However, as they consider, and as discussed below, such slope adjustments may not be as fresh as they appear. Fortunately, there is new evidence confirming that the dunes in Proctor Crater are indeed active from year to year, although the season in which these movements occur is not constrained. Figures 3.6d and 3.6e show the same area roughly one year apart. Figure 3.6d is the same area shown in Figure 17 of *Edgett and Malin* [2000]. In the first frame a frost-covered slope shows superimposed dark tongues of sand that are typical of dune slipface adjustments from easterly winds. In the second frame, taken nearly one year later, seasonal frost has since sublimated away and reformed on the dunefield. The slipface features of the previous year are barely discernable beneath the recent year's accumulation of CO_2 frost. However, new dark tongues of sand have formed farther south, overriding some older scars that are faintly visible in the first frame. In both cases the sand-moving winds come from the east. These dunes are without question active with fresh slipface scars forming each year. However, these movements do not appear to be very common, as not all of the slope adjustments of the previous year are buried by subsequent activity.

There is enough coverage over enough time to show that some slipface adjustment scars remain for at least a year, and that they therefore may superimposed on annual frost cover as suggested by *Edgett and Malin* [2000]. Figure 3.6f, g, and h show the same area at three different times, each showing the same set of slipface adjustments. Figure 3.6f was taken during the time of partial frost cover, in late winter. Arrows point to a prominent dark slope adjustment lobe that appears to have formed over the frost. Figure 3.6g shows the same area later that year, when most of the frost has sublimated away. In this frame, most of the bright surfaces are sunlit slopes, whereas in Fig. 3.6f most of the bright surfaces are frosted slopes. Even though the frost is gone, the dark stripes from slipface adjustments are still visible. The following winter, in Figure 3.6h, the same dark slope adjustments are still visible, although a new larger and darker scar has formed in the intervening year. Clearly, although these features appear to be superimposed on seasonal frost, they are not. Some aspect of the nature of these scars inhibits frost from forming, and/or allows frost to sublimate more easily than on the surrounding slopes. Slipface adjustments loosen the surface material, and it may be that these less densely packed surfaces expose more surface area to the air and thus allow frost to sublimate more quickly than on a more densely packed surface.

The assessment of frost features on the Proctor Crater dunes reveals more about the nature of the dunes than it does about the frost that covers them. In particular, the defrosting surfaces of dunes indicate two aspects of the dunes: that they are active in the current wind regime, but only barely so, and that there may be lenses of ice trapped within the dunes, causing the formation of dark defrosting spots.

3.4 Bright Duneforms

MOC Narrow Angle images have revealed the almost ubiquitous presence of small, generally bright aeolian features over much of the Martian surface [*Malin and Edgett,* 2001]. Morphologically, these features are similar to terrestrial granule ripples, and thus they have generally been given the title "granule ripples" or "ripple-like bedforms" [*Malin and Edgett,* 2001; *Zimbelman and Wilson,* 2002; *Williams et al.,* 2002]. The difficulty with the presence of granule ripples on Mars is the well-known correlation of ripple wavelength with the size of the grains that comprise them [*Sharp*, 1963; *Greeley and Iversen,* 1985]. For example, *Sharp* [1963] found granule ripples in the Coachella Valley, California, with wavelengths up to 3 m and surface grain sizes in the range of 2–5 mm with a few grains ranging up to 10 mm in size. The bright duneforms on Mars are an order of magnitude larger than the granule ripples of the Coachella Valley. Present day winds on Mars that are strong enough to saltate sand-sized grains, much less granules, are rarely if ever measured by lander experiments [*Hess et al.,* 1977; *Schofield et al.,* 1997] or predicted by atmospheric model simulations [*Greeley et al.,* 1993; *Fenton and Richardson,* 2001b; see also Paper 2]. If granule ripples are formed by the saltation of granules or even larger grains, then their existence must be explained given the current wind regime. It may be that they were formed in an ancient wind regime in which winds were stronger than they are today. If this is the case then the bright duneforms are indeed old, because model simulations of the past few million years show that winds do not dramatically increase in intensity simply by varying Mars' eccentricity, obliquity, or passage of perihelion [*Fenton and Richardson,* 2001b]. An alternative explanation may be that granule ripples form by the rolling of large grains rather than by saltation, as has been proposed for terrestrial granule ripples, thus lowering the wind stress required to set these particles into motion [*Sharp,* 1963; *Williams et al.,* 2002]. In order to understand how these features formed it is important to take a close look at their morphology, stratigraphic relation to other features, and state of degradation.

The locations and orientations of bright bedforms within Proctor Crater have been identified and mapped (see Fig. 3.7a). White boxes outline the locations of Narrow Angle images. Like dust devil tracks, the bright bedforms are generally only visible in Narrow Angle images, and so inferring the distribution of bright bedforms is an interpretation dependent on the spatial coverage of the MOC NA frames. The bright duneforms cover most of the floor of Proctor Crater, including the western and central pits. As described by *Malin and Edgett* [2001], they are more common in low-lying areas such as small craters and local troughs. This is true on a larger scale as well, because these features are less common on the nearby intercrater plains than they are on the floor of Proctor Crater, which can itself be regarded as a low-lying area with respect to the surrounding highlands (see Fig 3.1b). The bright bedforms appear to be absent along the northernmost and southernmost rim of the crater floor, although coverage is too poor to determine if this is a trend that spans the entire outer edge of the crater floor.

To determine the average orientation of the bright bedforms, the along-crest direction of 961 bedforms was measured. The resulting rose diagram is shown in Figure 3.7b. Like the dust devils, these linear features appear symmetrical at this scale, with no obvious upwind or downwind slopes, and thus there is a directional ambiguity of 180°. All directions are therefore constrained to greater than 270° or less than 90°. There are two modal directions that appear in the wind rose: a primary one at 330–350° and a secondary one at 5°. If these bright duneforms are

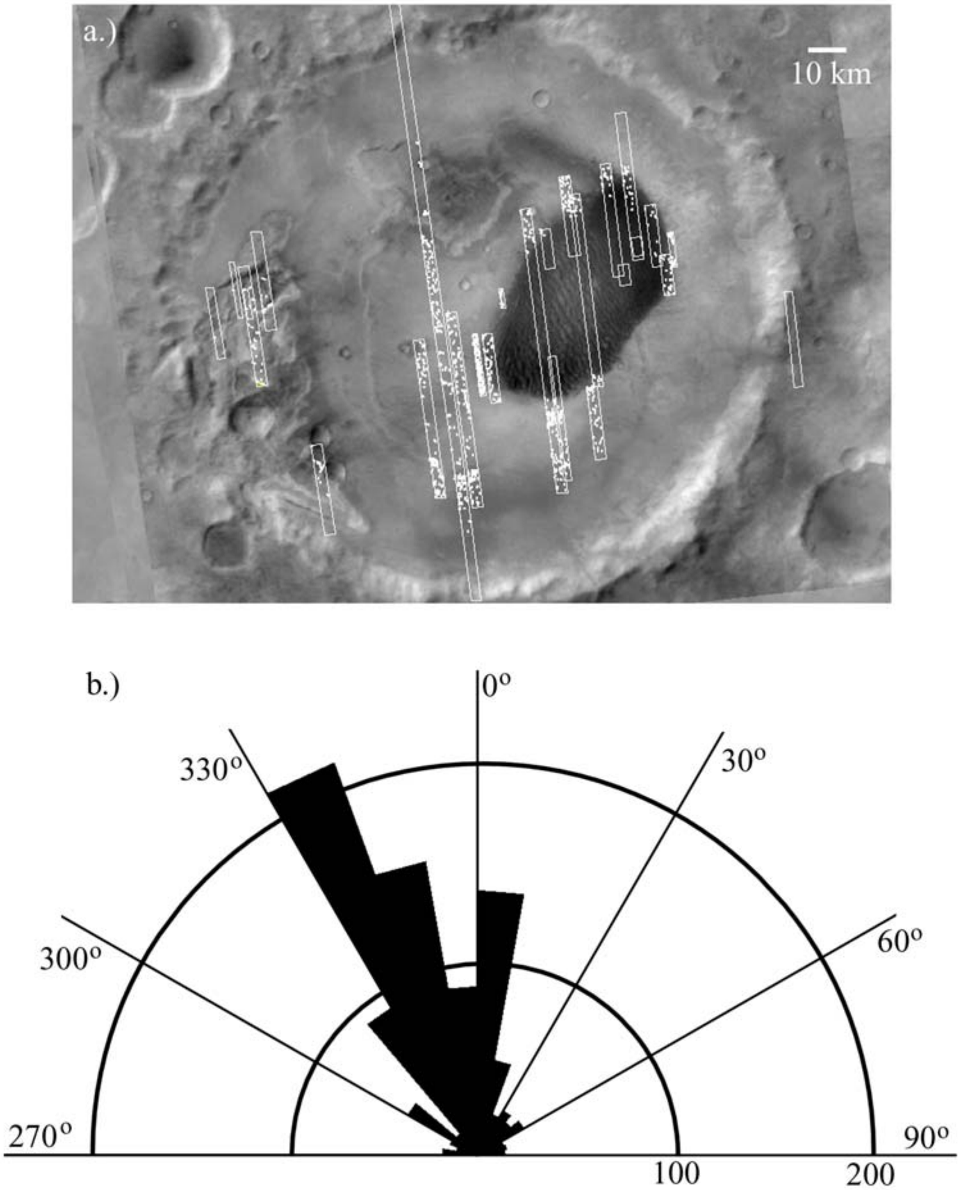

Fig. 3.7. a.) MOC Wide Angle mosaic of Proctor Crater. Boxes outline the location of Narrow Angle images. White dots locate the bright duneforms on the floor of Proctor Crater, which are generally only visible at Narrow Angle resolutions. b.) Rose diagram of bright duneform orientations. If these features are transverse the winds that form them are orthogonal to these directions. An orientation of 0º indicates a north-south alignment, while orientations of 90º or 270º indicate an east-west alignment. Because of an upwind versus downwind measurement ambiguity, all orientations are restricted to an orientation of 90º–270º. Note two concentrations of orientations at 330–350º and 0–30º.

oriented transverse to the winds that most recently shaped them, as would be the case if they are granule ripples, then they reflect winds oriented ENE–WSW and ESE–WNW, respectively. The first of these matches the dust devil track orientation, and both directions correspond to measured dune slipface orientations (discussed in Section 4.2). Although the dust devil tracks are known to be contemporary, the bright duneforms may be ancient in comparison (see discussion below). Thus the fact that the wind orientations that formed them are similar to current wind directions suggests that circulation patterns have changed little since they were created. *Fenton and Richardson* [2001b] showed that over the past several million years, surface wind stresses and directions on Mars have remained very stable. If these features are indeed granule ripples that formed under wind stresses strong enough to saltate granules, then it must have happened long ago enough under conditions that cannot be predicted by current atmospheric models, but recently enough that wind patterns have not changed since their formation. Alternative explanations must be considered, such as the rolling traction motion described by *Williams et al.* [2002] that allows the bright duneforms to be contemporary, or the possibility that these bedforms are not granule ripples but rather that they are small, cemented dunes.

The bright bedforms on the floor of Proctor Crater display a wide variety of morphologies. Several examples are shown in Figure 3.8. Figure 3.8a shows an area southwest of the main dunefield in which the bright duneforms appear to be either eroding away or being buried. Arrows point to an example of a crest that appears intermittently. The appearance of this bedform crest could indicate that it has been either degraded by erosion or buried in low places, an ambiguity that is resolved by considering the density of boulders in the area. Boulders should preferentially disappear under any mantle that might also bury the bright duneforms, but this is not the case in Fig. 3.8a. Rather, the boulders become more prevalent in areas where the dunes appear less crisp, indicating that the

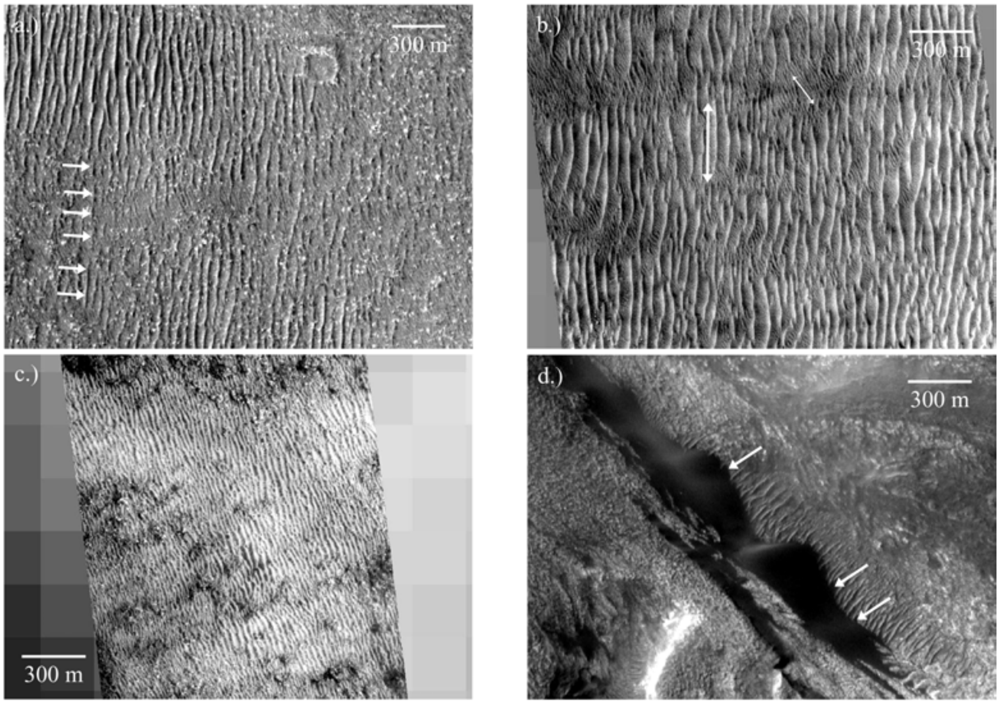

Fig. 3.8. Bright duneforms on the Proctor Crater floor. a.) Degraded crests of bright duneforms, with arrows delineating one example (MOC NA M0301614). b.) Two sets of bright duneforms, differing in wavelength and orientation (MOC NA M0802629). c.) Rounded crests of bright duneforms east of the dark dunefield, possibly indicating gradual abrasion or deflation (MOC NA M1002249). d.) Dark falling dunes overriding smaller bright duneforms (MOC NA M0300338).

process influencing the bright duneforms is erosion, not burial. It is unclear what process causes the erosion of the bright duneforms, but the fact that not all regions of the Proctor Crater floor show this degradation demonstrates that this process is local rather than regional.

Figure 3.8b shows an area south of the main dunefield in which two sets of bright duneforms can be seen (indicated by large and small arrows). Figure 3.8a also shows two sets of duneforms, although they are less obvious. Note that both sets of bedforms in Fig. 3.8b have sharper crests than those in Fig. 3.8a. Each set of bedforms has a distinct wavelength and orientation. These two sets of duneforms were produced at different times under different wind conditions. The smaller set

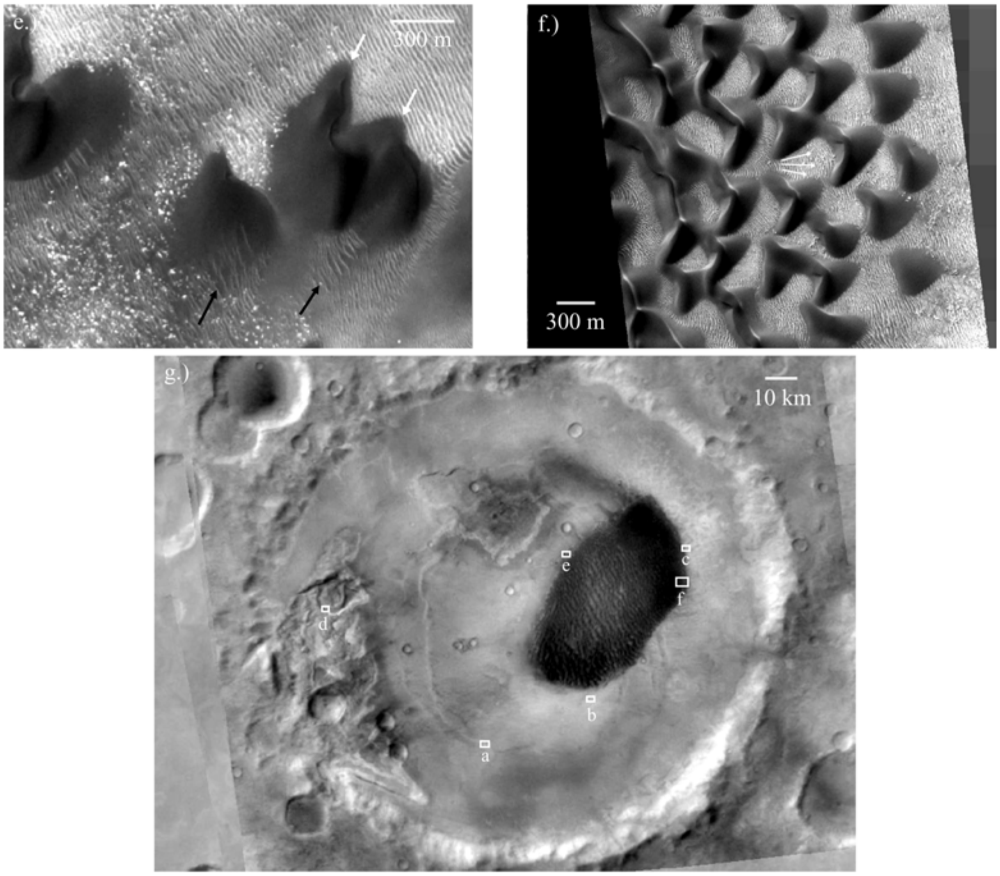

Fig. 3.8 (cont.) e.) Dark barchans overriding bright duneforms. As the barchans pass by they erode away the bright duneforms, but small ripple-like features reform in the wake of the barchans (MOC NA M1001334). f.) In the interior of the dark dunefield, bright duneforms reflect local winds influenced by the large dark dunes. This is not generally the case at the edge of the dunefield (MOC NA M1900307). g.) Context for frames a through f.

of duneforms must postdate the larger, because they crosscut these larger, more degraded bedforms. The smaller bedforms were likely formed from material eroding off the larger bedforms. In addition, while the larger bedforms were created by winds coming from either the east or west, the smaller bedforms were produced from winds from either the southwest or the northeast. This may represent a change in dominant wind directions with time. Alternatively, if the bright duneforms are indeed granule ripples then the difference in characteristic bedform size indicates either a change in grain size or a change in wind strengths. These smaller, newer bedforms may be influenced by weaker and more persistent winds from one direction, while the larger bedforms may have been created by much stronger wind gusts that were less frequent, but that were strong enough to move the larger grains that form the larger bedforms.

Figure 3.8c shows bright duneforms just off the eastern edge of the dark dunefield. These features appear to be much more rounded (*i.e.,* eroded) than the sharp-crested features of Fig. 3.8b. This rounding is an erosional process distinct from that shown in Fig. 3.8a. It may be caused by wind deflation or abrasion, either of which could preferentially erode crests, leaving behind rounded remnants. The rounded crests also suggest some amount of cohesion in these bright bedforms in that some part of their structure has remained resistant to the process that has eroded them. *Malin and Edgett* [2001] found stabilized dark dunes in the Herschel Basin that also display wind erosion in what may be a process similar to that acting on the bright dunes east of the dark dunefield in Proctor Crater.

Previous work by *Malin and Edgett* [2001] has demonstrated that the large dark sand dunes stratigraphically overlie the small bright bedforms where they are found together. In Proctor Crater there is a similar relationship wherever dark dunes and bright bedforms coincide. Figure 3.8d shows dark falling dunes in a depression in the western pit overriding bright duneforms. Arrows point to areas where the dark dunes, migrating northwestward, have piled dark sand against the upwind side of bright duneforms. This demonstrates not only that the dark dunes lie stratigraphically above the bright duneforms, but also that they have been active more recently than the bright duneforms. Figure 3.8e shows a similar relationship between bright duneforms on the northwestern edge of the main dunefield. Here, barchans traveling to the northeast ride over the smaller, bright features. White arrows point to places where dark sand can be seen burying bright duneforms. In the wake of the dark dunes (*i.e.,* upwind of the dunes), the bright features are no longer present, indicating that the passage of the dark barchans disturbs the bright duneforms and erodes them. Similar erosion in the wake of dunes occurs on the eastern side of the dark dunefield, demonstrating that at some point dark sand existed to both the east and southwest of the current dunefield perimeter. In Figure 3.8e, a few small darker ripple-like duneforms have reformed on the upwind side of some of the barchans (see dark arrows), suggesting that the process that forms the small bedforms is still active when the proper materials are present. The fact that dark dunes in one part of the crater floor erode bright duneforms as they migrate over them, but in another area have little effect, indicates that there is a spatial variation in either the amount of cohesion of the bright duneforms or the strengths of the winds that saltate dark sand and abrade the bright duneforms.

Within the main dark dunefield, the relationship between dark dunes and bright bedforms is more complex. Figure 3.8f shows both types of features near the eastern edge of the dunefield. On the right, dark dunes pass over bright duneforms without influencing their orientations. Farther into the dunefield, on the left, the large dark dunes clearly affect the orientations of the small bright duneforms. *Malin and Edgett* [2001] describe the refraction of bright bedforms around topographic obstacles. The same pattern appears to be in effect here, even illustrating Huyguen's Principle by creating hemispherical waves in the wake of two closely spaced dark dunes (see arrows). It seems that at the edge of the dunefield, bright bedforms are unaffected, older and possibly more stabilized than the dark sand. However, farther into the dunefield the bright bedforms are clearly affected by windflow around the dark dunes, indicating that the dunes and bright bedforms are coeval. It is likely that inside the dunefield, wind gusts accelerate when channeled between dark dunes, causing winds that are strong enough to reactivate the bright bedforms. This suggests that the bright duneforms, while stable relative to the dark dunes, are not so cemented that they cannot be reactivated by strong winds.

The bright duneforms are an ambiguity in several ways. It is not certain whether they are partially cemented dunes or granule ripples, or whether they were formed by saltating or creeping grains. Although they lie stratigraphically beneath the dark sand dunes, indicating that they are older, their morphology is clearly affected by the presence of the dark dunes, suggesting that in some places they have been remobilized since the accumulation of the dark dunefield. Varying states of degradation indicate that either the bright duneforms were not cemented to the same degree in all places, or that erosional processes have not acted uniformly across the crater floor.

Although many aspects of the bright duneforms are unresolved, it is possible to speculate on the origin of these features. The widespread presence of these duneforms throughout the crater floor, their apparent difficulty of mobilization, as well as the lack of transport pathways of bright material into the crater, indicate that these features were probably produced from local material. The numerous boulders and degraded craters on the floor of Proctor Crater indicate that a large amount of material has been stripped off the surface, some of which accumulated into these bright bedforms. In contrast, the dark dunefield is localized in the center of the crater floor, with indications of a transport pathway from the southwest. Because some of the bright duneforms are eroded by the passage of the dark dunes, the bright duneforms must have accumulated and become relatively immobile before the dark sand first entered Proctor Crater.

4. The Dark Dunes of Proctor Crater

4.1 MOC Narrow Angle images

Close examination of MOC Narrow Angle images of the dark dunefield in Proctor Crater has led to a number of surprising discoveries regarding the aeolian environment on the surface of Mars. Figure 3.9a shows the dunefield with all available MOC Narrow Angle images superimposed on a MOC Wide Angle mosaic. At the scale of the Wide Angle mosaic, the dunes display their characteristic northwest-to-southeast trend, which has led to the interpretation that these dunes are transverse to either a southwesterly wind [*Cutts and Smith,* 1973] or a northeasterly wind [*Ward et al.,* 1985].

Closer inspection of the dunes leads to a new interpretation of dune morphology. Figure 3.9b shows widely spaced dunes at the eastern edge of the dunefield. The edges of dunefields are useful locations to study dune morphology, because here the sand deposits tend to be thinner than in the center of the dunefield [*Porter,* 1986], often leading to barchanoid dunes [*Wasson and Hyde,* 1983] with smaller and simpler slipfaces that are easier to interpret. The smaller dunes are about 300 m across and, as determined from MOLA elevations, they are ~50 m high. Based on their overall crescentic shape, these dunes appear to be barchans created by ENE winds (*e.g.,* wide arrows). In fact these dunes also have slipfaces oriented to the NNE, indicating another dune-influencing wind from the SSW (*e.g.,* thin arrow). Thus, even at the edge of the dunefield where a thin sand cover limits dune morphology, the situation is not as simple as originally thought. It seems that both previous estimates of directionally opposed dune-forming wind orientations were correct [*Cutts and Smith,* 1973; *Ward et al.,* 1985].

A sample of the interior of the dunefield is shown in Figure 3.9c. The large dunes have a spacing of up to 2 km and heights determined by MOLA elevations of up to 300 m. These dunes are not transverse, but rather they have the

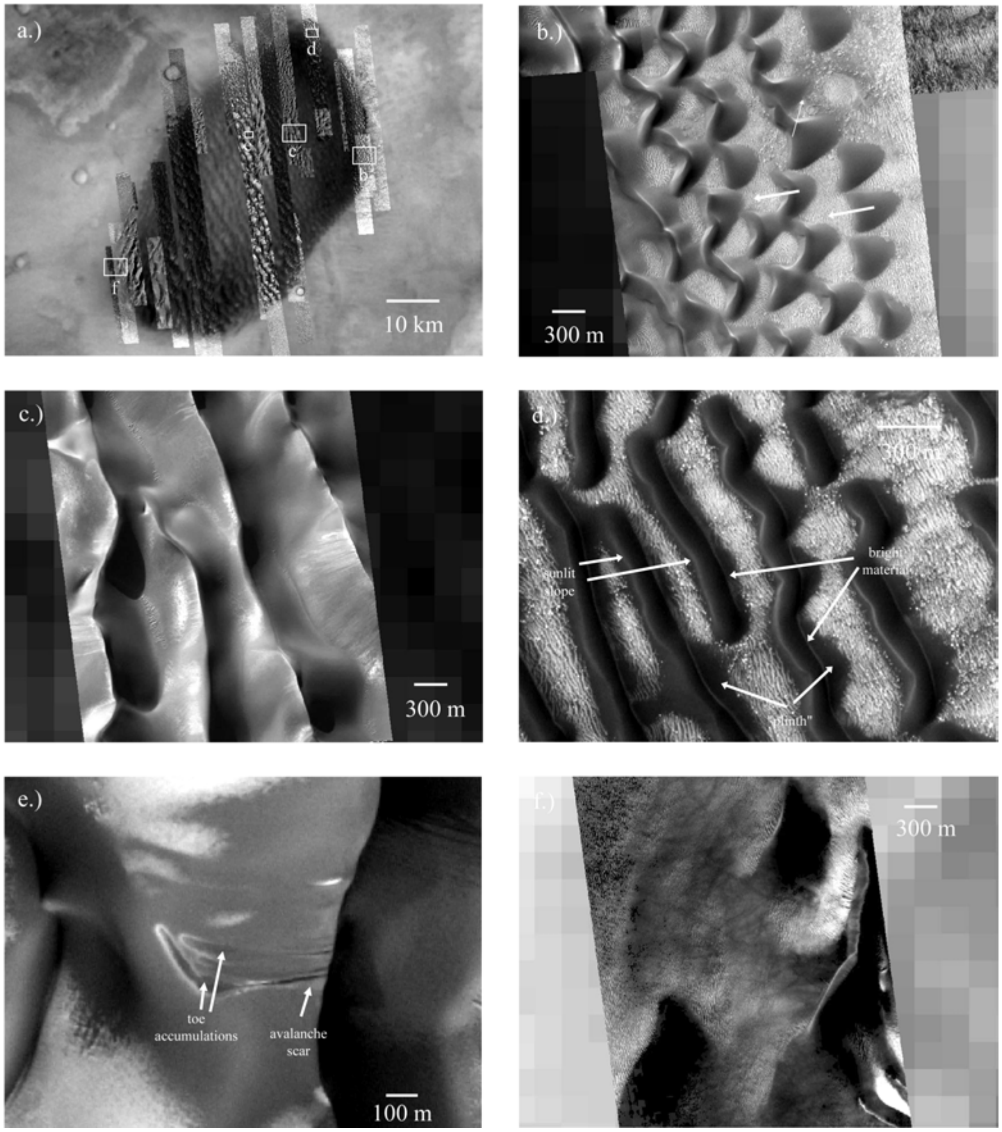

Fig. 3.9. The dark dunes of Proctor Crater. a.) Context for frames b through f. b.) Barchans at the eastern edge of the dunefield containing two differently oriented slipfaces (see arrows) (MOC NA M1900307). c.) Large dark sand ridges (in this case covered in frost) with an appearance similar to reversing transverse dunes, because neither side is obviously a slipface. Note the lack of superimposed secondary dunes (MOC NA M2301221). d.) Dunes near the eastern edge of the dunefield with accumulations of bright sand on their eastern slopes (MOC NA M0702777). e.) Unusual slope adjustment resembling a typical landslide, indicating some amount of dune induration (MOC NA E0301039). f.) Transverse dunes dominate the northwest edge of the dunefield. This example is partially defrosted (MOC NA M1501278).

appearance of reversing transverse dunes and star dunes, as inferred by *Lancaster and Greeley* [1987]. Reversing dunes are produced by two winds oriented roughly 180° apart, leading to a slipface that reverses direction depending on whichever wind is dominant at the time of observation. The constant slipface reversal generally leads to steep inclines on both the stoss and lee slopes (*e.g.,* the reversing crests of the Kelso Dunes, California [*Sharp,* 1966]). In the case of the Proctor Crater dunes, it is difficult to determine which slipface is active in these images. Star dunes are produced by more than two dune-influencing winds of differing orientations, leading to at least two overlapping transverse slipfaces that create a star-like form in plan view. The dunes in Figure 3.9c appear most like reversing transverse dunes (*e.g.,* the large ridges are symmetrical, indicating that slipfaces form on either side of the crest), implying that at least two wind directions affect the morphology of the dunes.

Perhaps more important even than the new morphological dune classification is the fact that there are no secondary dune structures on the slopes of these features. On Earth, large dunes (> ~500 m) nearly always have smaller, superimposed dunes, either of the same type (*i.e.,* small barchans on a large barchan), or of a different type (*i.e.,* small star dunes on a large linear dune) [*Lancaster,* 1988]. By the classification of *Breed and Grow* [1979], the former system is termed a "compound" dune, and the latter is termed a "complex" dune. Dunes with no superimposed dune structures, such as those in Proctor Crater, are called "simple." The transition from simple dunes to compound and complex dunes is not well understood. The difference has been attributed to changes in climatic wind strengths [*Kocurek et al.,* 1991], a shift in bedform type akin to that between ripples and dunes [*Wilson,* 1972], and variations in transport rates on the larger dunes, as though dune slopes grow to approximate a small desert floor that accumulates their own small dunes in turn [*Lancaster,* 1985]. Regardless of what causes the shift between simple and compound/complex dunes, this transition is not seen on Mars, even at the 1–2 km scale of the Proctor Crater dunes. It may be that the scale at which this transition occurs on Mars is much larger than that on the Earth. It is tempting to dismiss this lack of superimposed dunes to a simple difference in atmospheric conditions on Mars and Earth, but previous studies comparing dune length, width, and spacing have shown that Martian dune dimensions in general correlate well with those of Earth dunes [*Breed et al.,* 1979]. Many of the terrestrial dunefields used in the study by *Breed et al.* [1979] consisted of compound and complex dunes that correspond well to the simple Martian dunes, suggesting that secondary bedforms likely have little effect on the overall structure of large primary dunes. There is no obvious reason why large Martian dunes should fail to produce secondary dunes. *Breed et al.* [1979] note the lack of secondary dunes from images at Viking resolutions, proposing that any secondary features that might have once existed have since eroded away. However, recent slipface adjustments (as discussed in Section 3.4) demonstrate that the Proctor Crater dunes are still active, and so secondary features, by the standards of terrestrial dunes, should form under the current wind regime. This observation may bring into question all currently understood theories of bedform climbing. Alternatively, it may simply be that conditions that would produce secondary dunes on terrestrial structures do not exist on Mars at the observed scales.

The interpretation of images of any surface involves discriminating the cause of brightness variations. These are most often created by changes in shading (*e.g.,* topography) and by inherent albedo patterns (*e.g.,* patches of ice on a dark surface). In some cases the interpretation requires careful consideration. Note that in the image analysis in this work, the terms "bright" and "dark" refer to relative brightness differences, and that no attempt is made to measure absolute brightnesses. Figure 3.9d shows a number of dark dunes at the northeastern edge of the dunefield. This image was taken during the summertime, when no frost cover was present. Like all of the narrow angle images in this area, the sun azimuth angle is NNW–NW. From this perspective, the sun should reflect strongly off all slopes facing roughly north and west. The west-southwest facing slopes of the dark dunes are thus bright because of reflected sunlight. The east-northeast facing dune slopes, however, have both a dark and a bright line. The dark stripe is likely a shady slope, most likely a slipface, oriented away from the sun. The bright stripes on the ENE slopes are less easy to interpret. They seem to lie on broad plinths of dark sand that underlie the top portion of the dunes. In places near the slipfaces, the plinths become thin, exposing the underlying surface beneath the dark dunes. Even along these places where the plinth is gone and the top part of the dune rests on the bright duneforms that comprise this layer of the crater floor, the bright stripe is still present. These bright stripes are interpreted as accumulations of bright material. They only appear on dunes near the eastern edge of the dunefield. It is possible that this bright material is accumulated dust. However, bright dust is easily kicked into suspension from the impact of saltating sand, which is easily cleaned off the majority of the dark dunes, and would also strip away this bright layer if it were composed of dust. It is more likely that the bright stripe is an accumulation of (relatively) bright sand that has been blown onto the ENE facing slipfaces. The source of the bright sand on the Proctor Crater dunes may be the tops of the bright duneforms rounded from erosion shown in Figure 3.3g. In a similar study of the White Rock structure, *Ruff et al.* [2001] also propose that lighter material concentrated at the tops of dark ripples comes from the nearby eroding bright massifs that comprise White Rock. If this is the case, this bright stripe of material may be evidence that the bright duneforms are composed of sand rather than granules, because the bright material has saltated up the dune to accumulate at the base of a slipface. There is a more detailed discussion of these bright stripes and how they related to seasonally shifting wind directions in Paper 2.

There are variations in the morphology of slipface adjustments on dunes in the center of the dunefield. In Figure 3.6f though 3.6h, the persisting dark lobes of material have no apparent topography. Most likely they are typical of slipface adjustments in loose sand, in that slender lobes of sand propagate downhill, only slightly disturbing the surface and leaving only a thin layer of loosened sand behind. Figure 3.9e shows a very different type of slipface adjustment. This feature has an appearance similar to a terrestrial landslide. Sublimating frost clings to the edges of the lobes on the lower part of the slope. Near the crest of the dune there is a scar indicating where material has been removed. At the bottom of the slope (*i.e.,* at the toe of the landslide) there is an accumulation of sand that formed from material excavated from the scar uphill. Avalanche scars such as the example shown in Fig. 3.9e are not stable in unconsolidated sand because they cannot retain their sharp edges, and thus they are not generally found on active sand dunes. The presence of an avalanche scar in the Proctor Crater dunes indicates some amount of sand cohesion. Because the more typical slipface adjustments are more common in the dunefield, such cohesion is not likely to be typical in the Proctor Crater dunes. It may be that trapped volatiles freeze the dune, allowing landslide-like structures to form and maintain their shape. However, this feature is also visible in an image from the previous winter, indicating that its structure survived a volatile-free summer. It is possible that parts of the dunefield are effectively stabilized from further activity by some cementation process.

The northwestern edge of the dunefield (see Fig. 3.9a) contains a series of dune structures oriented obliquely to the NW–SE trend of the bulk of the dunefield. Closer inspection (Fig. 3.9f) shows that *Cutts and Smith* [1973] correctly interpreted these features as large transverse dunes with slipfaces indicating winds from the southeast. These slipfaces correspond to yet another wind direction influencing dune morphology. Residual frost coats a few areas on the upwind sides of these dunes, and dust devil tracks cover irregularly shaped sand sheets that fill in and cover the underlying small bright duneforms.

The MOC Narrow Angle images have provided a new view of the Proctor Crater dunes. In some cases, they have confirmed the work of previous studies, as with the case of dune orientations. In other cases, the higher resolution provides new information on dune morphology and activity, requiring modifications to the previous understanding of dune formation.

4.2 Slipface orientations

One of the main goals of this work is to understand the relationship between the aeolian features in Proctor Crater and the atmosphere in its current climatic state. Dune slipfaces are created by slope adjustments to oversteepening (*i.e.,* landslides) created in part by an influx of saltating sand to the brink of the dune slipface from upwind. Grain fall from suspended sand may also contribute to the slipface surface. Transverse dunes have slipfaces that dip downwind, and longitudinal dunes often have slipfaces that are oriented at an angle to their crests but that dip downwind of the last wind to influence them. Even oblique dunes, which are produced in a bi-directional wind regime that forces the dunes to move in a direction different from predominating winds, have slipfaces oriented downwind from the winds that shape them [*Hunter et al.,* 1983]. Barchan dunes are the main exception to this rule in that they have crescentic slipfaces, the central axis of which is oriented downwind, although this axis is simple to identify. Thus, slipfaces are a reliable marker of wind direction in that they almost always face downwind. In this work, slipfaces were identified by their crescent-shaped slipface brinks if the dunes are barchans (*i.e.,* Fig. 3.9b), and by long sharp slipface brinks on steep slipfaces that reach from the brink to the crater floor if they are transverse dunes (*i.e.,* Fig. 3.5h). The large reversing crests are not considered slipface brinks because the slopes on either side are not obviously recent slipfaces and therefore may not directly reflect wind directions (*i.e.,* Fig. 3.9c). Only the clearest cases are considered slipfaces. To provide the best "ground truth" possible for comparison with the mesoscale model experiments (discussed in Paper 2), the orientations of as many slipfaces as possible were measured. Measurements were made by hand, and directions were marked only for obvious slipfaces and where the orientation was clear. Care was taken to avoid marking dune crests rather than slipface brinks, which are not necessarily co-located.

Figure 3.10a shows the dunefield with all slipface markings (lines are parallel to the wind directions that produce each slipface). We found that three main wind directions influence dune morphology. Figures 3.10b and 3.10c show specific examples of slipfaces exhibiting each of the three orientations. Figure 3.11 shows wind roses of each of the three main slipface directions and the mean wind orientations that produce them. Almost all of the measured slipface brinks were crisp, suggesting that they have not undergone erosion since they were last modified. Terrestrial dunes that experience more than one sand-moving wind tend to develop rounded brinks and subdued slipfaces under modification from oblique winds [*Sharp*, 1966]. This rounding process is not so obvious in the Proctor Crater dunefield, suggesting that these dunes may be partially cemented. In Antarctic dunes, snowfall buried by subsequent slipface activity has been observed to allow oversteepened cornices of sand cemented by snow to develop on lee slopes [*Calkin and Rutford,* 1974]. Similar lenses of snow have remained in terrestrial dunes throughout the summer season, such as those of Wyoming [*Steidtmann,* 1973] and the Antarctic dunes [*Calkin and Rutford,* 1974], and for a good portion of spring, Alaskan dunes [*Koster and Dijkmans,* 1988]. Like the sides of the landslide scar shown in Fig. 3.9e, these sharp brinks in the Proctor Crater dunes may indicate the presence of seasonal CO_2 frost trapped within the dunes. Although it is unlikely that the CO_2 frost would remain throughout the summer, it may persist long enough to allow old slipface brinks to retain their crispness.

The first slipface orientation, shown in yellow (see Fig. 3.10), is pervasive throughout the dunefield, producing barchanoid dunes near the edges and contributing to the large reversing dunes that dominate the central portion of the dunefield. Because they are so pervasive, these slipfaces are referred to as the primary slipfaces. The average orientation of 354 measured primary slipfaces (see Fig. 3.11a) indicates formative winds from 239° ± 18° (mean ± standard deviation), or WSW. (In this system, 0° indicates winds from the north). The spread in slipface orientations is caused by a gradual shift from WSW in the western and central portions of the dunefield to SW on the eastern edge of the dunefield (compare arrows in Figs. 3.10b and 3.10c). These slipfaces are consistent with the southwesterly wind regime proposed by *Cutts and Smith* [1973]. They also match the trend of most dust devil tracks (see Figs. 3.3a and 3.4), most bright duneforms (see Fig. 3.7), and a number of small dark sand streaks extending off the southeast edge of the dunefield (see Fig 3.1a).

A secondary wind, shown in turquoise in Figures 3.10a and 3.10b, has an average wind orientation from 150 measurements of 110° ± 18° (see Fig. 3.11b), or from the ESE. This secondary wind is found in all but the easternmost portions of the dunefield. This wind produces the transverse dunes on the northwest edge of the dunefield, shown in Figure 3.9f. It is also partly responsible for creating the large reversing dunes found in the center of the dunefield, in conjunction with the primary WSW winds. This ESE wind also produces the large dark sand streak that extends to the west-northwest from the northernmost tip of the dunefield (see Fig. 3.1a). Finally, it matches the orientations of the secondary set of bright duneforms that cover the crater floor.

The third wind orientation found is shown in magenta in Figures 3.10a and 3.10c. Unlike the primary and secondary winds, it appears to affect only the eastern portion of the dunefield, although here this wind is dominant. Based on 154

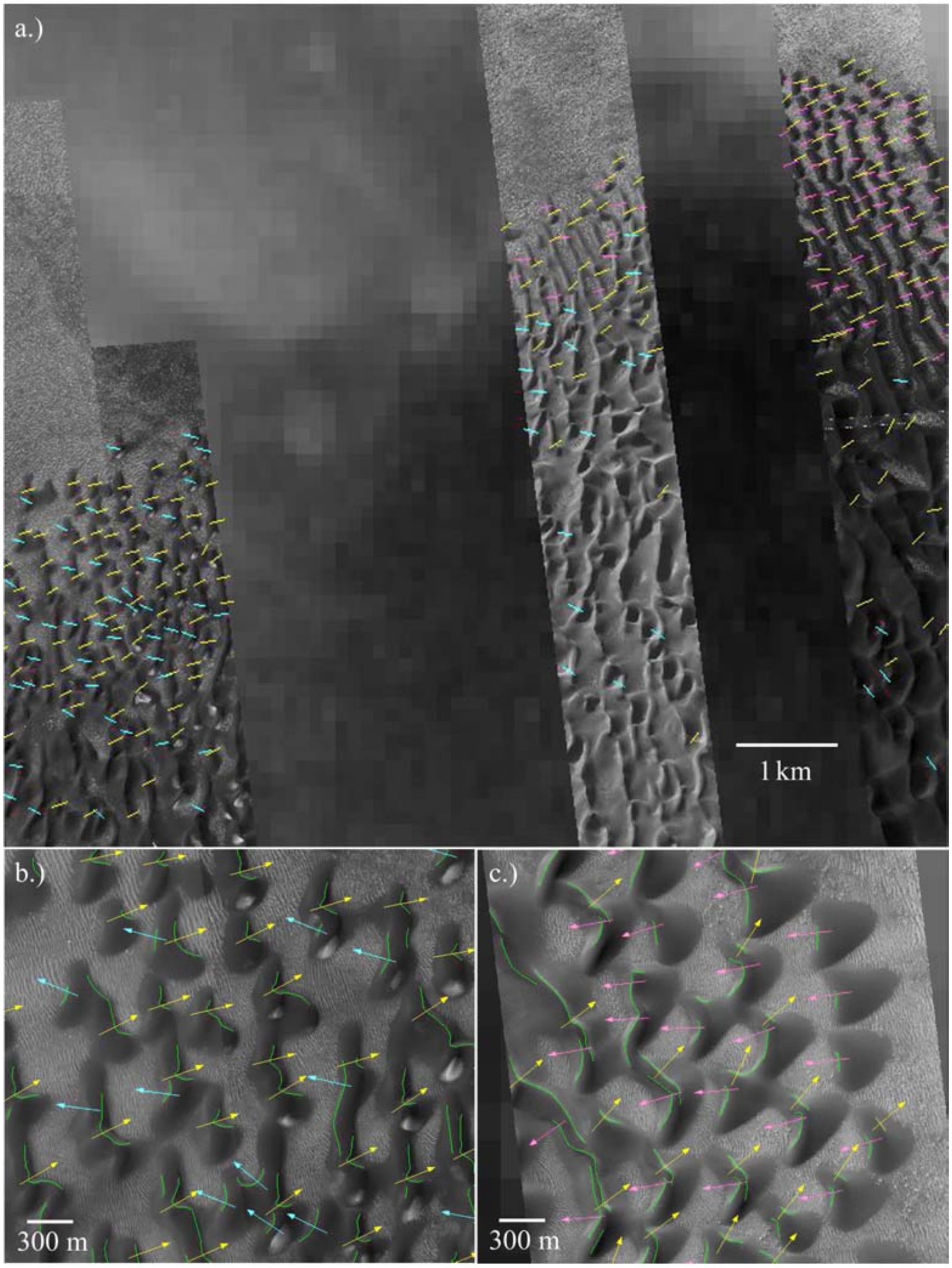

Fig. 3.10. a.) The northern part of the dark dunefield with markers on measured slipfaces. Colors correspond to wind direction: Primary winds (yellow) are from the WSW, secondary winds (blue) are from the ESE, and tertiary winds (magenta) are from the ENE. Frames b.) and c.) show examples of the three different slipface orientations.

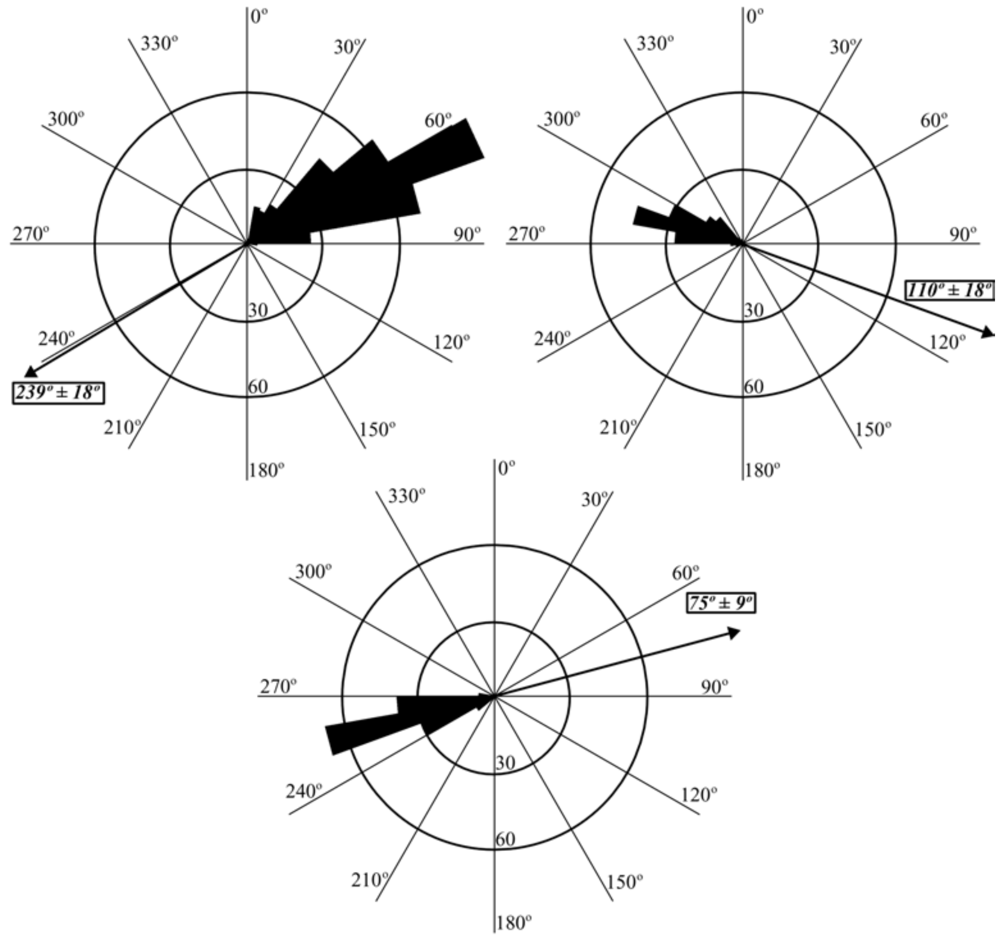

Fig. 3.11. Rose diagrams of the three dune slipface orientations shown in Figure 3.10. Boxed numbers and thick arrows indicate the mean and standard deviation wind direction of the primary, secondary, and tertiary winds. In this system, 0º represents winds from the north.

measurements, this tertiary wind has an orientation of 75º ± 9º, or ENE (see Fig. 3.11c), consistent with the dune orientations mapped by *Ward et al.* [1985]. Both the secondary and the tertiary winds are oriented obliquely to almost 180º with respect to the primary winds, leading to the observed mixture of reversing transverse dunes and star dunes at the center of the dunefield. The tertiary wind is oriented roughly 180º from the primary wind, which may mean that dust devil tracks and bright duneforms that appear to align with the primary wind in fact correspond to this wind. However, this third wind only appears on the eastern portion of the dunefield, and thus it is likely only present over the northern and eastern portion of the crater floor. North and east of the dunefield, dust devil tracks are conspicuously absent and bright duneforms are either rounded from erosion or absent. Thus, there are no surface features other than dune slipfaces and a small area of rounded bright duneforms that reveal this wind in the MOC NA images.

The dunes as seen today correspond well to the orientations of not only bright duneforms, which are older and less mobile than the dark dunes, but also dust devils, which are reformed and erased on an annual basis and thus are much younger than the dunes. It appears that the wind regime that built the dunefield is still active today. Given the three opposing winds, the dunes are clearly located in an area where winds converge. This is expected of reversing transverse and star dunes. *Christensen* [1983] proposed that the intracrater dunes in the southern highlands are trapped because the winds are strong enough to saltate sand downhill into the crater, but not strong enough to saltate sand uphill out of the crater. Here, the measurement of wind directions shows that the dunefield is located where winds are balanced, leading to net sand deposition. If the sand were truly trapped by topography alone then the dunes would be located in the lowest places on the crater floor, the western and central pits (see Fig. 3.1b), but this is not the case. Outside the crater walls the dominant wind must have been from the west-southwest, in order to transport material into the crater and leave behind falling dunes as the remnants of an ancient transport path. Inside the crater, however, the winds must be influenced by the crater walls, producing a convergent airflow that traps the sand quite effectively. This suggests that all of the intracrater dunefields in the southern highlands of Mars are features trapped, not by topography alone, but by convergent local winds that are influenced by topography.

4.3 Dunefield Volume, Structure, and EST (Equivalent Sand Thickness)

The volume of the Proctor Crater dunefield is a useful parameter for comparison to other dunefields on Earth and Mars. *Wasson and Hyde* [1983] define the equivalent sand thickness (EST) of a dunefield as "the thickness of a continuous sheet of sand which results from the hypothetical spreading out of dunes over a specified area." They used this parameter as an estimate of net sand supply to a dunefield to show that dunes of differing morphology form in areas where sand is accumulating or migrating. If the volume of the dunefield is known, the EST can be calculated by dividing the volume by the area covered by the dunefield. Below is a discussion of volume and EST estimates using two different techniques, both of which use MOLA elevations.

The first method uses tools built into ArcView to directly estimate the volume of a three-dimensional figure. A "triangulated irregular network" (TIN), or a three-dimensional construct of the dunefield, was created using MOLA elevations. Using this topographic model, the amount of dune sand was calculated using a volume defined to be above the local crater floor (at a height of 541 m) and within a perimeter defined by the edge of the dark dunes as observed in MOC Wide Angle and Narrow Angle images. The resulting volume is 140 km^3. The estimated planimetric surface area defined by the perimeter at the edge of the dunefield is 1728 km^2. One difficulty with using the TIN to estimate volume is that although most of the large dunes are resolved along each MOLA track, the distance between tracks is usually too large to fully construct a proper model of the dunefield (*i.e.,* the dunes are aliased). The volume calculation only accounts for the volume beneath the modeled TIN, and it is subject to inaccuracies caused by the aliasing.

The second method of determining the dunefield volume uses each MOLA track that crosses the dunefield, but only considers along-track estimates of dune height. Many of the dunes are well resolved along each MOLA track, allowing for an accurate determination of sand area beneath each track, or an integration of the area below the curve for each track. Once this value is determined, the average height of sand for each track can be calculated by dividing the integrated area by the length of that MOLA track across the dunefield. This leads to an estimate of the equivalent sand thickness (EST) for each track. Forty-eight MOLA tracks are distributed uniformly across the dunefield, and thus the mean EST from all of the tracks provides a reasonable estimate of the average EST of the entire dunefield. This mean dunefield EST value multiplied by an estimate of the surface area beneath the dunes leads to a sand volume estimate. Using the planimetric surface area of 1728 km^2 calculated in ArcView, the estimated volume of the dunefield is 180 km^3. This value is larger than that calculated by the built-in script in ArcView. The second method is considered to be more reliable because it relies only on the along-track MOLA distances in which most of the dunes are resolved, rather than on a three-dimensional construct in which cross-track surfaces are calculated using aliased data.

The first volume estimate method described above leads to an EST of 80 m, and the second leads to an EST of 105 m. Both estimates are very high values, larger than those for most dunefields on the Earth. It is consistent with a convergent wind regime in which the sand transport into the dunefield is greater than that out of the dunefield. *Wasson and Hyde* [1983] found that star dunes form in areas with large EST values and a high variability of wind direction. The reversing and star dunes of Proctor Crater are certainly located in an area of convergent and variable winds, as evidenced by the three different slipface orientations described above. The northern polar sand dunes have a mean EST of only 1.8 m, consistent with the barchanoid and transverse dunes that are observed in these ergs [*Lancaster and Greeley,* 1990]. It seems that while the dunefields of Mars can be directly compared to those of Earth both morphologically and dynamically, the variations among dunefields on Mars is at least as great as that on Earth.

Figures 3.12a and 3.12b show MOLA reflectivities and elevations, respectively, for a traverse across the dark dunefield in Proctor Crater. This is a nighttime groundtrack, thus avoiding any complications caused by reflected sunlight. Each MOLA footprint is 170 m wide, and the along-track shot spacing is 300 m [*Smith et al.,* 2001]. The location of the traverse is shown in a MOC Wide Angle mosaic in Figure 3.12d and in the 400 m resolution shaded relief DEM in Figure 3.12e. Although most of the track crosses the dark dunefield, only the large dunes in the southern two-thirds of the track are fully resolved. The northern third of the groundtrack crosses dunes that are smaller than the spacing of the MOLA shots. Although the larger dunes are barely resolved, a number of observations can be made based on MOLA data alone. First, the largest dunes are superimposed on a mound of sand that reaches up to 50 m thick. The large dunes themselves range from 100 m to 250 m high, or phrased another way, 50 m to 200 m on the 50 m high sand mound. In places where net deposition of sand occurs, sand seas accumulate. If the deposition outpaces the rate of migration, then eventually bedforms will migrate over one another, causing dunefields to accumulate strata of sand beneath the current overriding dunes [*Rubin and Hunter,* 1982]. The presence of the mound supports the conclusion that the dunes of Proctor Crater are and have been located in an area of net deposition since the dunefield began accumulating. Considering that the wind regime is convergent, and appears to have been convergent for the history of the dunefield, this result is not surprising.

One way of determining the location of the underlying sand mound within the dunefield is to use MOC NA images. Boulders are strewn over the entire area surrounding and underlying the dunefield, but only appear where the sand is thin enough to reveal their presence. The area in which MOC NA images do not

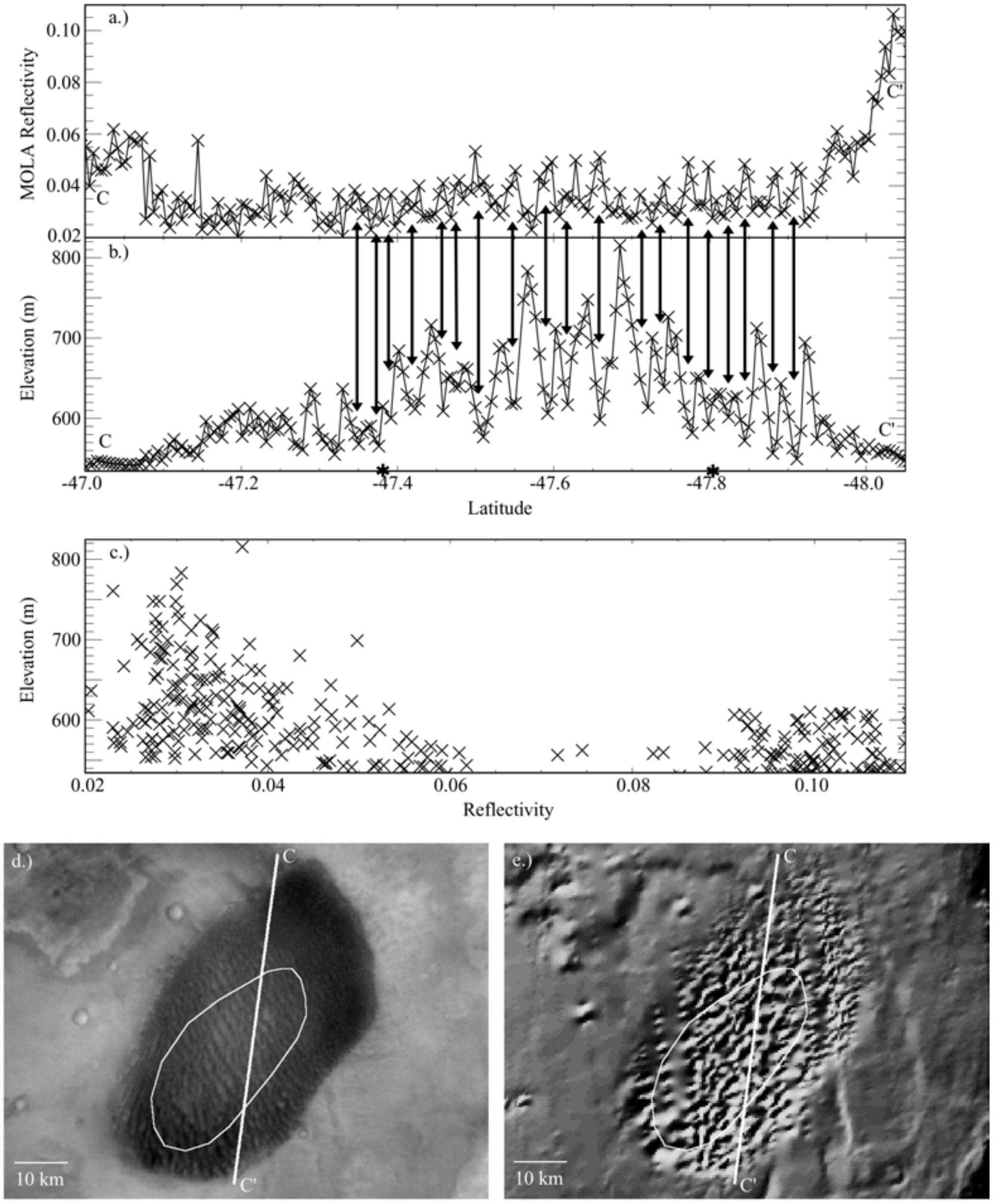

Fig. 3.12. a.) MOLA reflectivities and b.) MOLA elevations for traverse CC' (shown in d.). Black arrows between a.) and b.) connect the low-lying areas between dunes, all of which correspond to higher MOLA reflectivities. Stars along the latitude axis indicate the edges of the 50 m high sand mound beneath the dunes. c.) Scatter plot of MOLA elevations vs. reflectivity showing that only the low elevations are bright (*i.e.,* are not purely dark sand). d.) MOC Wide Angle image of the dunefield. e.) Shaded relief based on a 400 m resolution MOLA DEM. In both d.) and e.), the traverse CC' and an outline of the sand mound is shown.

show any boulders is outlined in Figures 3.12d and 3.12e. Boulders visible in MOC NA frames in Proctor Crater are 5–20 m wide, and presumably as high, so where the boulders disappear the sand cover must be at least 5 m thick. The boulders are barely resolved, and so it is difficult to tell from inspection whether they are partially buried or fully exposed. Because of the incomplete coverage of NA images over the dunefield, the border of the sand deposit is highly uncertain. Stars have been marked on Fig. 3.12b where the border of the sand deposit intersects with the MOLA track. These locations match fairly well where the sand deposit begins to thin out in the MOLA track. The bulk of the sand accumulation is in the central and western portions of the dunefield. This suggests that in the eastern and northern portions, where the dunes are smaller (and poorly resolved by MOLA as a result), either the wind regime leads to less net deposition than in the rest of the dunefield, or that the northern and eastern portions are simply younger and have not had the time to accumulate as much underlying sediment.

A second observation from Figure 3.12b is that the large dunes resolved by MOLA are fairly symmetrical. In general, transverse dunes have a long shallowly-angled stoss (upwind) and a short, steep lee (downwind) slope. The fact that this is not the case on the large ridges in the dark dunefield indicates that these dunes cannot be simple transverse ridges. A symmetrical cross section is more consistent with reversing transverse dunes, as suggested by MOC NA images, or with longitudinal dunes.

Another observation made using the MOLA track is that MOLA reflectivity correlates inversely with elevation. That is, the dune peaks are dark and the troughs between dunes are bright. This is well illustrated in a scatter plot of elevation versus reflectivity in Fig. 12c, in which high elevations always have low reflectivities but some low areas have relatively high reflectivities. This correlation of bright material in interdune areas is not surprising given the appearance of bright duneforms in these areas. However, arrows in Figs. 3.12a and 3.12b indicate that this relationship appears to hold true for every dune and trough that is resolved by MOLA, even over the 50 m accumulation of sand in the center of the dunefield where bright duneforms are nonexistent. Given this inhomogeneity and the multidirectional wind regime, the central deposit of sand is not likely to be a stratigraphically simple unit. In most cases on terrestrial dunes, grains decrease in size from the base of a dune to its crest [*Lancaster,* 1995], and so this change in reflectivity may reflect a shift in average grain size. If this is the case then there may be two populations of sand: one that is finer grained and dark, and one that is coarser and relatively bright. This violates the classic interpretation of Martian aeolian grains in that dark particles are considered to be sand-sized while the bright grains are considered to be finer dust-sized particles. However, interdunes contain sediments that are much more poorly sorted than adjacent dunes [*Lancaster,* 1995], and so the brighter interdunes may merely reflect a higher concentration of bright dust that has not bee stripped by saltation. Like many terrestrial dunefields, the interdune areas in the Proctor Crater dunefield may serve as a depositional location for fines.

4.4 Comparison with the Kelso Dunes, California, USA

The Kelso Dunes are a well-studied set of dunes located in the Mojave Desert of California. They are situated in a valley surrounded by three mountain ranges. A multidirectional wind regime balances the flow of sand, causing the sand to accumulate into tall reversing transverse sand ridges [*Sharp,* 1966]. *Lancaster* [1993] estimated that the Equivalent Sand Thickness (EST) might reach 46 m over these large ridges, placing them in the range of star and transverse dunes as calculated by *Wasson and Hyde* [1983]. The dunefield is much smaller than that of Proctor Crater, with an estimated volume of 1 km^3 and covering an area of 100 km^2 [*Lancaster,* 1993], but morphologically the two sand seas are similar.

Figure 3.13 shows spacecraft data from the Kelso Dunes, presented in a similar format as Figure 3.12. The traverse in Fig. 3.13a was constructed from the DEM, which has been represented as a shaded relief map in Fig. 3.13c. The shaded relief map comes from a recently released 30 m resolution DEM from the Shuttle Radar Topography Mission (SRTM) [*Farr and Kobrick,* 2000]. The SRTM was conducted aboard the Space Shuttle Endeavor in February, 2000, collecting the highest quality topographic data of the Earth to date between the latitudes 60° N and 56° S. Although the data over many sandy areas cannot be correlated, leading to gaps in the data, the Kelso Dunes are largely well correlated. Two data gaps (black spots) are visible on either side of the traverse near the point D'; most of the rest of the dunefield has no such data losses.

Figure 3.13b shows a 15 m resolution VNIR (visible to near infrared) image of the Kelso Dunes from the Advanced Spaceborne Thermal Emission and Reflection Radiometer (ASTER). This image is a grayscale version of a three color composite from the three VNIR channels of ASTER. Some of the streaks running from northwest to southeast are clouds and their respective shadows, but careful inspection reveals a bright sand sheet stretching northwest from the dunefield, slowly feeding sand to the Kelso Dunes. Three prominent dune ridges are evident in the dunefield, both in this image and in the SRTM DEM (Fig. 3.13c).

The traverse across the Kelso Dunes in Fig. 3.13a is shown at a much higher spatial resolution than that across the Proctor Dunes in Fig. 3.12a. Nevertheless, information similar to that obtained for the Proctor Dunes can be measured for comparison. The Kelso Dunes have been pushed up against the north face of the Granite Mountains, the mountain range visible in the bottoms of Figs. 3.13b and 13c. To reach the dunefield, the incoming sand has climbed uphill onto an alluvial fan emanating from the Granite Mountains [*Sharp,* 1966]. This uphill

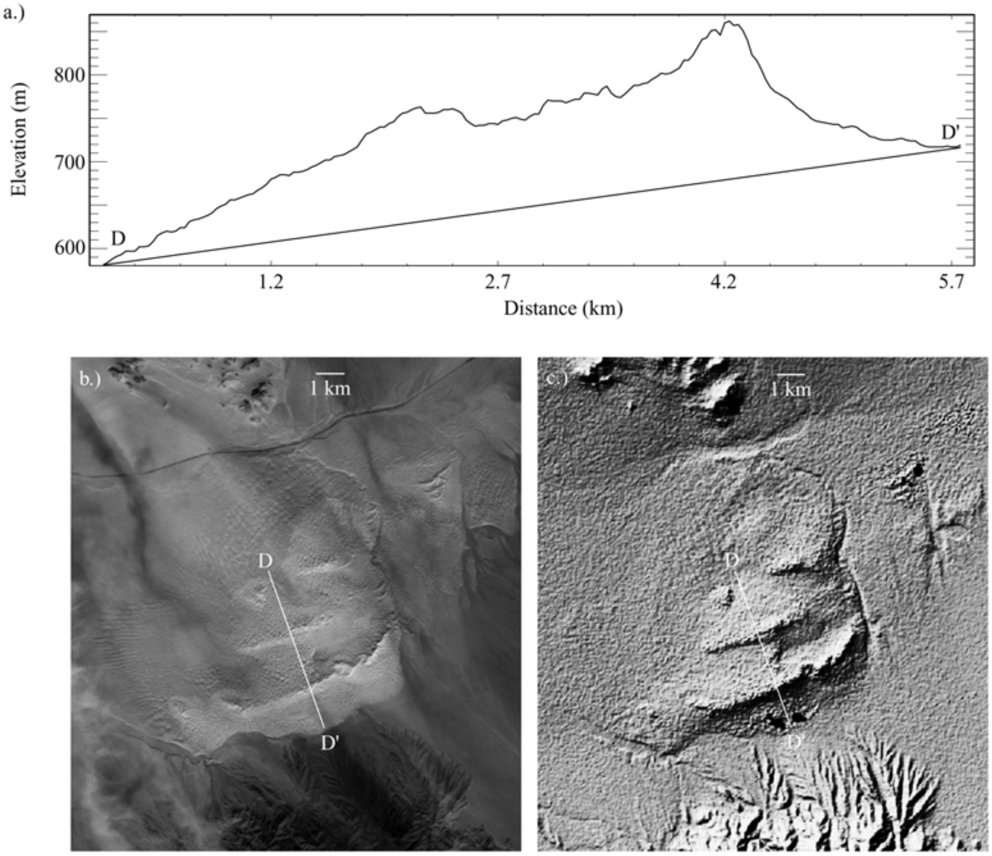

Fig. 3.13. The Kelso Dunes of the Mojave Desert. a.) SRTM elevations of traverse DD' across the Kelso Dunes. b.) ASTER image of the Kelso Dunes at a resolution of 15 m/pix. c.) Shaded relief at a resolution of 30 m/pix based on the SRTM DEM. The location of traverse DD' is shown in both b.) and c.).

slope is approximated as a straight line beneath the dunes in Fig. 3.13a, although the underlying surface is most likely slightly concave. The two peaks that the profile crosses are 130 m and 180 m above the approximated alluvial fan surface. Like the Proctor Crater Dunes, the Kelso dunes are superimposed on an accumulation of sand, in this case 100 m deep. In comparison, the Kelso dunefield is composed of smaller dunes superimposed on a deeper mound of sand relative to those in Proctor Crater. The Kelso dunes may reside in a more highly depositional environment than the Proctor Crater dunes, given that the sand mound at Kelso is twice as deep as that in Proctor Crater. The wind regime and local topography in Proctor Crater likely allows for more lateral migration of sand, although the net result is still a deep sand heap where winds converge.

5. Composition

Dunes tend to have a composition distinct from that of their surroundings; thus, composition is a useful tool in studying sand dunes and locating sand sheets and sand sources. On the Earth, thermal infrared multispectral scanner (TIMS) and Landsat thematic mapper multispectral images have been used for a number of purposes: to identify changes in composition within dunefields [*Blount et al.,* 1990], to discover previously unrecognized or misidentified sand sources [*Ramsey et al.,* 1999], and to provide a more accurate estimate of mineral concentrations at the surface [*Bandfield et al.,* 2002].

On Mars, spectra obtained from both ground-based and spacecraft interferometers have been used to identify surface mineralogy. In particular, TES has provided high-resolution spectra in the thermal infrared at a surface resolution of 3 by 6 km, which has been used to determine the correlation of rock compositions with geological units on the surface. The most detailed work with TES data involves the deconvolution of spectra using several endmembers, including both surface and atmospheric components [*Bandfield et al.* 2000; *Smith et al.* 2000]. In their work on global surface compositions, *Bandfield et al.* [2000] identified two spectral signatures that comprise a large percentage of the martian surface. The first component, labeled Type 1, has a shape similar to that of terrestrial Deccan Traps flood basalts that are composed predominantly of plagioclase and clinopyroxene. This is the same endmember identified in initial aerobraking TES data from Cimmeria Terra by *Christensen et al.* [2000a]. The second component identified by *Bandfield et al.* [2000], labeled Type 2, matches spectra from basaltic andesites to andesites made of plagioclase, glass, and pyroxene. In general, the low albedo surfaces of Mars are composed of spectral Types 1 or 2, or some mixture of the two. Areas with a mixed spectral signature may indicate either a composition intermediate between basalt and andesite or a physical mixture of the basaltic and andesitic components [*Bandfield et al.,* 2000].

A reassessment of the deconvolution of TES spectra indicates that the Type 2 surface component may be indicative of weathered basalt rather than andesite [*Wyatt and McSween,* 2002]. *Wyatt and McSween* [2002] reasoned that because sheet silicates such as clays have spectra similar to high-silica glass, surface Type 2 may not be andesitic, but instead may be aqueously altered basalt. They performed a deconvolution of TES spectra using a library of minerals that omitted the high-silica glass found by *Bandfield et al.* [2000] to compose part of surface Type 2. Their deconvolutions provided reasonable fits to the spectra, indicating that their hypothesis cannot be ruled out. Each conclusion regarding surface Type 2 has contrasting but important implications for the geological history of Mars. Because at this point either conclusion may be correct, surface Type 2 will be referred to as such in this work rather than as andesite or weathered basalt.

Further spectral studies using TES data have identified surface compositions other than igneous rocks. *Christensen et al.* [2000c] found the distinct signature of hematite in Sinus Meridiani. This mineral is considered to be coarsely crystalline based on the spectral shape observed by TES. It is associated with layered deposits and may indicate the former presence of near-surface water. *Clark et al.* [2002] found outcrops of olivine, indicating that at least in some regions on the surface, aqueous weathering has not occurred. *Bandfield and Smith* [2002] have used spectra from multiple emission angles to better separate atmospheric and surface components in TES data. This has produced the first mineral identifications of bright regions. They found that the bright region spectra match well with fine particulate silicate minerals. In particular, the bright regions have spectra consistent with intermediate to high-calcium plagioclase feldspar and minerals with either bound or adsorbed water, indicating that the surfaces here have not been completely altered by chemical weathering.

Using TES data analyzed with the techniques described above and further data from HST, work has progressed on identifying the composition of Martian dune sand. Early work using Viking Orbiter camera filters led to the idea that dark dune sands were composed of iron oxides, such as goethite [*Thomas and Veverka,* 1986]. Basaltic sand has been found in Cimmeria Terra in the southern highlands [*Christensen et al.,* 2000a] and in Nilosyrtis Mensae in the northern lowlands [*Rogers et al.,* 2000]. Intracrater sand in Arabia Terra has been interpreted as having a basaltic core surrounded by an andesitic arc on the downwind side, suggesting a compositional sorting of sand based on particle size [*Wyatt et al.,* 2001]. The large northern polar erg has been studied with both Hubble Space Telescope (HST) near-infrared data and TES spectra. The HST has detected the signature of pyroxene, indicating the presence of mafic rocks [*Bell et al.,* 1996]. Analyses of TES data have shown that plagioclase feldspar and sheet silicates and/or high-Si glass are also present [*Noe Dobrea and Bell*, 2001; *Bandfield*, 2002], leading to the conclusion that the polar dunes are andesitic [*Bandfield*, 2002].

In this work, the deconvolution method described in *Bandfield et al.* [2000] and *Smith et al.* [2000] has been applied to TES spectra to determine the composition of the Proctor Crater dune sand and the surrounding crater floor. Using the same software written for the global analysis, J. Bandfield (pers. comm.) provided deconvolutions of TES spectra from summertime groundtracks over Proctor Crater. A total of eight endmembers were used in this analysis: four atmospheric components and four surface components. The atmospheric spectral endmembers included dust at both high and low dust opacity, and water ice at two particle size distributions. The surface endmembers included the surface

Types 1 and 2 from *Bandfield et al.* [2000], hematite [*Christensen et al.* 2000c], and a blackbody spectrum to account for differences in spectral contrast.

The concentration of surface Type 2 (andesite/weathered basalt) is strongly influenced by the presence of atmospheric dust. The spectral signatures of andesite and dust are similar enough that under non-ideal conditions, the surface component and the atmospheric component are not properly separated. Thus it is important to consider only the clearest spectra, to minimize contamination by dust. Because Proctor Crater is located in a known dust-raising area, the air is dusty in the summer when the signal is strongest and most reliable. However, full spatial coverage of the study area, and therefore the use of as many viable orbital tracks as possible, is desirable in order to seek out sand deposits and transport pathways. Therefore data from a single orbit, that were obtained over a warm surface with a clear atmosphere, is discussed first to provide a basis for comparison with the rest of the data. The discussion then extends to all orbits crossing the study area.

Figure 3.14a shows original and modeled spectra averaged from eight TES pixels centered on the dark dunefield in Proctor Crater. The TES pixels were chosen from a warm summertime orbit ($L_s = 282.6°$) with a relatively dust-free atmosphere (ock or orbit 5498, see Fig. 3.14b). The original spectrum measured by TES, in magenta, shows the strong 667 cm^{-1} (15 μm) absorption due to CO_2 gas, a broad absorption between 800 and 1200 cm^{-1} (8–12 μm), and a relatively shallow absorption with small, sharp spectral features short of 500 cm^{-1} (>20 μm) due mostly to water vapor. The model produced by the linear least squares fit of the endmembers described above is shown in blue. The modeled spectrum closely matches the original spectrum, indicating that the fit is good. The spectral RMS error for the fit is 0.002, a low value for this dataset [*Bandfield et al.,* 2000]. The dust opacity for this orbit is 0.12, and the ice opacity is 0.0. Figure 3.14a also

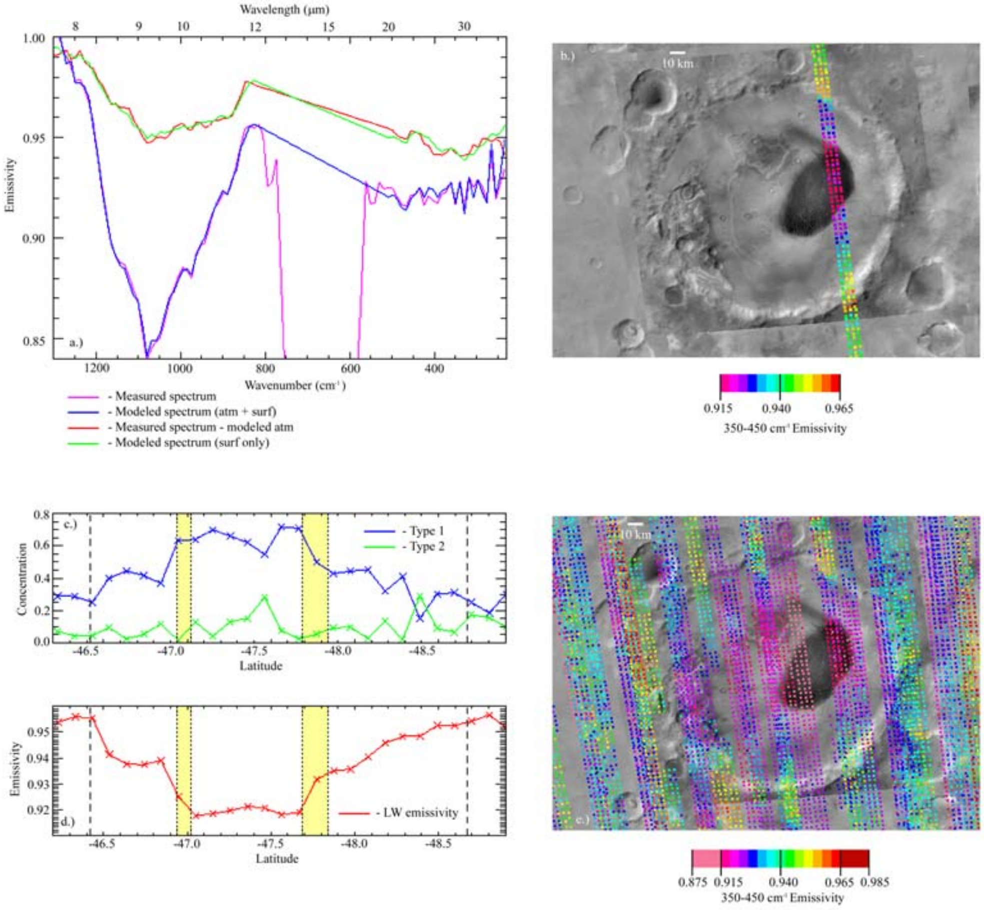

Fig. 3.14. Composition and thermal inertia from TES. a.) Results from the deconvolution of TES spectra over the dark dunes. The dune spectra are consistent with basalt spectra. b.) Plot of long wavelength emissivity for a nondusty traverse across the dark dunes. c.) Concentrations of spectral endmembers Type 1 (basalt) and Type 2 (andesite or weathered basalt) across the traverse shown in b.). d.) Long wavelength emissivity for the traverse across the dark dunes shown in b.). In both c.) and d.), dashed lines mark the inner edge of the crater rim, and yellow shaded regions mark the obliquely-oriented edge of the dark dunefield. e.) Long wavelength emissivity for all summertime groundtracks over Proctor Crater. Variations from orbit to orbit are caused by changes in atmospheric dust content.

shows the original spectrum with the modeled atmospheric components removed (red) and the modeled surface components only (green). Both of these spectra closely resemble surface Type 1 from *Bandfield et al.* [2000], providing a qualitative

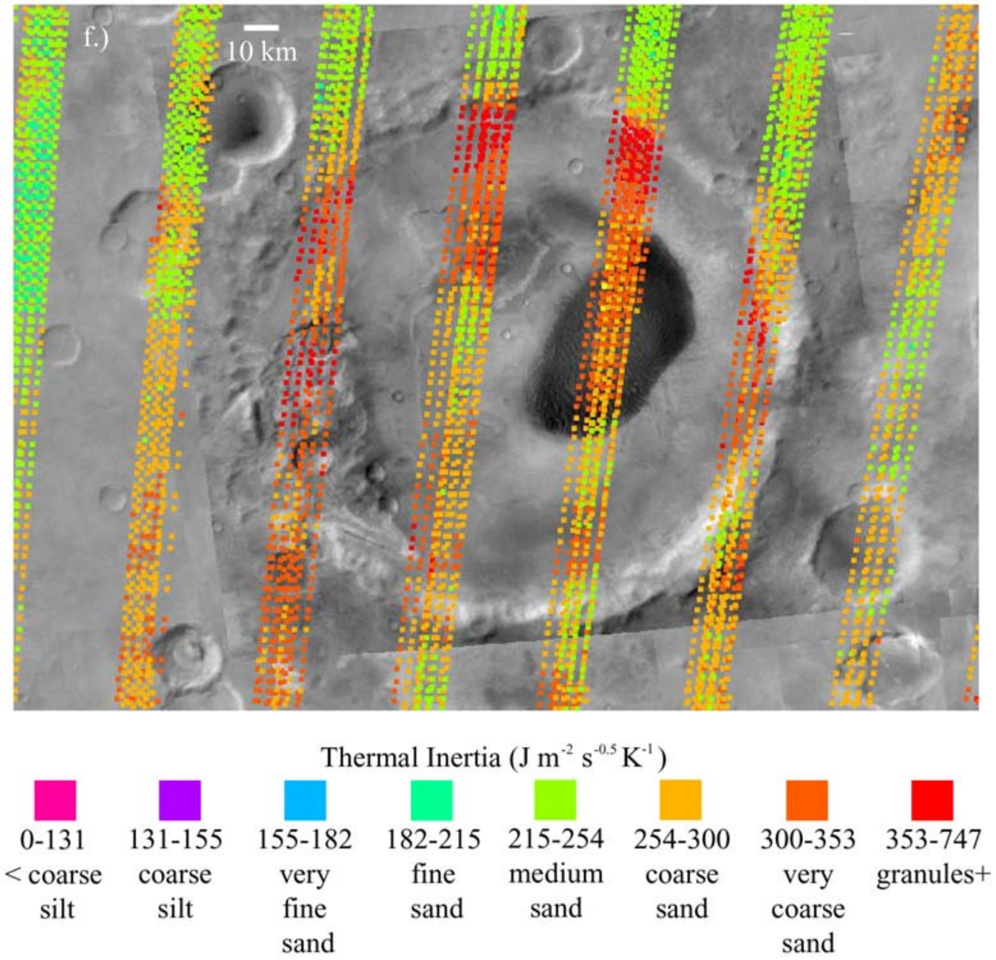

Fig. 3.14 (cont.) f.) Thermal inertia of summertime groundtracks over Proctor Crater, binned by effective grain size. The dark dunes have a thermal inertia consistent with coarse to very coarse sand.

identification of basaltic sand. Concentrations from the endmember fit are 66.1% for the Type 1 component (basalt) and 7.5% for the Type 2 component (andesite/weathered basalt). The concentrations represent the amount of spectral contrast relative to the other endmembers used in the deconvolution. The spectral contrast present in the Proctor Crater dune spectra is consistent with that of terrestrial basalt sands [*Christensen et al.* 2000a; *Bandfield et al.* 2000; *Bandfield* 2002].

Figure 3.14b shows the location of the TES orbit for ock 5498. Concentrations for surface Types 1 and 2 along this track are plotted in Figure 3.14c. The concentrations have been averaged into bins of six pixels to account for any differences in the calibration of the six detectors on TES. Dashed lines mark the edges of Proctor Crater in Figure 3.14c, and the edges of the combined dunefield and the dark sand streak on its north edge are marked by dotted lines. Because the TES groundtrack crosses both the dunefield and the dark sand streak at an oblique angle, there is an area of transition in Figure 3.14c from the crater floor to the sand deposits, marked as the light yellow area between dotted lines. The concentration of surface Type 1 (basalt) increases over the dunes and the large dark streak, although it appears to be present in lower quantity along the rest of the track across the floor of Proctor Crater. Surface Type 2 (andesite/weathered basalt) generally remains at or below the detection limit of ~0.15, indicating that it may not be present at all, although there are a few spots where the concentration climbs to 0.3, suggestive of a small local accumulation or outcrop. Unlike the basalt component, the surface Type 2 profile has no trend along the TES track, indicating that if any such material is present, it does not correspond with the location of the dark dunefield or any other surface structure.

Another measurement of use is a simple band index from original TES spectra in a useful wavelength range. *Bandfield* [2000] shows that band indices of spectral Types 1 and 2 are simply calculated and compare well to maps produced from the linear deconvolution method. Band indices are affected by changes in elevation and atmospheric interference, and they provide only a qualitative estimate of composition. However, because the calculation for the band index is not subject to sensitive discrimination between different endmembers, unlike the compositions derived from deconvolution, the resulting values are less variable from point to point. *Bandfield et al.* [2000] discuss an absorption in Type 1 (basalt) spectra from ~200 to 500 cm^{-1}. Although this feature is present in both surface

Types 1 and 2, the low concentrations of surface Type 2 along the single clear track (see Fig. 3.14c) indicate that little if any of this endmember is present in Proctor Crater. In addition, dust accumulations have very low spectral contrast throughout the TES spectral range, which would elevate the emissivity in this wavelength range. Therefore low emissivities in this band index are used as an indicator of surface Type 1 (basalt) only, and high emissivities are used as an indicator of dust. The band index used here to distinguish this feature is the average emissivity of uncorrected spectra between 350 and 450 cm^{-1}. It is this parameter that is mapped in Figure 3.14b and plotted in Figure 3.14d. The long wavelength emissivity mirrors the basalt track in Figure 3.14c, lending weight to the argument that this band index is diagnostic for basalt in this area. In Figure 3.14b the dunefield is well marked by low emissivity (*i.e.,* stronger absorptions). On either side of the dunefield there are moderately low emissivities (in violet and blue), indicating an intermediate amount of basalt in the middle and northern part of the crater floor.

Figure 3.14e shows the long wavelength emissivity for all daytime, nadir-looking TES pixels with a surface temperature above 250 K. This figure is shown with an extended version of the scale used in Fig. 3.14b. There is a great deal of variation in the long wavelength band index in this data set. Within each orbit, each of which is three pixels wide, there is little variation in dust opacity, so along-track variations in emissivity reflect actual changes in surface composition. However, differences in emissivity from orbit to orbit show the effects of uncorrected atmospheric parameters, especially atmospheric dust. The changes in emissivity from one orbit to another make interpretation difficult, however features persisting from one track to the next are considered real even if their relative emissivities are different.

As with the single orbit shown in Figure 3.14b, the strongest signals in Figure 3.14e are those over the dunefield and the dark streak of sand emerging northwestward from the northernmost tip of the dunefield. There is a general concentration of basalt west of the dunefield and in the bottoms of both the western and the central pits, reflected by fairly low emissivities (blue and violet). The low-lying floors of the pits undoubtedly retain some amount of basalt sand that passes through the area, causing the low emissivities there (*i.e.,* see Fig. 3.3e), although the concentrations may also be indicative of exposed outcrops of basalt in the basin fill. Outside the crater walls, the emissivity rises, indicating the presence of finer, brighter particles. The transition from low to high emissivity is rather sharp along the northern rim of the crater floor, suggestive of a contact between floor materials and intercrater and rim materials. The transition across the northwestern and southern parts of the crater floor is not as well defined, suggesting that more dust has accumulated along this border. This area may be more sheltered from wind relative to the rest of the crater floor, where either fewer dust devils pass by or winds are not strong enough to saltate sand that would scour away seasonal dust fallout. Alternatively, the poorly defined change in emissivity may be caused by surface features that preferentially retain dust, for example, by a surface texture that impedes the effect of the wind. This lack of spectral contrast is most likely caused by accumulated dust, and affected more by local meteorology than by surface morphology.

Much of the area surrounding the dunefield, especially to its west, has a fairly low emissivity, indicating a moderate level of basalt on the crater floor. Bright duneforms are absent northeast of the dark dunefield but present south of the dunefield, and this lack of correlation with composition indicates that they are not likely responsible for these moderately low emissivities. Boulders are present almost everywhere on the crater floor outside the dunefield, including areas of both high and low emissivity, so they also are not responsible for the variation in emissivity. The lower emissivities around the dunefield likely indicate the lack of accumulated dust, and they may indicate the presence of basalt in the materials comprising the crater floor. Thus the crater floor materials are potentially some combination of basalt grains plus fines that have become indurated over time.

Proctor Crater is located in the southern midlatitudes, a zone in which the surface transitions from a strongly basaltic signature to the north, to a Type 2 surface to the south [*Bandfield*, 2002]. *Bandfield* [2002] also points out that TES spectra only sample surficial, particulate materials and that this latitudinal compositional transition does not appear to have distinctive boundaries. The zonal shift may well be caused by a regional sorting of sand grains by the wind, potentially from midlatitude westerlies that produce the primary slipfaces in the Proctor Crater dunefield. Compositional sorting of sand by the wind has been studied in terrestrial basaltic dunes by *Bandfield et al.* [2002] and, as discussed above, proposed in dunefields on Mars by *Wyatt et al.,* [2000]. The lack of evidence for sand of surface Type 2 in Proctor Crater implies that, if there is any such material in this particular region of the compositional transition, it is most likely obscured by dust deposits. However, basalt sand dominates the dunefield and much of the floor of Proctor Crater, indicating that basaltic sand has accumulated on the crater floor and remained exposed at the surface.

Transport pathways for basaltic sand outside Proctor Crater, if they ever existed, have been since buried, eroded away, or both. In this situation, compositional information is not very useful in locating sand sources or transport pathways, save for providing the information that they are not easily discernable at the surface. While it is possible that the western pit is the source of the basalt sand that now comprises the dunefield, the presence of dark falling dunes on east-facing cliffs within the western pit (*i.e.,* see Fig. 3.3e) suggests that the sand originated to the west of the western pit, and thus most likely from beyond the western rim of Proctor Crater. Several other craters in Noachis Terra also have large dunefields, and not all of these have pits that could have supplied such a quantity of dark sand. Since transport pathways in the vicinity of Proctor Crater are not apparent, it may be necessary to search for them on a larger scale.

Although the compositional data are difficult to interpret, broad conclusions may be made from investigating this data set. The dark sand in Proctor Crater is without doubt basaltic. Other regions on the crater floor appear to have some amount of basalt, but it is unclear whether this is from the presence of sand that has been transported into the crater or from basaltic outcrops from the layered materials. The bright duneforms do not have a composition distinct from their environment, suggesting that they are composed of easily available local materials, and that there may be no compositional selection based on grain size. There appears to be a difference in wind regimes between the northern rim and the rest of the crater, in which the rest of the crater contains more accumulated dust, indicating less erosive winds. The true value of compositional analysis comes through the comparison to other data sets, in which some of these ambiguities may be resolved.

6. Thermal Inertia

6.1 Background

Thermal inertia is a measure of a material's thermal response to the diurnal heating cycle. Loose, fine-grained sediments lose heat rapidly after sunset, leading to low thermal inertia values. Increasingly consolidated sediments and coarser-grained materials (*i.e.,* sand, gravel, boulders, and bedrock) lead to successively weaker diurnal temperature extrema from higher heat retention and therefore they produce progressively higher thermal inertia values. In ideal situations where all other factors are accounted for, thermal inertia can be used to estimate the average grain size of a particulate surface material. Typical values of thermal inertia for various grain sizes are listed in Table 3.1.

Table 3.1. Thermal Inertia and Effective Grain Size[a]

Name	Phi	Diameter	Thermal Inertia ($J\ m^{-2}\ s^{-0.5}\ K^{-1}$)
Pebbles	-4 to -2	4–16 mm	417–580
Granules	-2 to -1	2–4 mm	353–417
Very coarse sand	-1 to 0	1–2 mm	300–353
Coarse sand	0 to 1	0.5–1 mm	254–300
Medium sand	1 to 2	250–500 μm	215–254
Fine sand	2 to 3	125–250 μm	182–215
Very fine sand	3 to 4	63–125 μm	155–182
Coarse silt	4 to 5	31–63 μm	131–155
Medium silt	5 to 6	16–31 μm	112–131
Fine silt	6 to 7	8–16 μm	95–112
Very fine silt	7 to 8	4–8 μm	80–95
Clay	8+	<4 μm	<80

[a] Using the relation from *Presley and Christensen* [1997a] with a surface atmospheric pressure of 5 mbar.

The thermal inertia of Martian dunes has been studied in detail since the first thermal models were produced for Mars. In particular, the dunefields of the Helluspontus area in Noachis Terra have been used as a basis for comparison between different models. In all of the thermal studies described below, thermal inertia was calculated using a single measured surface temperature that was matched to a predicted temperature from a thermal model that involved thermal inertia and other various parameters such as albedo, season, and dust opacity. Methods differ mostly in how the atmosphere influences predicted and measured surface temperatures.

Christensen [1983] made the first thorough study of the thermal inertia of dark intracrater materials with Viking IRTM data, using a thermal model developed by *Kieffer et al.* [1977]. This model calculates thermal inertia based on estimated surface temperature variations for a particular albedo, local time, latitude, and season. *Christensen* [1983] calculated a modal value of 397 $J\ m^{-2}\ s^{-0.5}\ K^{-1}$ for the dark intracrater deposits, and using the relationship from *Kieffer et al.* [1973] converted this value to an effective grain size of 0.9 mm. Although this value is large for dune sand, *Christensen* [1983] correctly concluded that the intracrater features are accumulations of dark aeolian material, which is easily trapped in topographic lows such as craters. Using an updated conversion relation by *Presley and Christensen* [1997a], the same thermal inertia at an atmospheric pressure of 5 mbar corresponds to a grain size of 3.3 mm, a larger value than originally calculated and in the range of granules (2–4 mm).

Edgett and Christensen [1991] also used the thermal model of *Kieffer et al.* [1977] to calculate thermal inertia with Viking IRTM data, although they modified the result with a correction for the effect of atmospheric dust on surface temperatures [*Haberle and Jakosky,* 1991]. For the Hellespontus dunes, *Edgett and Christensen* [1991] calculated a thermal inertia of 322 ± 33 J m^{-2} $s^{-0.5}$ K^{-1} for a clear atmosphere and 301 ± 33 J m^{-2} $s^{-0.5}$ K^{-1} for a dusty atmosphere, leading to an average dune sand grain size of roughly 500 ± 100 μm (medium to coarse sand) using the relation from *Kieffer et al.* [1973]. Using the updated relation by *Presley and Christensen* [1997a], these thermal inertias correspond to 1.02 and 1.36 mm, respectively, and both are in the range of very coarse sand (1–2 mm).

Edgett and Christensen [1994] compared the thermal inertias of Proctor Crater dune sand produced by three different techniques: the method of *Kieffer et al.* [1977] alone, and the *Kieffer et al.* [1977] method modified by two different atmospheric corrections modeled by *Haberle and Jakosky* [1991] and *Paige et al.* [1994]. In a dusty atmosphere with a visible opacity of 0.4, the Proctor Crater dunes have a thermal inertia of 340 J m^{-2} $s^{-0.5}$ K^{-1} using the *Kieffer et al.* [1977] model, 230 J m^{-2} $s^{-0.5}$ K^{-1} when adjusted by the *Haberle and Jakosky* [1991] correction, and 120 J m^{-2} $s^{-0.5}$ K^{-1} when adjusted using a correction from *Paige et al.* [1994]. Although the different methods produce grain size estimates ranging from silt to coarse sand, *Edgett and Christensen* [1994] conclude that the dunes are most likely composed of sand-sized grains based on physical and compositional considerations.

Herkenhoff and Vasavada [1999] made the most recent estimates of thermal inertia of the Proctor Crater dunes for comparison with the sand of the northern polar erg. They used the thermal model developed by *Paige et al.* [1994] on IRTM data. In this case, they used an atmospheric correction with optical properties for dust developed for IRTM data by *Clancy and Lee* [1991]. All previous thermal inertia calculations involved optical properties developed for the Viking Lander 1 site [*Pollack et al.,* 1979], which produced overestimated surface albedos. *Herkenhoff and Vasavada* [1999] argue that using the method of *Paige et al.* [1994] with updated dust optical properties most appropriately accounts for atmospheric effects on IRTM data, because this was the first model to include both a realistic treatment of the effect of the atmosphere on surface temperatures and the effect of the atmosphere on measured IRTM surface radiances. *Herkenhoff and Vasavada* [1999] calculate a thermal inertia range of 245–280 J m^{-2} $s^{-0.5}$ K^{-1} for the Proctor Crater dunes. Using the relation of *Presley and Christensen* [1997a], this corresponds to a particle size range of 430–755 µm (medium to coarse sand) at an atmospheric pressure of 5 mbar.

To study the thermal properties of the floor of Proctor Crater, we have used thermal inertia values calculated from TES thermal bolometer measurements [*Jakosky et al.,* 2000; *Mellon et al.,* 2000]. They matched single nighttime (2 AM) temperature measurements from TES to a large lookup table of temperatures produced by a thermal model. The lookup table includes several parameters required for the model calculations, such as albedo, dust opacity, time of day, season, surface pressure, latitude, and thermal inertia. The thermal dust optical depth is assumed to be 0.1, scaled to the mean pressure level at 6.1 mbar. *Jakosky et al.* [2000] and *Mellon et al.* [2000] use a thermal model based on that of *Haberle* *and Jakosky* [1991], with additional considerations of seasonal and latitudinal variations. Although the thermal inertia values used here were calculated using brightness temperatures from the TES bolometer rather than from a single spectral band (as was previously done with the 20 μm channel of the IRTM data set), *Jakosky et al.* [2000] showed that the difference between the two surface temperature measurements had little effect on thermal inertias in the range of 50 to 300 J m^{-2} $s^{-0.5}$ K^{-1}.

In this work, thermal inertia measurements were converted into particle size estimates using the empirical relation determined by *Presley and Christensen* [1997a]. This calculation employed a surface atmospheric pressure of 5 mbar, a typical value for summer nights at the latitude of Proctor Crater according to the model results from the work discussed in Paper 2. In order to choose the most reliable values, we used only thermal inertias measured during southern summer (L_s = 240°–360°), with emission angles less than 10°, and with the best data quality ratings (values of 0 or 1).

It must be emphasized that the particle sizes discussed here do not necessarily represent actual particle sizes, but rather the *effective* particle sizes for unconsolidated particulate materials in each TES pixel. One challenge in interpreting thermal inertia measurements is that each TES pixel represents a thermal response from a 3 km by 6 km area on the surface, which could easily contain any combination of dust, outcrops, boulders, sand, and consolidated materials, each with its unique thermal signature. A further complication is that consolidated fine material produces the same thermal effect as larger but unconsolidated particles. Thus thermal inertia maps are most valuable for studying either places containing unconsolidated fine materials, which produce the lowest and least ambiguous values, or areas where the particle size range of the surface has been previously constrained.

Dunefields are one of the few geological structures in which the degree of consolidation and range of particle sizes is predictable. By definition, active sand dunes are composed of unconsolidated sand grains, relieving the thermal ambiguity introduced by consolidated materials. In addition, sand dunes consist almost entirely of particles in a narrow size range that are lifted into saltation by the wind, thereby doing away with another complication of thermal inertia caused by poorly sorted materials. Thus, dunes are among the most ideal features to study using thermal inertia. It is for these reasons that dunes have been consistently targeted as a control for new thermal inertia calculations of Mars.

Nevertheless, once grain sizes are estimated from thermal inertia, it can be quite a challenge to relate these grain sizes of dune sands to such geological processes as transport, deflation, and accumulation. On Earth, the grain size most easily lifted by the wind is in the range of very fine sand, or ~75 µm [*Iversen and White,* 1982]. However, most terrestrial dunefields are composed of fine to medium sand (160–330 µm), two to four times this optimum grain size [*Lancaster,* 1995]. Given that Earth has the only well-studied analogs for Martian aeolian processes, this disparity must be clarified before interpretations can be made of Martian dune sand.

Experimental work done on the abrasive action of subareal saltation on Earth indicates that sand grains undergo an average loss of about 10 per cent of their mass in transit, which tails off asymptotically upon grain rounding [*Kuenen,* 1960b]. Furthermore, smaller grains (less than 100 to 150 µm) experience much less abrasion than larger grains, indicating that sand grains simply never wear down to the optimally moved size of 75 µm [*Kuenen,* 1960a]. *Kuenen* [1960b] attributes this lack of abrasion to the lower momentum sustained by smaller particles during saltation, thus inhibiting these grains from chipping on impact. Further measurements of field samples show that silt and smaller-sized grains

(<63 µm) are produced by the chipping of sand-sized grains during saltation, explaining an apparent dearth of particles in the range between 50 and 250 µm (very fine to fine sand) [*Rogers et al.,* 1963]. Thus, although terrestrial dunes are composed of sand-sized particles that are capable of transport under saltation, it might appear that the nature of the transport process itself inhibits grains from being reduced to the optimal grain size for saltation. One might conclude that this reflects the distribution of the original grain population that supplies terrestrial sand, for if the original sand source contained particles of 75 µm then these grains would almost certainly saltate downwind to become incorporated in terrestrial dunefields.

However, there is observational evidence that the situation on Earth is more complex. In a study of the petrology of dune sand of the Ka'u Desert on the island of Hawaii, *Gooding* [1982] demonstrated a genetic relationship between the dunes and volcanic ash beds located upwind. Although the source material had a broad grain size distribution, including grains at the optimum size of ~75 µm, the dune sands clustered at ~330 µm. Clearly the source material does not necessarily reflect the grain size distributions found downwind. In addition, some other process must be found to explain why the optimally saltated grains are not found downwind in dunes, which are depositional features composed wholly of saltated grains.

On Mars, the situation for aeolian grains is less constrained. The most easily saltated sands have a diameter of ~115 µm [*Iversen and White,* 1982]. Experimental work on the abrasion of basalt grains under Martian atmospheric conditions indicates that lithic fragments, such as those composing the Proctor Crater dunefield, can easily survive saltation long enough to accumulate into dunes [*Greeley and Kraft,* 2001]. In that experiment, *Greeley and Kraft* [2001] found that basalt grains with an average diameter of ~540 µm abrade quickly at first, then asymptotically approach a diameter of ~470 μm. The quick drop in size is attributed to sharp edges that easily chip off, effectively rounding the grains. This loss in size of ~70 μm amounts to a mass loss of about 35 per cent, indicating that, like on the Earth, saltation on Mars is an ineffective process for abrading sand grains into successively smaller particles. If the original sand source contained sand grains at the optimally moved size of 115 μm, one might expect that they would preferentially saltate downwind and collect in sand dunes. The situation for Mars may well be more extreme than that for Earth, because Martian winds above the threshold stress for saltation are so rarely observed at lander sites [*Hess et al.,* 1977; *Schofield et al.,* 1997] or produced by atmospheric models [*Greeley et al.,* 1993; *Fenton and Richardson,* 2001b]. If winds on Mars tend to just barely exceed the saltation threshold, then one might expect that only sand near the optimum size of 115 μm will be transported downwind.

The situation of observed versus predicted particle sizes is resolved by investigating the conditions required for particle suspension. If the terminal velocity of a particle (U_F) is equal to or less than the lowest threshold friction speed for which that particle can saltate (u_*), then that particle will rise into suspension when the wind blows strong enough (*i.e.,* $U_F/u_* < 1$) [*Iversen et al.,* 1976]. This threshold occurs at a particle size of 52 μm on Earth. *Edgett and Christensen* [1991] calculated a range of particle sizes for which "modified saltation" would occur ($0.7 < U_F/u_* < 2.5$). "Modified saltation" may be considered a transition between saltation and suspension in which saltation path lengths are so long they may almost be considered infinite. On Earth, dune sand is consistently coarser than the grains in the "modified saltation" range of 50–80 μm. This suggests that dunes grow only from those sand grains that are transported by pure saltation, and not at all by grains moving in "modified saltation." While it may require a lower wind to saltate 75 μm grains than any other size on Earth, these particles are too easily carried into "modified saltation" and thus rarely form dunes.

On Mars, a lower gravity, lower atmospheric drag, and stronger required threshold friction velocities for saltation combine to create very long saltation path lengths [*Iversen et al.,* 1976]. The resulting particle size for which $U_F/u_* = 1$ is 210 μm. The "modified saltation" range of *Edgett and Christensen* [1991] is 200–250 μm. They conclude, as did *Greeley and Iversen* [1985], that Martian dunes should therefore be composed of sand grains coarser than those of terrestrial dunes.

Because of the downwind isolation of a particular grain size in dunes, it is a challenge to determine the size distribution of the source material of the dunes. What may be concluded from the grain size measurements is that whatever range of particle sizes are observed in a dunefield must also be present in the source material.

6.2 Thermal Inertia of Proctor Crater Dunes, Broad View

6.2.1 Results. TES thermal inertias over Proctor Crater are shown in Figure 3.14f. Colors are chosen to represent standard divisions in the Wentworth (phi) scale. The dark dunefield displays a distinctive and fairly uniform thermal inertia relative to the surrounding terrain. The mean and standard deviation thermal inertia is 305 ± 22 J m^{-2} $s^{-0.5}$ K^{-1}. Using the relation of *Presley and Christensen* [1997a] with a surface atmospheric pressure of 5 mbar, the thermal inertia converts to grain sizes of 1.1 ± 0.3 mm, in the range of coarse sand (see Table 3.1). This thermal inertia is fairly consistent, if on the high end of, previous thermal inertia estimates of the dune sand. However, this size estimate suggests the dunes are composed of sand with grain sizes ten times the most easily moved grain size for Mars of ~115 μm [*Iversen and White,* 1982], and several times the estimated upper limit of the "modified saltation" range defined by *Edgett and Christensen* [1991]. This apparent inconsistency must be examined in detail in order to explain how measurements relate to actual conditions on the surface of Mars.

First, uncorrected atmospheric effects must be considered. In their model, *Mellon et al.* [2000] include thermal radiation from a dusty, CO_2 atmosphere and latent heat from seasonal condensation of CO_2. However, they assume that the atmospheric dust optical depth remains at a constant value of 0.1, normalized to a 6.1 mbar pressure level. During the southern summer, in which the relevant TES data in Proctor Crater were obtained, the dust opacity easily climbs higher than this value, leading to a potential overestimate in thermal inertia values and therefore in effective particle sizes. At the elevation of the dunefield, ~700 m above the datum, the dust opacity scales to 0.094. *Liu et al.* [2002] have calculated thermal infrared dust opacities using TES spectra, and so it is possible to investigate the effect of atmospheric dust on thermal inertia calculations from *Mellon et al.* [2000]. *Liu et al.* [2002] calculated 9 μm dust optical depths for TES data for comparison with Viking and Mariner 9 data. Figure 3.15a shows 9 μm dust opacities provided by J. Liu (pers. comm.) over the floor of Proctor Crater during the summer season in which thermal inertia values are available. The optical depths slowly drop throughout the summer season, only reaching values near 0.094 at the end of the summer. Six nighttime tracks of TES crossed the dunefield during this season. Their respective thermal inertias are shown in Figure 3.15b. Of the six tracks, ocks (*i.e.,* orbits) 4425 and 5079 only cross the northernmost part of the dunefield. The remaining four traverse the entire dunefield, as shown in Fig. 3.14f. Like the dust opacities in Fig. 3.15a, the thermal inertia values drop as the summer season progresses, reflecting the influence of uncorrected atmospheric dust on surface temperatures. The track with the closest correspondence to dust opacities near 0.094 is the last one, ock 5406. Thus the thermal inertias from the last track are considered the most accurate of the six. The average thermal inertia of ock 5406 over the dunefield is 277 ± 17 J m^{-2} $s^{-0.5}$ K^{-1}, leading to a grain size estimate of 740 ± 170 µm. This is in the range of coarse sand (500–1000 µm), which is more consistent with previous work and less surprising than the original estimate of 1.1 ± 0.3 mm.

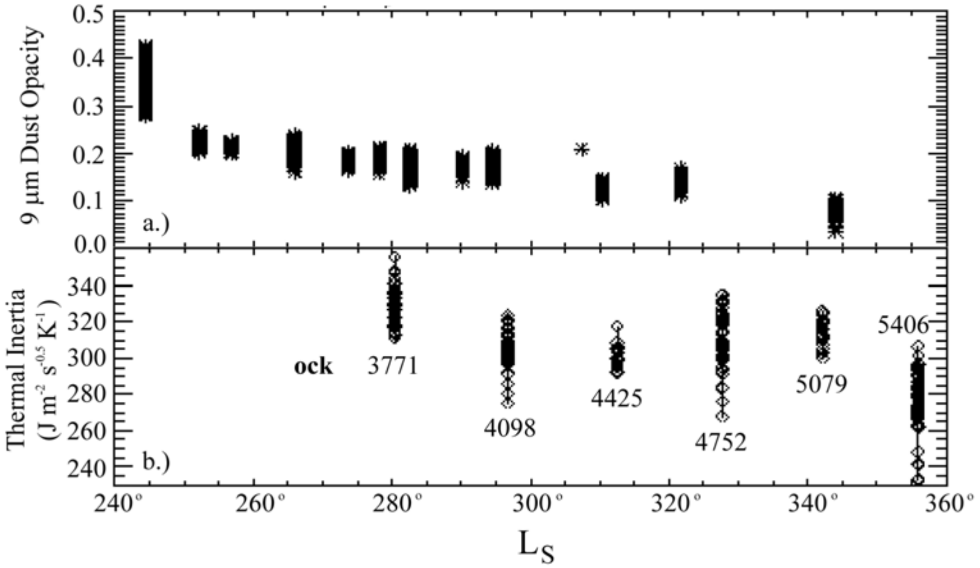

Fig. 3.15. a.) Thermal infrared dust optical depths as a function of season inside Proctor Crater. Note the slow decay as fall approaches. b.) Measured thermal inertias from over the dark dunefield as a function of season. Note how the highest thermal inertias roughly correlate with higher dust opacity.

A second simplification of most previous thermal inertia calculations, including that of *Mellon et al.* [2000], is that they do not account for the effect of slope on surface temperatures. However, dunefields are by definition comprised of slopes of varying degrees and azimuths. Depending on the orientation of the average slope within a TES pixel, the effective surface may be either more or less heated by the sun during the day. Slopes facing away from the sun (southward) will receive less direct sunlight for a shorter time during the day than will sunward-facing (northward) slopes. In addition, the excess surface area created by topography will lead to more radiative cooling at night than is accounted for by the current assumption of a flat, horizontal surface. The effect of daytime heating will vary depending on the geometry of the dunefield; the effect of nighttime cooling is to slightly lower the measured thermal inertia. At the scale of TES pixels this effect is difficult to estimate, but daytime heating is considered in detail in the following section.

Another possible error may come through the conversion from thermal inertia to effective particle size. The relation of *Presley and Christensen* [1997a] involves surface air pressure, for which we selected a constant value of 5 mbar, chosen from typical summertime values predicted in Proctor Crater by the Mars Mesoscale Model 5 (described in Paper 2). It may be that the model predictions are incorrect, or that the assumed constant value is unrealistic. However, the dependence of thermal inertia on air pressure is not strong. If the air pressure were lower by as much as 1 mbar, which is unlikely, then *Presley and Christensen* [1997a] predict an average grain size of 820 μm corresponding to the measured thermal inertia of 277 J m^{-2} $s^{-0.5}$ K^{-1}. At an air pressure as much as 1 mbar higher, the equivalent grain size is 640 μm. In either case, the estimated particle sizes are still in the range of coarse sand. Thus an incorrect air pressure does not greatly change the estimated particle size.

The packing *Presley and Christensen* [1997a] used in their samples is described as "medium dense," like that of loose sediments on a surface, and not unlike that expected for dune sand. Thus grain packing differences between Martian dunes and their samples do not seem to be an issue. *Presley and Christensen* [1997b] discuss the effect of bulk density on thermal inertia. In their samples, they used spherical glass beads that pack more tightly than angular grains of the same size distribution. A lower bulk density from more poorly packed grains, likely more representative of real dune sand than their glass spheres, produces a lower thermal conductivity and therefore a lower thermal inertia estimate than spherical particles. Thus the measurement of 740 ± 170 μm sized spherical grains may also be explained by even larger angular grains with a lower bulk density, although the transport of larger grains into the dunefield would be difficult to explain.

Presley and Christensen [1997b] discuss the effect of particle size sorting on thermal inertia. Preliminary studies may indicate that thermal inertia measurements reflect only the largest particles in a sample. If this is indeed the case, then it may well be that the majority of the dune sand is smaller than the observed coarse sand fraction estimated from the thermal inertia measurement. Further work is necessary to determine if this effect is real.

6.2.2 Interpretation. A further challenge of the thermal inertia measurement is in its interpretation. *Edgett and Christensen* [1994] point out that the surface grains of dunes may be coarser than the average grains of the dune volume because ripples composed of larger grains tend to form on the surface of dunes. Additionally, it is possible that the thermal inertia measurement of 277 ± 17 $J\ m^{-2}\ s^{-0.5}\ K^{-1}$ actually indicates that the dunes are composed of grains, smaller than the estimated size of 740 ± 170 μm, that are partially cemented. This is consistent with two observations made in MOC Narrow Angle images, in which unexpectedly sharp slipfaces and landslide scars on the dunes may indicate some amount of induration (see discussion in Sections 4.1 and 4.2). However, the lack of seasonal dust accumulations on the dunes would seem to indicate that the dunes are regularly cleaned of any dust deposits, and therefore that they are active. Perhaps a thin top layer of uncemented sand is present and sweeps the dunes clean, while not providing enough of a thermal signal to block an underlying cemented layer of grains.

Alternatively, the dune sand may truly be in the range of 740 ± 170 µm, or coarse sand. If this is the case, then interpretations can be made on the nature of the source material. Because of the downwind isolation of a particular grain size in dunes, it is a challenge to determine the size distribution of the source material of the dunes. The only information provided by the grain size distribution of dune sand is that the range of particle sizes that are observed in a dunefield must also be present in the original source, and thus a number of source materials must be considered.

Experimental work intended as a study of the lunar surface showed that roughly five per cent of the impact ejecta from a basalt surface is composed of grains in the range of coarse sand (500–1000 µm) [*Gault et al.,* 1963]. Actual lunar soil samples, created by impacts and subsequent bombardment ranged in mean particle sizes from 380 µm down to 32 µm [*Lindsay,* 1976]. He proposes that soil grains decrease in size with age as continual impacts pulverize the surface material into increasingly smaller and well-sorted particles. Recent calculations of impact gardening on Mars indicate that since the Noachian era several tens of meters of regolith should have been produced by the constant bombardment of small impactors [*Hartmann et al.,* 2001]. However, only the least exposed surfaces would have created particles in the size range of the coarse sand grains in the Proctor Crater dunes, because according to the reasoning of *Lindsay* [1976], surfaces exposed to more bombardment would accumulate successively finer soils less likely to contain the coarse sand now present in the Proctor Crater dunefield. However, before reaching this steady-state of soil fining, such surfaces may have been buried and later re-exposed, exposing the preserved sand-sized grains to the wind and allowing them to become a sand source for the dunes. Thus, although unlikely, impact gardening cannot be completely ruled out as a source of Martian dune sand.

Measurements of volcanic ash from phreatomagmatic eruptions of the Kilauea volcano show a broad distribution of particle sizes [*Gooding,* 1982], indicating that this is one possible source of coarse sand. *Edgett and Lancaster* [1993] have proposed that Martian dune sand could be created by the fluvial erosion of lava flows or by the aeolian reworking of pyroclastic materials. *Malin and Edgett* [2000a] consider volcanic material as an unlikely source for the extensive layered deposits on Mars because the lack of Martian plate tectonics inhibits widespread explosive volcanism. However, phreatomagmatic eruptions, such as those of the Kilauea volcano that produced thick ash beds, clearly do occur on volcanoes without the need for global processes such as plate tectonics. Instead of changes in magmatic composition caused by subduction, it is ground water that is responsible for the explosive eruptions. Recent studies of MOC Narrow Angle images have revealed structures morphologically similar to rootless cones, volcanic structures found in Iceland that are produced by the explosive interaction of lava with ground water [*Lanagan et al.,* 2001]. Such eruptions produce beds of glassy ash and scoria that could easily be a source of the coarse basaltic grains in the Proctor Crater dunes. Phreatomagmatic eruptions may in fact be prevalent on Mars, although the extent of the material they have produced is at this time unquantifiable. Thus volcaniclastic material cannot be ruled out as a source of basalt sand on Mars.

Meteoritic material may also be considered as a potential source of dune sand. *Flynn and McKay* [1990] calculated that given the mass influx of meteorites to Mars and their chance of surviving entry into the atmosphere without being melted or vaporized, the meteoritic component of 60–1200 μm particles in the Martian soil is expected to be between 2 and 29% by mass. However, the basaltic composition of the Proctor Crater dunes is inconsistent with meteoritic material. Furthermore, it is likely that any sand-sized meteoritic particles in the Martian soils are too fragile to withstand sustained saltation (see Fig. 3 of *Flynn and McKay* [1990]), and thus fragment into smaller grains before they reach the large dunefields. If this is the case then the fact that the dark dunefields are composed almost entirely of basalt indicates that the sand grains were transported farther from their source material than any meteoric material could survive under saltation.

Of the three source materials considered (impact ejecta, volcaniclastic grains, and meteoric material), only meteoric material may be ruled out based on compositional differences. Alternate grain sources, such as dust aggregates [*Greeley,* 1979], may be ruled out on a compositional basis. It is possible that dune material may have multiple sources, particularly if it has traveled a great distance from its source. It is possible that a sand transport path may cross various sources, each of which adds to the saltating material as it progresses downwind. Thus the most likely source, volcaniclastic grains, and the potential secondary source, impact ejecta, may both be responsible for various accumulations of basaltic sand on Mars, although to what extent each process plays a role in Martian aeolian history remains to be determined.

6.3 Thermal Inertia of Proctor Crater Dunes, Spatial View

6.3.1 Results. We have discussed the mean thermal inertia of the Proctor Crater dunes and how it may relate to the provenance and transport of the dune sand. However, close inspection of particle sizes across a dunefield can reveal a pattern that has implications for the history of the dunefield itself. On Earth, the finest sand grains are those most easily moved by the wind. Thus the coarser grains generally remain behind as the finer grains are transported downwind, often leading to a subtle trend across a dunefield [*e.g., Lancaster,* 1995]. The Proctor Crater dunefield on Mars shows a tantalizing trend in thermal inertia that may be indicative of a progression in particle size.

Figure 3.16a shows thermal inertia versus latitude for the six nighttime passes over the dunefield for which bolometric thermal inertias are available (shown

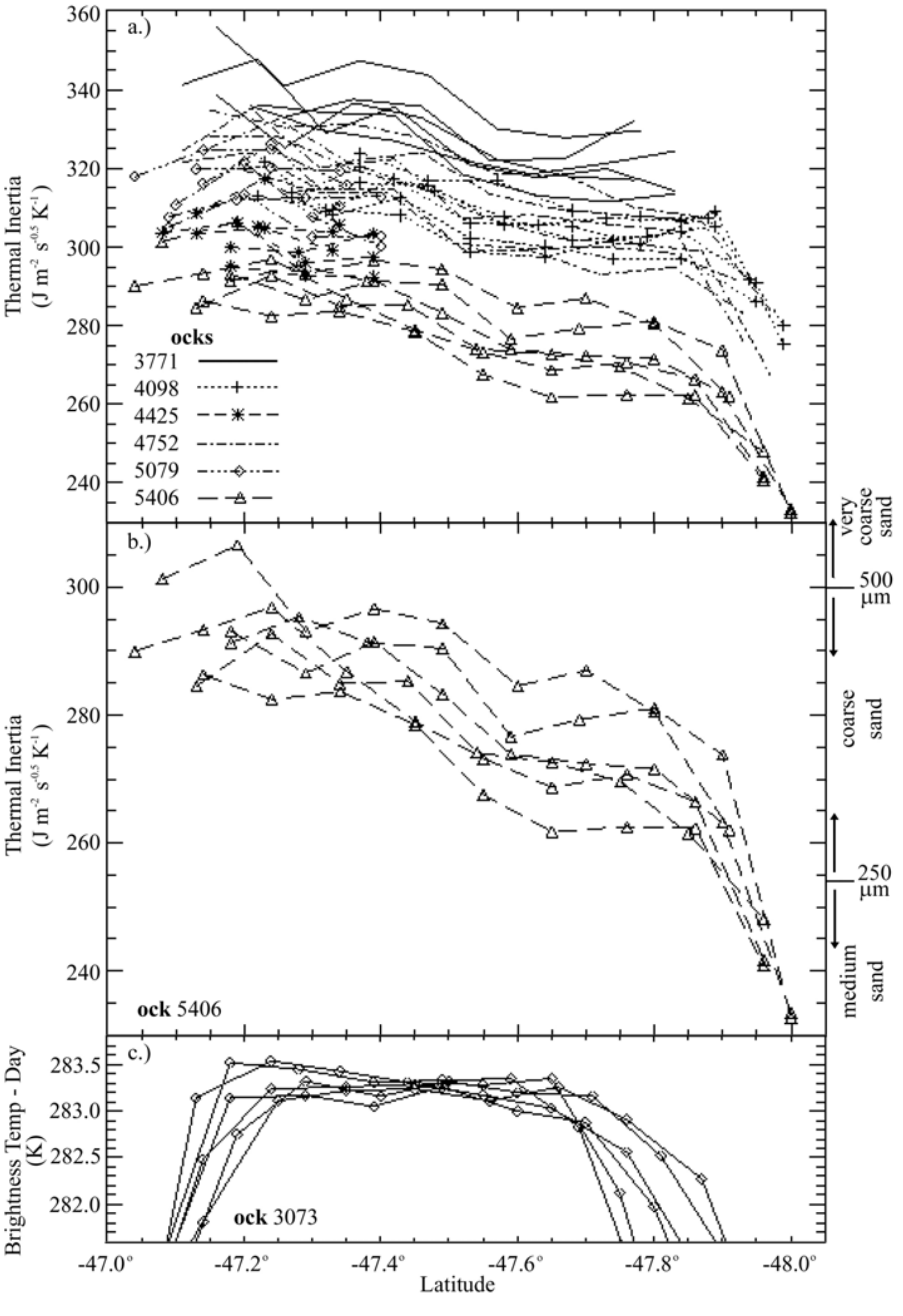

Fig. 3.16. Trends in thermal inertia across the dunefield. a.) All summertime thermal inertia measurements for each of six orbits (see Fig. 3.15b) and each of six detectors. Note the general downward trend to the south. b.) Thermal inertias from ock 5406 only. Ock 5406 is considered to have dust opacities closest to those used in the thermal inertia calculation, and thus ock 5406 has the most accurate thermal inertia values. c.) Daytime brightness temperatures from ock 3073.

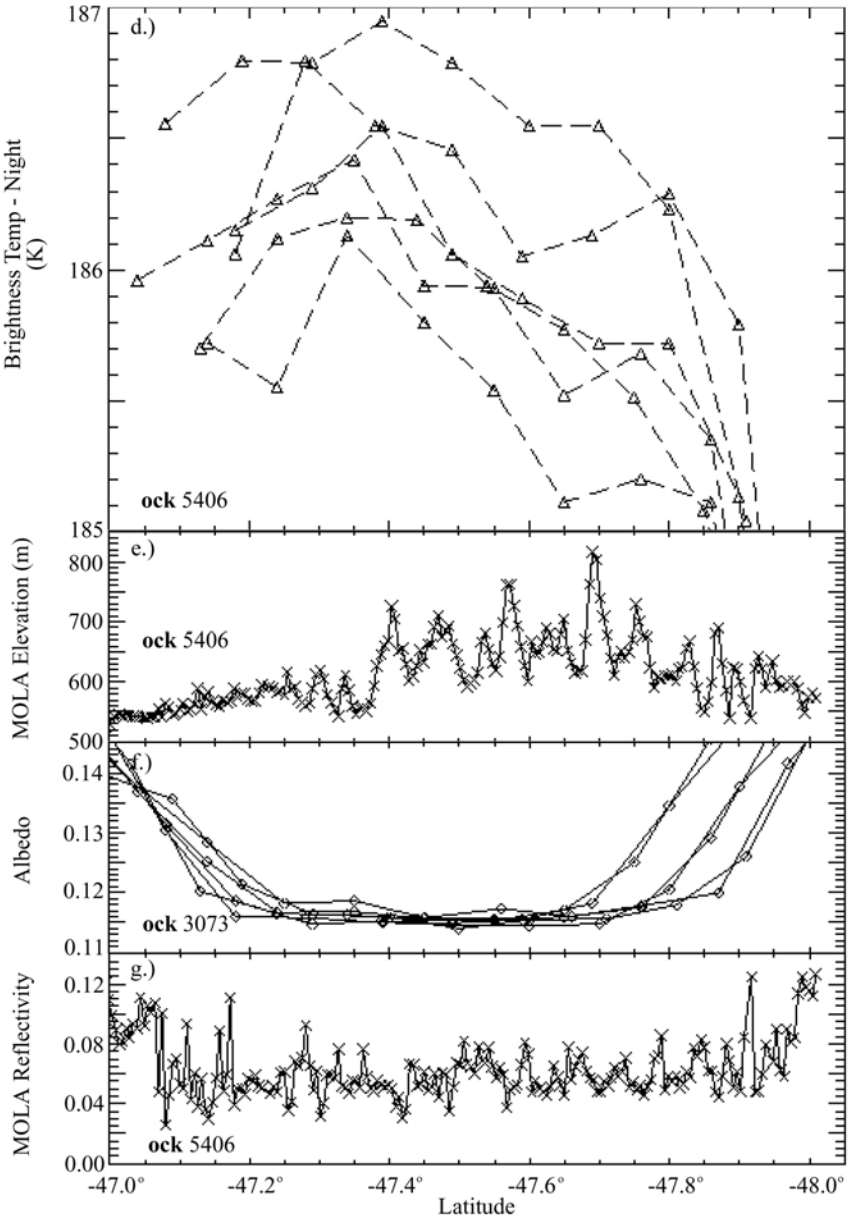

Fig. 3.16 (cont.) d.) Nighttime brightness temperatures from ock 5406. e.) MOLA elevations from ock 5406. f.) TES albedos from ock 3073. g.) MOLA reflectivities from ock 5406. Note that the downward trend in thermal inertia in frames a and b do not correlate with any measured parameter other than nighttime brightness temperature, from which the thermal inertias are calculated.

spatially in Fig. 3.14f). For each orbit, each of the six detectors is plotted separately to reduce any confusion caused by calibrational inconsistencies from one detector to another. Two of the passes only cover the northernmost edge of the dunefield. The TES tracks cross the dunefield at an oblique angle, causing differences in the latitude of the dunefield edges. In addition, the tracks vary in length because they cross the dunefield at different longitudes.

Figure 3.16a demonstrates that there is a wide spread in calculated thermal inertia values over the dunes, varying from ~233 to ~355 J m^{-2} $s^{-0.5}$ K^{-1}. This effect is alsoshown in Fig. 3.15b. The variation from orbit to orbit is far greater than that between detectors within a single orbit. As discussed in the previous section, the dominant cause of these variations is in differences in atmospheric dust opacity from one orbit to another. As before, we consider the measurements of ock 5406 to provide the thermal inertias most representative of actual surface properties. These values are replotted on a different scale in Fig. 3.16b.

The thermal inertias of ock 5406 show a clear downward trend from north to south across the dunefield, ending in a steep drop at the southernmost edge. The plot also shows effective particle sizes estimated using the empirical relation from *Presley and Christensen* [1997a], assuming a surface atmospheric pressure of 5 mbar. If this trend is real, rather than an artifact of the data or data processing, then it may indicate a change in effective particle size or cementation across the dunefield. However, first it must be shown that this trend is a real effect on the Martian surface.

The trend in thermal inertia may be caused by a shift in daytime temperature across the dunefield. As discussed in the previous section, irregularities in the geometry of the dunefield could lead to differential daytime heating. One pass over the dunefield is shown in Fig. 3.16c. This orbit is the one spatially closest to the nighttime orbits, but it crosses the dunefield farther east and at a different angle, leading to a shorter and more northerly track across the dunes than is shown in the nighttime tracks. The daytime temperature clearly peaks over the dunes, which have a low albedo and thus absorb a higher percentage of incident solar energy. At the edge of the dunefield the temperatures fall off to reflect the brighter surface of the crater floor. However in the center of the track, from latitude 47.3° S to 47.7° S, the daytime temperatures show little variation. Thus at the scale of TES, there are no observable effects on the surface temperature from any features on the surface.

Nighttime temperatures, on which the thermal inertia values are based, do show a change across the dunefield. Figure 3.16d shows measurements from ock 5406, which clearly shows the downward trend in temperatures to the south. Note that the southernmost measurements are cut off in this plot to emphasize the trend along the remainder of the track. Thus the shift in thermal inertia originated in the surface temperatures in the original measurements from the bolometer. In addition, the southward shift in thermal inertia appears in all tracks crossing the dunes with an L_s range spanning the southern summer (see Fig. 3.16a). This repeatability indicates that the shift is not caused by uncorrected atmospheric effects or a calibration problem in TES, but rather that it is a real phenomenon on the Martian surface.

It is possible that physical factors other than particle size or degree of cementation are affecting the surface temperatures and thus the thermal inertias across the dunefield. Figure 3.16e shows MOLA elevations across ock 5406. Because *Mellon et al.* [2000] correct for elevation using a 1° by 1° MOLA map, the majority of the dunefield is assumed to be at a single elevation in thermal inertia calculations. However, the central and southern region of the dunefield is actually about 150 m higher than the northern end of the dunefield. A lapse rate of

-2.5 K/km [*Zurek et al.,* 1992] indicates a mean decrease in air temperature of 0.4 K with an increase in height of 150 m, a value similar to the drop seen in each detector in Fig. 3.16d. Thus it might appear that the gradient in thermal inertias is simply due to a change in altitude. However the sensible heat flux from the surface to the atmosphere on Mars is so small (*e.g., Sutton et al.,* [1978]), particularly at night, that surface temperatures should not be expected to reflect the ambient air temperature. Therefore the change in air temperature with elevation will not affect thermal inertia calculations.

Thermal inertia is also directly affected by changes in air pressure, and thus with elevation [*Presley and Christensen,* 1997a]. However, the 150 m of elevation change leads to a drop in surface pressure of 1.4%, or 0.07 mbar. A change in air pressure this small has little effect on calculated thermal inertias, and therefore does not explain the change in thermal inertia across the dunefield.

It is also possible that a change in surface albedo could cause differences in daytime surface heating and thus create the observed downward trend in thermal inertias. For example, a relative increase in brighter interdune areas towards the southern end of the dunefield could lead to lower daytime temperatures, which would in turn lead to the slightly lower nighttime surface temperatures measured by TES. Figures 3.16f and 3.16g show surface reflectivity from the broadband visible TES bolometer and from MOLA at 1.064 μm, respectively. The TES track in Fig. 3.16f shows measurements from the same orbit in which daytime surface temperatures were measured (Fig. 3.16c). In the TES track the dunefield appears as a consistently dark area with a visible albedo ranging from 0.115 to 0.12. There is no trend across the dunefield that corresponds to the nighttime surface temperatures. Likewise, MOLA reflectivity, taken from the nighttime pass corresponding to ock 5406 in Fig. 3.16b, shows a uniform low value across the dunefield, save for a few bright interdune spots. The frequency of bright interdune spots remains low and constant, except at the edges of the dunefield where the spots become larger and more common. It is clear from both TES and MOLA reflectivities that the drift in thermal inertia is not influenced by a spatial variation in albedo across the dunefield. Even if there were some effect from albedo, it should be reflected in daytime surface temperatures, and no such trend appears in Fig. 3.16c.

6.3.2 Interpretation. Thus far, effects from dust opacity, atmospheric temperatures, changes in air pressure with altitude, daytime surface temperatures, and both TES and MOLA albedo have been ruled out as influencing the trend of thermal inertias across the Proctor Crater dunefield. Therefore the trend in thermal inertia, directly reflected in nighttime surface temperatures, does reflect differential cooling rates of surface materials within the dunes. A number of situations could lead to the observed trend.

First, there may be bright interdunes that are unresolved at the scale of both TES and MOLA. These areas may be composed of material that is more indurated and thus effectively has a higher thermal inertia than loose sand. The northern part of the dunefield (between -47.0° and -47.4° S) has smaller dunes that are largely unresolved in MOLA profiles (see Fig. 3.16e). This area of the dunefield is not superimposed on the broad 50 m thick layer of sand discussed in Section 4.3, and it may well have a higher percentage of indurated interdune areas. However, south of latitude -47.4° S, where the dunes are superimposed on the layer of sand and where interdune areas are nonexistent, the gradient in thermal inertia continues. In any event, the surface of the crater floor just outside the dunefield has lower thermal inertias relative to the dunefield (see Fig. 3.14f). Since the interdunes are small exposures of the same lower thermal inertia surface surrounding the dunefield, then a higher frequency of interdune areas should decrease the average thermal inertia of a TES pixel, rather than increasing it as is observed.

Second, the degree of dune cementation may vary across the crater. This could be the case if one side of the dunefield experienced more frequent winds above the saltation stress threshold relative to the other side. However, the entire dunefield seems to be swept clean of bright fines that might otherwise collect on more cemented and thus less active dunes. Furthermore, there is no obvious change in dune morphology across the dunefield that reflects any change in cementation (*i.e.,* erosional slumps or sandblasting on solidified dunes). Therefore a change in cementation across the dunes seems unlikely.

Finally, the thermal inertia gradient may be caused by a steady decrease in grain size to the south. If this is the case then this trend has implications for the history of the dunefield. Because any such implications on Mars are almost entirely unknown at this time, studies of terrestrial dunefields will be used as a basis for comparison. In terrestrial sand seas where there is a single upwind sand source and a dominant prevailing wind direction, the sand tends to become both finer and better sorted downwind, reflecting the transportability of smaller grains [*e.g., Lancaster*, 1989]. The Proctor Crater dunes have a single sand source, from the west-southwest, but the wind regime reflected in slipfaces indicates convergent wind orientations. Based on terrestrial studies, one would expect the coarsest grains to be located in the western and southern parts of the dunefield, but instead thermal inertias suggest a general fining of grains to the south. It may be that the east-southeasterly and east-northeasterly winds have recently been more dominant, causing the finer grains to move back towards the west and south. MOC Narrow Angle images show recent slope adjustments indicative of winds from the east-northeast (shown in Fig. 3.6f through 3.6h, and discussed in Section 4.1). If these slope adjustments show more than just a seasonal trend that is erased by reversing winds each year, then these winds may have sent the finer grains downwind. It is unclear how readily a shift in prevailing winds could affect the grain size distribution across an entire dunefield, but only the top layer of sand is represented in a thermal inertia calculation and thus only this layer need be affected.

Other possibilities explaining a trend in grain size must be considered. In the dunes of the northern Sahara, it has been found that the grain size and dune size are directly correlated [*Wilson,* 1973]. However, measurements from several other dunefields have shown that this relation does not generally hold true [*e.g., Wasson and Hyde,* 1983]. If this translates to Martian conditions, then there is no correspondence between the increasing dune size in the southern part of the dunefield and the finer estimated grain size in that area. In any case, *Wilson* [1973] proposed a positive correlation between dune size and grain size, opposite of the effect indicated in the Proctor Crater dunes. Thus the effective grain size across the Proctor dunes likely has little bearing on the pattern of dune size and spacing.

6.4 Thermal Inertia of the Proctor Crater Floor

The remainder of the Proctor Crater floor shows an interesting patchwork of varying thermal inertias. Surrounding the dark dunefield and covering a great deal of the floor of Proctor Crater are smaller, brighter duneforms (see Figures 3.7 and 8, Section 3.4). Where these features predominate, the average thermal inertia appears to be that of medium to coarse sand. In addition, the areas where these bright duneforms are most plentiful correspond to the lowest thermal inertias measured on the floor of Proctor Crater (compare Figures 3.7a and 3.14f). High-resolution images of these areas shows boulders that could raise the average thermal inertia and dust devil tracks revealing the presence of bright dust accumulations that would lower the average thermal inertia of these areas. The complications caused by these other features makes thermal inertia interpretations of the small bright duneforms difficult. The bright duneforms are most likely either small, cemented dunes composed of sand-sized particles or the granule ripples proposed by *Malin and Edgett* [2001], *Zimbelman and Wilson* [2002], and *Williams et al.* [2002]. This is supported by two observations. First, these smaller duneforms are relatively immobile with respect to the large, dark dunes (see Section 3.4). Smaller dunes contain less material than larger dunes and, all other factors being equal, should move faster as a result. Second, some of the bright duneforms are highly eroded (see Figures 3.8a and 3.8c), leaving behind rounded or fragmented remnants that are suggestive of some amount of induration. However, their indurated or granular nature is not demonstrated in thermal inertia measurements.

Because the bright duneforms are probably not composed of medium to coarse sand, other factors must be considered that would lead to this thermal inertia result. It may be that a layer of seasonal dust fallout partially obscures the surface of the bright duneforms, thereby effectively lowering their thermal inertia. Such a dust layer would be intermediate in the *Pelkey et al.* [2001] terms "thermally thick" and "thermally thin." If this dust layer is present then the correspondence of bright duneforms with the lowest thermal inertia measurements in Proctor Crater suggests that the bright duneforms preferentially retain accumulated dust relative to the surrounding terrain, perhaps by sheltering dust in the cracks between granules or pebbles. A good test for the preferential accumulation of dust would be to seek progressive seasonal shifts in thermal inertia with increasing concentrations of dust devil tracks. TES and MOC data are too sparse for such a study, but the THEMIS data set could provide such information.

The compositional analysis discussed in Section 5.1 indicates that many bright duneforms are located in areas with a moderate basalt signature. This implies that the material forming the bright duneforms is partially composed of basalt. This compositional signature is surprising given that it is in an area we have interpreted as partially thermally obscured by dust accumulations. However, dust devil tracks are prevalent over the bright duneforms, exposing parts of the underlying bright duneforms. It is likely that these swaths of uncovered material contribute to the basaltic signature in these areas.

The northern region of the crater floor has a high thermal inertia, indicative of a gravelly or well-consolidated surface. The northern rim of Proctor Crater experiences strong drainage air flows during the night during part of the year (see Paper 2). It may well be that these areas are scoured clean of loose sediments, as suggested by *Christensen* [1983], exposing a rocky or consolidated surface. Indeed the bright duneforms in this area, nearly ubiquitous across the rest of the crater floor, appear to be highly eroded or absent (see Figs. 3.7a and 3.8c, Section 3.4). The moderate basaltic signature in this area, shown in Fig. 3.14e, indicates that this scoured surface contains some amount of basalt.

Outside the crater rim to the north, the thermal inertia sharply drops to a value consistent with medium sand. This sharp contact indicates a fundamental change either in the surface or in the wind regime at the edge of the crater. Based on atmospheric modeling (see Paper 2), strong nighttime spring and summer winds should carry any loose sediments across this contact from the intercrater plains to the crater floor, and yet there appears to be no thermally distinct evidence for such transport. Perhaps the most plausible explanation for the sudden change in effective particle size is a change in surface roughness inside the crater. If winds sweeping down the crater rim abruptly encounter a smoother, flatter surface with a lower roughness height, then loose particles will be much more easily lifted into saltation, in turn kicking any dust into suspension, and leaving behind a scoured surface of immobile material that will have a relatively high thermal inertia. These strong drainage flows will also serve to keep new dust from settling onto the surface.

The southern edge of the crater floor grades into the rim and intercrater plains, much as the long wavelength emissivity does in this area. This area has a weaker basalt signature than on the rest of the crater floor (see Fig. 3.14e) and no bright duneforms (see Fig. 3.7). It is probably a terrain like that on the northern edge of the crater floor, only this area does not experience strong nighttime drainage winds that would scour the surface clean. Thus some amount of dust can settle out on the surface here, partially obscuring the higher thermal inertia of the indurated sediments and almost completely obscuring their basaltic signature.

The floor of the large western pit, like the northern part of the crater floor, also has a fairly high thermal inertia. There are known dark sand accumulations, bright duneforms, and abundant boulders in the pit (see Fig. 3.3e), but overall the area seems to be swept clean of fines, much like the northern area of the crater floor. This implies that the western pit floor is composed of consolidated materials, like that on the northern crater floor. The central pit has a slightly lower thermal inertia, suggestive of more accumulated fines. Much of the exposed materials in the western pit are the layered sediments comprising its walls and local relief. The terrain exposed in the western and central pits and along the north edge of the crater floor are most likely the same sedimentary unit, indicating that the ~450 m of basin fill in Proctor Crater is composed of indurated material. Given the relief and steep slopes evident in Figure 3.3e, this result is hardly surprising. Combined with the basaltic signature in the pits discussed in Section 5.1 and shown in Fig. 3.14e, the correlation of composition with high thermal inertias are more evidence for the presence of basalt in the layered sediments within Proctor Crater.

The high thermal inertias of the pits and northern crater floor coupled with their moderate basalt signature may have implications for the origin of the sedimentary deposits filling Proctor Crater. *Malin and Edgett* [2000a] proposed that sedimentary deposits such as these were produced by one of two processes: either they collected as lake sediments in low-lying basins, or they were transported by the wind through suspension to their current location. If the sedimentary layers in Proctor Crater were deposited as lakebeds then some amount of the basaltic material would have been aqueously altered. *Wyatt and McSween* [2002] reinterpreted the "andesitic" surface Type 2 of *Bandfield et al.* [2000] as low-temperature aqueously altered basalts. However, very little of Surface Type 2 is found on the crater floor (see Fig. 3.14c). Rather, the areas on the crater floor and in the pits interpreted as swept clean of fines have a signature that indicates some amount of unaltered basalt. The evidence suggests that the layered material in Proctor Crater was deposited by aeolian processes, the second of the two hypotheses proposed by *Malin and Edgett* [2000a].

7. Conclusions and Geomorphic Sequence

This study has led to an understanding of the sedimentary history of the interior of Proctor Crater. Each of the different data sets incorporated into the GIS has provided a unique set of information about the surface of the Proctor Crater floor. Here the conclusions are summarized in chronologic form, so that results from each data set are integrated into a single consistent history.

Proctor Crater was formed during the period of heavy bombardment. It is 150 km in diameter, in the size range of peak ring basins. Wall slumping is expected in a crater this size, although currently no such features are visible.

After the crater was formed, up to 450 m of layered sediments filled the crater basin. These deposits have a thermal inertia consistent with indurated material and a partially basaltic composition. Much of the material is hard enough to produce boulders upon impact, but friable enough to be eroded by the wind. The basaltic component of the surface composition indicates that the layers are probably not lake sediments, which would produce aqueously altered minerals. Rather, the sediments are probably produced by accumulated fallout of aeolian material, possibly volcaniclastic. Some volcanic flows may be interfingered with the aeolian deposits, although evidence for them is difficult to establish in the images. This influx of material was part of a global-scale deposition of layered sediments reported by *Malin and Edgett* [2000a], who proposed that these deposits were formed by either subaerial or subaqueous processes. The results in this work support deposition by subaerial processes.

There is a 50 m high ridge concentric to the crater rim at half the crater diameter. This "concentric ridge" is proposed to be one of three constructs: 1.) It may be an outcrop of resistant sedimentary layers. If so then the sedimentary material in Proctor Crater consists of contiguous layers that were deposited uniformly across the entire crater floor. Like the strata of *Malin and Edgett* [2000a], these layers dip so that they follow the crater walls, probably as a result of basin subsidence from the immense weight of 450 m of sediments. Furthermore, at least 50 m of material has been differentially eroded from the surface of the crater floor in order to leave these erosional remnant ridges. Aeolian erosion is the most probable source of deflation. 2.) The concentric ridge may simply be the remnant top of the peak ring that was formed during the impact that created Proctor Crater. 3.) In places the concentric ring has a morphology similar to wrinkle ridges. Such features have been formed in craters, either along the floor as part of a larger system, or along the crater rim in a material that previously buried the crater. If it is a wrinkle ridge, then it most likely formed from thrust faults along shallow décollement surfaces in the layered sediments within the crater. Compression could have been forced by a number of processes, such as subsidence of basin fill, or by a regionally uniform removal of ground water or cooling of ponded lava. It is difficult to conclude from morphology alone which of these processes contributed to the formation of the concentric rings.

After the sediments were emplaced, further small impacts bombarded the Proctor Crater floor, producing small craters with associated boulder fields. Today these craters are in varying states of erosion, some of which are barely discernable. Ubiquitous boulder fields with no apparent source crater hint at a large quantity of long-erased craters, indicating that a great deal of the fine sediment on the crater floor has been stripped away by the wind.

Two large pits have been eroded out of the sedimentary layers filling the floor of Proctor Crater. The larger of the two, the western pit, covers approximately one tenth of the crater floor and reaches to a depth of one kilometer. The pits were likely eroded by aeolian abrasion and deflation, although there may have been weakening from below, for instance from underground water, that contributed to the erosion of these features. Large craters on the western side of the Protor Crater floor may also have initiated the weathering process that produced the western pit, although this seems unlikely because no such craters are present near the central pit.

Layers exposed in the walls of the western pit provide evidence for the former accumulation of sediments. Steep slopes in the walls and thermal inertias consistent with consolidated material indicate that the sediments are highly indurated. Indeed, the presence of boulders produced by impact onto the surface of these strata indicates that highly consolidated material and possibly clasts are present. The composition of the floor of the western pit is basaltic. Although falling dunes of dark sand are present, they do not dominate the interior of the pit, and therefore this compositional signature is probably indicative of basaltic material in the ~450 m of sedimentary layers.

After and perhaps during the erosion of the pits, small bright bedforms appeared throughout the crater floor. These features are superimposed on pits and craters, and thus postdate them. They are much more common on the Proctor Crater floor than the surrounding intercrater plains. The bright bedforms are most likely formed from locally eroding basin fill, and thus represent the lag deposit of material that is not raised into suspension and blown out of the crater. A moderate basaltic signature supports the suggestion that the eroding sedimentary layers are at least partially basaltic.

These duneforms may be either small dunes composed of bright sand, or ripples composed of larger grains. Thermal inertias of these features are consistent with medium sand, but their eroded nature and lack of movement with respect to much larger, dark dunes suggests that if they are dunes then they must be at least partially cemented. It is possible that dust fallout, made obvious from the plentiful dust devil tracks that form every summer season, obscures the true thermal response of the material comprising the bright duneforms. It is also possible, that, if these features are granule ripples, they are composed of a mixture of fine and coarse materials that can produce a thermal inertia consistent with medium sand.

Some of the bright duneforms have rounded crests and eroded structures, indicating that in places they may have become cemented. However, in the interior of the dark dunefield, the orientations of these bedforms are strongly influenced by the presence of the large dunes. In addition, they reform after a dark dune has passed by, as the dark dune slowly destroys the older bright duneforms it encroaches on. Thus the processes and materials that produce bright duneforms are still active today. These recently influenced or newly created bedforms are less likely to be cemented than their older, eroded counterparts. However, these young bright bedforms also move more slowly than the large dark dunes, like the older bright bedforms, which is not expected if any of the bright bedforms are dunes as well. Therefore, the bright duneforms are probably granule ripples rather than dunes.

Some time after the bright bedforms were established on the Proctor Crater floor, dark basaltic sand entered the crater from the southwest. Several other craters in Noachis Terra also contain large dunefields of dark sand, which were probably emplaced concurrently with the sand in Proctor Crater. The provenance of this sand is unknown. It cannot be derived from the south polar layered deposits, which have been shown to be composed of accumulated fines deposited from suspension [*Murray et al.,* 2001]. Regardless of the source of sand, its presence in craters in the southern highlands indicates that a large quantity of basalt sand was released in a single event, and that it was subsequently redistributed by the wind into dunes now trapped on crater floors.

A transport pathway, now largely defunct save for a few remaining falling dunes, carried sand towards the center of Proctor Crater by the primary winds from the WSW. Upon intersection with ESE and ENE winds, the incoming dark sand halted in a region defined by zero net transport and began to accumulate into large dunes. By the time the sand supply was cut off or depleted, a 50 m thick mound of sand in the center of the dunefield had been established, with large dunes superimposed on top. This deposit indicates a long history of sand accumulation, and it is likely to contain interfingered dust deposits. The dunefield location has probably not changed much since the dunes first accumulated, although slight deviations to the north and east have occurred as the dune-forming winds varied in strength relative to one another. The large dunes take the form of reversing and star dunes, consistent with a converging wind regime.

A new observation regarding these dunes is that they do not contain smaller superimposed secondary dunes as terrestrial dunes of this size do (*i.e.,* they are simple dunes). This effect is not caused by the erosion of previously formed secondary dunes, because the dunes are still active and should be continuously forming smaller dunes. However, slipface avalanches appear to flow down the entire slipface of either side of the large dune ridges. The reason for this difference between Martian and terrestrial dunes may be related to different atmospheric conditions between the two planets, or by some influence of trapped volatiles on Martian dune morphology.

Parts of the dark dunes are clearly active today. Slipface adjustments that change in position from year to year are present, indicating that continual avalanching occurs. Because the dunes are influenced by winds from opposing directions, they do not migrate in any direction, but instead they probably fluctuate around a mean position, with the variations depending on the relative strengths of the winds in a particular year. In a few places, slope adjustments take the form of small narrow landslides that are not erased by subsequent slope activity. The fact that these avalanche scars retain their form indicates that the underlying sand in these locations is at least somewhat indurated.

The dark dunefield has an average thermal inertia of 277 ± 17 J m^{-2} $s^{-0.5}$ K^{-1}, leading to a grain size estimate of 740 ± 170 μm. This size is in the range of coarse sand, consistent with that expected and previously measured for this dunefield. As a result, three possible sand sources are considered: impact ejecta, meteoritic material, and volcaniclastic grains. Although with time impact gardening creates smaller particles than are present in the dunefield, such surfaces may be buried before such a steady-state condition is reached, thus preserving sand-sized grains that may later be exposed by weathering. Thus impact ejecta, although unlikely, is a possible source of basaltic dune sand. Compositional arguments rule out meteoric material and aqueously altered sand. The remaining obvious source of sand is volcanic ash, which easily forms in the grain size and compositional range observed, and therefore this material is considered to be the most likely source of sand grains for the Proctor Crater dunefield.

The dunefield displays a uniform and repeatable decrease in thermal inertia from north to south that is interpreted to be a real physical phenomenon. It is not caused by a shift in percentage of interdune flats or by any observable change in dune cementation. It may reflect a change in grain size, indicating a decrease in grain size to the south. However, the primary wind blows from the WSW, and logically this wind should preferentially blow finer particles northward. Nevertheless, the wind regime is complex, and an expected particle size distribution is therefore difficult to predict. Only a higher spatial resolution data set, and perhaps *in situ* measurements, will resolve whether or not it is grain size changes that cause this shift in thermal inertia.

The observed wind pattern of all the aeolian features indicates that three main winds influence the floor of Proctor Crater. Dune slipfaces indicate three formative winds. The primary wind blows from the WSW, and this is the wind originally responsible for transporting sand into the crater. Slipfaces oriented to this wind occur throughout the dark dunefield. Both bright bedforms and dust devil tracks are aligned with this wind, indicating that this wind has blown since before the dark sand arrived and that it still blows today. Dust devil tracks are produced by spring and summer early afternoon winds, but these winds are most likely too light to produce movement on the dune slipfaces. A secondary wind blows from the ESE. This wind is represented by slipfaces throughout all but the easternmost portions of the dunefield. A subset of the bedforms is oriented to this wind, indicating that these winds, like the primary winds, must blow strong enough to produce granule ripples. A tertiary wind blows from the ENE, but corresponding slipfaces in the dunes only occur in the eastern portion of the dunefield. Some sand movements in the center of the dunefield may be formed by this wind, although the dune slopes here are not obviously slipfaces. Dust devils tracks are not aligned with this wind, but some of the bright duneforms may be.

One region of the crater, to the northeast of the dark dunefield, is unique in several respects. The single MOC Narrow Angle image of this area shows a surface devoid of boulders and bright duneforms, which is an unusual characteristic of the Proctor Crater floor. It is also the location of the only summertime image that does not contain dust devil tracks. This region has a thermal inertia typical of indurated materials and a composition with a moderate basalt signature. This area is probably a windy zone, such that dust deposits, bright duneforms, and even boulders do not remain. The boulders, which are created from impact into the sedimentary deposits filling the crater, may withstand ejection upon impact but erode away under the persistent action of the wind. This area may be subject to strong slope winds, perhaps even the same tertiary winds from the ENE that influence the eastern portion of the dunefield. Only atmospheric modeling, discussed in Paper 2, confirms the existence of such winds.

The remainder of the geomorphic sequence of Proctor Crater includes seasonal features such as frost and dust accumulations. Dark dust devil tracks develop during the spring and summer, indicating that prior to this season some amount of dust has accumulated on the surface since the previous summer season. In the springtime tracks are most prevalent over dark sand, where the surface warms enough to produce dust devils. As the summer approaches the tracks expand to include most of the rest of the crater floor. Dust devil tracks change little during the summer season, indicating that few are erased over the summer, and thus little sand is present beyond the edge of the dark dunefield that might otherwise saltate under strong winds and erase the tracks by removing nearby dust.

Frost forms on dunes at $L_s = 50°$ (mid fall) and sublimates away completely by $L_s = 165°$ (late winter). The sun-facing slopes quickly lose their frost as spring approaches, but the pole-facing slopes retain frost for a much longer time. On these south-facing slopes the frosts form dark spots as they slowly sublimate away. These spots persist in location from year to year, and they form lineations that may parallel exposed bedding structures from within the dunes. The largest sublimation spots have bright cores, which may simply be reaccumulated ice. Sintering potentially leads to increased transparency along bedding plains, which is one possible explanation for the coherent spacing of the dark spots.

The sedimentary history of Proctor Crater is one of a complex interaction of accumulating and eroding sediments. This history began with the eventual accumulation of ~450 m of potentially aeolian material that has subsequently been indurated, impacted, eroded, and reworked into bright duneforms. The sand in the dark dunefield is but the most recent set of sediments to enter the crater. All aeolian features indicate a very stable wind regime throughout the observable aeolian history, which is reflected both in old and stabilized bright duneforms and in recent seasonal dust and frost accumulations. Thus from its earliest history onward, the story of Proctor Crater has been one dominated by aeolian processes.

8. Acknowledgments.

I would like to thank several people who made invaluable contributions to this paper. Trent Hare and Shane Byrne provided technical expertise with image processing and using Arcview and IDL. Anton Ivanov aided in assembling MOLA data. Josh Bandfield provided concentrations of compositional endmembers as well as his expertise. Junjun Liu provided optical depth calculations. In addition, Wes Ward, Arden Albee, Mark Richardson, Andy Ingersoll, Jeff Plescia, Mike Mellon, Matt Golombek, Bruce Murray, and Shane Byrne aided with constructive discussions regarding the manuscript and various parts of the analysis.

Chapter 4

AEOLIAN PROCESSES IN PROCTOR CRATER ON MARS: 2. MESOSCALE MODELING OF DUNE-FORMING WINDS

Lori K. Fenton and Mark I. Richardson

Division of Geological and Planetary Sciences, California Institute of Technology, Pasadena, California

Anthony D. Toigo

Center for Radiophysics and Space Research, Cornell University, Ithaca, New York

Abstract. Both atmospheric modeling and spacecraft imagery of Mars are now of sufficient quality that the two can be used in conjunction to acquire an understanding of regional- and local-scale aeolian processes on Mars. We apply a mesoscale atmospheric model adapted for use on Mars to Proctor Crater, a 150 km diameter crater in the southern highlands. Proctor Crater contains numerous aeolian features that indicate wind direction, including a large dark dunefield with reversing transverse and star dunes containing three different slipface orientations, small and older bright duneforms that are most likely transverse granule ripples, and seasonally erased dust devil tracks. Results from model runs spanning an entire year with a horizontal grid spacing of 10 km predict winds aligned with two of the three dune slipfaces as well as spring and summer winds matching the dust devil track orientations. The primary (most prevalent) dune slipface direction corresponds to a fall and winter westerly wind created by geostrophic forces. The tertiary dune slipface direction is caused by spring and summer evening katabatic flows down the eastern rim of the crater, influencing only the eastern portion of the crater floor. The dunes are trapped in

the crater because the tertiary winds, enhanced by topography, counter transport from the oppositely oriented primary winds, which originally carried sand into the crater. The dust devil tracks are caused by light spring and summer westerly winds during the early afternoon caused by planetary rotation. The secondary dune slipface direction is not predicted by model results from either the Mars MM5 or the GFDL Mars GCM. The reason for this is not clear, and the wind circulation pattern that creates this dune slipface is not well constrained. The Mars MM5 model runs do not predict stresses above the saltation threshold for dune sand of the appropriate size and composition. As with previous work, the calculated wind velocities are too low, which may be caused by too large a grid spacing.

1. Introduction

The dominance of wind action over other contemporary surface processes on Mars became evident during the Mariner 9 mission in 1971–1972 [*e.g., McCauley et al.,* 1972; *Sagan et al.,* 1972; *Smith,* 1972; *Cutts and Smith*, 1973; *Arvidson,* 1974]. Wind circulation patterns determine the location and magnitude of sources, sinks, and transport pathways of particulate materials. Because of this coupling between surface materials and the atmosphere, the study of one is not complete without the study of the other. In particular, dune morphology is dependent on winds that are strong enough to saltate sand. Thus a study of dune morphology leads to an understanding of the orientations of strong local winds. Furthermore, there are few wind measurements available for use as "ground truth" of atmospheric models. Aeolian features are often aligned with the winds that formed them, providing the only indicator of surface wind direction than spans the globe. Thus a comparison of modeled wind predictions with orientations of surface features is the only current verification technique for both the modeled surface winds and the applied boundary layer scheme. It is the atmospheric counterpart to surficial geology that is discussed in this work.

Shortly after the discovery of sand dunes on Mars, experimental work in wind tunnels began in order to better understand the physics behind sand saltation under Martian atmospheric conditions [*Iversen et al.*, 1973; *Iversen et al.*, 1976]. The results indicate that there are many differences in the mechanics of saltation on Mars and Earth. *Greeley et al.* [1980] found that threshold friction speeds an order of magnitude larger than those measured on the Earth are required to move similarly sized sand grains on Mars (u_{*t} of 0.22 m s^{-1} for Earth versus 2.2 m s^{-1} for Mars). *Iversen and White* [1982] improved on previous work, producing new empirical relations for threshold friction speeds. They found that saltating particles on Mars would have longer path lengths than those on Earth, and that this parameter varies with temperature and atmospheric conditions. In addition, *White* [1979] showed that although it takes stronger winds to saltate sand on Mars, once saltation begins, the sand flux on Mars would be significantly higher than that on Earth. Now that sand grain sizes and compositions are being constrained using Thermal Emission Spectrometer (TES) data from the Mars Global Surveyor (MGS), a more precise estimate of saltation threshold stresses may be utilized in detecting sand saltation and calculating sand mass fluxes.

In the last decade, atmospheric models have been applied in conjunction with the results from wind tunnel experiments to better understand aeolian processes on Mars. *Greeley et al.* [1993] used a Mars general circulation model (GCM) to study the correlation of surface wind patterns to aeolian features with measurable wind orientations. They found that bright depositional streaks correspond well to the southern summer Hadley circulation, but that dark erosional streaks and yardangs did not agree well with any modeled winds above the saltation threshold. *Fenton and Richardson* [2001b] later found that a higher time resolution (hours rather than days) in a Mars GCM resolved the nighttime winds that correlated well with dark erosional streaks, implying that temporal and spatial resolution in models is one of the keys to understanding some of the previously unexplained aeolian features. Yardang orientations remain unaligned with current winds, but some of these features may be so old that they were formed under ancient and unconstrained wind conditions that cannot be properly modeled without further information. Other applications of modeling the Martian surface on a regional or global scale have included finding bimodal winds in an area where longitudinal dunes indicate such a wind regime should exist [*Lee and Thomas*, 1995]; locating global sand sources and sinks [*Anderson et al.*, 1999]; and looking for changes in surface wind patterns caused by variations in orbital parameters [*Fenton and Richardson*, 2001b].

With the advent of mesoscale atmospheric models, the circulation of a small region can be examined in high-resolution detail for the first time. These models can be used in concert with spacecraft data, and in particular MOC NA (Mars Orbiter Camera Narrow Angle) images, which can provide detailed wind orientations at the scale of tens of meters. Comparing the two provides not only a verification of the mesoscale model and the GCM to which it is coupled, but also an understanding of the source of the winds that influence the surface. This in turn can lead to a better understanding of landscape morphology and the sources and sinks of mobile material. Recently, a mesoscale model has been applied over a crater and a valley, demonstrating that topographic and diurnal effects dominate the local windflow on Mars [*Greeley et al.,* 2001]. A mesoscale model applied over the Antarctic ice sheets has recently been used as an analog to the north polar residual ice cap on Mars in order to explain the presence of most of the surface features [*Howard*, 2000]. Mesoscale airflow has been modeled over a typical crater to show that the highest wind stresses correlate with the downwind crater rim, consistent with erosion patterns observed in small craters [*Kuzmin et al.,* 2001]. It

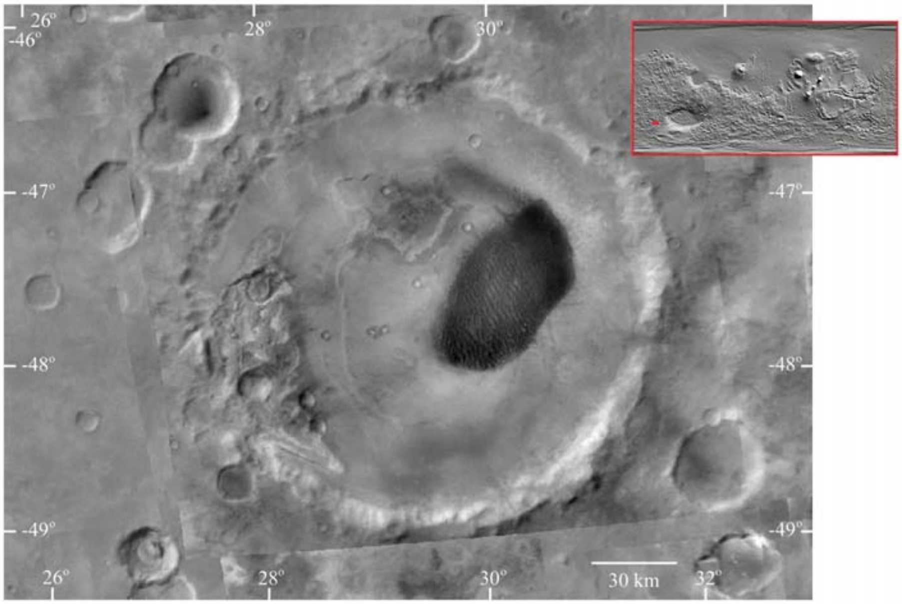

Fig. 4.1. Proctor Crater is a 150 km diameter crater with an interior dark dunefield, located in the southern highlands ~900 km west of Hellas Basin (see inset.)

has become clear that models with both higher spatial and temporal resolution are necessary to understand local and even regional wind patterns.

This work is the second of two papers describing aeolian processes in Proctor Crater, a 150 km diameter crater in the ancient cratered highlands of Noachis Terra (see Fig. 4.1). The first paper, *Fenton* [2003] (hereafter called Paper 1), discusses the morphology, composition, thermal properties, and stratigraphic history of the floor materials within Proctor Crater. With use of a number of different data sets in conjunction, it is shown in Paper 1 that the sedimentary history of Proctor Crater has involved a complex interaction of accumulating and eroding sedimentation. Aeolian features spanning much of the history of the crater interior dominate its surface, including large erosional pits, hundreds of meters of stratified beds of aeolian sediments, sand dunes, erosional and depositional streaks, dust devil tracks, and small bright bedforms that are probably granule ripples. In this work we apply a mesoscale model to the atmosphere above Proctor Crater in order to determine how modeled winds correspond to the aeolian features described in Paper 1. First we review the orientations of aeolian features found in Paper 1, with an additional discussion regarding evidence for seasonally reversing slipfaces found in newly released MOC NA images. We then describe the mesoscale model and how the resulting wind predictions correlate to known surface features. We discuss seasonal and daily wind changes and the spatial variation of wind patterns on the Proctor Crater floor. Using sand grain density and particle sizes estimated in Paper 1 we discuss the likelihood of sand lifting under the predicted wind conditions.

2. MOC NA Observations of Proctor Crater Dunes

2.1 Measured Orientations

Wind orientations are visible in at least three different types of aeolian features: in the large dark dunefield in the center of the crater floor, in dust devil tracks that cover the floor during the spring and summer, and in small bright duneforms that are nearly ubiquitous on the crater floor. Each type of feature indicates a different time scale, indicating either recent or ancient winds. For example, dust devil tracks form and are subsequently obliterated each year, and therefore the winds that move dust devils downwind must be currently active. However, the large dark dunes may move on timescales of thousands of years or more, and thus may reflect older winds. Some of the bright duneforms may be ancient stabilized features, possibly indicative of winds dating to hundreds of thousands of years or more. Each type of feature and the wind information it provides is discussed in detail below. A summary of the results is presented in Table 4.1.

2.1.1 Dark Dunes. As discussed in Paper 1, the dark dunefield in the floor of Proctor Crater (see Fig. 4.1) displays three slipface orientations. Slipfaces are

Table 4.1. Current wind regime in Proctor Crater (based on MOC NA images)

Wind	Locale	Features reflecting wind direction	Time of occurrence
Primary (WSW: 239° ± 18°)	Entire crater floor	Dune slipfaces, Bright duneforms	Fall and winter afternoon geostrophic-induced westerlies (strong)
		Dust devil tracks	Sprint and summer early afternoon westerlies from planetary rotation (weak)
Secondary (ESE: 110° ± 18°)	Central and western portion of dunefield	Dune slipfaces	?
Tertiary (ENE: 75° ± 9°)	Eastern portion of dunefield, possibly eastern portion of crater floor	Dune slipfaces, Bright duneforms (?)	Spring and summer evening katabatic flow (strong)

produced by two processes. In the lesser process, grains are deposited by a sand-laden wind, coating the lee side of a dune. However, the morphology of the lee side of a dune is usually dictated by sand flow, produced by the avalanching of sand which is oversteepened by the downwind movement of sand from the stoss (windward slope). Continued avalanching produces the characteristic slipfaces that are used both to identify dunes and to determine the wind orientation, because slipfaces are always oriented transverse to the wind (*i.e.,* they dip downwind).

Figure 4.2a shows a rose diagram (*i.e.,* a histogram on a polar plot) of the measured slipface dip orientations, or downwind directions, from Paper 1. Each of the three slipface orientations is labeled with a mean and standard deviation formative wind orientation (note that although the rose diagram shows downwind slipface directions, following the geological convention, the labeled wind orientations refer to the upwind directions, following the meteorological convention). The three directions are labeled primary, secondary, and tertiary based on their spatial frequency within the dunefield. The primary dune slipfaces

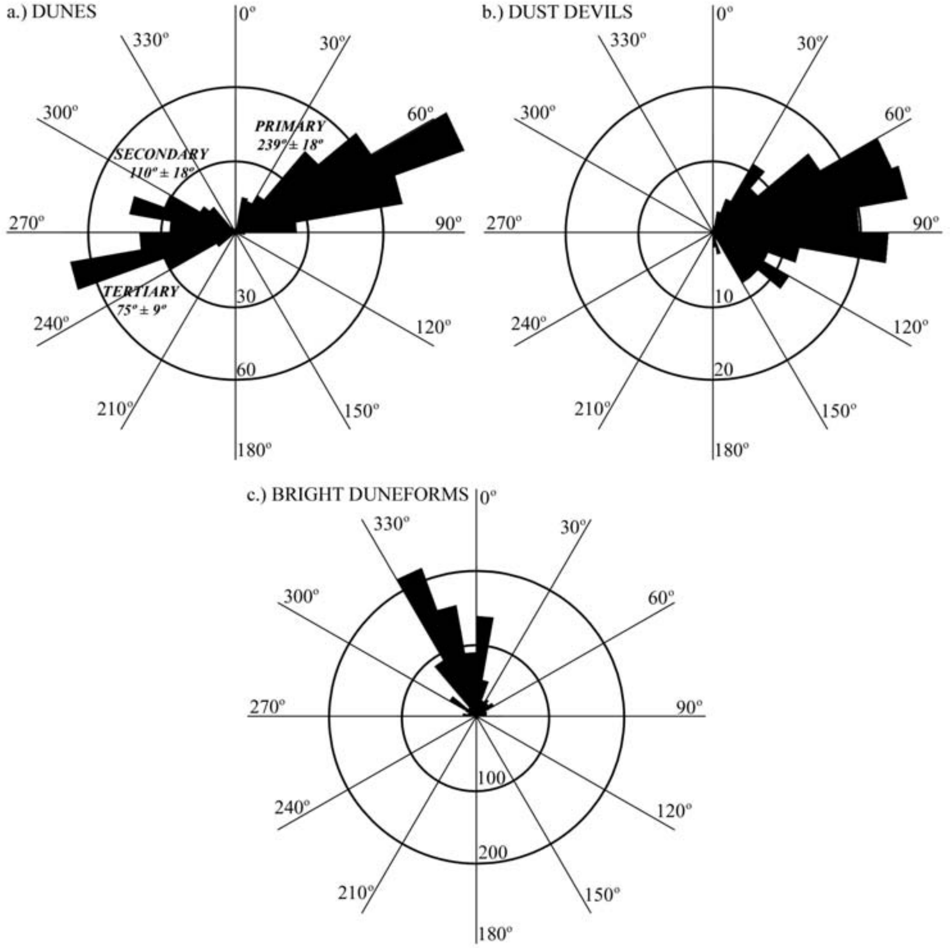

Fig. 4.2. Rose diagrams showing the azimuthal orientations of a.) dune slipfaces, b.) dust devil tracks, and c.) bright duneforms as measured in MOC NA images.

are created by winds from the WSW. These slipfaces are visible throughout the dunefield. Falling dunes on the eastern sides of hills and cliffs southwest (*i.e.,* upwind) of the dunefield are aligned with this wind, and have been interpreted in Paper 1 as the winds that carried the dark dune sand to its current location from the southwest. The secondary winds are consistent with winds from the ESE. They are prevalent throughout all but the easternmost portion of the dunefield, and dominate in the form of transverse dunes along the west-northwest edge of the dunefield. A large dark streak of sand emanating from the northern tip of the dunefield is aligned with the secondary wind (see Fig. 4.1). The tertiary slipfaces indicate winds from the ENE. They are only present on the easternmost edge of the dunefield, where they are the principal dune-shaping winds. The tri-directional wind regime observed in the Proctor Crater dunefield is also a convergent wind regime, indicating that the dunefield resides in a location on the crater floor with zero or low net transport. As discussed in Paper 1, the transverse reversing and star dunes found in the dunefield are consistent with the observed convergent wind regime.

Individual images of dunes generally do not provide information on the season or local time of the winds that influence them. However, they do provide the orientations of the winds that last influenced them, which may indicate dune activity ranging from saltation up to and during the data acquisition to indurated surfaces that reflect ancient and now defunct wind systems. Therefore, in order to interpret the Proctor Crater dune slipface orientations in terms of the current wind circulation patterns, it must first be established that the dunes are currently active. The Proctor Crater dunes are free of dust accumulations that mantle the local surface each year, and although the surrounding crater floor becomes covered with dust devil tracks each spring and summer, the dunes display few such dust devil tracks. This suggests that the dunes are active, clearing away dust fallout with sand saltation, and that any dust devils that pass over dark sand leave behind no tracks because there is no dust left to be cleared away. Furthermore, the dune thermal inertia indicates the dunes are made of coarse-grained sand, consistent with previous measurements and predictions (see Paper 1). Thick dust deposits on the dunes would lower the thermal inertia to a value consistent with dust grains (besides being unlikely based on the low albedo of the dunes), and dune cementation would increase the thermal inertia to a value too large to be indicative of sand-sized grains. In addition, there are few if any indications of hillslope erosion on the dunes or softening of slipface brinks, both of which are consistent with their being currently active. Thus the evidence suggests that each of the three measured slipface orientations corresponds to present-day winds.

2.1.2 Dust devil tracks. Dust devil tracks were identified in most of the spring and summer images on the Proctor Crater floor. They form first over dark patches of sand in the springtime, eventually spreading over much of the crater floor as the season progresses. Tracks overlap one another but generally are not erased within a single summer season. By the following year the tracks have been erased, indicating that fresh tracks form each year after new dust fallout has accumulated on the crater floor.

Most dust devil tracks are oriented WSW–ENE (see Fig. 4.2b). Because of a lack of obvious starting and ending points of the dust devil tracks, it is difficult to determine which direction the dust devils moved and thus the ambient wind direction in the early afternoon during spring and summer. No actual dust devils were imaged in Proctor Crater. However, as discussed in Paper 1, there is one springtime image showing dust devil tracks forming on a dark sand patch and moving downwind, pushed by winds from the WSW. Thus it is likely that all of the dust devil tracks, which form in the same season and during the same time of day, indicate winds from the WSW.

Dust devil tracks are visible throughout the spring and summer seasons in seventeen different images. It is possible that the mean wind direction drifts as the season progresses, perhaps reflecting changes in the strength of Hadley circulation or tidal flow. Thus we measured the mean orientations of the dust devil tracks as a function of L_s, including tracks from newly released images acquired during the second Martian summer. Where the dust devil tracks were plentiful, only the longest and most prominent tracks were measured. Where the dust devils were faint and scarce, as was the case for all wintertime tracks, all visible tracks were measured. It is not clear whether tracks observed during the winter are fresh features or relics from the previous summer season. As a result, there is a measurement bias towards larger, longer-lasting dust devils during the spring and summer and towards small and potentially old tracks during the winter. The results are shown in Fig. 4.3, with small dots marking the orientation of individual dust devil tracks and large asterisks indicating the mean track orientation in each image. As with Fig. 4.2b, all tracks are assumed to be oriented between 0° and 180°, thus avoiding the directional ambiguity. Although there is a wide distribution is track orientations, they generally tend to cluster between 45° and 135°. The mean orientations in each image are always near 90°. Both of these observations are consistent with the WSW–ENE orientation shown in Fig. 4.2b.

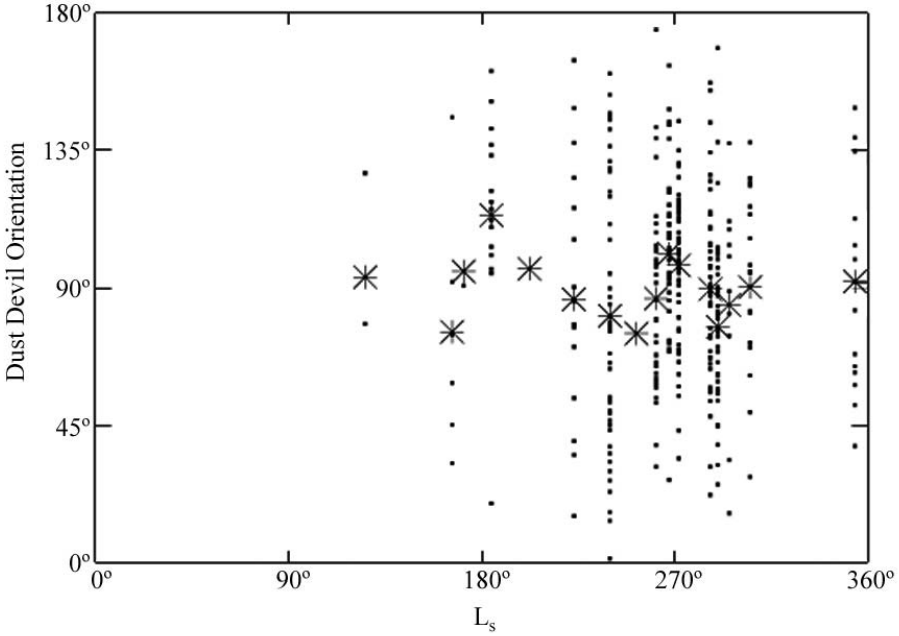

Fig. 4.3. Dust devil orientation as a function of season. Dots represent individual track orientations; large stars indicate mean orientations across a single MOC NA image.

Thus, according to the MOC NA images, there is no observable change in dust devil orientation in Proctor Crater during the year, indicating that the mean daytime wind direction during the spring and summer and possibly during the winter is fairly constant.

2.1.3 Bright duneforms. Bright duneforms cover much of the floor of Proctor Crater. They are visible in the interdunes in the large dark dunefield, indicating that these features were present before dark sand entered the crater. Although they are an order of magnitude smaller than the dark dunes, they are relatively immobile, indicating that they are either smaller stabilized dunes or very large granule ripples. The TES bolometric albedos of these features range from 0.12–0.14, making them "bright" relative to the dark dunes that have an albedo ranging from 0.06–0.12. For these reasons, they are referred to in this work as "bright duneforms" or "bright bedforms." They are most likely some sort of ripple, because there is an example shown in Paper 1 of a large dark barchan eroding bright duneforms as it slowly migrates by, only to have a few small features similar to the bright duneforms reform in its wake after it passed by. If these duneforms are in fact small dunes, then they would quickly migrate by the large dark dunes in an active wind regime. If most of the bright duneforms are simply stabilized dunes, then these features could not be recreated after being destroyed, as observed. Therefore these features are most likely very large granule ripples, which may migrate more slowly than dunes and yet still remain active.

The bright duneforms seem to be symmetric with no obvious slipfaces at the resolution of MOC NA images, making it difficult to determine whether they are aligned parallel or transverse to the local winds. Granule ripples tend to be transverse to the wind [*Sharp,* 1963], so if these features are ripples, as proposed, then they are probably transverse as well. Figure 4.2c shows a rose diagram of the along-crest direction of the bright duneforms. If they are transverse then they were formed by winds from either the WSW or the ENE. These directions are consistent with both the primary and tertiary slipfaces found in the dark dunes. It is possible that where the primary winds dominate, the bright duneforms were created by winds from the WSW, and that where the tertiary winds dominate, the bright duneforms were created by winds from the ESE. Some of the bright duneforms may be ancient features, far older than the dark dunefield. If this is the case then they reflect ancient winds, indicating that wind circulation patterns have changed little since they were created.

2.2 Annual Slipface Reversal

Although dune slipface orientations show the predominating wind directions that influence the dunefield, they do not indicate the season or time of day in which these winds blow. In fact, without evidence for recent dune movement, it is difficult to prove conclusively that these slipfaces were not formed by ancient winds that no longer blow, and that the dunes are not largely dormant. The paucity of erosional features on the dunes supports the idea that the dunes are not stabilized, relic features. In addition, movement of dunes the size of those in the Proctor dunefield could take a century or more to identify using data with the currently available image resolution, and thus their lack of movement cannot be used to conclude that they are stabilized.

However, there is evidence for slipface reversal in dunes on the eastern edge of the Proctor dunefield that clearly indicates dune activity within the timespan of the MGS mission. The eastern portion of the dunefield consists of relatively smaller dunes with visible interdune areas, in contrast to the huge dunes atop the 50 m deep mound of sand found in the central and western-central portions of the dunefield (see Fig. 12 of *Fenton* [2003]). The eastern part of the dunefield is likely a younger offshoot of the main accumulation of sand. At some point, winds from the southwest (the primary winds) blew sand from the main dunefield to the northeast, where it halted upon encountering east-northeasterly winds (the tertiary winds), which only influence the eastern part of the dunefield. Here the dark sand is largely balanced between the primary and tertiary winds, producing reversing transverse dunes common to the dunefield.

In Paper 1, bright material was described on slipfaces of double-sided barchans at the eastern edge of the dunefield. This bright material was attributed to the erosion of nearby underlying bright bedforms, which have a rounded appearance consistent with deflation and abrasion. It is only off the eastern edge of the dunefield that the bright bedforms have this rounded appearance, and it is only at the eastern edge of the dunefield that the dark barchans display bright slipfaces. This bright material cannot be residual frost because it is visible even in summertime images, when the surface is far too warm to support either CO_2 or H_2O frost.

The slipface containing bright material switches sides of the double-sided barchans, as shown in Fig. 4.4. Figure 4.4 compares two overlapping MOC Narrow Angle images of the same area at different times of the year. Figure 4.4a shows mid-fall frosted dune surfaces with bright material on northeast slopes. Figure 4.4b shows an overlapping image from the following year during the late spring, with fully defrosted dune surfaces bearing bright material on western slopes. Note that although the solar azimuth is similar in Figs. 4.4a and 4.4b, the solar altitude is much higher in Fig. 4.4b leading to fewer shadows and an increased emphasis on albedo contrast. The albedo contrast in Fig. 4.4b is enhanced by the lack of frost cover present in Fig. 4.4a. Figures 4.4c and 4.4d illustrate the slipface brinks and accumulations of bright material with colors corresponding to the formative wind directions (yellow is primary, magenta is tertiary). Figure 4.4e shows both slipface directions, emphasizing that they are on

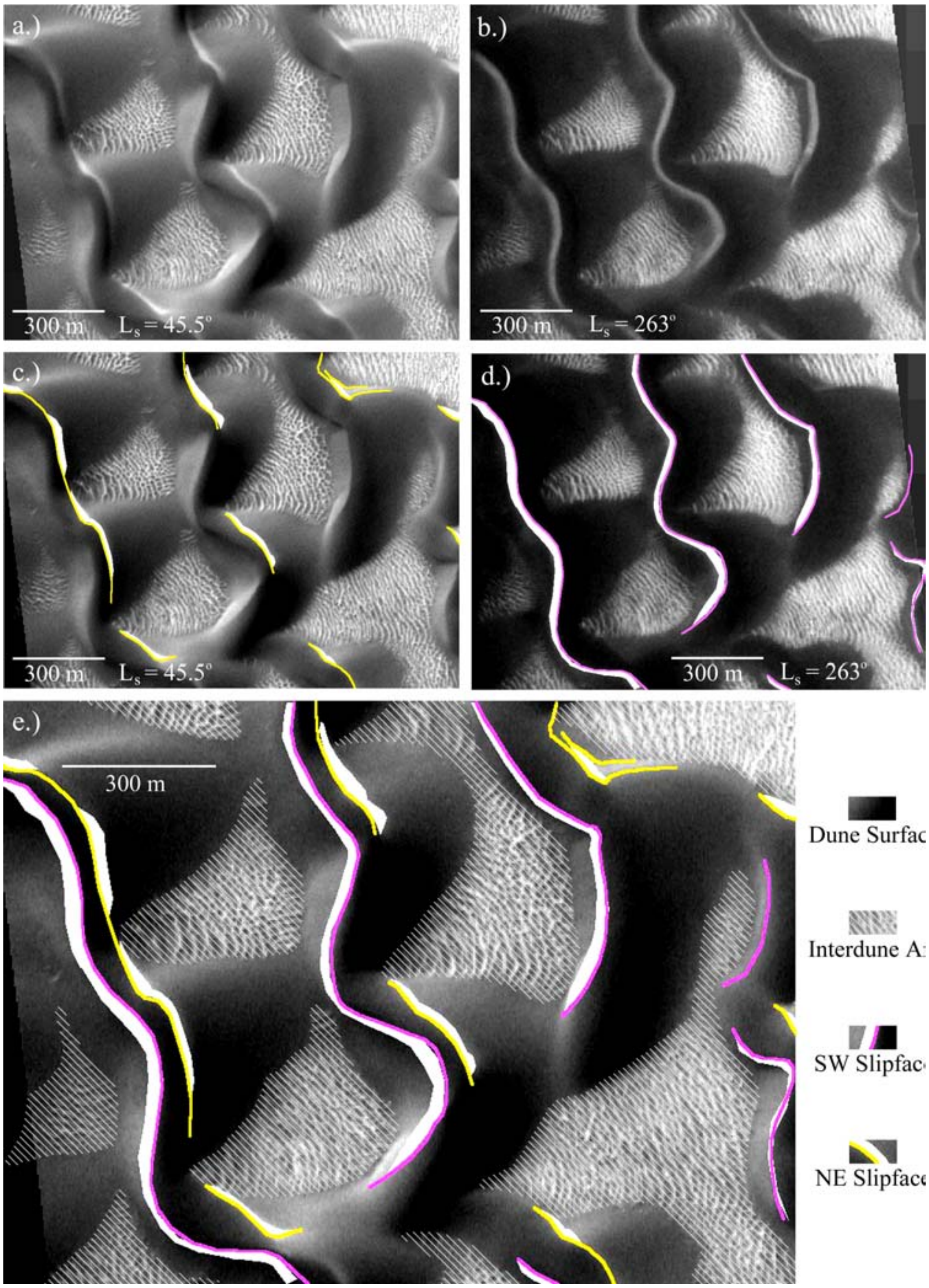

Fig. 4.4. Reversing slipfaces on dunes at the eastern edge of the dunefield. a.) MOC NA M1900307 during the fall and b.) MOC NA E0902707 during the spring show the same area with bright accumulations on opposing slipfaces. c.) and d.) illustrate the locations of slipface brinks and bright accumulations. e.) shows both sets of slipfaces and bright material. Note the slight shifting of one slipface brink in the upper right.

opposite sides of the barchans. Typical terrestrial reversing dunes switch sides with opposing seasonal winds, erasing the old slipface from the preceding season. The dunes in Proctor Crater display both slipfaces at different seasons, indicating that the slipfaces are not fully erased by opposing winds, leading to seasonally activated slipfaces. The fact that seasonal slipfaces are not fully erased may be caused by some amount of internal cementation of the dune, or by the fact that the slipfaces are too large to be demolished in a single Martian season.

In Figure 4.4c, one dune in the upper right corner of the image has two slipface brinks drawn on it. The more southwesterly and larger slipface corresponds to that in Figure 4.4a, and the smaller and more northeasterly brink corresponds to that in Figure 4.4b. This shift in slipface position probably indicates movement of this slipface toward the northeast between mid-fall and the following spring, although the dune itself has not shifted position. This movement indicates a shift of 13 to 37 m, depending on where along the brinks the movement is measured. Such a shift indicates strong and persistent seasonal winds. No other slipfaces in the frame moved and no dunes changed position, suggesting that movement of this type is rare.

Figure 4.4 indicates that between mid-fall and late spring, the prevailing winds change direction and that both winds influence the dunes. Bright material is likely blown from the stoss (upwind) slope onto the slipface along with any loose dark sand from the dune surface. If the dark sand on the dunes is mobile then an explanation must be found for why mobile bright material does not mix with the dark sand as it moves back and forth over the dune. Rather, the bright material remains on the surface, unmixed and unburied. It is possible that the dark sand in the dune is somewhat indurated, and that only the bright sand is moving back and forth as the seasons progress. However, the thermal inertia of the Proctor Crater dunes is consistent with loose, coarse sand (see Paper 1 and references within). It is more likely that some amount of dark sand moves back and forth over the dune as the winds shift, but that the bright material is more easily mobilized by the wind, and thus is the last to settle onto the slipfaces as the winds decrease. This may indicate that the bright saltating material is made of smaller or less dense particles, causing them to saltate under lighter winds than the coarse basaltic grains comprising the dark sand.

Six MOC Narrow Angle images pass over the eastern edge of the Proctor Crater dunefield, imaging slipfaces at different seasons. Following the hypothesis that the bright material accumulates on the downwind side of the dunes, the dunes in this region are influenced currently by the primary and tertiary winds. Figure 4.5 shows each inferred wind orientation as a function of L_s, labeled by the MOC

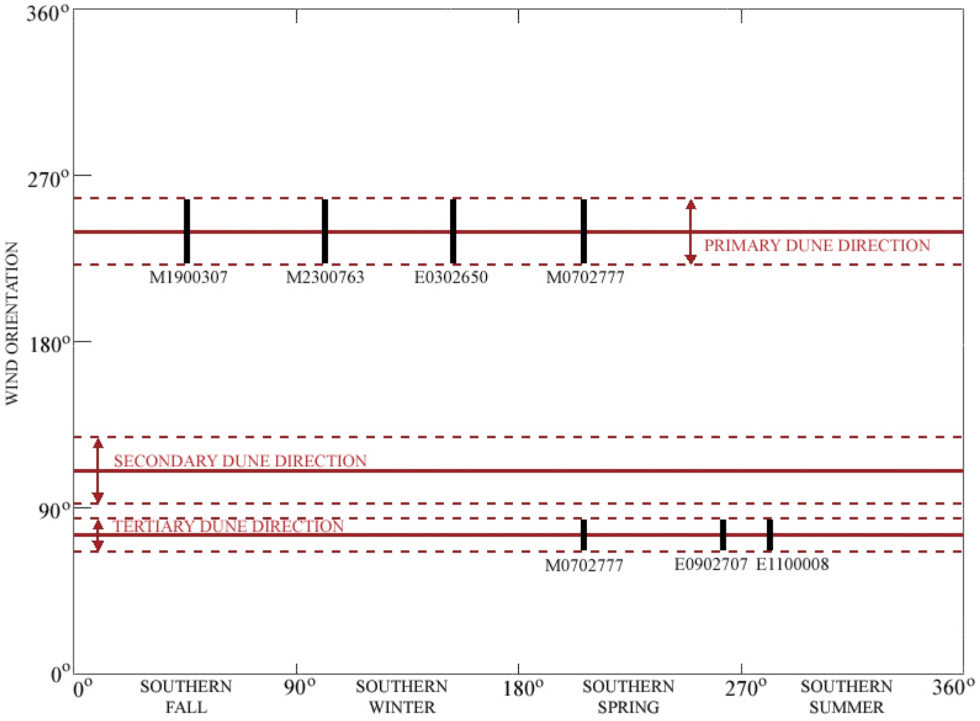

Fig. 4.5. MOC NA frames showing accumulations of bright material on oppositely oriented slipfaces. Horizontal red lines correspond to the three dune slipface orientations.

NA frame in which it was found. The red lines mark the three mean and standard deviation dune slipface directions. Reading from this plot, the primary slipfaces are active throughout fall and winter, and the tertiary slipfaces are active during spring and summer. MOC frame M0702777 from L_s = 206.68° appears to have bright material on both slipfaces, and likely indicates a transition time between the two seasonal wind regimes. As discussed next, the modeled winds reflect the activity of these slipfaces.

3. Mesoscale Modeling of Surface Winds

3.1 The Mars MM5

Mesoscale atmospheric models are tools that have recently been made applicable to Martian conditions. These models function similarly to Mars GCM's, but they can examine atmospheric patterns that vary from the synoptic (1000's km) down to the microscale (10's m). The goal of applying a mesoscale model to Proctor Crater is to determine how well predicted wind directions correlate with dune slipface orientations.

We applied the Mars MM5, developed from the PSU/NCAR 5th Generation Mesoscale Model (MM5) by *Toigo* [2001]. The model is nonhydrostatic and uses terrain-following sigma coordinates. Initial and boundary conditions are provided by the Geophysical Fluid Dynamics Laboratory (GFDL) Mars General Circulation Model (GCM), which inherently couples the Mars MM5 to the GCM. The boundary layer parameterization scheme used in the Mars MM5 is that used in the Medium Range Forecast (MRF) [*Hong and Pan,* 1996], which has been modified for Martian surface conditions [*Toigo,* 2001].

Most of the Martian-specific parameterizations used in the Mars MM5 are taken directly from the GFDL Mars GCM. Radiative transfer is modeled using the scheme of *Wilson and Hamilton* [1996], which involves solar absorption by CO_2

and atmospheric dust of two particle sizes. The surface is represented by a MOLA topographic map [*Smith et al.,* 2001]; albedo maps by *Pleskot and Miner* [1981], *Paige et al.* [1994], and *Paige and Keegan* [1994]; and thermal inertia maps from *Palluconi and Kieffer* [1981] and *Vasavada et al.* [2000]. Ground temperatures are calculated using a 12-layer subsurface heat diffusion model that uses initial temperatures from the GCM.

We ran twelve 10-day simulations equally distributed around the Martian year. Twenty-four pressure levels were defined, from near the surface (~50 m height) to the top at ~80 km above the surface. Horizontally, we used a 50 x 50 horizontal point grid with a resolution of 10 km. The grid was centered on Proctor Crater and it extended more than one crater diameter in each direction to avoid potential edge effects. The timestep used in the simulations was 5 seconds, and parameters such as wind velocity and stress were saved once every hour as instantaneous values. In the past, hourly averaged values have been commonly used to provide a representative set of parameters. However, in this case the instantaneous values at the top of each hour were used instead to avoid washing out varying parameters that can be caused by using mean values.

3.2 Model Results

3.2.1 Seasonal Winds. Because the strongest daily winds are those that will move the most sand, it is these winds that will most affect dune morphology. Therefore we first discuss the orientations of the winds with the strongest daily stresses. These maximum winds are shown in Fig. 4.6 as a function of L_s and wind orientation. Daily maximum winds are indicated by black boxes with sizes that correspond to wind stress, which is discussed in more detail in Section 3.2.3. The time of year included in each model run is shown as a blue shaded strip. The three mean wind directions observed in the dunefield and their standard deviations are indicated and labeled in red.

The strongest daily winds shift in direction with the seasons. Fall and winter winds come from the west and west-southwest. Spring and summer winds blow from the east-northeast, but they are weaker than their fall and winter counterparts. The fall and winter winds correspond well with the primary dune slipfaces, and they are most likely responsible for both the dune slipfaces and the

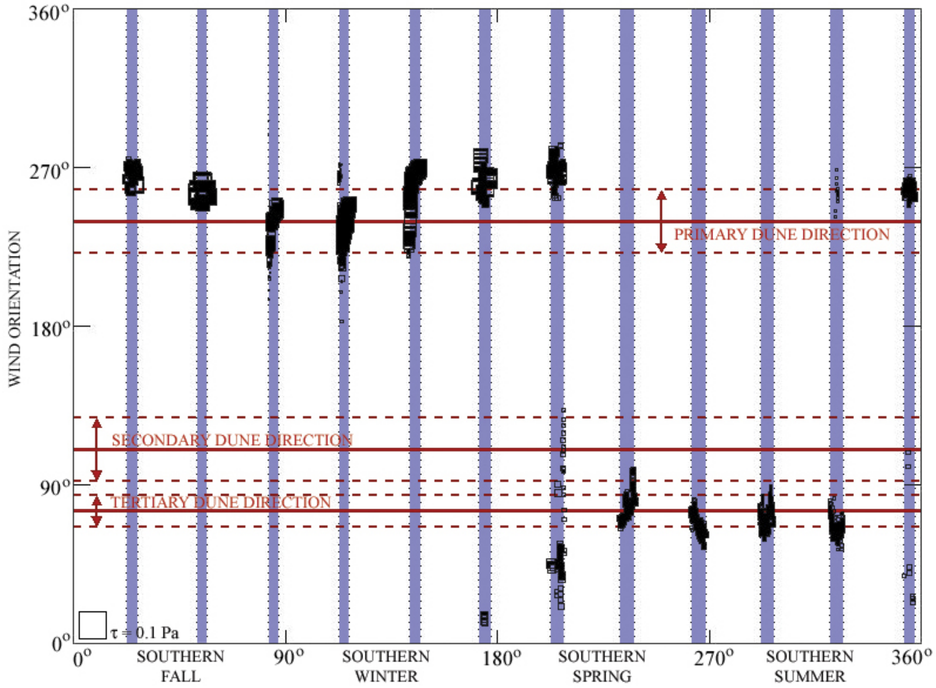

Fig. 4.6. Maximum daily stresses from model grid points located on the dunefield. The symbol size indicates magnitude of stress. Horizontal red lines correspond to the three dune slipface orientations.

orientations of most of the bright duneforms that are common on the Proctor Crater floor. The timing of the strongest winds compares well with the slipface reversal (compare Figs. 4.5 and 4.6). Even the MOC NA frame M0702777 that shows bright material on both slipfaces coincides with the season at which the strongest daily winds switch direction, indicating that this image has caught the dunes during a transition from one wind regime to the other.

Dust devil tracks are also aligned with the primary wind, but they are generally only visible in spring and summertime images, indicating that this fall and winter wind is not responsible for creating the majority of dust devil tracks. The dunes do become covered in CO_2 frost during the winter, which may inhibit sand activity, precluding the winter winds from producing slipfaces. However, MOC NA images show fully frosted dunes only for the time period between L_s = 50º–145º, with partial frost lasting until L_s = 165º. According to the model results in Fig. 4.6, the primary winds blow from L_s = 350º to 200º.Therefore even if the frost cover temporarily stabilizes the dunes, the winds before and after the period of frost cover may account for the observed dune activity.

The winds in general are stronger during the winter, which likely indicates why they produce the most common slipfaces in the dunefield. However, the tertiary winds appear to dominate on the eastern edge of the dunefield, where these slipfaces are larger and the outlines of the barchan dunes appear to emphasize the tertiary winds. Further examination of the physics of saltation may explain why the tertiary winds have more control over the dunes they affect than the primary winds (see Section 3.2.3).

The secondary winds, from the ESE, are absent from Fig. 4.6. They are also absent from the dunes in Fig. 4.4, but this is on the eastern edge of the dunefield where slipfaces oriented with secondary winds are not present. It is not clear why the ESE winds do not appear as the strongest winds at some point of the year, but it may be that they are produced by slightly weaker winds at some point during the day that does not appear in Fig. 4.6. Therefore, before we can state that the model does not predict the secondary winds, we must discuss wind orientation and strength as a function of time over the course of the day.

3.2.2. Daily Winds. To understand changes in winds during the day, we saved hourly winds when running Mars MM5 over Proctor Crater. The strongest daily winds correspond to two of the three observed dune slipface directions, but they do not explain the missing secondary winds that produce another dune slipface direction in the dunefield. They also do not explain the orientation of dust devil tracks during the spring and summer, which seem to be oriented 180º from the strongest winds during that season. Hourly winds during each model run show much more detail than in Fig. 4.6. The origins of the observed winds are discussed below in Section 3.2.4.

Figure 4.7 shows the orientation of winds over the Proctor crater dunefield for each hour in each model run. A total of twenty-five grid points in the model were located over the dunefield, and each point is plotted in Fig. 4.7. As with Fig. 4.6, the three mean and standard deviation slipface directions are marked, and the black boxes indicating modeled winds are scaled by wind stress. Each model run is shown separately and labeled, although all ten days included in each run are shown in a single plot. Spring and summer model runs clearly show tertiary winds during the evening hours, and WSW winds during the daytime. The evening winds are the strongest winds of the day, as shown in Fig. 4.6, but the early afternoon winds correspond well with the dust devil track orientations.

Fall and winter winds that are aligned with primary winds are the strongest of the year, and they blow during the afternoon. Winds from the WSW occur throughout the year, but they become much stronger during the fall and winter. Thus a weak WSW produces dust devil tracks during the spring and summer, and a strong WSW wind creates slipfaces during the fall and winter.

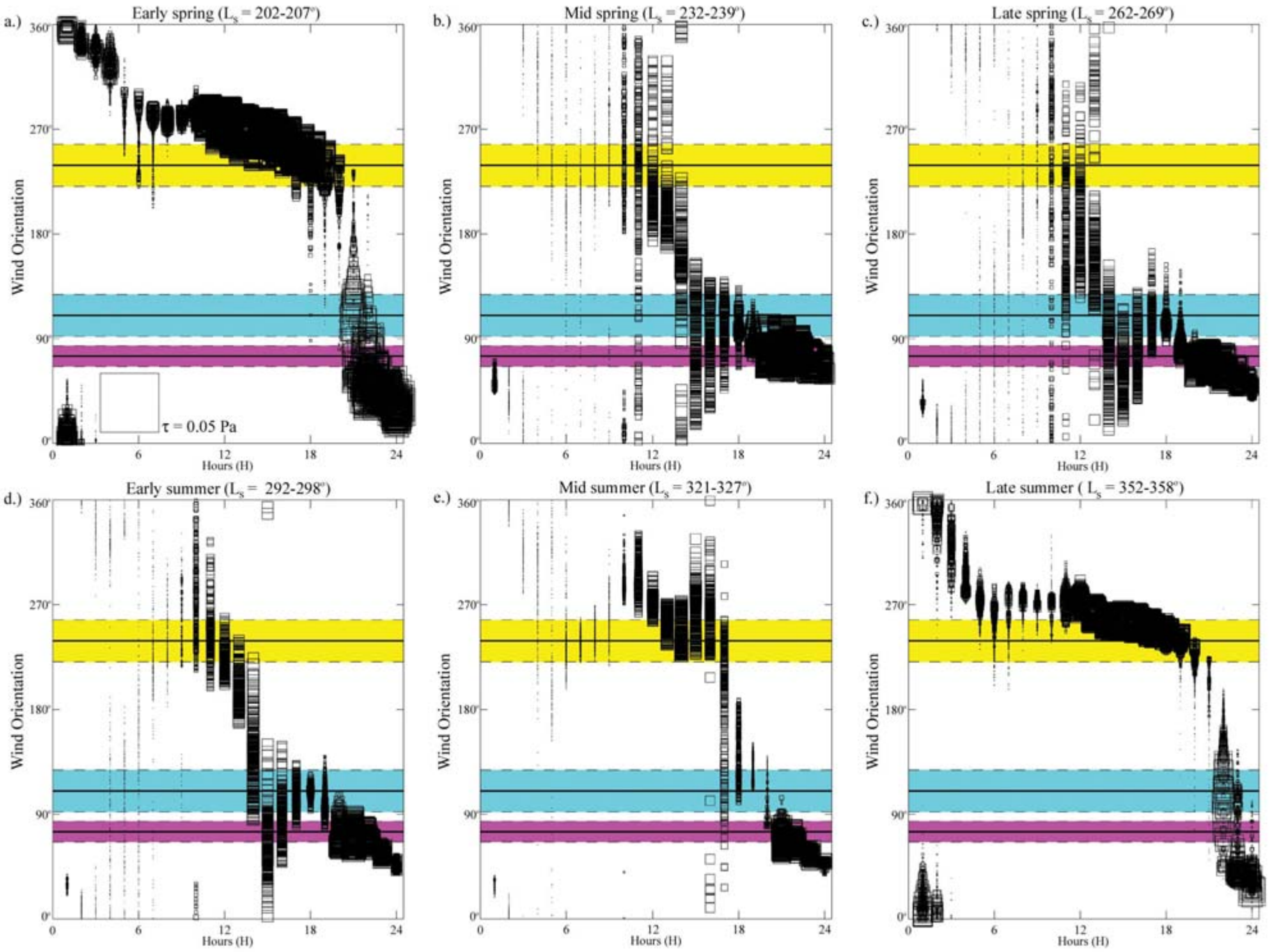
a.)
Early spring (L_s = 202-207°)
b.)
Mid spring (L_s = 232-239°)
c.)
Late spring (L_s = 262-269°)
d.)
Early summer (L_s = 292-298°)
e.)
Mid summer (L_s = 321-327°)
f.)
Late summer (L_s = 352-358°)
Wind Orientation
0°
90°
180°
270°
360°
Hours (H)
0
6
12
18
24
τ = 0.05 Pa

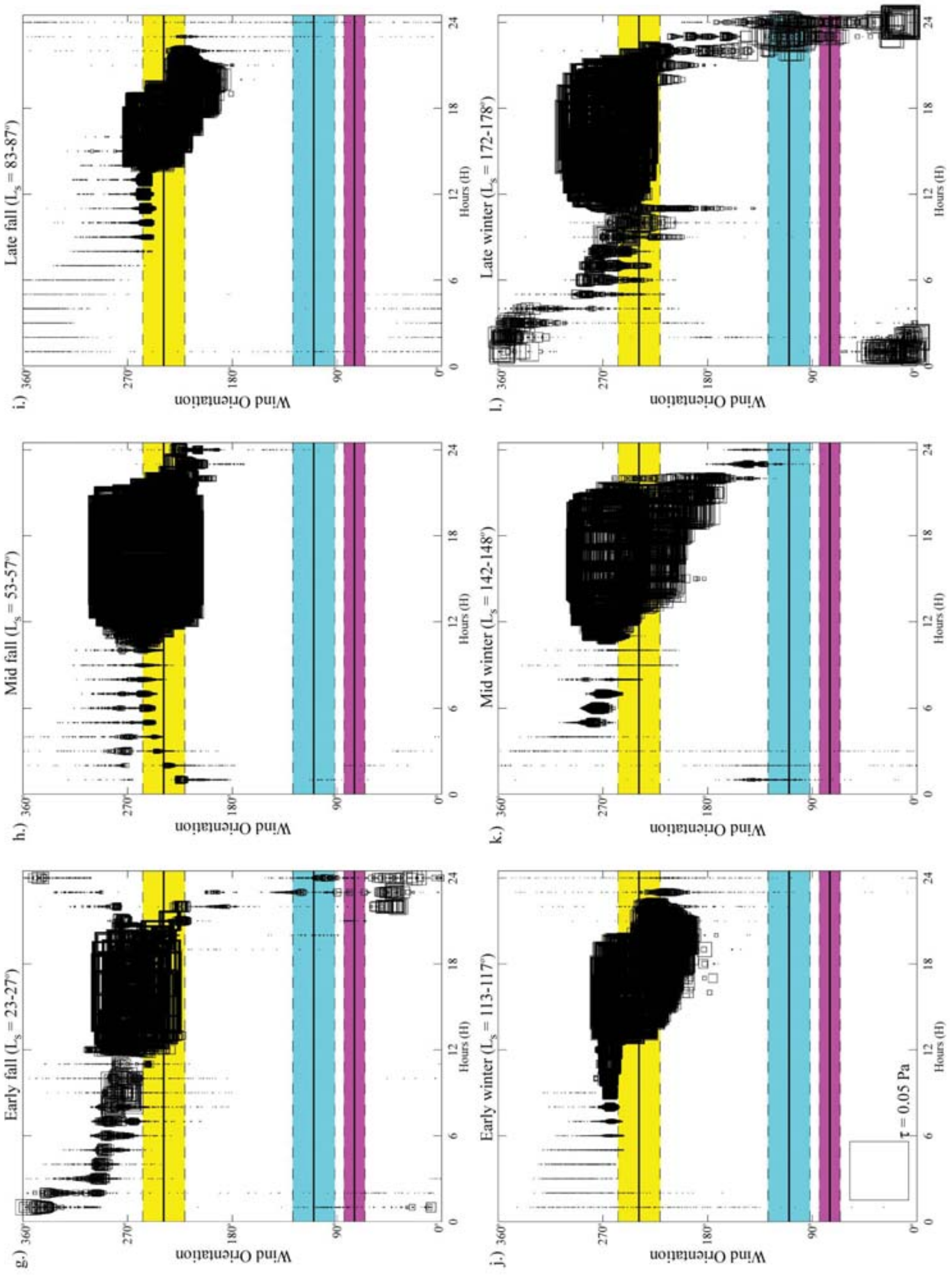

Fig. 4.7. Modeled hourly wind orientations over the dunefield for each model run. Data symbols are scaled by the magnitude of stress.

None of the daily winds indicate any alignment with slipfaces oriented to secondary winds, suggesting that perhaps these winds no longer blow. However, the slipfaces made by ESE winds are crisp and uneroded, implying that they probably not relics of an old wind regime. There are winds that briefly align with these secondary winds during the time of transition between the winter and summer circulation patterns (see Fig. 4.7 at L_s = 352º–358º and 172º–178º) and in the late afternoon during the summer (see Fig. 4.7 at L_s = 232º–239º, 262º–269º, and 292º–298º). But these winds are not strong and do not appear to be part of any persistent and unidirectional wind pattern. It may be that a full year's run would produce a time when the secondary winds dominate, although the model runs here appear to be fairly representative of modeled winds throughout the Martian year.

3.2.3. Wind Stresses. Although the modeled winds may align with observed wind features, only winds above a particular threshold stress value are strong enough to initiate saltation. Some wind features, such as dust devil tracks, do not rely on sand saltation, and in these cases the modeled stress is not a directly relevant parameter. However, saltation initiation is important for explaining features such as dunes, which are morphologically controlled solely by sand saltation. *Iversen and White* [1982] conducted wind tunnel experiments, finding an empirical relation for the saltation threshold under Martian atmospheric conditions. They found that the threshold varied as a function of particle size, particle density, atmospheric temperature, and atmospheric pressure. Because the saltation threshold is sensitive to so many parameters, it is crucial to constrain these values in order to determine whether the mesoscale model truly predicts the saltation of sand within the Proctor Crater dunefield.

In Paper 1, thermal inertia values derived from TES led to an estimated effective sand grain size for the Proctor Crater dunes of 740 ± 170 μm. In addition, the compositional analysis described in Paper 1 indicated that the dunefield is almost exclusively composed of basalt grains, where the basalt is inferred from the identification of pyroxene and plagioclase in TES spectra. In this work we assume the grains have a density typical of terrestrial basalt (3200 kg m^{-3}), although it is possible that the sand could be composed of grains with a lower bulk density (*e.g.,* scoria). Modeled surface air pressures and air temperatures vary with local time and season. In the early afternoon during the southern winter solstice, when the primary winds dominate over all other winds crossing the dunefield, the air temperature is ~155 K and the air pressure is 6 mbar. In the evening hours during the southern summer solstice, when the tertiary winds blow, the air temperature is ~235 K and the air pressure is 6 mbar. It is interesting to note that the daytime winter air pressure is roughly equivalent to the evening summertime air pressure. Figure 4.8a shows the saltation stress threshold for 740 μm diameter basalt grains at an air pressure of 6 mbar as a function of near-surface air temperature based on the relation by *Iversen and White* [1982]. The upper curve indicates the fluid stress threshold, or the stress required by the air alone to lift grains in to saltation. The lower curve indicates the impact stress threshold, or the stress necessary to saltate grains from the impact of already saltating grains. The impact stress threshold may be considered roughly equivalent to ~0.8 that of the fluid stress threshold [*Bagnold,* 1941; *Andersen and Haff,* 1988; *Toigo et al.,* 2002a]. Because movement from such impacts is the mechanism that causes most grains to saltate, the impact stress threshold is considered to be the most representative threshold stress value. Figure 4.8a shows the estimated threshold stress values for typical conditions under which both the primary and tertiary winds blow. In the winter the stress required to lift the dune sand is 1.5 times that required in the summer, indicating that conditions leading to saltation vary with the seasons in Proctor Crater. This difference may explain why the tertiary winds dominate over the primary winds in dune morphology on the eastern edge of the dunefield, as

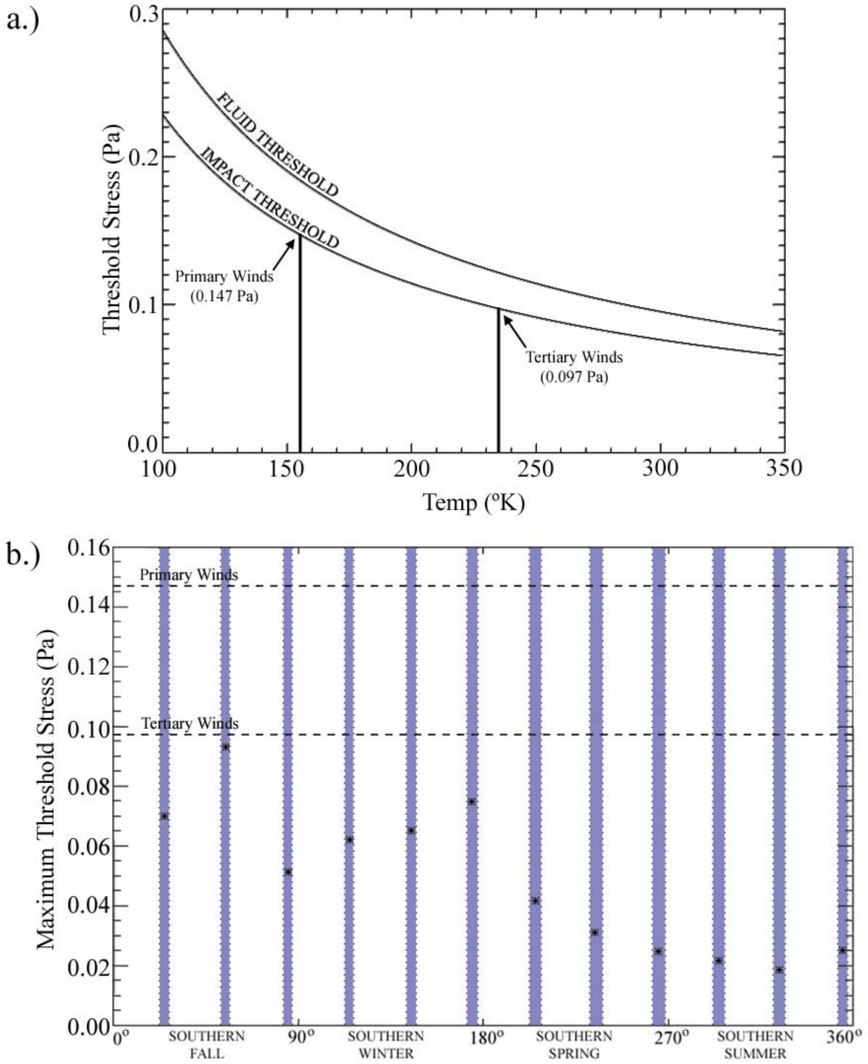

Fig. 4.8. a.) Saltation threshold as a function of air temperature. Note the difference in threshold stress values between the primary and tertiary winds. b.) Maximum predicted stresses over the dunefield in each model run.

discussed in Section 2.1.1. Even though the winter winds are stronger than the summer winds that are aligned with the Tertiary slipfaces (see Fig. 4.7), the lower threshold stress during the summer suggests that these winds may be relatively more effective in moving sand.

Although winds predicted by the Mars MM5 are well aligned with two observed slipface orientations, the calculated wind stresses are not high enough to predict sand saltation. Figure 4.8b shows the maximum calculated wind stresses over the dunefield in each of the twelve model runs. Even though the winter winds are the strongest of the year, they are still not above the lower summertime saltation threshold. There are a number of reasons why the model may not be predicting winds that are strong enough to saltate sand. The first and most obvious reason is that the grid spacing of 10 km by 10 km is too large to capture local wind gusts, with each grid point representing an average predicted wind over a 100 km^2 area. This is a problem that has plagued modelers applying GCM wind predictions to sand saltation [*e.g., Greeley et al,*. 1993; *Anderson et al.,* 1999; *Toigo et al.,* 2002b]. A recent sensitivity study of model resolution in a terrestrial mesoscale model indicates that predicted wind stresses are more accurate at higher resolutions in which the topography is better defined [*Liu and Westphal,* 2001]. Thus model resolution appears to be a significant factor in predicting wind strength, and this may be the case for our model runs as well. A second possibility is that during the model runs, although the timestep was 5 seconds, we only outputted winds from the top of each hour to conserve disk space. It may be that winds above the saltation threshold would have been captured if instead the strongest winds of each hour were considered, because rare wind gusts may produce saltation. We consider the 10 km scale of the model runs in this work to be the source of the problem of weak winds.

3.2.4. Spatial Variation and Origin of Wind Orientations. The primary winds appear to influence dunes, falling dunes, and bright duneforms throughout the interior of Proctor Crater. The tertiary dunes only affect the eastern edge of the dunefield and perhaps the orientations of some of the bright duneforms in the eastern portion of the crater floor. Modeled winds should reflect this pattern if they truly represent actual surface winds.

Figure 4.9 shows two maps of instantaneous winds. The winds are superimposed on a MOLA elevation map, with violets and blues indicating low elevations. The dunefield is visible as a lighter blue mound at 30.2º E, -47.7º S. Figure 4.9a shows afternoon winds during fall, when the primary winds blow (see Fig. 4.7). The arrows represent the velocities of the lowest-level winds, at a height of ~250 m. The winds across the whole area are oriented from the WSW, indicating that the primary winds do in fact influence the entire crater floor. These fall and winter winds are simply midlatitude westerlies created by a geostrophic force that is strengthened by the strong latitudinal temperature gradient present in the winter hemisphere. The slight deflection to the south is caused by the presence of the Hellas basin some 900 km to the east, which warps the approaching winds.

Figure 4.9b shows another wind map, this time from the early evening hours during the spring. Strong winds from the east-northeast dominate the eastern portion of the crater. These are the tertiary winds that control dune morphology on the eastern edge of the dunefield. As the evening progresses, the ENE winds sweep across the crater floor until they are the sole winds blowing in this area, but the fact that they blow for a longer period of time in the eastern part of the crater floor likely explains why they are only visible there. This set of winds is caused by the diurnal tide, in which winds east of the subsolar (noonday) point surge towards this point to fill the vacuum caused by rising air in the summer noontime heat. Furthermore, as the ENE winds cross the eastern rim of Proctor Crater, they encounter relatively warmer air rising from the crater floor ~1500 m below. The air spills beneath this lighter air into the crater in a katabatic flow, accelerating down and across the crater floor. It is these winds that explain why sand has become trapped in Proctor Crater: the primary winds blew sand into the crater from the WSW, but the sand stopped when it encountered the tertiary winds from the ENE that effectively stop dune migration to the east. Sand outside the crater does experience ENE winds at this time of year, but on the

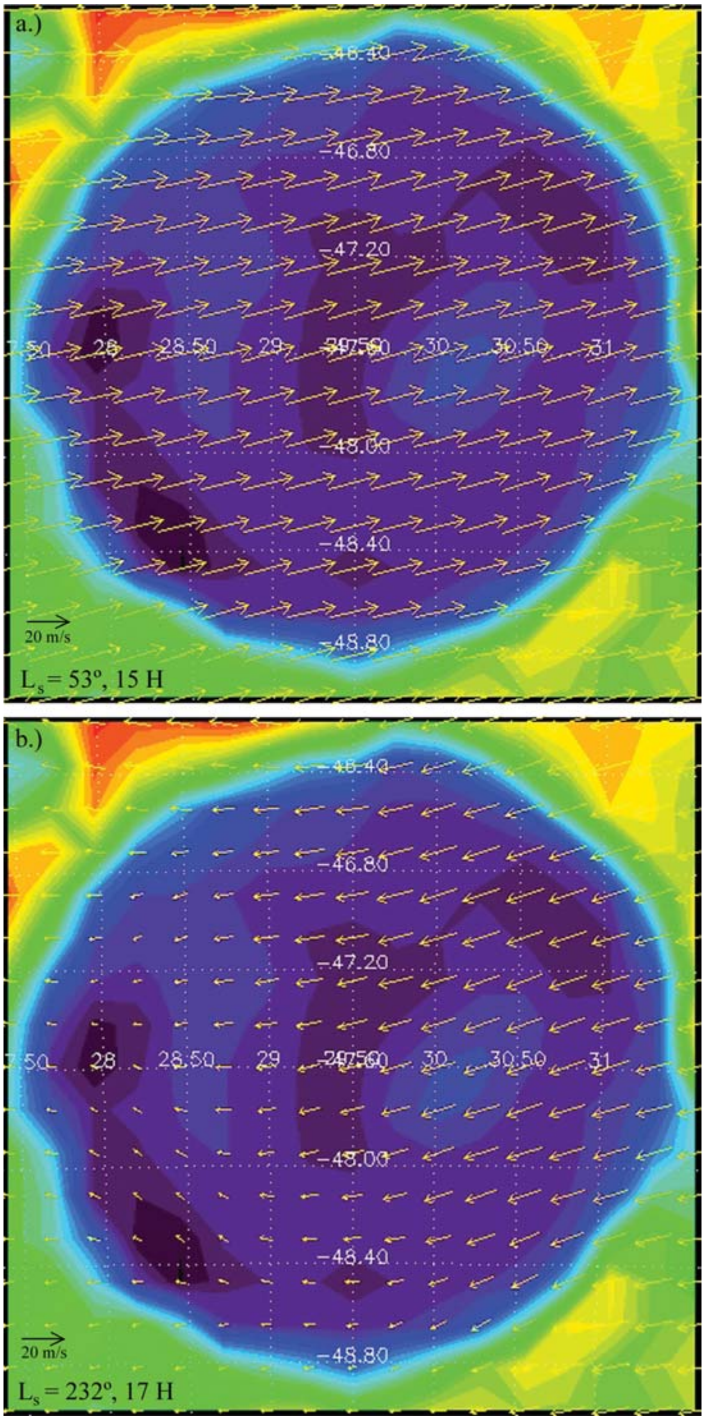

Fig. 4.9. Surface wind vectors illustrating a.) primary winds during the afternoon in the fall and b.) tertiary winds in the evening during spring. The dark dunefield is indicated by a local topographic high at 30.2º E, -47.7º S.

intercrater plains these winds are not enhanced by topography as they are in the floor of Proctor Crater, and so sand did not accumulate on the intercrater plains. Material that was not trapped in craters in Noachis Terra most likely continued to migrate downwind and was likely trapped in the Hellas basin to the east.

Another way to show the spatial distribution of wind orientations across the dunefield is to show rose diagrams for each grid point in the model run. Figure 4.10a shows a rose diagram for each such grid point summed over each of the twelve model runs. The histograms show frequency of wind orientation without regard to wind strength, and thus they emphasize wind persistence. The outer white ring outlines the Proctor Crater rim, and the smaller inner ring defines the edge of the dunefield. Like the histograms of surface feature orientations, these rose diagrams show the downwind direction (for example, an accumulation of winds oriented to the north in these diagrams indicates winds blowing from the south). In most areas of the crater floor, winds from the WSW dominate over all other wind directions throughout the year. In no cases are secondary winds, from the ESE, present in any quantity. In the northwest and southeast edges of the crater floor, a northwesterly wind predominates, but it is not reflected in any observed aeolian feature on the surface. These winds are likely too weak to carry sand or scour material from the surface, but they do occur frequently enough to appear on this figure.

A better way to emphasize the variation in wind variation is to subtract from all grid points the histogram from a single control grid point. Figure 4.10b shows the cumulative winds at each grid point minus the winds at the control point, which we chose from the center of the dunefield (marked in boldface). Thus all of the differenced rose diagrams show winds with respect to those predicted over the center of the dunefield. Note that the scale of the histograms, marked on the left, varies from one plot to the next. Compared to Fig. 4.10a, the variation in wind

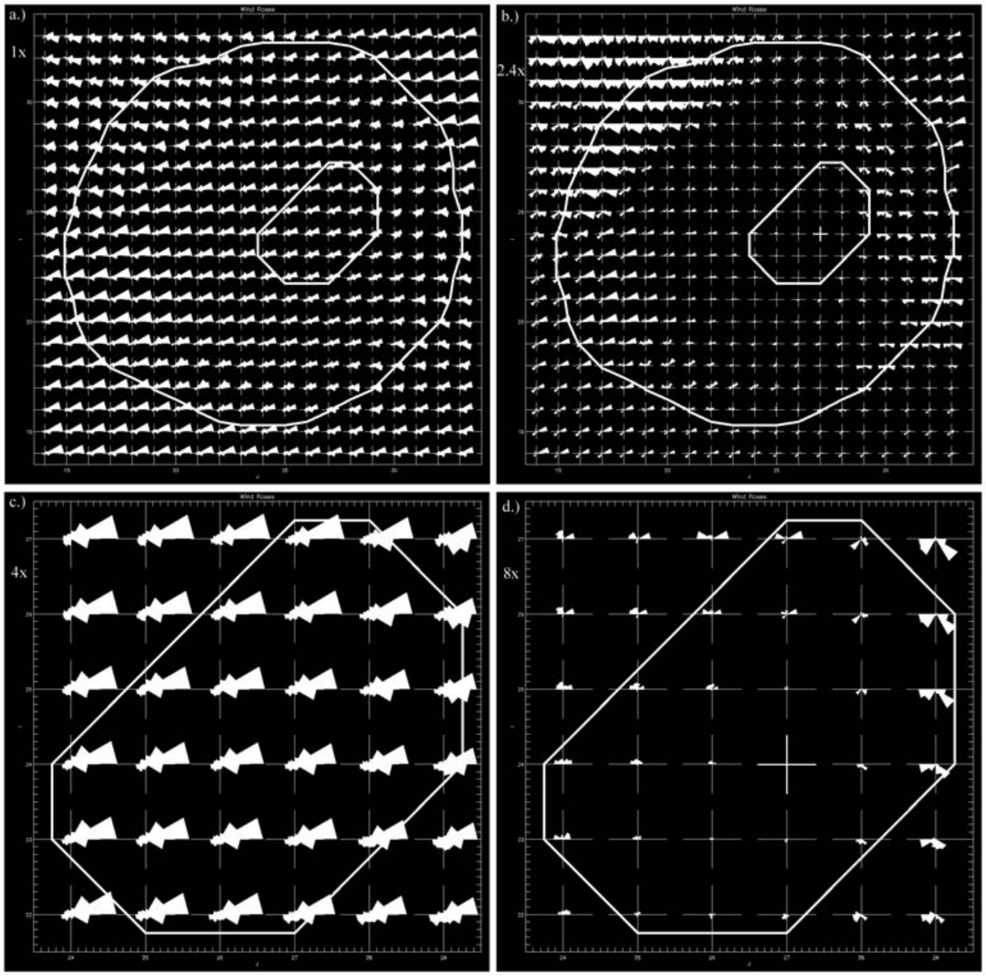

Fig. 4.10. a.) Rose diagram of all wind orientations in all model runs for each grid point across the crater, and b.) the same differenced with a control rose diagram from the center of the dunefield (marked in boldface). The crater rim and dunefield are outlined in white. c.) and d.) show the same as a.) and b.), zoomed in on the dunefield. Note that these diagrams indicate downwind direction.

orientation from point to point in Fig. 4.10b is much more visible. The center of the crater has winds fairly similar to those observed on the dunefield. The northwesterly winds at the northwestern and southeastern edge of the crater are much easier to discern. Tertiary winds from the ENE are clearly more common in the eastern portion of the crater floor, precisely where aeolian features in MOC images indicate that they exist. The primary winds are more persistent at the edge of the crater, in the southeast, than elsewhere, which may indicate that more erosion and sand migration is occurring near the edge of the crater floor than downwind near the dunefield.

Figure 4.10c shows summed rose diagrams for all model runs over the dunefield, with the dunefield outlined in a thick white ring. The dunefield itself shows rose diagrams that appear to vary little from point to point. The primary winds, from the WSW, are clearly the most frequent winds that blow over the dunefield. When the control point is subtracted from the rose diagrams, more detail appears (see Fig. 4.10d). The tertiary winds from the ENE influence the eastern portion of the dunefield, which is consistent with the distribution of the tertiary dune slipfaces. The northwesterly wind that appeared in Fig. 4.10a and 4.10b appears again on the eastern edge of the dunefield, again reflecting frequent but weak winds that cannot saltate sand.

On the northwest edge of the dunes, there are signs of winds that are aligned with the mysterious secondary winds. This is the portion of the dunefield in which the secondary-facing dune slipfaces dominate. The ESE winds in Fig. 4.10d are caused by winds in transition from one dominant direction to another. For example, modeled winds correlate with the secondary winds in the late afternoon during spring and summer as winds shift from the early and mid afternoon WSW winds that produce dust devil tracks to the evening ENE tertiary winds (see Fig. 4.7b–d). In addition, modeled winds aligned with the secondary winds occur in the evening during the seasonal transition from the winter to summer wind regime (see Fig. 4.7a and 4.7l) and again during the transition from the summer to the winter wind regime (see Fig. 4.7f). The winds are not strong in either case, and they do not persist in the direction of the secondary winds for any length of time. Thus although some winds aligned with the secondary winds are predicted by the model, they are not likely responsible for forming the observed slipfaces.

4. Discussion and Conclusion

The Mars MM5 model runs predict and explain the wind patterns behind two of three observed dune slipface orientations as well as dust devil track orientations. However, it does not produce winds matching a third dune slipface orientation of any strength or duration. One possible explanation for the missing secondary winds is that the Mars MM5 model runs covered too small a domain and thus did not account for regional effects that might influence wind directions, such as the deep Hellas basin 900 km to the east. One way to check for such an inconsistency is to compare the Mars MM5 results to those from a GCM.

The primary and tertiary winds, as well as the WSW summer winds that produce dust devil tracks, are visible in GCM wind predictions as well as in Mars MM5 model runs. *Fenton and Richardson* [2001b] made global predictions of surface winds using the GFDL Mars GCM. The average southern fall and winter winds at the location of Proctor Crater (47.5° S, 30° E) are from the WNW to WSW, fairly consistent with the primary winds (see Figs. 1a and 1b of *Fenton and Richardson* [2001b]). Summer evening winds come from the ENE following the diurnal tide, and summer afternoon winds come from the WSW following a deflection of Hadley circulation winds (see Plates 1c and 1d of *Fenton and Richardson* [2001b]). The daytime wind that *Fenton and Richardson* [2001b] found matched bright streaks is responsible for creating dust devil tracks, and the evening wind that they found matched dark streaks is the tertiary wind that also produces one of the dune slipface directions. Modeled winds aligned with the secondary winds are absent from the GFDL Mars GCM runs as well as the Mars MM5 runs described here. Therefore, the Mars MM5 runs are consistent with global model results, and no large-scale effects have been erased by the use of a small domain.

Further possible sources of the secondary winds must be considered. For example, there may be unusual but strong storms that occasionally pass through the area, with wind gusts that carry large quantities of sand. Such storms may be infrequent enough that they are not predicted by GCM's, but of enough strength that the secondary slipfaces are maintained.

If the secondary winds are instead produced by a common annually-reproduced wind pattern, then a method must be found for discovering why they are not represented in this work. A number of craters in Noachis Terra contain dunefields, each of which has slipfaces indicating the strongest surface winds that influence the area. If these secondary winds persist throughout the region, perhaps to different degrees in different dunefields, then an understanding of the regional distribution of winds can be gained. A potential way to resolve the issue of the missing wind is to model winds over nearby craters to determine if these secondary winds are predicted elsewhere, and how well those predictions match the dune morphology.

Regardless of the missing secondary wind, the Mars MM5 successfully predicts all other wind orientations indicated by aeolian features on the surface. The primary winds are fall and winter afternoon westerlies that dominate the crater floor. The tertiary winds are spring and summer evening easterly katabatic flows that are concentrated in the eastern portion of the crater floor, consistent with observed dune slipfaces. These tertiary winds also explain the trapping of sand in crater floors, for they oppose the primary winds that move sand through the area. The tertiary winds are present throughout the region but they are only strong enough on the crater floors to counter the strong primary winds. Dust devil tracks are produced by weak early afternoon westerly spring and summer winds produced by planetary rotation. The Mars MM5 results explain the source of the winds that produce aeolian features, making it a useful tool for understanding and predicting aeolian processes on the Martian surface.

5. Acknowledgements

We would like to thank Arden Albee for a helpful review of the manuscript, and Shawn Ewald for keeping the model chugging along.

Chapter 5

FUTURE WORK

There is more work is planned for these projects. Some of the proposed future work fell out of the questions and problems that arise while first attempting to solve a problem. Some of it was originally intended to be encompassed in the thesis work, but work at an earlier stage grew to dominate the project as a result of the sheer volume of data available.

Many questions were left unanswered in the work described in Chapter 4. It is not clear why the MM5 does not predict the secondary winds that clearly must exist in the current wind regime. These winds do not appear in GFDL GCM model runs, and they may not exist in any current atmospheric model. It is possible that they are produced by rare storms (*i.e.,* storms that occur once a decade or century), and I would like to look into the possibility of observing or predicting these storms.

The MM5 also does not predict winds strong enough to lift basaltic grains into saltation. This may simply be a problem of model resolution, and it is not a difficult prospect to run the model at a higher resolution and/or to output the strongest hourly winds at each grid point rather than the winds at the top of each hour. There is also the problem that the MM5 is meant to hold subgrids that are no more than three times smaller than their parent grids – and yet our model runs at a scale of 10 km were more than an order of magnitude higher resolution than the parent grid. It is unlikely that this large resolution step caused serious error in model output. However, for the sake of thoroughness, it would be wise to nest grids with proper resolution steps in order to be certain that winds are modeled correctly.

One planned extension of Chapters 3 and 4 involves looking beyond just Proctor Crater to the surrounding region. This part of the research was funded by the MDAP, so it must be completed in any case. The study of Proctor Crater alone proved to be so interesting and fruitful that I never had a chance to look far beyond Proctor Crater, although I did spend a good amount of time preparing topographic maps and processing images for this task. A quick glance at these images reveals that the dunes in nearby craters (Kaiser, Rabe, etc.) are of similar size, composition, and complexity as those in Proctor Crater. The orientations of these dune slipfaces are similar to those of Proctor Crater, although the relative strengths of these winds (*i.e.,* their prevalence in the dunefield) vary from crater to crater. A regional study will reveal spatial trends in dune morphology, wind circulation patterns, sand sediment volumes, and possibly sand source locations. This work will benefit from the detailed study of Proctor Crater, which may be regarded as a single precise and well-defined reference for the many points of interest in a regional study.

Finally, mesoscale models are rarely put to use for the study of terrestrial dunefields. Even the models focusing on dust lifting are done so ultimately to better constrain the radiative effects of atmospheric dust, not for estimates of surface erosion or deposition. I would like to apply the terrestrial MM5 to the area over a few well-studied dunefields to determine how realistic the modeled stress and wind orientations are. First it should be applied over a simple barchan field, where deviations from the expected results may be more easily understood. Then it may be applied over a dunefield with atmospheric conditions similar to the convergent wind regime of the Proctor Crater dunes. A prime and well-studied example is the Kelso Dunefield in California, which are reversing transverse dunes like those of Proctor Crater, and situated in a valley that experiences two or three opposing winds. Projects such as these will clear up a number of gaps in our understanding of how atmospheric models translate to another planet, and how our interpretations vary from one case to another.

BIBLIOGRAPHY

Anderson, F. S., R. Greeley, P. Xu, E. Lo, D. G. Blumberg, R. M. Haberle, and J. R. Murphy, Assessing the Martian surface distribution of aeolian sand using a Mars general circulation model, *J. Geophys. Res., 104,* 18,991-19,002, 1999.

Anderson, R. S. and P. K. Haff, Simulation of eolian saltation, *Science, 241,* 820-823, 1988.

Arvidson, R. E., Wind-blown streaks, splotches, and associated craters on Mars: Statistical analysis of Mariner 9 photographs, *Icarus, 21,* 12-27, 1974.

Bagnold, R. A., The Physics of Blown Sand and Desert Dunes,Methuen, New York, 1941.

Bandfield, J. L., Global mineral distributions on Mars, *J. Geophys. Res., 107,* 10.1029/2001JE001510, 2002.

Bandfield, J. L., K. S. Edgett, and P. R. Christensen, Spectroscopic study of the Moses Lake dune field, WA: Determination of compositional distributions and source lithologies, Submitted to *J. Geophys. Res.,* 2002.

Bandfield, J. L., V. E. Hamilton, and P. R. Christensen, A global view of Martian surface compositions from MGS-TES, *Science, 287,* 1626–1630, 2000.

Bandfield, J. L. and M. D. Smith, Multiple emission angle surface-atmosphere separations of Thermal Emission Spectrometer data, *Icarus,* In press, 2002.

Bell, J. F. III, P. C. Thomas, M. J. Wolff, S. W. Lee, and P. B. James, Mineralogy of the Martian north polar sand sea from 1995 Hubble Space Telescope near-IR observations, In *Lunar and Planet. Sci. XXVIII,* 87–88, 1996.

Blount, G., M. O. Smith, J. B. Adams, R. Greeley, and P. R. Christensen, Regional aeolian dynamics and sand mixing in the Gran Desierto: Evidence from Landsat Thematic Mapper images, *J. Geophys. Res., 95,* 15,463–15,482, 1990.

Breed, C. S., Terrestrial analogs of the Hellespontus Dunes, Mars, *Icarus, 30,* 326-340, 1977.

Breed, C. S., M. J. Grolier, and J. F. McCauley, Morphology and distribution of common 'sand' dunes on Mars: Comparison with the Earth, *J. Geophys. Res., 84,* 8183-8204, 1979.

Breed, C. S. and T. Grow, Morphology and distribution of dunes in sand seas observed by remote sensing, *USGS Prof. Pap., 1052,* 253-304, 1979.

Bridges, N. T., R. Greeley, A. F. C. Haldemann, K. E. Herkenhoff, M. Kraft, T. J. Parker, and A. W. Ward, Ventifacts at the Pathfinder landing site, *J. Geophys. Res., 104,* 8595-8615, 1999.

Bridges, N. T., K. E. Herkenhoff, T. N. Titus, and H. H. Kieffer, Ephemeral dark spots associated with Martian gullies, In *Lunar and Planet. Sci. XXXII,* Abst #2126, LPI, Houston (CD-ROM), 2001.

Calkin, P. E. and R. H. Rutford, The sand dunes of Victoria Valley, Antarctica, *Geograph. Rev., 64,* 189-216, 1974.

Chicarro, A. F., P. H. Schultz, and P. Masson, Global and regional ridge patterns on Mars, *Icarus, 63,* 153-174, 1985.

Christensen, P. R. Eolian intracrater deposits on Mars: Physical properties and Global distribution, *Icarus, 56,* 496-518, 1983.

Christensen, P. R., J. L. Bandfield, M. D. Smith, V. E. Hamilton, and R. N. Clark, Identification of a basaltic component on the Martian surface from Thermal Emission Spectrometer data, *J. Geophys. Res., 105,* 9609–9621, 2000a.

Christensen, P. R., J. L. Bandfield, V. E. Hamilton, D. A. Howard, M. D. Lane, J. L., Piatek, S. W. Ruff, and W. L. Stefanov, A thermal emission spectral library of rock-forming minerals, *J. Geophys. Res., 105*, 9735–9739, 2000b.

Christensen P.R., J. L. Bandfield, R. N. Clark, K. S. Edgett, V. E. Hamilton, T. Hoefen, H. H. Kieffer, R. O. Kuzmin, M. D. Lane, M. C. Malin, R. V. Morris, J. C. Pearl, R. Pearson, T. L. Roush, S. W. Ruff, M. D. Smith, Detection of crystalline hematite mineralization on Mars by the Thermal Emission Spectrometer: Evidence for near-surface water, *J. Geophys. Res., 105,* 9623-9642, 2000c.

Clancy, R. T. and S. W. Lee, A new look at dust and clouds in the Mars atmosphere - Analysis of emission-phase-function sequences from global Viking IRTM observations, *Icarus, 92,* 135-158, 1991.

Clark, R. N., T Hoefen, and J. Moore, Martian olivine global distribution and stratification using spectral feature mapping of Mars Global Surveyor Thermal Emission Spectrometer data, DPS Abst. Birmingham meeting Oct 6-11, 2002. #3.06.

Cutts, J. A. and R. S. U. Smith, Aeolian deposits and dunes on Mars, *J. Geophys. Res., 78,* 4139-4154, 1973.

Edgett, K. S. and P. R. Christensen, The Particle size of Martian aeolian dunes, *J. Geophys. Res., 96,* 22,765-22,776, 1991.

Edgett, K. S. and P. R. Christensen, Mars aeolian sand: Regional variations among dark-hued crater floor features, *J. Geophys. Res., 99,* 1997-2018, 1994.

Edgett, K. S. and N. Lancaster, Volcaniclastic aeolian dunes: terrestrial examples and application to martian sands, *J. Arid Environ., 25,* 271-297, 1993.

Edgett, K. S. and M. C. Malin, New views of Mars eolian activity, materials, and surface properties: Three vignettes from the Mars Global Surveyor Mars Orbiter Camera, *J. Geophys. Res., 105,* 1623-1650, 2000.

Eluszkiewicz, J. On the microphysical state of the Martian seasonal caps, *Icarus, 103,* 43-48, 1993.

Farr, T. G. and M. Kobrick, Shuttle Radar Topography Mission produces a wealth of data, *Eos Trans., 81,* 583-585, 2000.

Fenton, L. K. Aeolian Processes in Proctor Crater on Mars: Sedimentary history as analyzed from multiple data sets, submitted to *J. Geophys. Res.,* 2003.

Fenton, L. K. and M. I. Richardson, In *Lunar and Planetary Science XXXII*, Abstract #1995, Lunar and Planetary Institute, Houston (CD-ROM), 2001a.

Fenton, L. K. and M. I. Richardson, Martian surface winds: Insensitivity to orbital changes and implications for aeolian processes, Submitted to *J. Geophys. Res.*, 2001b.

Flynn, G. J. and D. S. McKay, An assessment of the meteoric contribution to the Martian soil, *J. Geophys. Res., 95,* 14,497-14,509, 1990.

Garvin, J. B., J. J. Frawley, S. E. H. Sakimoto, and C. Schnetzler, Global geometric properties of Martian impact craters: An assessment from Mars Orbiter Laser Altimeter (MOLA) digital elevation models, in *Lunar and Planetary Science XXXI,* Abstract #1619, Lunar and Planetary Institute, Houston (CD-ROM), 2000.

Garvin, J. B., S. E. H. Sakimoto, J. J. Frawley, and C. Schnetzler, Gobal geometric properties of Martian impact craters, in *Lunar and Planetary Science XXXIII,* Abstract #1255, Lunar and Planetary Institute, Houston (CD-ROM), 2002.

Gault, D. E., E. M. Shoemaker, and H. J. Moore, Spray ejected from the lunar surface by meteoroid impact, NASA TN D-1767, 39 pp., 1963.

Golombek, M. P., J. B. Plescia, and B. J. Franklin, Faulting and folding in the formation of planetary wrinkle ridges, *Proc. Lunar Planet. Sci. Conf. 21st,* 679-693, 1991.

Golombek, M. P., F. S. Anderson, and M. T. Zuber, Martian wrinkle ridge topography: Evidence for subsurface faults from MOLA, *J. Geophys. Res., 106,* 23,811-23,822, 2001.

Gooding, J. L. Petrology of dune sand derived from basalt on the Ka'u Desert, Hawaii, *J. Geology, 90,* 97-108, 1982.

Grant, J. A. and P. H. Shultz, Possible tornado-like tracks on Mars, *Science, 237,* 883-885, 1987.

Greeley, R. Silt-clay aggregates on Mars, *J. Geophys. Res., 84,* 6248-6254, 1979.

Greeley, R. and J. D. Iversen, *Wind as a geological process on Earth, Mars, Venus and Titan,* Cambridge Univ. Press, Oxford, U.K., 1985.

Greeley, R. and M. D. Kraft, Survivability of aggregate sands on Mars, in *Lunar and Planetary Science XXXII,* Abstract #1839, Lunar and Planetary Institute, Houston (CD-ROM), 2001.

Greeley, R., M. D. Kraft, R. O. Kuzmin, and N. T. Bridges, Mars Pathfinder landing site: Evidence for a change in wind regime from lander and orbiter data, *J. Geophys. Res. 105,* 1829-1840, 2000.

Greeley, R., M. Kraft, R. Sullivan, G. Wilson, N. Bridges, K. Herkenhoff, R. O. Kuzmin, M. Malin, and W. Ward, Aeolian features and processes at the Mars Pathfinder site, *J. Geophys. Res., 104,* 8573-8584, 1999.

Greeley, R., N. Lancaster, S. Lee, and P. Thomas, Martian aeolian processes, sediments, and features, in *Mars*, edited by H. H. Kieffer et al., pp. 730-766, Univ. of Ariz. Press, Tucson, 1992.

Greeley, R., R. Leach, B. White, J. Iversen, and J. Pollack, Threshold windspeeds for sand on Mars: Wind tunnel simulations, *Geophys. Res. Lett, 7,* 121-124, 1980.

Greeley, R., S. C. R. Rafkin, R. M. Haberle, R. O. Kuzmin, Topography and aeolian features: Dunes and streaks compared with global and meso scale wind predictions, In *Lunar and Planet. Sci. XXXII,* Abstract #2003, LPI, Houston (CD-ROM), 2001.

Greeley, R., A. Skypeck, and J. B. Pollack, Martian aeolian features and deposits: Comparisons with general circulation model results, *J. Geophys. Res., 98,* p. 3183-3196, 1993.

Haberle, R. M. and B. M. Jakosky, Atmospheric effect on the remote determination of thermal inertia on Mars, *Icarus, 90,* 187-204, 1991.

Haberle, R. M., C. B. Leovy, and J. B. Pollack, Some effects of global dust storms on the atmospheric circulation of Mars, *Icarus, 50,* 322-367, 1982.

Hale, W. and R. A. F. Grieve, Volumetric analysis of complex lunar craters: Implications for basin ring formation, *J. Geophys. Res, 87*, A65-A76, 1982.

Hartmann, W. K., J. Anguita, M. A. de la Casa, D. C. Berman, and E. V. Ryan, Martian cratering 7: The role of impact gardening, *Icarus, 149,* 37-53, 2001.

Herkenhoff, K. E. and A. R. Vasavada, Dark material in the polar layered deposits and dunes on Mars, *J. Geophys. Res., 104,* 16,487-16,500, 1999.

Hess, S. L., R. M. Henry, C. B. Leovy, J. A. Ryan, and J. E. Tillman, Meteorological results from the surface of Mars: Viking 1 and 2, *J. Geophys. Res., 82,* 4559-4574, 1977.

Holton, J. F., *An Introduction to Dynamic Meteorology,* 511 pp., Academic, Sand Diego, Calif., 1992.

Hong, S.-Y. and H.-L. Pan, Nonlocal boundary layer vertical diffusion in a medium-range forecast model, *Mon. Wea. Rev., 124,* 2322-2339, 1996.

Howard, A. D., The role of eolian processes in forming surface features of the martian polar layered deposits, *Icarus, 144,* p. 267-288, 2000.

Hunter, R. E., B. M. Richmond, and T. R. Alpha, Storm-controlled oblique dunes of the Oregon coast, *Geol. Soc. Am. Bull., 94,* 1450-1465, 1983.

Iversen, J. D., R. Greeley, J. B. Pollack, and B. R. White, Simulation of Martian aeolian phenomena in the atmospheric wind tunnel, *Proc. 7th Conf. Space Simulation,* NASA SP-336, 191-213, 1973.

Iversen, J. D., J. B. Pollack, R. Greeley, and B. R. White, Saltation threshold on Mars: the effect of interparticle force, surface roughness, and low atmospheric density, *Icarus, 29,* 318-393, 1976.

Iversen, J. D. and B. R. White, Saltation threshold on Earth, Mars and Venus, *Sediment., 29,* 111-119, 1982.

Jakosky, B. M., Mellon, M. T., H. H. Kieffer, P. R. Christensen, E. S. Varnes, and S. W. Lee, The thermal inertia of Mars from the Mars Global Surveyor Thermal Emission Spectrometer, *J. Geophys. Res., 105,* 9643-9652, 2000.

James, P. B., H. H. Kieffer, and D. A. Paige, The seasonal cycle of carbon dioxide on Mars, In *Mars*, pp. 934-968, Univ. of Ariz. Press, Tucson, AZ, 1992.

Joshi, M. M., S.R. Lewis, S.R., P.L. Read, and D.C. Catling, Western boundary currents in the Martian atmosphere: Numerical simulations and observational evidence, *J. Geophys. Res., 100,* 5485-5500, 1995.

Joshi, M. M., R. M. Haberle, J. R. Barnes, J. R. Murphy, and J. Schaeffer, Low--level jets in the NASA Ames Mars general circulation model, *J. Geophys. Res., 102,* 6511-6523, 1997.

Kieffer, H. H., S. C. Chase, Jr., E. Miner, G. Münch, and G. Neugebauer, Preliminary report on infrared radiometer measurements from the Mariner 9 spacecraft, *J. Geophys. Res., 78,* 4291-4312, 1973.

Kieffer, H. H., T. Z. Martin, A. R. Peterfreund, B. M. Jakosky, E. D. Miner, and F. D. Palluconi, Thermal and albedo mapping of Mars during the Viking primary mission, *J. Geophys. Res., 82,* 4249-4291, 1977.

Kocurek, G., K. G Havholm, M. Deynoux, and R. C Blakey, Amalgamated accumulations resulting from climatic and eustatic changes, Akchar Erg, Maritania, *Sedimentology, 38,* 751-772, 1991.

Koster, E. A. and Dijkmans, J. W. A. Niveo-aeolian deposits and denivation forms, with special reference to the Great Kobuk Sand Dunes, northwestern Alaska, *Earth Surf. Proc. Landf., 13,* 153-170, 1988.

Kuenen, P. H., Experimental abrasion 4: Eolian action, *Geology, 68,* 427-449, 1960a.

Kuenen, P. H., Sand, *Scientific American, 202,* 94-110, 1960b.

Kuzmin, R. O., R. Greeley, S. C. R. Rafkin, and R. Haberle, Wind-related modification of some small impact craters on Mars, *Icarus, 153,* 61-70, 2001.

Lanagan, P. D., A. S. McEwen, L. P. Keszthelyi, and T. Thordarson, Rootless cones on Mars indicating the presence of shallow equatorial ground ice in recent times, *Geophys. Res. Lett., 28,* 2365-2367, 2001.

Lancaster, N. Variations in wind velocity and sand transport rates on the windward flanks of desert sand dunes, *Sedimentology, 32,* 581-593, 1985.

Lancaster, N. Controls of eolian dune size and spacing, *Geology, 16,* 972-975, 1988.

Lancaster, N. *The Namib Sand Sea, Rotterdam: Balkema,* 1989.

Lancaster, N. Development of Kelso Dunes, Mojave Desert, California, *Res. and Explor., 9,* 444-459, 1993.

Lancaster, N. *Geomorphology of Desert Dunes,* New York: Routledge, 1995.

Lancaster, N. and R. Greeley, Mars: Morphology of southern hemisphere intracrater dunefields, *NASA Tech. Mem. 89810,* 264-265, 1987.

Lancaster, N. and R. Greeley, Sediment volume in the north polar sand seas of Mars, *J. Geophys. Res., 95,* 10921-10927, 1990.

Lee, P. and P. C. Thomas, Longitudinal dunes on Mars: Relation to current with regimes, *J. Geophys. Res., 100,* 5381-5395, 1995.

Lindsay, J. F. *Lunar Stratigraphy and Sedimentology.* Elsevier, Amsterdam, 302 pp., 1976.

Liu, J., M. I. Richardson, and J. Wilson, *Submitted to J. Geophys. Res.,* 2002.

Liu, M. and D. L. Westphal, A study of the sensitivity of simulated mineral dust production to model resolution, *J. Geophys. Res., 106,* 18,099-18,122, 2001.

Magalhães, J. A., The Martian Hadley circulation: Comparison of "viscous" model predictions to observations, *Icarus, 70,* 442-468, 1987.

Magalhães, J. A., and R. E. Young, Downslope windstorms in the lee of ridges on Mars, *Icarus, 113,* 277-294, 1995.

Mainguet, M and L. Cossus, Sand circulation in the Sahara: Geomorphological relations between the Sahara Desert and its margins, *Paleoecology of Africa and of the surrounding Islands and Antarctica, 12*, 69-78, 1980.

Malin, M. C. and K. S. Edgett, Sedimentary rocks of early Mars, *Science, 290,* 1927-1937, 2000a.

Malin, M. C. and K. S. Edgett, Frosting and defrosting of Martian polar dunes, In *Lunar and Planet. Sci. XXXI,* Abst #1056, LPI, Houston (CD-ROM), 2000b.

Malin, M. C. and K. S. Edgett, Mars Global Surveyor Mars Orbiter Camera: Interplanetary cruise through primary mission, *J. Geophys. Res., 106,* 23,429-23,570, 2001.

Mangold, N., P. Allemand, and P. G. Thomas, Wrinkle ridges of Mars: Structural analysis and evidence for shallow deformation controlled by ice-rich décollements, *Planet. Space Sci., 46,* 345-356, 1998.

McCauley, J. F., M. H. Carr, J. A. Cutts, W. K. Hartmann, H. Masursky, D. J. Milton, R. P. Sharp, and D. E. Wilhelms, Preliminary Mariner 9 report on the geology of Mars, *Icarus, 17,* 289-327, 1972.

Mellon, M. T., B. M. Jakosky, H. H. Kieffer, and P. R. Christensen, High resolution thermal inertia mapping from the Mars Global Surveyor Thermal Emission Spectrometer, *Icarus, 148,* 437-455, 2000.

Metzger, S. M., J. R. Carr, J. R. Johnson, M. Lemmon, and T. J. Parker, Sediment flux from dust devils on Mars – Initial calculations, In *Lunar and Planet. Sci. XXX,* Abst #2022, LPI, Houston (CD-ROM), 1999.

Molnar, P., and K. A. Emanuel, Temperature profiles in radiative-convective equilibrium above surfaces at different heights, *J. Geophys. Res., 104,* 24,265-24,271, 1999.

Murray, B., M. Koutnik, S. Byrne, L. Soderblom, K. Herkenhoff, and K. L. Tanaka, Preliminary geological assessment of the northern edge of Ultimi Lobe, Mars south polar layered deposits, *Icarus, 154,* 80-97, 2001.

Noe Dobrea, E. Z. and J. F. Bell III, Composition and mineralogy of the Martian north polar dune deposits: Constraints from TES and HST observations, In *Lunar and Planet. Sci. XXXII,* Abstract #2099, LPI, Houston (CD-ROM), 2001.

Paige, D. A., J. E. Bachman, and K. D. Keegan, Thermal and albedo mapping of the polar regions of Mars using Viking thermal mapper observations. 1. North polar region, *J. Geophys. Res., 99,* 25,959-25,991,1994.

Paige, D. A., and K. D. Keegan, Thermal and albedo mapping of the polar regions of Mars using Viking thermal mapper observations. 2. South polar region, *J. Geophys. Res., 99,* 25,993-26,013, 1994.

Palluconi, F. D. and H. H. Kieffer, Thermal inertia mapping of Mars for 60° S to 60° N, *Icarus, 45,* 415-426, 1981.

Pelkey, S. M., B. M. Jakosky, and M. T. Mellon, Thermal inertia of crater-related wind streaks on Mars, *J. Geophys. Res., 106,* 23,909-23,920, 2001.

Peterson, J. E., Geologic Map of the Noachis Quadrangle of Mars, U.S. Geol. Surv. Misc. Geol. Inv. Map I-910, 1977.

Pike, R. J. and P. D. Spudis, Basin-ring spacing on the Moon, Mercury, and Mars, *Earth, Moon and Planets, 39* 129-194, 1987.

Piqueux, S., S. Byrne, and M. I. Richardon, The sublimation of Mars' southern seasonal CO_2 ice cap and the formation of "spiders," submitted to *J. Geophys. Res.,* 2002.

Plescia, J. B. and M. P. Golombek, Origin of planetary wrinkle ridges based on the study of terrestrial analogs, *Geol. Soc. Am. Bull., 97,* 1289-1299, 1986.

Pleskot, L. K., and E. D. Miner, Time variability of Martian bolometric albedo, *Icarus, 45,* 179-201, 1981.

Pollock, J. B., D. S. Colburn, F. M. Flasar, R. Kahn, C. E. Carlston, and D. Pidek, Properties and effects of dust particles suspended in the Martian atmosphere, *J. Geophys. Res., 84,* 2929-2945, 1979.

Porter, M. L., Sedimentary record of erg migration, *Geology, 14,* 497-500, 1986.

Presley, M. A. and P. R. Christensen, Thermal conductivity measurements of particulate materials. 2. Results, *J. Geophys. Res., 102,* 6551-6566, 1997a.

Presley, M. A. and P. R. Christensen, The effect of bulk density and particle size sorting on the thermal conductivity of particulate materials under Martian atmospheric pressures, *J. Geophys. Res., 102,* 9221-9229, 1997b.

Ramsey, M. S., P. R. Christensen, N. Lancaster, and D. A. Howard, Identification of sand sources and transport pathways at the Kelso Dunes, California, using thermal infrared remote sensing, *GSA Bull., 111,* 646–662, 1999.

Richardson, M. I., A general circulation model study of the Mars water cycle, Ph.D. thesis, 220 pp., Univ. of Calif. At Los Angeles, May 1999.

Rogers, D., J. L. Bandfield, P. R. Christensen, Identification of small isolated basalt regions in the northern hemisphere of Mars, DPS Abst Pasadena meeting Oct 23-27, 2000. #59.04.

Rogers, J. J. W., W. C. Krueger, and M. Krog, Sizes of naturally abraded materials, in *J. Sediment. Petrol., 33,* 628-632, 1963.

Rubin, D. M. and R. E. Hunter, Bedform climbing in theory and nature, *Sedimentology, 29,* 121-138, 1982.

Ruff, S. Christensen PR, Clark RN, Kieffer HH, Malin MC, Bandfield JL, Jakosky BM, Lane MD, Mellon MT, Presley MA, Mars' "White Rock" feature lacks evidence of an aqueous origin: Results from Mars Global Surveyor, *J. Geophys. Res., 106,* 23,921-23,927, 2001.

Sagan, C., J. Veverka, P. Fox, L. Quam, R. Tucker, J. B. Pollack, and B. A. Smith, Variable features on Mars: Preliminary Mariner 9 television results, *Icarus, 17,* p. 346-372, 1972.

Schofield, J. T., J. R. Barnes, D. Crisp, R. M. Haberle, S. Larsen, J. A. Magalhaes, J. R. Murphy, A. Seiff, and G. Wilson, The Mars Pathfinder atmospheric structure investigation/meteorology (ASI/MET) experiment, *Science, 278,* 1752-1757, 1997.

Sharp, R. P. Wind ripples, *J. Geology, 71,* 617-636,1963.

Sharp, R. Wind-driven sand in the Coachella Valley, California, Geol. Soc. Am. Bull., 75, 785-804, 1964.

Sharp, R. P. Kelso Dunes, Mojave Desert, California, *Geol. Soc. Am. Bull., 77,* 1045-1074, 1966.

Sharp, R., Wind-driven sand in the Coachella Valley, California: Further data, Geol. Soc. Am. Bull., 91, 724-730, 1980.

Sharpton, V. L. and J. W. Head III, Lunar mare ridges: Analysis of ridge-crater intersections and implications for the tectonic origin of mare ridges, *Proc. Lunar Planet Sci. Conf, 18,* 307-317, 1988.

Smith, D. E., M.T. Zuber, H.V. Frey, J.B. Garvin, J.W. Head, D.O. Muhleman, G.H. Pettengill, R.J. Phillips, S.C. Solomon, H.J. Zwally, W.B. Banerdt, T.C. Duxbury, M.P. Golombek, F.G. Lemoine, G.A. Neumann, D.D. Rowlands, O. Aharonson, P.G. Ford, A.B. Ivanov, P.J. McGovern, J.B.Abshire, R.S. Afzal, and X. Sun, The global topography of Mars and implications for surface evolution, *Science, 284,* 1495-1503, 1999.

Smith, D.E., M.T. Zuber, H.V. Frey, J.B. Garvin, J.W. Head, D.O. Muhleman, G.H. Pettengill, R.J. Phillips, S.C. Solomon, H.J. Zwally, W.B. Banerdt, T.C. Duxbury, M.P. Golombek, F.G. Lemoine, G.A. Neumann, D.D. Rowlands, O. Aharonson, P.G. Ford, A.B. Ivanov, P.J. McGovern, J.B.Abshire, R.S. Afzal, and X. Sun, Mars Orbiter Laser Altimeter (MOLA): Experiment summary after the first year of global mapping of Mars, *J. Geophys. Res, 106,* 23689-23722, 2001.

Smith, H. T. U., Aeolian deposition in Martian craters, *Nature - Physical Science, 238,* 72-74, 1972.

Smith, M. D., J. L Bandfield, and P. R. Christensen, Separation of atmospheric and surface spectral features in Mars Global Surveyor Thermal Emission Spectra (TES) spectra, *J. Geophys. Res, 105,* 9589-9607, 2000.

Steidtmann, J. R., Ice and snow in eolian sand dunes of southwestern Wyoming, *Science, 179,* 796-798, 1973.

Sutton, J. L., C. B. Leovy, and J. E. Tillman, Diurnal variations of the Martian surface layer meteorological parameters during the first 45 sols at two Viking lander sites, *J. Atmos. Sci., 35,* 2346-2355, 1978.

Thomas, P. Present wind activity on Mars: Relation to large latitudinally zoned sediment deposits, *J. Geophys. Res., 87,* 9999-10,008, 1982.

Thomas, P. Martian intracrater splotches: Occurrence, morphology, and colors, *Icarus, 57,* 205-227, 1984.

Thomas, P., and J. Veverka, Seasonal and secular variation of wind streaks on Mars: An analysis of Mariner 9 and Viking Data, *J. Geophys. Res., 84,* 8131-8146, 1979.

Thomas, P. and J. Veverka, Red/violet contrast reversal on Mars: Significance for eolian sediments, *Icarus, 66,* 39-55, 1986.

Thomas, P., J. Veverka, D. Gineris, and L. Wong, "Dust" streaks on Mars, *Icarus, 60,* 161-179, 1984.

Thomas, P., J. Veverka, S. Lee, and A. Bloom, Classification of wind streaks on Mars, *Icarus, 45,* 124-153, 1981.

Toigo, A. D. Behavior of dust in the Martian atmosphere, Ph.D. Thesis, California Institute of Technology, 139 pp., 2001.

Toigo, A. D., M. I. Richardson, R. J. Wilson, H. Wang, and A. P. Ingersoll, A first look at dust lifting and dust storms near the south pole of Mars with a mesoscale model, *J. Geophys. Res., 107,* 10.1029/2001JE001592, 2002a.

Toigo, A. D., M. I. Richardson, S. P. Ewald, P. J. Gierasch, and R. J. Wilson, Numerical simulation of Martian dust devils, submitted to *J. Geophys. Res.,* 2002b.

Toigo, A. and M. I. Richardson, Comparison of a Mars mesoscale model to Martian Lander meteorological data, paper presented at Division for Planetary Sciences Meeting, Div. for Planet. Sci., Am. Astron. Soc., Pasadena, Calif., Oct. 23-27, 2000.

Vasavada, A. R., J.-P. Williams, D. A. Paige, K. E. Herkenhoff, N. T. Bridges, R. Greeley, B. C. Murray, D. S. Bass, and K. S. McBride, Surface properties of Mars' polar layered deposits and polar landing sites, *J. Geophys. Res, 105,* 6961-6970, 2000.

Vaucouleurs, G. H. de, *Physics of the Planet Mars, An Introduction to Aerophysics*, London: Faber and Faber, 1954.

Veverka, J., P. Gierasch, and P. Thomas, Wind streaks on Mars: Meteorological control of occurrence and mode of formation, *Icarus, 45,* 154-166, 1981.

Ward, A. W., K. B. Doyle, P. J. Helm, M. K. Weisman, and N. E. Witbeck, Global map of eolian features on Mars, *J. Geophys. Res., 90,* 2038-2056, 1985.

Ward, A. W., Yardangs on Mars: Evidence of recent wind erosion, *J. Geophys. Res., 84,* 8147-8166, 1979.

Ward, W. R., Long-term orbital and spin dynamics of Mars, in *Mars,* edited by H. H. Kieffer et al., pp. 298-320, Univ. of Ariz. Press, Tucson, 1992.

Wasson R. J. and R. Hyde, Factors determining desert dune type, *Nature, 304,* 337-339, 1983.

Watters, T. R. Wrinkle ridge assemblages on the terrestrial planets, *J. Geophys. Res., 89,* 10,236-10,254, 1988.

White, B. R. Soil transport by winds on Mars, *J. Geophys. Res., 84,* 4643-4651, 1979.

Williams, S. H., J. R. Zimbelman, A. W. Ward, Large ripples on Earth and Mars, In *Lunar and Planet. Sci. XXXIII,* Abst #1508, LPI, Houston (CD-ROM), 2002.

Wilson, I. G., Desert sandflow basins and a model for the development of ergs, *Geographical Journal, 137,* 180-199, 1971.

Wilson, I. G., Aeolian bedforms — their development and origins, *Sedimentology, 19,* 173-210, 1972.

Wilson, I. G. Ergs, *Sediment. Geol., 10,* 77-106, 1973.

Wilson, R. J., A general circulation model simulation of the Martian polar warming, *Geophys. Res. Lett., 24,* 123-126, 1997.

Wilson, R. J., and K. Hamilton, Comprehensive model simulation of thermal tides in the Martian atmosphere, *J. Atmos. Sci., 53,* 1290-1326, 1996.

Wilson, R. J., and M. I. Richardson, Comparison of Mars GCM dust storm simulations with Viking Mission observations, The Fifth International Conference on Mars [CD-ROM], LPI Contrib. 972, abstract 6234, Lunar Planet. Inst., Houston, Tex., 1999.

Wilson, R. J., and M. I. Richardson, The Martian atmosphere during the Viking Mission, 1: Infrared measurements of atmospheric temperatures revisited, *Icarus, 145,* 555-579, 2000.

Wood, C. A. and J. W. Head, Comparison of impact basins on Mercury, Mars, and the Moon, *Proc. Lunar Sci. Conf. VII,* 3629-3651, 1976.

Wyatt, M. B., J. L. Bandfield, H. Y. McSween, Jr., and P. R. Christensen, Compositions of low albedo intracrater materials and wind streaks on Mars: Examination of MGS TES data in western Arabia Terra, In *Lunar and Planet. Sci. XXXII,* Abst #1872, LPI, Houston (CD-ROM), 2001.

Wyatt, M. B., and H. Y. McSween, Jr., Spectral evidence for weathered basalt as an alternative to andesite in the northern lowlands of Mars, *Nature, 417,* 263-266, 2002.

Zimbleman, J. R., S. H. Williams, and V. P. Tchakerian, Sand transport paths in the Mojave desert, Southwestern United States, In *Desert Aeolian Processes*, edited by V. P. Tchakerian, pp. 101-130, St. Edmundsbury Press, Bury St. Edmonds, 1995.

Zimbleman, J. R. and S. Wilson, Ripples and dunes in the Syrtis Major region of Mars, as revealed in MOC images, In *Lunar and Planet. Sci. XXXIII,* Abst #1514, LPI, Houston (CD-ROM), 2002.

Zurek, R. W., J. R. Barnes, R. M. Haberle, J. B. Pollock, J. E. Tillman, and C. B. Leovy, Dynamics of the atmosphere of Mars, in *Mars,* pp. 835-933, Univ. of Ariz. Press, Tucson, 1992